

**Active Control of Sound Transmission/Radiation From
Elastic Plates Using Multiple Piezoelectric Actuators**

by

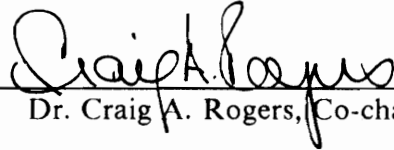
Bor-Tsuen Wang

Dissertation submitted to the Faculty of the
Virginia Polytechnic Institute and State University
in partial fulfillment of the requirements for the degree of
Doctor of Philosophy
in
Department of Mechanical Engineering

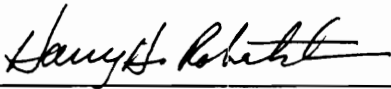
APPROVED:



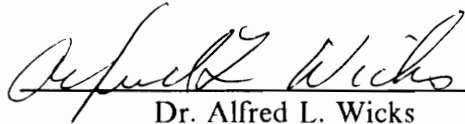
Dr. Chris R. Fuller, Co-chairman



Dr. Craig A. Rogers, Co-chairman



Dr. Harry H. Robertshaw



Dr. Alfred L. Wicks



Dr. Mahendra P. Singh

June, 1991

Blacksburg, Virginia

**Active Control of Sound Transmission/Radiation From
Elastic Plates Using Multiple Piezoelectric Actuators**

by

Bor-Tsuen Wang

Dr. Chris R. Fuller, Co-chairman

Dr. Craig A. Rogers, Co-chairman

Department of Mechanical Engineering

(ABSTRACT)

This thesis presents a theoretical analysis of active control of sound radiation from elastic plates with the use of piezoelectric transducers as actuators. A strain-energy model (SEM), based upon the conservation of strain energy, for a laminate beam with attached or embedded finite-length spatially distributed induced strain actuators was first developed to determine the induced strain distribution. The equivalent axial force and bending moment induced by the embedded or surface bonded actuators were also calculated. The one-dimensional SEM was then extended to a two-dimensional model by employing the classical laminate plate theory and utilizing Heaviside functions to integrate the actuator influence on the substructure. The mechanics model can determine the structural coupling effect and predict the structural response as a result of piezoelectric actuation.

A baffled simply-supported rectangular plate subjected to harmonic disturbances was considered as the plant. Piezoceramic materials bonded to the surfaces of the plate or point force shakers were applied as control actuators. Both microphones in the radiated far-field and accelerometers located on the plate were considered as error sensors. In addition, distributed sensors for pressure and structural motion were modelled. The

cost function was formulated as the modulus squared of the error signal. Linear quadratic optimal control theory was then applied to minimize the cost function to obtain the optimal input voltages to the actuators. Both near-field and far-field pressure and intensity responses as well as plate displacement distributions were presented to show the effectiveness and mechanisms of control for various configurations of the actuators and sensors. Plate wavenumber analysis was also shown to provide a further insight into control technique. The results show that piezoelectric actuators perform very well as control sources, and that pressure sensors have many advantages over acceleration sensors while distributed sensors are superior to discrete sensors.

The optimal placement of multiple fixed size piezoelectric actuators in sound radiation control is also presented. A solution strategy is proposed to calculate the applied voltages to piezoelectric actuators with the use of linear quadratic optimal control theory. The location of piezoelectric actuator is then determined by minimizing an objective function, which is defined as the sum of the mean square sound pressure measured by a number of error microphones. The optimal location of piezoelectric actuators for sound radiation control is found so as to minimize the objective function and shown to be dependent on the excitation frequency. In particular, the optimal placement of multiple piezoelectric actuators for on-resonance and off-resonance excitation is presented. Results show that the optimally placed piezoelectric actuators perform far better in sound radiation control than arbitrarily selected. This work leads to a design methodology for adaptive or intelligent material systems with highly integrated actuators and sensors. The optimization procedure also leads to a reduction in the number of control transducers.

Acknowledgements

The author is greatly indebted to his advisors, Drs. Chris R. Fuller and Craig A. Rogers, for their guidance and patient assistance. Without their invaluable directions and suggestions, the author would not be able to complete this work. The author is very grateful for their help.

The author would like to thank Dr. Ricardo A. Burdisso for his helpful discussion and suggestions in completing this dissertation. The author also thank Drs. Harry H. Robertshaw, Alfred L. Wicks and Mahendra P. Singh for serving on his graduate committee. The author like to acknowledge their kind support.

Siew-Hock Yeo deserves special thanks for his help in editing this thesis. The author would like to express his appreciation to his fellows in the Department of Mechanical Engineering for their friendship. The author extends his gratitude to the staff in User Services and in Writing Center for their invaluable assistance on solving the computer problems and their patience in correcting my writing.

The author would like to thank his parents, Cheng Hsin and Hsien-Teh Wang, and his family for their support and encouragement from overseas. The author like to express his love and affection to his wife, Jane, and his son, Vinson. Their presence in his life strengthened the author to struggle through the most stressful time and fulfilled the author a colorful memory during his graduate study.

Table of Contents

Chapter 1 : Introduction	1
1.1 Background	1
1.2 Active Control Systems for Structural Acoustic Control	3
1.2.1 Plant	3
1.2.2 Sensors	8
1.2.3 Actuators	10
1.2.4 Controller	13
1.3 Scope and Objectives	14
1.4 Organization of Thesis	17
Chapter 2 : Mechanics Model of Piezoelectric Actuator-Beam and Actuator-Plate Systems ..	19
2.1 Theoretical Analysis	22
2.1.1 Strain-Energy Model for a Laminate Actuator-Beam	22
2.1.2 Strain-Energy Model for a Laminate Actuator-Plate	28
2.2 Examples	39
2.2.1 Illustration of Actuator-Beam (Pure Bending)	39
2.2.1.1 Static Analysis	43

2.2.1.2 Dynamic Analysis	44
2.2.2 Illustration of Actuator-Plate	50
2.2.2.1 One Isotropic Layer with Two Piezoceramic Patches (Pure Bending)	50
2.2.2.2 One Isotropic Layer with Two Piezoceramic Patches (Pure Extension)	60
2.2.2.3 Two-Layered ($\theta^\circ / -\theta^\circ$) Laminate with One Piezoceramic Patch	61
2.3 Summary	63
Chapter 3 : Active Control of Sound Radiation	66
3.1 Plate Vibration	69
3.1.1 Point Force	71
3.1.2 Uniformly Distributed Pressure	72
3.1.3 Incident Plane Wave	72
3.1.4 Piezoelectric Excitation	73
3.2 Sound Radiation	75
3.2.1 Sound Pressure in the Near-Field	75
3.2.2 Sound Pressure in the Far-Field	76
3.3 Linear Quadratic Optimal Control	78
3.3.1 Distributed Pressure Sensor	78
3.3.2 Discrete Pressure Sensor (Microphone)	82
3.3.3 Distributed Acceleration Sensor	85
3.3.4 Discrete Acceleration Sensor (Accelerometer)	90
3.4 Special Topics in Structural Acoustics	93
3.4.1 Plate Transmission Loss	93
3.4.2 Time-Averaged Intensity	94
3.4.3 Plate Wavenumber Analysis	96
3.4.4 Radiation Efficiency	98
3.4.4.1 Mode Radiation Efficiency	99

3.4.4.2 Average Radiation Efficiency	107
3.5 Analytical Results	108
3.5.1 Structural Disturbance Input Controlled by Piezoelectric Actuators	109
3.5.1.1 Effect of Number of Actuators	114
3.5.1.2 Effect of Size of Actuators	124
3.5.1.3 Effect of Location of Actuators	127
3.5.1.4 Summary	132
3.5.2 Incident Plane Wave Disturbance Controlled by Point Force or Piezoelectric Actuators	133
3.5.2.1 Effect of Number of Control Sources	134
3.5.2.2 Comparison Between Piezoelectric and Point Force Actuators	144
3.5.2.3 Summary	157
3.5.3 Near-Field Pressure and Intensity Distributions	158
3.5.3.1 Pressure and Intensity Distributions	161
3.5.3.2 Wavenumber Distributions	178
3.5.3.3 Summary	182
3.5.4 Comparison of Different Forms of Cost Functions	183
3.5.4.1 Modal Radiation Efficiency	184
3.5.4.2 On-Resonance Excitation	188
3.5.4.3 Off-Resonance Excitation	195
3.5.4.4 Radiated Power and Average Radiation Efficiency	201
3.5.4.5 Summary	205
3.6 Summary	206

Chapter 4 : Optimal Placement of Piezoelectric Actuators for Controlling Sound Radiation

from Plates	208
4.1 Mathematical Formulation for Optimization Problem	210
4.1.1 Design Variable	210

4.1.2 Objective Function	212
4.1.3 Design Constraint	214
4.2 Application to Optimal Placement of Piezoelectric Actuators	215
4.3 Optimization Algorithm	216
4.4 Solution Strategy	218
4.4.1 LQOCT for Solving Applied Voltages to Actuators	220
4.5 Analytical Results	221
4.5.1 Sub-Region Search Method	221
4.5.2 Optimal Location of One Actuator for Different Excitation Frequencies	228
4.5.3 Optimal Location of Multiple Actuators for Different Excitation Frequencies	231
4.5.3.1 On-Resonance Excitation, $f = 357$ Hz, Near (3,1) Resonant Mode	231
4.5.3.2 Off-Resonance Excitation, $f = 272$ Hz, Between (2,1) and (3,1) Resonant Modes	236
4.6 Computing Time Analysis	242
4.7 Summary	242
Chapter 5 : Overall Conclusions and Recommendations	246
5.1 Overall Conclusions	246
5.1.1 Category (1)	247
5.1.2 Category (2)	247
5.1.3 Category (3)	249
5.2 Recommendations	250
Appendix A. Nomenclature	253
References	261

Vita 272

List of Illustrations

Figure 1. Schematic of feedback and feedforward control block diagrams 4

Figure 2. Overview of active structural acoustic and vibration control 5

Figure 3. Arrangement of the LMS adaptive feedforward control (Fuller et al., 1989) 15

Figure 4. Arrangement and coordinates of laminate actuator-beam 23

Figure 5. Equivalent force and moment induced by the k-th actuator 24

Figure 6. Arrangement and coordinates of laminate actuator-plate 29

Figure 7. Illustration of Heaviside and Delta functions 33

Figure 8. Illustration of actuator-beam (pure bending) 40

Figure 9. Relative error of tip displacement 45

Figure 10. Modal amplitude and modal response for $t_b/t_a = 10.49$ 49

Figure 11. Modal amplitude and modal response for $t_b/t_a = 3.15$ 51

Figure 12. One isotropic layer with two piezoceramic patches (pure bending) 52

Figure 13. Illustration of C_0/C''_0 and C'_0/C''_0 by varying thickness and modulus ratios 56

Figure 14. Illustration of C''_0 by varying thickness and modulus ratios 59

Figure 15. Two-layered ($\theta^\circ / -\theta^\circ$) laminate with one piezoceramic patch 62

Figure 16. Arrangement and coordinates of the baffled simply-supported plate 70

Figure 17. Schematic of intensity calculation 95

Figure 18. The radiation efficiency of the (m,n) mode for a square plate (Wallace, 1972) 101

Figure 19. Illustration of wavenumber distribution (Mathur, Gardner, and Burge, 1990; Maidanik, 1974)	105
Figure 20. Illustration of corner, edge and surface mode radiations (Fahy, 1985)	106
Figure 21. Illustration of mode shapes of simply-supported rectangular plate and modal radiation directivity (Clark and Fuller, 1990b)	110
Figure 22. Plate displacement distribution for different number of piezoelectric actuators, $f=68.4$ Hz	115
Figure 23. Radiation directivity pattern for different number of piezoelectric actuators, $f=68.4$ Hz	116
Figure 24. Plate displacement distribution for different number of piezoelectric actuators, $f=148.8$ Hz	118
Figure 25. Radiation directivity pattern for different number of piezoelectric actuators, $f=148.8$ Hz	119
Figure 26. Radiation directivity pattern for different number of piezoelectric actuators, $f=108.0$ Hz	121
Figure 27. Radiated power for different number of piezoelectric actuators	123
Figure 28. Plate displacement distribution for different location of piezoelectric actuators, $f=148.8$ Hz	129
Figure 29. Radiation directivity pattern for different location of piezoelectric actuators, $f=148.8$ Hz	130
Figure 30. Radiated power for different location of piezoelectric actuators	131
Figure 31. Radiation directivity pattern for different location of piezoelectric actuators, $f=85$ Hz	136
Figure 32. Plate displacement distribution for different location of piezoelectric actuators, $f=85$ Hz	139
Figure 33. Radiation directivity pattern for different location of piezoelectric actuators, $f=190$ Hz	142
Figure 34. Plate displacement distribution for different location of piezoelectric actuators, $f=190$ Hz	145
Figure 35. Radiation directivity pattern for one disturbance and one actuator, $f=85$ Hz	147
Figure 36. Plate displacement distribution for one disturbance and one actuator, $f=85$ Hz	148

Figure 37. Radiation directivity pattern for one disturbance and two actuators, f= 190 Hz	150
Figure 38. Plate displacement distribution for one disturbance and two actuators, f= 190 Hz	151
Figure 39. Radiation directivity pattern for one disturbance and three actuators, f= 140 Hz	152
Figure 40. Plate displacement distribution for one disturbance and three actuators, f= 140 Hz	153
Figure 41. Plate transmission loss versus excitation frequency	156
Figure 42. Radiation directivity for 2 mm plate, f= 357 Hz	162
Figure 43. Pressure distribution (xy-plane) for the primary source only, 2 mm plate, f= 357 Hz	164
Figure 44. Pressure distribution (xy-plane) for the controlled, 2 mm plate, f= 357 Hz, error mike at (1.8 m, 0°, 0°)	165
Figure 45. Time-averaged intensity distribution (xy-plane) for the primary source only, 2 mm plate, f= 357 Hz	166
Figure 46. Time-averaged intensity distribution (xy-plane) for the controlled, 2 mm plate, f= 357 Hz, error mike at (1.8 m, 0°, 0°)	167
Figure 47. Pressure distribution (xy-plane) for the controlled, 2 mm plate, f= 357 Hz, error mike at (1.8 m, 50°, 0°)	169
Figure 48. Time-averaged intensity distribution (xy-plane) for the controlled, 2 mm plate, f= 357 Hz, error mike at (1.8 m, 50°, 0°)	170
Figure 49. Pressure distribution (xz-plane) for the primary source only, 2 mm plate, f= 357 Hz	172
Figure 50. Intensity vector (xz-plane) for the primary source only, 2 mm plate, f= 357 Hz	173
Figure 51. Pressure distribution (xz-plane) for the controlled, 2 mm plate, f= 357 Hz, error mike at (1.8 m, 0°, 0°)	174
Figure 52. Intensity vector (xz-plane) for the controlled, 2 mm plate, f= 357 Hz, error mike at (1.8 m, 0°, 0°)	175
Figure 53. Pressure distribution (xz-plane) for the controlled, 2 mm plate, f= 357 Hz, error mike at (1.8 m, 50°, 0°)	176
Figure 54. Intensity vector (xz-plane) for the controlled, 2 mm plate, f= 357 Hz, error mike at (1.8 m, 50°, 0°)	177

Figure 55. Wavenumber spectra of modal velocity along κ_x and κ_y axis	179
Figure 56. The (m,n) mode radiation efficiency versus wavenumber ratio	185
Figure 57. The (m,n) mode radiation efficiency versus excitation frequency	186
Figure 58. Radiation directivity for on-resonance excitation, $f=357$ Hz	189
Figure 59. Plate displacement distribution for on-resonance excitation, $f=357$ Hz	191
Figure 60. Wavenumber spectra of plate modal velocity along κ_x and κ_y axis, for on-resonance excitation, $f=357$ Hz	194
Figure 61. Radiation directivity for off-resonance excitation, $f=272$ Hz	196
Figure 62. Plate displacement distribution for off-resonance excitation, $f=272$ Hz	198
Figure 63. Wavenumber spectra of plate modal velocity along κ_x and κ_y axis, for off-resonance excitation, $f=272$	200
Figure 64. Radiated power versus excitation frequency	202
Figure 65. Average radiation efficiency versus excitation frequency	204
Figure 66. Illustration of design variables	211
Figure 67. Flow chart of solution strategy	219
Figure 68. Location of error microphones	223
Figure 69. Distribution of objective function and control voltage for $f=87$ Hz . .	225
Figure 70. Distribution of objective function and control voltage for $f=357$ Hz .	226
Figure 71. Distribution of objective function and control voltage for $f=272$ Hz .	227
Figure 72. Radiation directivity pattern for $f=357$ Hz	234
Figure 73. Plate displacement distribution for $f=357$ Hz	237
Figure 74. Radiation directivity pattern for $f=272$ Hz	240
Figure 75. Plate displacement distribution for $f=272$ Hz	241

List of Tables

Table 1.	Physical meaning of the derivatives of the generalized location function .	34
Table 2.	Comparison between strain-energy and pin-force models (Lazarus and Crawley, 1989)	42
Table 3.	Physical properties of G-1195 piezoceramic patch (Piezo Systems, 1987)	47
Table 4.	Natural frequencies of simply-supported beam (rad/sec)	48
Table 5.	Summary of frequency and wavenumber	104
Table 6.	Plate specification	112
Table 7.	Natural frequencies of plate $h = 1.5875$ mm (Hz)	113
Table 8.	Effect of size of piezoelectric actuators, $f = 68.4$ Hz	125
Table 9.	Effect of size of piezoelectric actuators, $f = 148.8$ Hz	126
Table 10.	Natural frequencies of plate $h = 2$ mm (Hz)	135
Table 11.	Total reduction of radiated acoustic power (dB)	138
Table 12.	Modal amplitude of plate vibration (dB), $f = 85$ Hz	140
Table 13.	Modal amplitude of sound pressure (dB), $f = 190$ Hz	143
Table 14.	Modal critical frequencies of plate (Hz)	187
Table 15.	Summary of on- and off-resonance excitation cases	193
Table 16.	Location of error microphones	222
Table 17.	Results for one actuator with different excitation frequencies	230
Table 18.	On-resonance excitation, $f = 357$ (Hz), near (3,1) mode	232
Table 19.	Off-resonance excitation, $f = 272$ (Hz), between (2,1) and (3,1) modes . .	238

Table 20. Typical example of CPU time for optimization 243

Chapter 1 : Introduction

1.1 Background

Noise control has become an increasingly important issue. Noise, unwanted sound usually irritating and bothersome, is a by-product of the highly industrialized societies. There are various kinds of noise sources, for examples jets, automobiles, machines and so on, which are necessary as part of our present society but they have the disadvantage of creating annoyance in many applications.

In addition to environmental concerns, noise control is also important for some special applications. Submarines need to be quiet while operating in order to keep their position undetected by enemy forces. Cabin noise from the aircraft engines can cause psychological fatigue to pilots and passengers, due to prolong exposure in a high level sound environment affecting not only comfort but also job performance. It is becoming increasingly important to maintain an "acceptable" quiet environment, which will provide passengers with a comfortable trip and ensure crew a safe performance.

Noise control is a process to attenuate the unwanted sound to an acceptable level. Most noises come from vibrating structures, whose motions arise from operating machines. Since sound transmission can be either air-borne or structure-borne, much effort has been made to identify the noise source and its paths such that a suitable, effective control method can be applied. There are two main categories of control methods, passive and active controls. Passive control is customarily adopted to reduce the noise transmission by changing the physical properties of the structures, for instance, absorption materials, damping layers, vibration isolators; however, their effectiveness is limited. Active control appears to be an effective way to reduce low frequency sound radiation and transmission without the disadvantages of passive control, such as weight, size, etc. The two main techniques of active control are (1) to apply active forces directly to vibrating structures so as to suppress the structural vibration, which contributes to the sound radiation, and (2) to employ active sound sources in the radiation field so as to cancel the radiating sound waves.

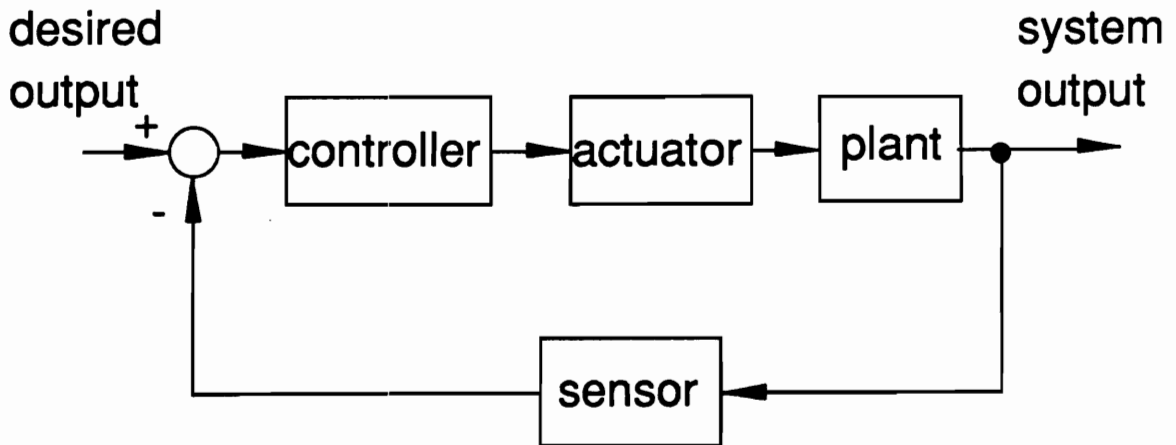
Recently, active control of noise and vibration has generated a great deal of interest, due to not only the control effectiveness but also the development of rapid microprocessors, low power distributed sensors and actuators, and suitable adaptive control algorithms. The so-called "smart, adaptive, or intelligent structures", which are structural systems with integrated sensors and actuators, have become an exciting new approach in the field of noise and vibration control. The following sections will discuss active control systems and detail the definition and application of their components as well as review the research and development of active control systems. In particular, the active structural acoustic control (ASAC) approach which is the main objective of this thesis is discussed.

1.2 Active Control Systems for Structural Acoustic Control

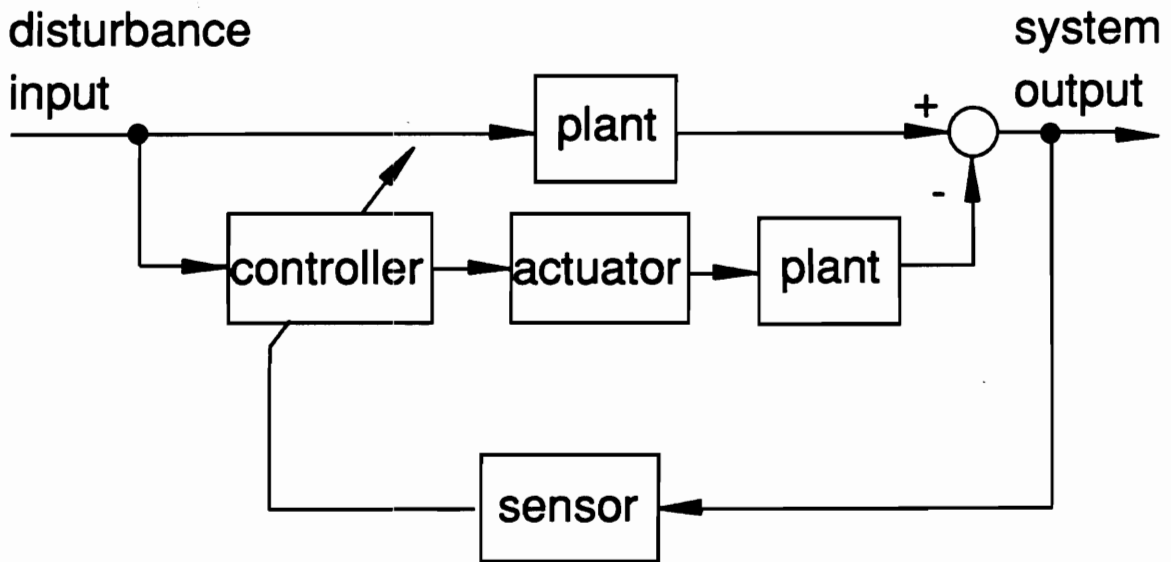
A basic active control system consists of a plant, sensor, actuator and controller. Figure 1(a) shows a schematic of the feedback control block diagram. The sensor is used to detect the system output, so that the measured output signal can be compared to the desired output. The compared error, the difference between the measured output and the desired output, is processed through a controller to drive the actuator which can affect the plant response. Therefore, the system output can be controlled as desired. Figure 1(b) shows a schematic of a feedforward control block diagram. The controller is optimized in order to minimize the least mean square of the error signal, which is the difference between the control input and system output measured by the sensor. Hence, the control actuator can change plant response as desired. The following sections individually describe more about the nature and characteristics of each component as well as a brief literature review of active noise control. Figure 2 shows an overview of active structural acoustic and vibration control systems.

1.2.1 Plant

The plant or the process whose variables are to be controlled is the central element of a control system. In structural acoustic control, plants can be structures, such as beams, plates, shells and cylinders or other enclosures, which can be found in the real world. There is extensive literature dealing with the active control of sound radiation from different structures. The following discussion reviews references in ASAC associated with various structures, including beams, circular plates, rectangular plates, cylin-



(a) feedback control



(b) feedforward control

Figure 1. Schematic of feedback and feedforward control block diagrams

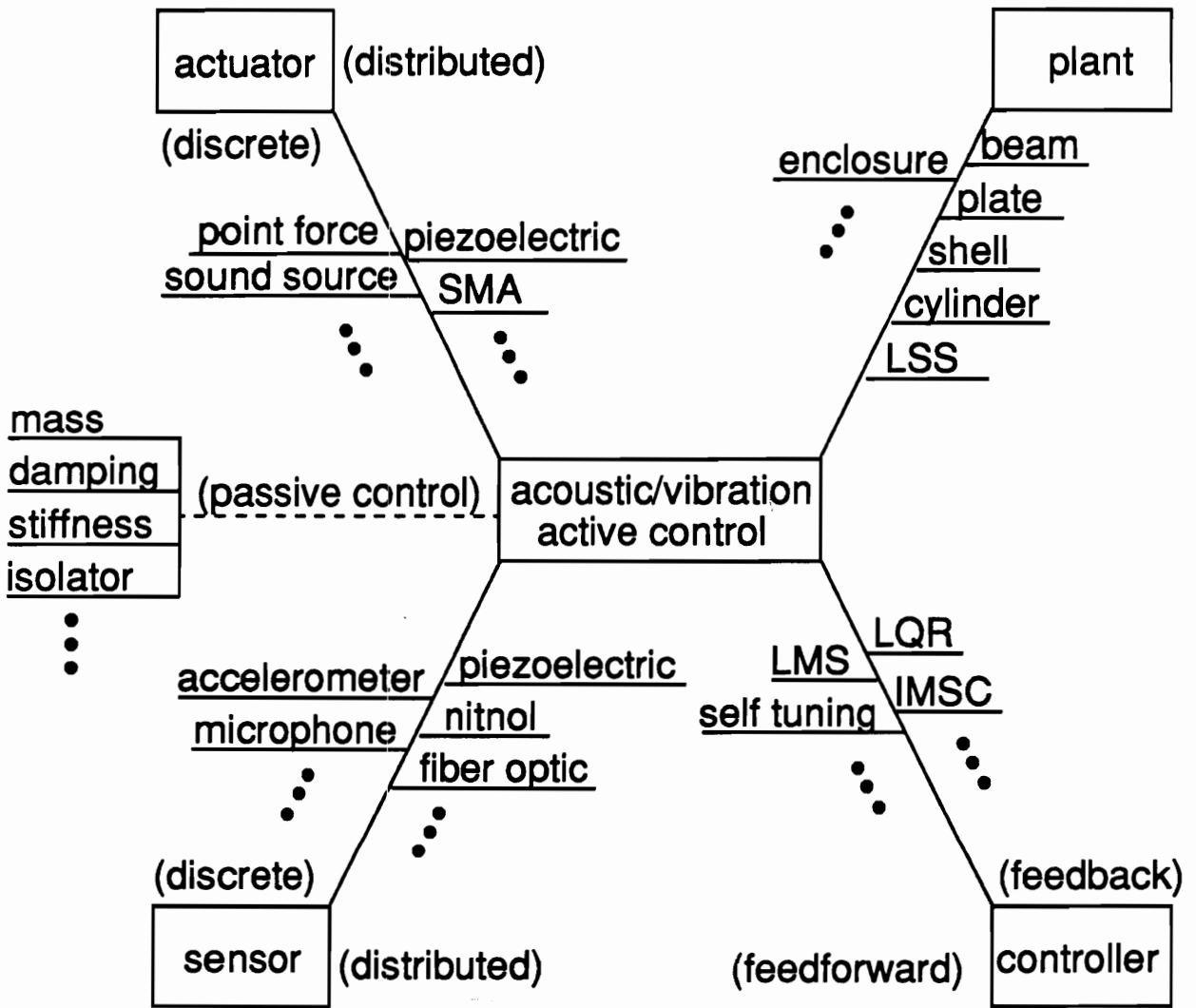


Figure 2. Overview of active structural acoustic and vibration control

ders and enclosures individually. Saunders, Robertshaw and Rogers (1990) presented the use of Shape Memory Alloy (SMA) fibers embedded in composite beams to minimize the sound radiation from harmonic beam vibration. They experimentally showed the feasibility of SMA for structural acoustic control. Burdisso and Fuller (1990) analytically studied the sound radiation from beam with the use of piezoelectric actuators by adopting feedforward control theory. Their work demonstrated that the controlled structure system will possess a new set of eigenvalues and eigenfunctions (mode shapes) due to the influence of the controller dynamics.

Fuller (1990a) analytically studied the active control of sound radiation from a clamped elastic circular thin plate by oscillating forces applied directly to the structures. The main advantage of applying control forces directly to the structure in the form of vibration inputs is that only a low number of control actuators are needed to suppress the structural modes coupling to the acoustic field. However, the implementation of vibrational forces (i.e., magnetic electric shakers) has some drawbacks, such as large volume and requiring a support structure. Dimitriadis and Fuller (1989) presented a theoretical study of using a pie-shaped piezoelectric actuators bonded to a circular plate surface and showed the control ability of piezoelectric actuators in sound radiation from a baffled thin clamped circular plate. These compact distributed actuators overcome the disadvantages of point force shakers.

Deffayet and Nelson (1988) proposed an active control technique which uses a number of discrete monopole "secondary" sound sources to suppress the radiated sound pressure due to the "primary" source from a baffled simply-supported rectangular plate. Quadratic optimization theory was used to minimize the total radiated power. Results showed appreciable reduction in power output can be achieved. However, a number of

the secondary sources are necessary to match the radiation characteristics of the plate mode. Wang, Dimitriadis and Fuller (1989, 1990) analytically studied the use of two small rectangular piezoceramic patches, which are bonded to two sides of the plate surfaces symmetrically and driven 180° out-of-phase, as actuators to actively control sound radiation from a baffled simply-supported rectangular plate in conjunction with the use of LMS adaptive control approaches. They showed the potential of using piezoelectric actuators in a two-dimensional structural acoustic control. Meirovitch and Thangjitham (1990a, 1990b) presented the active control of sound radiation from rectangular plate with/without coupled fluid loading. They essentially proposed to generate feedback control forces (point forces) to suppress structural vibration so as to reduce sound radiation in the far-field. With their approach, a high number of actuators are required to control a relatively large number of modes participating in the sound radiation. The structural system with such a large number of shakers become "bulky" and impractical. Compact distributed actuators and adaptive feedforward control approaches which will be discussed further in Sections 1.2.3 and 1.2.4 respectively can overcome this disadvantage.

Lester and Fuller (1987, 1990) and Jones and Fuller (1989) studied the active control of interior noise inside a flexible cylinder as a simulation of an aircraft fuselage. Lester and Fuller (1987, 1990) applied multiple monopole control sources (termed "active acoustic control", AAC) distributed inside the cylinder to minimize the area-weighted, mean-square acoustic pressure in the circular plane. Jones and Fuller (1989) applied multiple vibrational control forces (termed "active vibrational control", AVC). The significant difference between the AAC and AVC is that the AAC requires twice the number of control sources as the circumferential mode order to be controlled, while the AVC needs only one point controller per mode regardless of circumferential mode order. This

is due to the difference of control physics between monopole sources and vibrational forces which will be explained in details in Section 1.2.3.

Bullmore et al. (1987) applied a number of secondary sources located in a rectangular enclosure to minimize the total time averaged acoustic potential energy in a harmonically excited enclosure. They analytically demonstrated that the optimal locations of secondary sources for maximum power reduction are to be positioned at the locations of maximum pressure response of the primary field. The performance and characteristic of different types of sensors will be discussed further in next section.

1.2.2 Sensors

A sensor is used to detect the system response such that the system output can be monitored and compared to the desired output in order to generate an error signal. The error can then be utilized to determine the control signal in order to operate the actuators and to modify the system response under direction of the control algorithms. In this way, the system output can then be controlled to within a desirable range; hence, the system is called "controlled."

Sensors can be categorized into two groups: (1) discrete and (2) distributed sensors. Accelerometers and microphones, essentially discrete sensors, are most commonly used in ASAC. A few previous works have used accelerometer sensors in ASAC, such as (Meirovitch and Thangjitham, 1990a,1990b). However, microphones are the most popular sensors used in ASAC, for examples (Lester and Fuller, 1990), (Simpson et al., 1989) and (Saunders, Robertshaw, and Rogers, 1990). It is noted that since microphones are to measure the sound pressures in the radiating field while accelerometers measuring the

vibration response, microphones generally perform superior to accelerometers in ASAC. This phenomenon was discussed by Fuller and Jones (1987). They concluded that for ASAC, the use of microphone sensors in the radiating field, which generates error signals containing the structural acoustic coupling information, is advantageous over the use of accelerometers on the structure, which only provide the structural response information.

Dimitriadis and Fuller (1989) and Wang, Dimitriadis and Fuller (1989, 1990) developed a formulation for sound radiation control associated with a cost function which is based on the continuous pressure sensor measurements over a hemisphere in the radiating field. This type of sensor is distributed in nature; however, it is difficult to build such a pressure sensor. Newly developed distributed sensors, such as piezoceramic, PVDF (Polyvinylidene fluoride) and optical fibers, which can be bonded or embedded in the structures, will result in electrical output signals due to the structural response, so they can also be applied to ASAC. Lee (1990a) presented a theory of laminated piezoelectric plates for the design of distributed sensors which can sense motions, such as bending, torsion, shearing, shrinking and stretching of a flexible plate. Lee and Moon (1990b) demonstrated a theory of distributed sensors with a one-dimensional modal sensors using PVDF thin film. The sensor was built similar to modal-filtering by properly shaping the PVDF film to sense each individual mode. Collins et al. (1990) presented a similar distributed piezoelectric film sensor, but different shape from that of Lee and Moon (1990b), applicable to space robotics. Optical fibers, another branch of compact distributed sensors, have also been successfully embedded into composite materials as strain sensors. Claus et al. (1989) presented a brief review of different sensing techniques for optical fiber induced by local strain field, and this will not be repeated here. A practical application of optical fiber strain sensors (Cox, 1990) to beam vi-

bration control is discussed. Cox designed a digital feedback control system to derive control signals from a modal domain fiber optic sensor, and applied them to piezoelectric actuators. He experimentally demonstrated the use of a modal domain fiber optic sensor for vibration control of a flexible cantilever beam.

Much literature was found dealing with the distributed sensors primarily focused on active vibration control (AVC), but little was found to have been concerned with ASAC. Recently, Clark and Fuller (1990b) have shown the feasibility of PVDF piezoelectric films attached to the surface of a plate as error sensors in LMS adaptive feedforward control approaches to minimize sound radiation to the far-field. They used two narrow strips of PVDF sensors positioned symmetrically on the plate in order to observe the odd-odd modes which are the more efficient acoustic radiators. Their work showed much encouragement for the use of compact near-field distributed sensors instead of far-field error microphones, which may not be practical in many circumstances. This work indicates that compact distributed near-field sensors will have a substantial impact in the future development of ASAC.

1.2.3 Actuators

An actuator is a device that can influence the plant response, e.g., the radiating sound from an active structural acoustic control system. Lueg (1936) first proposed to cancel the primary sound wave with the use of secondary sound wave 180° out-of-phase with respect to the primary wave. The sound source (speaker) is applied in the acoustic radiating field to cancel the sound wave. The sound source is not a "real" actuator, which can actively drive structures and then influence the structural sound radiation, but

it acts like an active sound source to cancel the radiated sound in the acoustic field. Many others have also shown the feasibility of using sound sources for sound cancellation. Lester and Fuller (1987, 1990) and Daffayet and Nelson (1988) made use of either monopoles or dipoles as the transducers in active control of sound radiation and showed a favorable noise reduction. However, the application of sound sources to active noise control has their limitation. A number of secondary sound sources are necessary to match the radiation characteristic of the plate mode, as demonstrated by Daffayet and Nelson (1988).

An effective form of actuator to achieve ASAC is to apply vibrational forces directly to vibrating structures. A small number of point force actuators are sufficient to suppress those structural modes which are well coupled to the radiated sound field, and to achieve an appreciable radiated power reduction. Point force shakers are commonly used in ASAC, such as mentioned previously (Jones and Fuller, 1989), (Meirovitch and Thangjitham, 1990a, 1990b) and (Fuller, 1988, 1990a). Those studies showed that shakers can effectively control the sound radiation; however, shakers have substantial disadvantages, due to their large volume, large weight and requiring support.

Distributed actuators have increasingly generated a great deal of interest in either sound or vibration control, because of their light weight and easy implementation. However, most works were concentrated on AVC, and only a few works were associated with ASAC. Recently, distributed actuators, such as piezoceramics and shape memory alloys (SMA), have been attached or embedded in structures to actively control structural vibration and sound radiation. Crawley and de Luis (1987) and Bailey and Hubbard (1985) introduced piezoceramic materials embedded or bonded to beams as control sources to suppress beam lateral vibration. Such an arrangement can also be

applied to ASAC. Dimitriadis, Fuller and Rogers (1991) extended the Crawley and de Luis's work to rectangular plates, i.e., two-dimensional structure problems, with piezoceramic patches ideally bonded to the top and bottom surfaces symmetrically and activated 180° out-of-phase. They showed that properly configured piezoceramic patches can effectively excite the plate out-of-plane motion so as to control plate vibration as well as sound radiation. Dimitriadis and Fuller (1989) and Wang, Dimitriadis and Fuller (1989,1990) presented the theoretical analysis for the use of piezoelectric actuators on active control of sound radiation from elastic plates. A cost function, which is the integration of mean square sound pressure over a hemisphere in the radiation field, was constructed based on the LMS adaptive control approach. Linear quadratic optimal control theory (LQOCT) (Lester and Fuller, 1990) was then employed to minimize the cost function in order to find the optimal control voltages applied to the piezoelectric actuators. Effective sound radiation control was shown to be achieved by appropriately tailoring the location and size of piezoelectric actuators.

Liang, Jia and Roger (1989) showed that a SMA reinforced composite structure can modify its eigenproperties (termed "active properties tuning," APT) and induce recovery forces (termed "active strain energy tuning," ASET) by activating the SMA fibers. Both characteristics of SMA, APT and ASET, have been applied to control sound radiation from composite plates. Analytical results showed that plate transmission loss (TL) profiles can be shifted due to the change of material properties such that TL is increased at fundamental frequencies. Saunders, Robertshaw and Rogers (1990) experimentally demonstrated the use of SMA embedded into a composite beam for ASAC. Two control methods were used to attenuate sound radiation. First, minimization control, based on gradient search techniques, was effective in reducing the measured radiated sound pressure to the background noise levels. Second, peak radiation frequency placement con-

trol, applying a first-order thermal model to drive the system response, allowed tuning of the beam radiation response. These works showed much potential of using distributed actuators in ASAC.

1.2.4 Controller

In addition to the above mentioned components in an active control system, an appropriate controller is needed to perform the system control. Several types of control algorithms have been successfully implemented for ASAC. However, very little work has been concerned with experiments. Meirovitch and Thangjitham (1990b) analytically developed a feedback control algorithm by monitoring the states of the system, namely the displacement and the velocity fields. Their approach is to suppress the total structural vibration so as to reduce the sound radiation. However, their approach required many actuators and sensors in order to achieve sound radiation control. This may not be practical because the plant physical properties, such as weight and size, will be changed due to the attachment of a large number of actuators and sensors, and hence the actual structural response becomes complicated and difficult to predict, thus affecting the optimal gains.

LMS adaptive feedforward control algorithms have been successfully applied to ASAC with a steady state sinusoidal input, such as (Elliott et al., 1987) and (Fuller et al., 1989). The algorithm is used to adjust the magnitude and phases of the sinusoidal inputs to the control actuators so as to minimize the sum of the mean squares pressures which are measured by a set of error microphone sensors. For a feedback control approach, only the system output measured directly from the sensor is processed to acti-

vate actuators in order to influence plant response. On the other hand, in addition to the measured system output, the feedforward control approach requires a reference input correlated to the primary (disturbance) source to control signals, as illustrated in Figure 1. Here, "adaptive" means that the actuation signals applied to actuators can be adjusted through controller by minimizing the least mean square (LMS) of error signal. Therefore, the control actuator inputs can be properly adjusted to affect the plate response and cancel the primary source input. Figure 3 shows an example of such an arrangement of the LMS adaptive feedforward control (Fuller et al., 1989) designed to reduce sound transmission through a plate by vibration inputs. Error microphones were used to measure the sound pressure in the radiating field. The LMS algorithm is then used to adjust the adaptive filters to drive the control shakers such that the mean square of error signals can be minimized. This type of control algorithm can effectively adapt and track the disturbance inputs in the time domain.

1.3 Scope and Objectives

To study sound radiation and control characteristics, this thesis is limited to steady state single frequency disturbance conditions. However, the results can be easily extended to broad-band disturbance signals by superposition. The dominant behavior of most practical structures of interest can be represented by rectangular, uniform, flat plates. Therefore, a simply-supported rectangular baffled plate was considered as the plant to study the control mechanism and to demonstrate the use of the newly proposed compact distributed actuators, i.e., piezoceramic patches bonded to the surfaces of plates, in ASAC. Both discrete and distributed accelerometers or microphones serve as

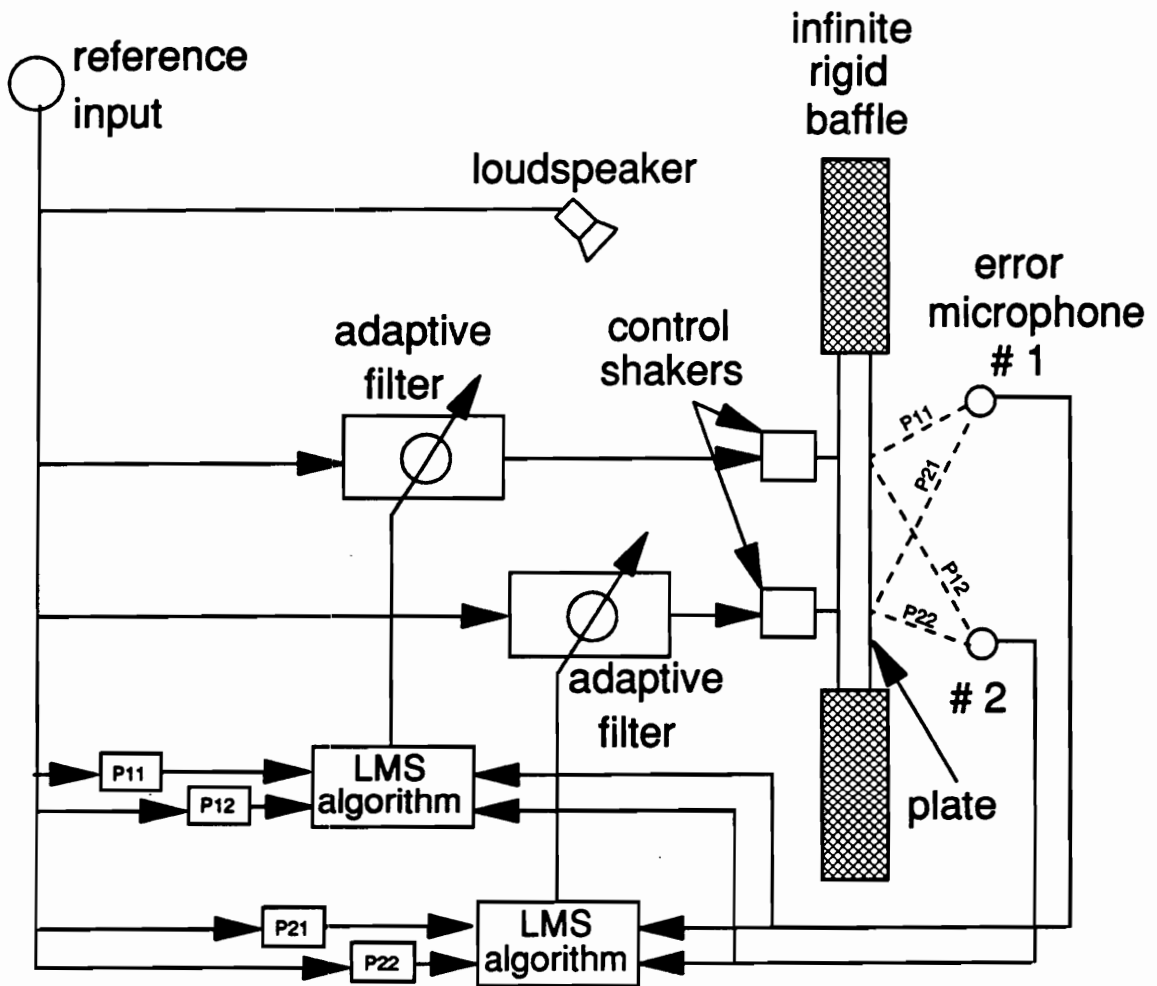


Figure 3. Arrangement of the LMS adaptive feedforward control (Fuller et al., 1989)

error sensors, and the corresponding cost functions are constructed based on the use of the feedforward control algorithm. Linear quadratic optimal control theory (LQOCT) is utilized to minimize a particular cost function corresponding to a specific type of sensors and to find the optimal control voltages applied to actuators. The specific objectives of this thesis are:

1. to develop a mechanics model which will describe the loading function due to the piezoelectric actuators embedded or attached to plates;
2. to employ the LQOCT to optimize control voltage inputs applied to the actuators so as to minimize a particular cost function associated with ASAC;
3. to compare the effectiveness of different forms of actuators and sensors in sound radiation control for feedforward control approaches;
4. to optimize the placement of piezoelectric actuators in sound radiation control for feedforward control approaches.

Two forms of primary inputs (disturbances) are considered in this thesis. They are point force and incident plane wave inputs. The main difference between these two disturbance inputs in terms of spatial transform is that the point force can equally induce all of the plate wavenumber components, while the incident plane wave will intensify the low plate wavenumber components. This can be understood by the analogy between the temporal and spatial transforms. The temporal transform of the impact force, which will result in a white noise response (i.e., equally induce all frequency contents), is analog to the spatial transform of the point force, which can equally induce all of the plate wavenumber components. Similarly, the temporal transform of an impact force with a

period of duration, which can intensify the low frequency contents, is analog to the spatial transform of the incident plane wave, which will intensify the low plate wavenumber components. More explanation of the difference between the point force and the incident plane wave disturbance inputs will be discussed in Section 3.5.

1.4 Organization of Thesis

This thesis basically deals with three main topics: (1) the development of mechanics model, in conjunction with the use of classical laminate plate theory, which describes the structural coupling effect between actuators and structures and predicts the structural response due to the piezoelectric actuation; (2) the application of multiple piezoelectric actuators to the feedforward active control of structural sound radiation from baffled elastic plates due to a harmonic primary input; (3) the optimal placement of piezoelectric actuators for feedforward control in ASAC. A brief literature review associated with each topic is given at the front of each chapter.

Chapter 2 discusses the development of a strain-energy model for a piezoelectric actuator-beam and -plate systems and shows several examples of its applications. A case of pure bending for an actuator-beam system is illustrated and verified by a finite element approach for both static and dynamic analyses. The cases of pure bending, pure extension and the combination of both for piezoelectric actuator-plate are also presented and compared to other models.

Chapter 3 analytically studies active control of sound radiation under various disturbance/actuator/sensor configurations. The Chapter first studies the vibration of plates excited by point forces, uniformly distributed pressures, incident plane waves and piezoceramic patches. The radiated sound pressure in the near- and far-fields is then evaluated by Rayleigh Integral. Next, linear quadratic optimal control theory is applied to obtain the control inputs to the actuators so as to minimize a cost function, which can be the mean square of acceleration or pressure for discrete sensors and vibration energy density or radiating power for distributed sensors individually. Several case studies are presented to show (1) the control effectiveness of point force and piezoelectric actuators, (2) the potential of using piezoelectric actuators in ASAC, (3) the near-field pressure and intensity distributions and plate wavenumber analysis under various control situations, and (4) the use and performance of different forms of cost functions.

Chapter 4 is concerned with the formulation of the optimization problem for the optimal placement of piezoelectric actuators in ASAC in conjunction with the feedforward control algorithm. Design variables, objective functions and physical constraints are identified respectively. A nonlinear constraint minimization IMSL subroutine, using the successive quadratic programming algorithm and a finite difference gradient, is then applied to solve for the optima. Optimal placements of multiple piezoelectric actuators in sound radiation from plates are demonstrated and shown to achieve efficient control.

Chapter 5 contains the main conclusions of the work and also recommends several promising related research topics.

Chapter 2 : Mechanics Model of Piezoelectric Actuator-Beam and Actuator-Plate Systems

"Intelligent material systems and structures", i.e., materials integrated with distributed sensors and actuators, have provoked a great deal of interest in the area of vibration and noise control in recent years. Distributed induced strain actuators, such as piezoceramic materials, have been widely chosen to achieve active control in both structural vibration (Crawley and de Luis, 1987; Bailey and Hubbard, 1985; Fanson and Chen, 1986) and structural acoustics (Dimitriadis and Fuller, 1989; Wang, Dimitriadis and Fuller, 1989,1990).

To fully understand induced strain actuators, a description of the mechanical coupling between the actuators and the structure is needed, and many researchers have been concentrating on developing a model for the interaction between actuators and structures. Fanson and Chen (1986) showed the feasibility of using piezoelectric materials as actuators and sensors in beam vibration control. They introduced the concept of piezoelectric active members to replace passive structural elements for the control of

large space structures (LSS). Crawley and de Luis (1987) developed a static model for one-dimensional piezoceramic patches bonded to the surface or embedded into the body of beams. They showed that piezoceramic patches perfectly bonded symmetrically to the top and bottom surfaces and driven 180° out-of-phase result in two equivalent concentrated moments acting at the edges of the actuator patches. Recently, Im and Alturi (1989) proposed a refined model including the transverse shear and axial forces in addition to the bending moments induced by actuators. Dimitriadis, Fuller and Rogers (1991) presented a two-dimensional model for piezoceramic patches ideally bonded to the top and bottom surfaces of a rectangular plate and subjected to 180° out-of-phase voltages, and showed that, under the assumption of spherical pure bending, the resultant moments induced by the piezoceramic patches were along the four edges. Clark, Fuller and Wicks (1990a) developed the one-dimensional beam and actuator formulation from the plate model obtained by Dimitriadis, Fuller and Rogers (1991), and experimentally verified the analytical model for a wide range of excitation frequencies applied to a simply-supported beam. Those results generally agree with previous one-dimensional results (Crawley and de Luis, 1987).

Tzou and Tseng (1990) developed a finite element formulation for the application of distributed actuators to flexible shells and plates and presented two case study examples. They studied a piezoelectric micro-position device and the distributed vibration identification and control. Ha and Chang (1990) also used finite element analysis to simulate the mechanical and electrical responses of fiber-reinforced laminated composites with the use of distributed piezoelectric actuators. Wang and Rogers (1991b) applied classical laminate plate theory (CLPT) for finite-length, spatially-distributed induced strain actuators embedded or bonded to a plate to determine the equivalent force and moment induced by actuators. They showed that actuators can induce in-plane forces and line

moments along the four edges of the actuator applied to the laminate and result in the coupling of laminate plate extension and bending.

In addition to the use of distributed induced strain actuators in vibration or noise control, the design of distributed induced strain actuators has been investigated with encouraging results. Lee (1987) applied the classical laminate plate theory to the design of piezoelectric laminate for bending and torsional modal control. His experimental results showed that PVDF or PVF₂ (polyvinylidene fluoride) actuators can generate plate bending and twisting independently or simultaneously, and PVDF is suitable for active damping control of a flexible structure. Lazarus and Crawley (1989) developed the pin-force and consistent-plate models for the design of induced strain actuators. Exact solutions can be found only for the unconstrained boundary conditions; however, they also employed the Ritz assumed mode method to solve for problems with other boundary conditions. However, although much progress has been made deriving the basic equations of piezoelectric actuator-structural response, there still remains many areas to investigate and behavior to be understood.

This chapter addresses the development of a theoretical model to determine the equivalent force and moment induced by spatially distributed induced strain actuators attached or embedded in laminate beams and plates either symmetrically or asymmetrically. The strain-energy model (SEM) for a laminate actuator-beam was derived first for a one-dimensional case and then extended to a two-dimensional, laminate actuator-plate problem. The CLPT for induced strain actuators developed by Wang and Rogers (1991b) was revised by the use of the strain-energy model for laminate beams described below. The current approach compares favorably with several other modelling approaches. The cases of pure bending in the beam and plate were illustrated and com-

pared to the pin-force model (Lazarus and Crawley, 1989), the spherical pure bending model (Dimitriadis, Fuller and Rogers, 1991) and a finite element formulation (Robbins and Reddy, 1990). The cases of pure extension and a two layer laminate were also presented.

2.1 Theoretical Analysis

2.1.1 Strain-Energy Model for a Laminate Actuator-Beam

Figure 4 shows the arrangement and coordinates of an arbitrary laminate beam with attached or embedded, finite-length, spatially-distributed actuators. The laminate actuator-beam with a length, L , and a width, b , has n layers, and contains m embedded actuators with a length, L_a , and a width, b_a . The purpose here is to determine the equivalent axial force and bending moment induced by these actuators. The basic assumptions are as follow:

1. utilization of the Euler-Bernoulli beam theory
2. ideal bonding between layers and actuators
3. infinite beam with finite-length actuators, i.e. $L \gg L_a$
4. linear strain distribution, as illustrated in Figure 5, due to an induced strain actuator

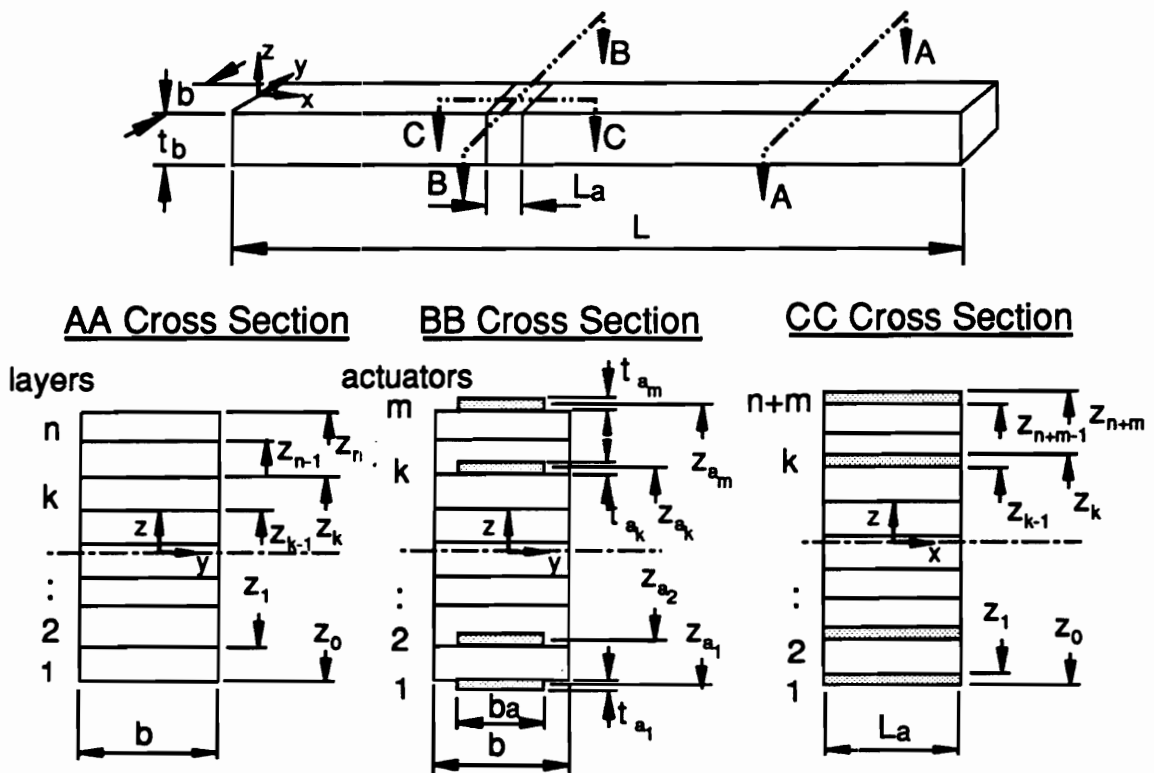


Figure 4. Arrangement and coordinates of laminate actuator-beam

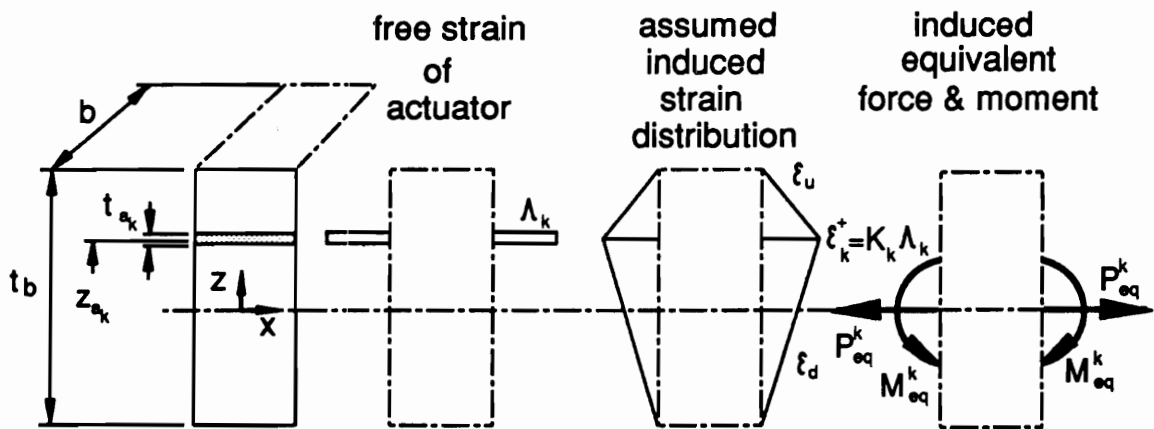


Figure 5. Equivalent force and moment induced by the k -th actuator

5. conservation of strain energy associated with the actuator and the assumed linear strain distribution of the laminate structure.

First, the k -th actuator, as shown in Figure 5, was considered to determine its induced axial force and bending moment. The free strain of the k -th actuator is:

$$\Lambda_k = \frac{d_{31}}{t_{a_k}} V_k \quad (2.1)$$

Furthermore, the induced strain of the beam by this actuator was assumed to be a linear distribution, as shown in Figure 5, and has a magnitude of $\varepsilon_k^+ = K_k \Lambda_k$ at the actuator's location. Note that K_k is the unknown parameter. The distributed strain equations through the thickness of the beam above and below of the actuator can be expressed as:

$$\varepsilon_u = \frac{\varepsilon_k^+}{\frac{t_b}{2} - z_{a_k}} \left(\frac{t_b}{2} - z \right) \quad (2.2)$$

$$\varepsilon_d = \frac{\varepsilon_k^+}{\frac{t_b}{2} + z_{a_k}} \left(\frac{t_b}{2} + z \right) \quad (2.3)$$

Because of the assumption of a linear strain distribution, the resultant actuator strain becomes the difference of the free strain of the actuator and the assumed strain. Therefore, the stress in the k -th actuator can be postulated to be uniform and expressed as

$$\sigma_{a_k} = E_{a_k} (\Lambda_k - \varepsilon_k^+) = E_{a_k} (1 - K_k) \Lambda_k \quad (2.4)$$

The axial force and bending moment drawn by this stress can be found by:

$$P_{a_k} = t_{a_k} E_{a_k} (1 - K_k) b_a \Lambda_k \quad (2.5)$$

$$M_{a_k} = z_{a_k} t_{a_k} E_{a_k} (1 - K_k) b_a \Lambda_k \quad (2.6)$$

Next, from the assumed linear strain distribution, the stress distribution can also be postulated. The induced equivalent bending moment can be obtained by the following integral through the beam thickness:

$$M_{eq}^k = \int_{-\frac{t_b}{2}}^{\frac{t_b}{2}} \sigma z b_a dz \quad (2.7)$$

where σ is the stress distribution due to the assumed strain. By substituting the strain Equations (2.2) and (2.3) into Equation (2.7) and integrating Equation (2.7), the equivalent bending moment becomes

$$M_{eq}^k = \lambda_k K_k b_a \quad (2.8)$$

where

$$\lambda_k = \sum_{\substack{i=1 \\ p < k}}^p \frac{E_i}{\frac{t_b}{2} - z_{a_k}} \left[\frac{t_b}{4} (z_i^2 - z_{i-1}^2) - \frac{z_i^3 - z_{i-1}^3}{3} \right] + \sum_{\substack{i=p \\ p > k}}^{m+n} \frac{E_i}{\frac{t_b}{2} + z_{a_k}} \left[\frac{t_b}{4} (z_i^2 - z_{i-1}^2) + \frac{z_i^3 - z_{i-1}^3}{3} \right] \quad (2.9)$$

Based upon the assumption of an infinite beam, the equivalent bending moment induced by the single actuator must be equal to the bending moment induced by the

assumed strain distribution. This statement is valid because of the conservation of strain energy, which is proportional to the bending moment. By setting Equations (2.6) and (2.8) equal, K_k can be found as:

$$K_k = \frac{z_{a_k} t_{a_k} E_{a_k}}{z_{a_k} t_{a_k} E_{a_k} + \lambda_k} \quad (2.10)$$

The equivalent axial force and bending moment induced by the k -th actuator can be found by substituting K_k into Equations (2.5) and (2.6):

$$P_{eq}^k = t_{a_k} E_{a_k} \left(\frac{\lambda_k}{z_{a_k} t_{a_k} E_{a_k} + \lambda_k} \right) b_a \Lambda_k \quad (2.11)$$

$$M_{eq}^k = z_{a_k} t_{a_k} E_{a_k} \left(\frac{\lambda_k}{z_{a_k} t_{a_k} E_{a_k} + \lambda_k} \right) b_a \Lambda_k \quad (2.12)$$

By superposition, the total equivalent axial force and bending moment induced by m actuators are

$$P_{eq} = \sum_{k=1}^m P_{eq}^k \quad (2.13)$$

$$M_{eq} = \sum_{k=1}^m M_{eq}^k \quad (2.14)$$

Therefore, the resultant force and moment can be considered as external loads to the laminate beam. In particular, for the application of the induced strain actuators to

the beam lateral vibration control, the equivalent axial force can be generally negligible. However, this axial normal force does exist and can generate the vibrational power flow as shown by Gibbs and Fuller (1990). Im and Alturi (1989) demonstrated that actuators result in both the bending moment and the axial force simultaneously, except for the case of pure bending or extension in which the bending moment and axial force exist independently.

2.1.2 Strain-Energy Model for a Laminate Actuator-Plate

Let us consider a rectangular, laminated plate with multiple, embedded induced strain actuators, such as piezoceramic patches. Figure 6 shows the arrangement and coordinates of the actuator-plate model. Under the plane stress state, the stress-strain relations for a lamina in 12-coordinate reduce to

$$\begin{bmatrix} \sigma_1 \\ \sigma_2 \\ \tau_{12} \end{bmatrix} = \begin{bmatrix} Q_{11} & Q_{12} & 0 \\ Q_{21} & Q_{22} & 0 \\ 0 & 0 & Q_{66} \end{bmatrix} \begin{bmatrix} \varepsilon_1 \\ \varepsilon_2 \\ \gamma_{12} \end{bmatrix} \quad (2.15)$$

or in short form

$$\{\bar{\sigma}\} = [Q]\{\bar{\varepsilon}\} \quad (2.16)$$

Then the stress-strain relations for a lamina in xy-coordinate can be shown as:

$$\{\sigma\} = [\bar{Q}]\{\varepsilon\} = \begin{bmatrix} \bar{Q}_{11} & \bar{Q}_{12} & \bar{Q}_{16} \\ \bar{Q}_{12} & \bar{Q}_{22} & \bar{Q}_{26} \\ \bar{Q}_{16} & \bar{Q}_{26} & \bar{Q}_{66} \end{bmatrix} \begin{bmatrix} \varepsilon_x \\ \varepsilon_y \\ \gamma_{xy} \end{bmatrix} \quad (2.17)$$

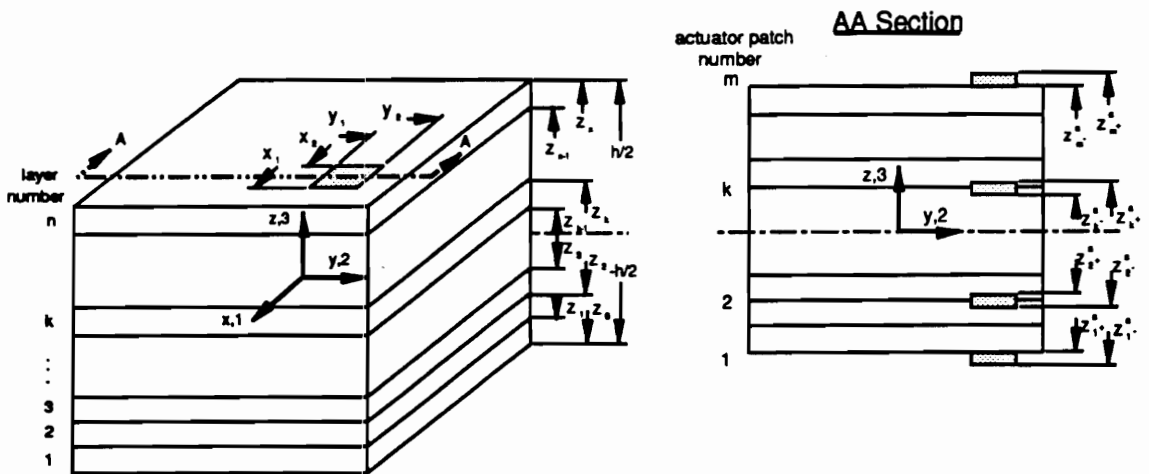


Figure 6. Arrangement and coordinates of laminate actuator-plate

The expressions for Q_{ij} and \bar{Q}_{ij} can be easily found (Jones,1975). The total strain can be shown as the sum of the mechanical and induced actuator strains.

$$\{\varepsilon\} = \{\varepsilon^m\} + \{\Lambda\} \quad (2.18)$$

Under the Kirchhoff's assumption, the mechanical strain vector is given by

$$\{\varepsilon^m\} = \{\varepsilon^0\} + z\{\kappa\} \quad (2.19)$$

where the midplane mechanical strains:

$$\{\varepsilon^0\} = \begin{bmatrix} \varepsilon_x^0 \\ \varepsilon_y^0 \\ \gamma_{xy}^0 \end{bmatrix} = \begin{bmatrix} \frac{\partial u_0}{\partial x} \\ \frac{\partial v_0}{\partial y} \\ \frac{\partial u_0}{\partial y} + \frac{\partial v_0}{\partial x} \end{bmatrix} \quad (2.20)$$

the midplane curvatures:

$$\{\kappa\} = \begin{bmatrix} \kappa_x \\ \kappa_y \\ \kappa_{xy} \end{bmatrix} = - \begin{bmatrix} \frac{\partial^2 w_0}{\partial x^2} \\ \frac{\partial^2 w_0}{\partial y^2} \\ 2 \frac{\partial^2 w_0}{\partial x \partial y} \end{bmatrix} \quad (2.21)$$

and the actuator strains:

$$\{\Lambda\} = \begin{bmatrix} \Lambda_x \\ \Lambda_y \\ \Lambda_{xy} \end{bmatrix} = \begin{bmatrix} \sum_{k=1}^m [H(z - z_{k^+}^a) - H(z - z_{k^-}^a)] \frac{(d_{31})_k}{z_{k^+}^a - z_{k^-}^a} V_k (1 - K_{k_x}) R_k(x, y) \\ \sum_{k=1}^m [H(z - z_{k^+}^a) - H(z - z_{k^-}^a)] \frac{(d_{32})_k}{z_{k^+}^a - z_{k^-}^a} V_k (1 - K_{k_y}) R_k(x, y) \\ \sum_{k=1}^m [H(z - z_{k^+}^a) - H(z - z_{k^-}^a)] \frac{(d_{36})_k}{z_{k^+}^a - z_{k^-}^a} V_k (1 - K_{k_{xy}}) R_k(x, y) \end{bmatrix} \quad (2.22)$$

Note that K_{k_x}, K_{k_y} and $K_{k_{xy}}$, the new terms not included in the previous work of Wang and Rogers (1991b), are defined similarly to K_k in Equation (2.10) except that λ_k should be replaced by $\lambda_{k_x}, \lambda_{k_y}$ and $\lambda_{k_{xy}}$ respectively, and E_i in Equation (2.9) should be replaced by E_{i_x}, E_{i_y} and $E_{i_{xy}}$. The Heaviside function, $H(z - z_0)$, is defined as follows:

$$\begin{aligned} H(z - z_0) &= 1, \quad z \geq z_0 \\ &= 0, \quad z < z_0 \end{aligned} \quad (2.23)$$

and the generalized location function is defined as:

$$\begin{aligned} R_k(x, y) &= 1, \quad (x_1)_k \leq x \leq (x_2)_k, (y_1)_k \leq y \leq (y_2)_k \\ &= 0, \quad \text{elsewhere} \end{aligned} \quad (2.24)$$

For simple application, it is assumed that each actuator patch has the same piezoelectric strain coefficient, i.e. $(d_{ij})_1 = (d_{ij})_2 = \dots = (d_{ij})_m = d_{ij}$, and the same location on the xy-plane, i.e. $R_1 = R_2 = \dots = R_m = R$. Let $R(x, y)$ be expressed with the Heaviside function:

$$R(x, y) = [H(x - x_1) - H(x - x_2)][H(y - y_1) - H(y - y_2)] \quad (2.25)$$

Also, the derivatives of generalized location function are expressed as:

$$\frac{\partial R}{\partial x} = [\delta(x - x_1) - \delta(x - x_2)][H(y - y_1) - H(y - y_2)] \quad (2.26)$$

$$\frac{\partial R}{\partial y} = [H(x - x_1) - H(x - x_2)][\delta(y - y_1) - \delta(y - y_2)] \quad (2.27)$$

$$\frac{\partial^2 R}{\partial x \partial y} = [\delta(x - x_1) - \delta(x - x_2)][\delta(y - y_1) - \delta(y - y_2)] \quad (2.28)$$

$$\frac{\partial^2 R}{\partial x^2} = [\delta'(x - x_1) - \delta'(x - x_2)][H(y - y_1) - H(y - y_2)] \quad (2.29)$$

$$\frac{\partial^2 R}{\partial y^2} = [H(x - x_1) - H(x - x_2)][\delta'(y - y_1) - \delta'(y - y_2)] \quad (2.30)$$

The mathematical interpretation of the Heaviside and Delta functions is illustrated in Figure 7. As $[H(x - x_1) - H(x - x_2)]$ represents a uniform distribution between x_1 and x_2 , $[\delta(x - x_1) - \delta(x - x_2)]$ represents two concentrated sources at x_1 and x_2 respectively, and $[\delta'(x - x_1) - \delta'(x - x_2)]$ represents two moment sources at x_1 and x_2 respectively. Thus the derivatives of generalized location function can be graphically shown in Table 1. The physical meanings of the derivatives of the generalized location function will be discussed further.

Equation (2.17) shows the stress-strain relation for the k-th layer lamina. Equation (2.17) is integrated through the thickness of the laminate to obtain the following Equation (2.31). Also, Equation (2.17) is multiplied by z and integrated through the thickness of the laminate to obtain the following Equation (2.32).

$$\{N\} = [A]\{\varepsilon^0\} + [B]\{\kappa\} - [E]\{d\} \quad (2.31)$$

and

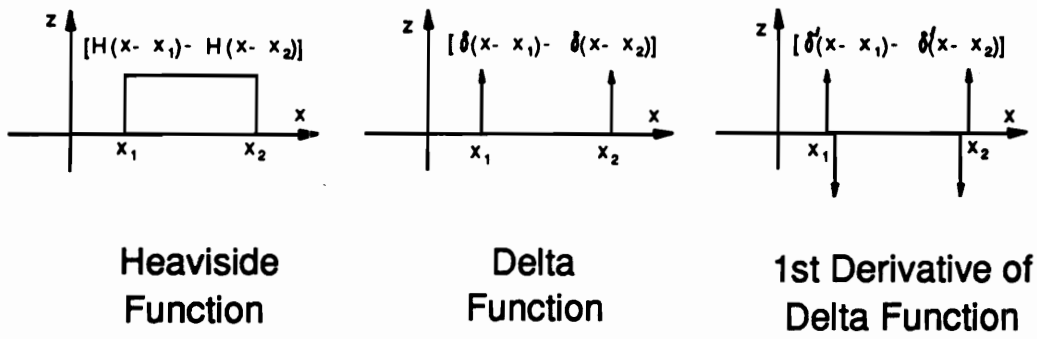


Figure 7. Illustration of Heaviside and Delta functions

Table 1. Physical meaning of the derivatives of the generalized location function

$R(x,y) = [H(x-x_1) - H(x-x_2)] [H(y-y_1) - H(y-y_2)]$	
$\frac{\partial R}{\partial x} = [\delta(x-x_1) - \delta(x-x_2)] [H(y-y_1) - H(y-y_2)]$	
$\frac{\partial R}{\partial y} = [H(x-x_1) - H(x-x_2)] [\delta(y-y_1) - \delta(y-y_2)]$	
$\frac{\partial^2 R}{\partial x^2} = [\delta'(x-x_1) - \delta'(x-x_2)] [H(y-y_1) - H(y-y_2)]$	
$\frac{\partial^2 R}{\partial y^2} = [H(x-x_1) - H(x-x_2)] [\delta'(y-y_1) - \delta'(y-y_2)]$	
$\frac{\partial^2 R}{\partial x \partial y} = [\delta(x-x_1) - \delta(x-x_2)] [\delta(y-y_1) - \delta(y-y_2)]$	

$$\{M\} = [B]\{\varepsilon^0\} + [D]\{\kappa\} - [F]\{d\} \quad (2.32)$$

where

$$\{N\} = \begin{bmatrix} N_x \\ N_y \\ N_{xy} \end{bmatrix} = \int_{-\frac{h}{2}}^{\frac{h}{2}} \begin{bmatrix} \sigma_x \\ \sigma_y \\ \tau_{xy} \end{bmatrix} dz \quad (2.33)$$

$$\{M\} = \begin{bmatrix} M_x \\ M_y \\ M_{xy} \end{bmatrix} = \int_{-\frac{h}{2}}^{\frac{h}{2}} \begin{bmatrix} \sigma_x \\ \sigma_y \\ \tau_{xy} \end{bmatrix} z dz \quad (2.34)$$

$$\{d\} = \begin{bmatrix} d_{31}R \\ d_{32}R \\ d_{36}R \end{bmatrix} \quad (2.35)$$

The i -th row and j -th column element of matrices $[A],[B],[D],[E]$, and $[F]$ is as follows:

$$A_{ij} = \sum_{k=1}^n (\bar{Q}_{ij})_k (z_k - z_{k-1}) \quad (2.36)$$

$$B_{ij} = \frac{1}{2} \sum_{k=1}^n (\bar{Q}_{ij})_k (z_k^2 - z_{k-1}^2) \quad (2.37)$$

$$D_{ij} = \frac{1}{3} \sum_{k=1}^n (\bar{Q}_{ij})_k (z_k^3 - z_{k-1}^3) \quad (2.38)$$

$$\begin{aligned}
E_{ij} &= \sum_{k=1}^m (\bar{Q}_{ij})_k^a (1 - K_{k_x}) V_k, \quad \text{if } j = 1 \\
&= \sum_{k=1}^m (\bar{Q}_{ij})_k^a (1 - K_{k_y}) V_k, \quad \text{if } j = 2 \\
&= \sum_{k=1}^m (\bar{Q}_{ij})_k^a (1 - K_{k_{xy}}) V_k, \quad \text{if } j = 3
\end{aligned} \tag{2.39}$$

$$\begin{aligned}
F_{ij} &= \frac{1}{2} \sum_{k=1}^m (\bar{Q}_{ij})_k^a (1 - K_{k_x}) V_k (z_k^a + z_k^a), \quad \text{if } j = 1 \\
&= \frac{1}{2} \sum_{k=1}^m (\bar{Q}_{ij})_k^a (1 - K_{k_y}) V_k (z_k^a + z_k^a), \quad \text{if } j = 2 \\
&= \frac{1}{2} \sum_{k=1}^m (\bar{Q}_{ij})_k^a (1 - K_{k_{xy}}) V_k (z_k^a + z_k^a), \quad \text{if } j = 3
\end{aligned} \tag{2.40}$$

Note that K_{k_x} , K_{k_y} and $K_{k_{xy}}$, the k -th actuator induced strain constants, are functions of the material and physical properties of the laminate actuator-plate, and relate the interaction of layers and actuators. The equilibrium equations are given as:

$$\frac{\partial N_x}{\partial x} + \frac{\partial N_{xy}}{\partial y} = \rho h \frac{\partial^2 u_0}{\partial t^2} \tag{2.41}$$

$$\frac{\partial N_{xy}}{\partial x} + \frac{\partial N_y}{\partial y} = \rho h \frac{\partial^2 v_0}{\partial t^2} \tag{2.42}$$

$$\frac{\partial^2 M_x}{\partial x^2} + 2 \frac{\partial^2 M_{xy}}{\partial x \partial y} + \frac{\partial^2 M_y}{\partial y^2} = \rho h \frac{\partial^2 w_0}{\partial t^2} - q(x, y, t) \tag{2.43}$$

where

$$\rho = \sum_{k=1}^N \frac{\rho_k h_k}{h} \quad (2.44)$$

If Equations (2.31) and (2.32) are substituted into the equilibrium equations in terms of the midplane displacements u_0 , v_0 and w_0 , and the symbols u , v and w are used for brevity, then the equations of motion become

$$\begin{aligned} & [A_{11} \frac{\partial^2 u}{\partial x^2} + 2A_{16} \frac{\partial^2 u}{\partial x \partial y} + A_{66} \frac{\partial^2 u}{\partial y^2} + A_{16} \frac{\partial^2 v}{\partial x^2} + (A_{12} + A_{66}) \frac{\partial^2 v}{\partial x \partial y} + A_{26} \frac{\partial^2 v}{\partial y^2}] \\ & - [B_{11} \frac{\partial^3 w}{\partial x^3} + 3B_{16} \frac{\partial^3 w}{\partial x^2 \partial y} + (B_{12} + 2B_{66}) \frac{\partial^3 w}{\partial x \partial y^2} + B_{26} \frac{\partial^3 w}{\partial y^3}] \quad (2.45) \\ & = \rho h \frac{\partial^2 u}{\partial t^2} + [(E_{11}d_{31} + E_{12}d_{32} + E_{16}d_{36}) \frac{\partial R}{\partial x} + (E_{16}d_{31} + E_{26}d_{32} + E_{66}d_{36}) \frac{\partial R}{\partial y}] \end{aligned}$$

$$\begin{aligned} & [A_{16} \frac{\partial^2 u}{\partial x^2} + (A_{12} + A_{66}) \frac{\partial^2 u}{\partial x \partial y} + A_{26} \frac{\partial^2 u}{\partial y^2} + A_{66} \frac{\partial^2 v}{\partial x^2} + 2A_{26} \frac{\partial^2 v}{\partial x \partial y} + A_{22} \frac{\partial^2 v}{\partial y^2}] \\ & - [B_{16} \frac{\partial^3 w}{\partial x^3} + (B_{12} + 2B_{66}) \frac{\partial^3 w}{\partial x^2 \partial y} + 3B_{26} \frac{\partial^3 w}{\partial x \partial y^2} + B_{22} \frac{\partial^3 w}{\partial y^3}] \quad (2.46) \\ & = \rho h \frac{\partial^2 v}{\partial t^2} + [(E_{16}d_{31} + E_{26}d_{32} + E_{66}d_{36}) \frac{\partial R}{\partial x} + (E_{21}d_{31} + E_{22}d_{32} + E_{26}d_{36}) \frac{\partial R}{\partial y}] \end{aligned}$$

$$\begin{aligned}
& [B_{11} \frac{\partial^3 u}{\partial x^3} + 3B_{16} \frac{\partial^3 u}{\partial x^2 \partial y} + (B_{12} + 2B_{66}) \frac{\partial^3 u}{\partial x \partial y^2} + B_{26} \frac{\partial^3 u}{\partial y^3} \\
& + B_{16} \frac{\partial^3 v}{\partial x^3} + (B_{12} + 2B_{66}) \frac{\partial^3 v}{\partial x^2 \partial y} + 3B_{26} \frac{\partial^3 v}{\partial x \partial y^2} + B_{22} \frac{\partial^3 v}{\partial y^3}] \\
& - [D_{11} \frac{\partial^4 w}{\partial x^4} + 4D_{16} \frac{\partial^4 w}{\partial x^3 \partial y} + 2(D_{12} + 2D_{66}) \frac{\partial^4 w}{\partial x^2 \partial y^2} + 4D_{26} \frac{\partial^4 w}{\partial x \partial y^3} + D_{22} \frac{\partial^4 w}{\partial y^4}] \\
& = \rho h \frac{\partial^2 w}{\partial t^2} - q(x,y,t) + (F_{11}d_{31} + F_{12}d_{32} + F_{16}d_{36}) \frac{\partial^2 R}{\partial x^2} \\
& \quad + (F_{21}d_{31} + F_{22}d_{32} + F_{26}d_{36}) \frac{\partial^2 R}{\partial y^2} \\
& \quad + 2(F_{16}d_{31} + F_{26}d_{32} + F_{66}d_{36}) \frac{\partial^2 R}{\partial x \partial y}
\end{aligned} \tag{2.47}$$

Equations (2.45)-(2.47) are the equations of motion in terms of the midplane displacement. The last two terms of the right hand side of Equations (2.45) and (2.46) include the $\partial R/\partial x$ and $\partial R/\partial y$ which can be recognized as vertical line forces illustrated in Table 1. The third and fourth terms of the right hand side of Equation (2.47) include $\partial^2 R/\partial x^2$ and $\partial^2 R/\partial y^2$ respectively which can be recognized as line moments along the edges of actuator patch illustrated in Table 1. Additionally, the fifth term of the right hand side of Equation (2.47) includes $\partial^2 R/\partial x \partial y$ which can be recognized as the concentrated forces at the corners of the actuator patch also shown in Table 1. It is noted that these concentrated forces result in laminate twisting.

To solve the equations of motion, boundary conditions need to be specified. The general boundary conditions can be categorized as follow (Whitney, 1989):

1. simply supported : $N_n = N_{nn} = w = M_n = 0$

2. hinged-free in the normal direction : $N_n = u_{,s} = w = M_n = 0$
3. hinged-free in the tangential direction : $u_n = N_{ns} = w = M_n = 0$
4. clamped : $u_n = u_s = w = M_n = 0$
5. free : $N_s = N_{ns} = w = \frac{\partial M_{ns}}{\partial s} + Q_n = 0$

2.2 Examples

2.2.1 Illustration of Actuator-Beam (Pure Bending)

Consider a beam with two actuators attached to the top and bottom of its surface symmetrically as shown on Figure 8, and activated 180 ° out of phase, i.e. $V_1 = -V_2$. The stresses of both actuators can be postulated as

$$\sigma_{a_1} = E_a(-\Lambda + \varepsilon^+) = -E_a(1 - K)\lambda \quad (2.48)$$

$$\sigma_{a_2} = E_a(\Lambda - \varepsilon^+) = E_a(1 - K)\lambda \quad (2.49)$$

where $\Lambda = V_1 d_{31} / t_a$. Therefore, the axial force and bending moment induced by these two actuators are:

$$P_a = P_{a_1} + P_{a_2} = 0 \quad (2.50)$$

$$M_a = M_{a_1} + M_{a_2} = t_a E_a (1 - K) b_a \Lambda \quad (2.51)$$

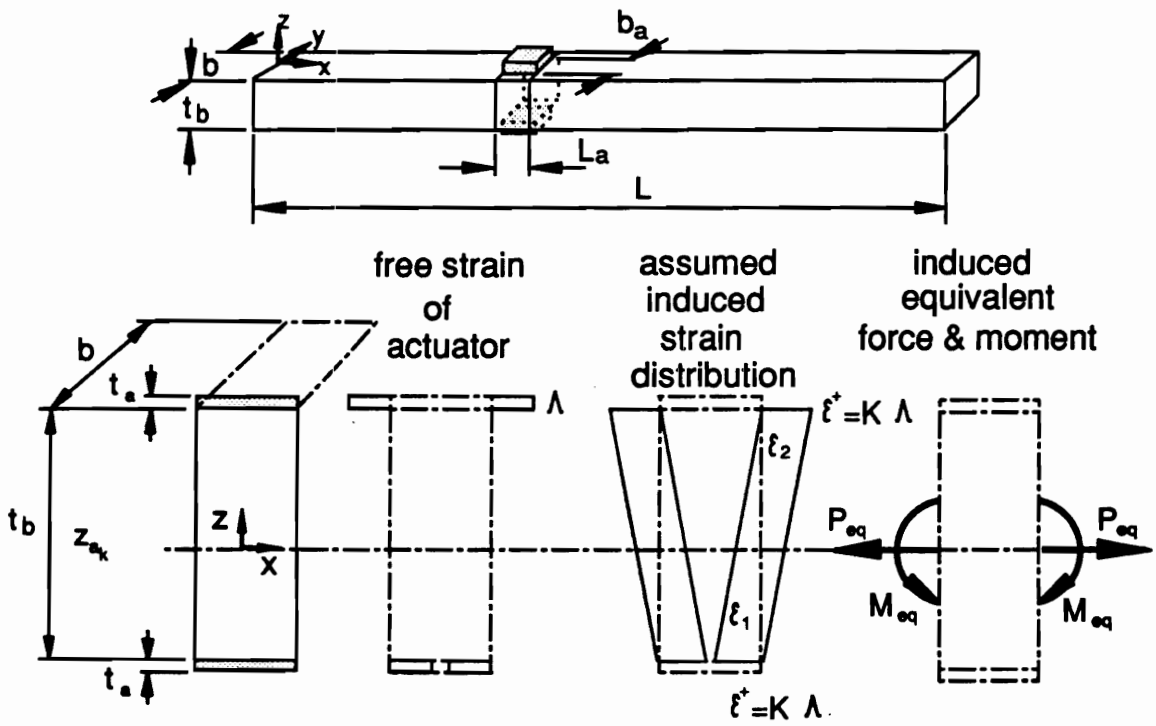


Figure 8. Illustration of actuator-beam (pure bending)

Note that the sum of the axial forces by these two actuators is zero because the actuators were arranged symmetrically and activated 180° out-of-phase. As shown in Figure 8, if the assumed induced strain distributions, ε_1 and ε_2 , are linear, then the equivalent bending moment drawn by these two assumed strain distributions can be derived as:

$$M_{eq} = \frac{t_b^2 E_b}{6} K b_a \Lambda \quad (2.52)$$

By setting Equations (2.51) and (2.52) equal, i.e. the conservation of the strain energy is maintained, K can be found as

$$K = \frac{6}{6 + \Psi} \quad (2.53)$$

where

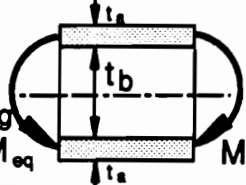
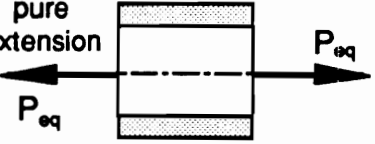
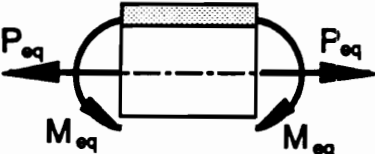
$$\Psi = \frac{t_b E_b}{t_a E_a} \quad (2.54)$$

Therefore, the induced equivalent bending moment can be determined by substituting Equation (2.53) into Equations (2.51) or (2.52)

$$M_{eq} = \frac{t_b^2 E_b}{6 + \Psi} b_a \Lambda \quad (2.55)$$

This result agrees with those of the pin-force model (Lazarus and Crawley, 1989) and the ideal bonding case (Crawley and de Luis, 1987) because, for the case of pure bending, all of these models have the same assumed linear strain distributions. Table 2 summarizes the results of several cases deduced from the strain-energy and the pin-force model. Only for cases (1) and (4) do both models conclude the same equivalent bending

Table 2. Comparison between strain-energy and pin-force models (Lazarus and Crawley, 1989)

case	strain-energy	pin-force
(1)  <p>pure bending</p>	$M_{eq} = \frac{t_b^2 E_b}{6 + \psi} b \lambda$	same $\left(\psi = \frac{t_b E_b}{t_a E_a} \right)$
(2) pure extension 	$P_{eq} = \frac{2 t_b E_b}{6 + \psi} b \lambda$	$P_{eq} = \frac{2 t_b E_b}{2 + \psi} b \lambda$
(3) 	$P_{eq} = \frac{t_b E_b}{6 + \psi} b \lambda$ $M_{eq} = \frac{t_b^2 E_b}{2(6 + \psi)} b \lambda$	$P_{eq} = \frac{t_b E_b}{1 + \psi} b \lambda$ $M_{eq} = \frac{t_b^2 E_b}{2(1 + \psi)} b \lambda$
(4) 	$P_{eq} = \frac{t_b E_b}{1 + \psi} b \lambda$	same

moment and axial force. For other cases, they are somewhat different. This discrepancy is caused by the assumption of different types of strain distribution.

2.2.1.1 Static Analysis

A cantilever beam, as shown on the top of Figure 9, is subjected to the actuation of a pair of piezoelectric patches attached symmetrically at the top and bottom of the beam and driven 180° out-of-phase. The piezoelectric actuation is equivalent to two concentrated moments, as indicated in Equation (2.55), with opposite signs acting on the two edges of the piezoelectric patches. The beam deflection can then be determined by classical beam theory.

For verification of the strain-energy model (SEM), a finite element code developed by Robbins and Reddy (1990) which utilizes generalized laminated plate theory (GLPT) was applied to obtain the static deflection of the beam. The GLPT, a generalization of existing high-order theories, accounts for transverse stresses and layer-wise approximation of the displacement through the plate thickness. To compare the results, the relative error of the tip displacement of the cantilever actuator-beam was shown respective to the FEM results obtained by varying the ratio of the modulus to the thickness of the beam and actuators (Figures 9(a) and 9(b), respectively). The results show that the prediction error is generally less than 10 % between the SEM and FEM. It is noted that for static analysis, the SEM overestimates the static response for low thickness ratios. However, it will be also shown that the SEM agrees well with the FEM for dynamic responses, because thickness effects become insignificant in dynamic analysis. Figure 9 also shows the similar results for the SPBM, spherical pure bending model (Clark, Fuller, and Wicks, 1990a). The prediction error is generally less than 15 % be-

tween the SPBM and FEM. However, for low thickness ratios, in contrast to the SEM, the SPBM underestimates the static response. Section 2.2.2.1 explains this difference, due to the different assumptions of strain distribution in piezoceramic patches used by the SEM and SPBM.

2.2.1.2 Dynamic Analysis

To illustrate the utility of the model for dynamic analysis, a simply-supported actuator-beam harmonically excited by piezoelectric actuators in a pure bending manner as described in the previous case study was considered. The configurations of the beam are the same as that of Figure 9 except the boundary conditions, which are simply-supported at both ends. The lateral displacement of the beam can be described as:

$$w(x) = \sum_{m=1}^{\infty} W_m \sin \frac{m\pi}{L} x \quad (2.56)$$

where

$$W_m = \frac{P_m}{\rho b t_b (\omega_m^2 - \omega^2)} \quad (2.57)$$

$$\omega_m = (m\pi)^2 \sqrt{\frac{E_b I}{\rho b t_b L^4}} \quad (2.58)$$

$$P_m = \frac{2M_{eq} m\pi}{L^2} \left(\cos \frac{m\pi}{L} x_1 - \cos \frac{m\pi}{L} x_2 \right) \quad (2.59)$$

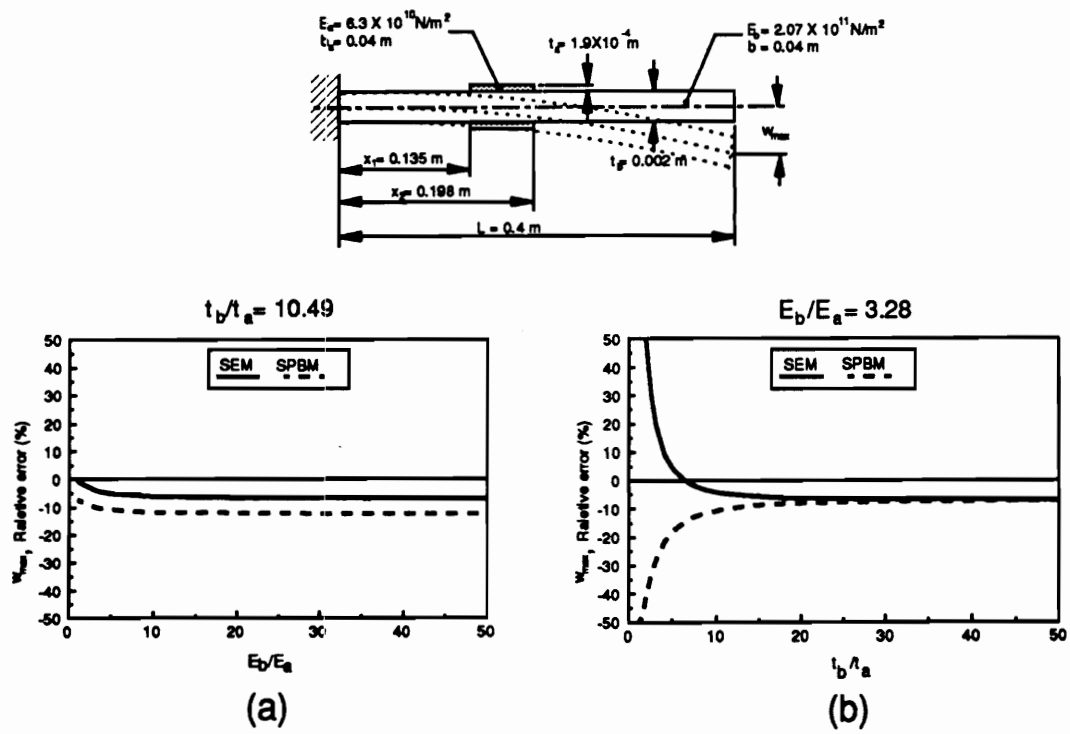


Figure 9. Relative error of tip displacement

Here, W_m is the modal amplitude, ω_m the natural frequency, I the moment of inertia, and P_m is the modal force for piezoelectric actuators which results in concentrated moments at both edges of the actuators.

For verification of the strain-energy model (SEM), the finite element code developed by Robbins and Reddy (1990) was applied to solve the modal amplitudes which were compared to the theoretical results from the SEM. Several numerical examples are presented. The simply-supported beam made up of steel with a length of 0.4 m and a thickness of 0.002 m ($t_b/t_s = 10.49$) or 0.0006 m ($t_b/t_s = 3.15$) with G-1195 piezoceramic attached to the top and bottom of the beam, as shown in the top of Figure 9, was considered. The material properties of the G-1195 piezoceramic patch are shown in Table 3, and the natural frequencies of the two beams are tabulated in Table 4.

Figure 10(a) shows the modal amplitude distributions and the steady-state modal response for piezoelectric actuators driven at $\omega = 400$ rad/sec, a frequency between the first and second modes, for the case of $t_b/t_s = 10.49$. The actuators can drive all modes, especially the first two. It is shown that the FEM predicts higher modal amplitudes than either the SEM or spherical pure bending models (SPBM) (Clark, Fuller and Wicks, 1990a); however, the modal amplitudes generally agree with one another. The modal response is exhibited a combination of the first and second modes.

Figure 10(b) shows the case of a driving frequency at $\omega = 700$ rad/sec, a frequency very near the second mode. It is seen that the second mode is more efficiently excited than other modes. The FEM predicts much higher amplitude for the second mode than for the others because the driving frequency is closer to the second natural frequency predicted by FEM than to that predicted by SEM. It should also be noted that the truncating error from the finite element formulation is unavoidable with the higher

Table 3. Physical properties of G-1195 piezoceramic patch (Piezo Systems, 1987)

$d_{31} = d_{32} = 166 \times 10^{-12} \left(\frac{\text{m}}{\text{volt}} \right)$	$d_{36} = 0$
$\rho_a = 7650 \left(\frac{\text{kg}}{\text{m}^3} \right)$	$E_a = 6.3 \times 10^{10} \left(\frac{\text{N}}{\text{m}^2} \right)$
$t_a = 1.905 \text{ (mm)}$	$\nu_a = 0.28$

Table 4. Natural frequencies of simply-supported beam (rad/sec)

mode	$t_b = 0.002 \text{ m}$ ($t_b/t_a = 10.49$)		$t_b = 0.0006 \text{ m}$ ($t_b/t_a = 3.15$)	
	Theoretical	FEM	Theoretical	FEM
1	182.6	181.1	54.8	54.9
2	730.6	728.1	219.2	220.6
3	1643.8	1649.2	493.2	502.4
4	2922.4	2968.5	876.7	907.9
5	4566.2	4708.9	1369.9	1399.7
6	6575.4	6849.1	1972.6	2087.8
7	8949.8	9531.2	2684.9	2814.6
8	11689.5	12666.4	3506.9	3755.2
9	14794.6	16451.4	4438.4	4807.5
10	18264.9	20633.8	5479.5	6039.5

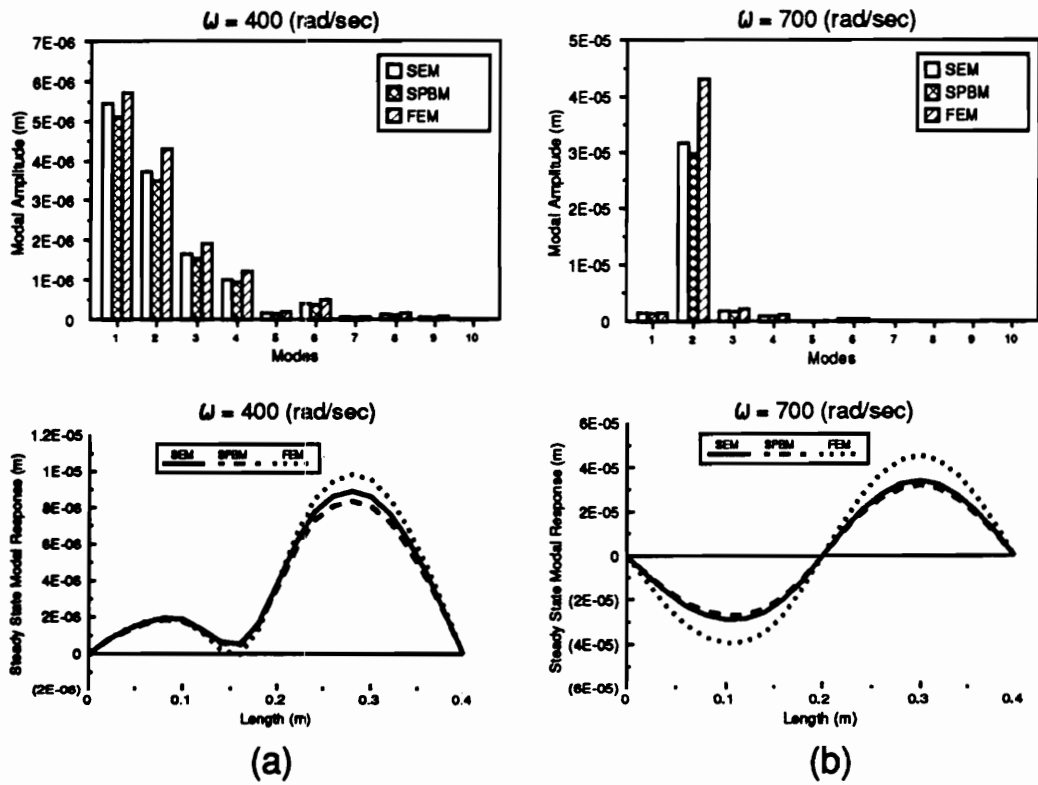


Figure 10. Modal amplitude and modal response for $t_b/t_a = 10.49$

modes. Nevertheless, this truncating error is assumed small if large numbers of elements are used (40 elements were used here). In terms of steady state modal response, the FEM approach also shows a 20 % higher than the two analytical models for the maximum. This corresponds to the higher prediction of the second modal amplitude from the FEM than others. However, the trend of the steady state modal response generally agrees to each other, and the SEM gives higher modal responses than the SPBM.

For low thickness ratios, i.e., $t_b/t_a = 3.15$, Figure 11(a) and 11(b) show the modal amplitude distribution and steady-state modal response for piezoelectric actuators driven at $\omega = 130$ rad/sec between the first and second modes and $\omega = 210$ rad/sec near the second mode respectively. It can be seen that the results of the SEM generally agree with those of the FEM; however, the SPBM underestimates the modal amplitudes. Therefore, the SEM is more favorable than the SPBM when the thickness ratio is low.

2.2.2 Illustration of Actuator-Plate

2.2.2.1 One Isotropic Layer with Two Piezoceramic Patches (Pure Bending)

Considered a simply-supported, isotropic lamina with two actuator patches (piezoceramic) bonded to the top and bottom surfaces of the plate subjected to 180° out-of-phase voltages, as shown in Figure 12. The material properties for the isotropic layer are given as:

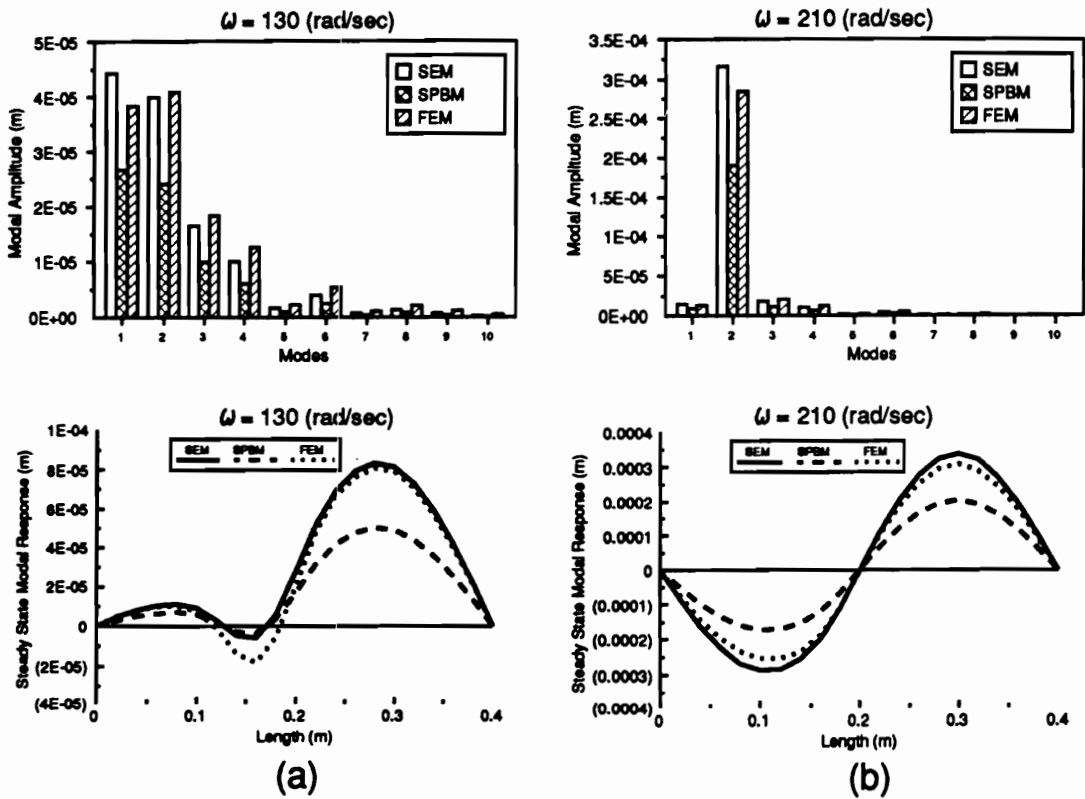


Figure 11. Modal amplitude and modal response for $t_b/t_a = 3.15$

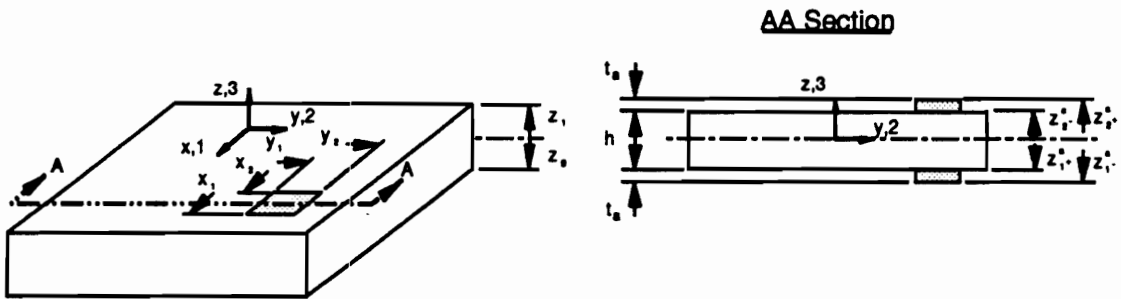


Figure 12. One isotropic layer with two piezoceramic patches (pure bending)

$$[\bar{Q}] = \begin{bmatrix} \frac{E}{1-\nu^2} & \frac{\nu E}{1-\nu^2} & 0 \\ \frac{\nu E}{1-\nu^2} & \frac{E}{1-\nu^2} & 0 \\ 0 & 0 & \frac{E}{2(1+\nu)} \end{bmatrix} \quad (2.60)$$

The material properties for the actuator patch are given as:

$$[\bar{Q}^a] = \begin{bmatrix} \frac{E_a}{1-\nu_a^2} & \frac{\nu_a E_a}{1-\nu_a^2} & 0 \\ \frac{\nu_a E_a}{1-\nu_a^2} & \frac{E_a}{1-\nu_a^2} & 0 \\ 0 & 0 & \frac{E_a}{2(1+\nu_a)} \end{bmatrix} \quad (2.61)$$

where E, ν, E_a and ν_a are engineering constants for the isotropic layer and actuator patches. The typical physical properties of G-1195 piezoceramic patch was shown in Table 3. It is noted that the laminate is symmetry. If the applied voltages of the piezoceramic patches were out-of-phase, i.e. $V_1 = -V_2 = -V$, then the following relations result

$$A_{ij} = \bar{Q}_{ij} h \quad (2.62)$$

$$B_{ij} = 0 \quad (2.63)$$

$$D_{ij} = \frac{h^3}{12} \bar{Q}_{ij} \quad (2.64)$$

$$E_{ij} = 0 \quad (2.65)$$

$$F_{ij} = \bar{Q}_{ij}^a V(1 - K)(h + t_a) \quad (2.66)$$

It is noted that $(h + t_a)$ is the distance between the two piezoceramic patches, and K is defined in Equation (2.53). The equations of motion can be reduced to

$$A_{11} \frac{\partial^2 u}{\partial x^2} + A_{66} \frac{\partial^2 u}{\partial y^2} + (A_{12} + A_{66}) \frac{\partial^2 v}{\partial x \partial y} = \rho h \frac{\partial^2 u}{\partial t^2} \quad (2.67)$$

$$(A_{12} + A_{66}) \frac{\partial^2 u}{\partial x \partial y} + A_{66} \frac{\partial^2 v}{\partial x^2} + A_{22} \frac{\partial^2 v}{\partial y^2} = \rho h \frac{\partial^2 v}{\partial t^2} \quad (2.68)$$

$$\begin{aligned} D_{11} \frac{\partial^4 w}{\partial x^4} + 2(D_{12} + D_{66}) \frac{\partial^4 w}{\partial x^2 \partial y^2} + D_{22} \frac{\partial^4 w}{\partial y^4} + \rho h \frac{\partial^2 w}{\partial t^2} \\ = q(x, y, t) + [(F_{11}d_{31} + F_{12}d_{32}) \frac{\partial^2 R}{\partial x^2} + (F_{21}d_{31} + F_{22}d_{32}) \frac{\partial^2 R}{\partial y^2}] \end{aligned} \quad (2.69)$$

One can observe that Equations (2.67) and (2.68) are coupled without any actuator effects, and Equation (2.69) with actuator effects is independent. Both Equations (2.67) and (2.68) are known as the stretching problem, and Equation (2.69) is known as the bending problem. These equations of motion show that the two actuator patches only induce laminate bending, and the equivalent external forces excited by the two actuator patches are the distributed line moments along the four edges of the actuator patch. This result is similar to that of the SPBM (Dimitriadis, Fuller and Rogers, 1991). The bending equation substituted by D_{ij} and F_{ij} can be written as:

$$D\nabla^4 w + \rho h \frac{\partial^2 w}{\partial t^2} = C''_0 \Lambda \left(\frac{\partial^2 R}{\partial x^2} + \frac{\partial^2 R}{\partial y^2} \right) \quad (2.70)$$

where

$$D = \frac{Eh^3}{12(1 - \nu^2)} \quad (2.71)$$

$$C''_0 = t_a(1 - K)(h + t_a) \frac{E_a}{1 - \nu_a} \quad (2.72)$$

It is noted that actuators result in the equivalent line moments with a magnitude of $C''_0 \Lambda$ acting along the edges of actuator. C''_0 is the induced bending moment coefficient. The corresponding equations derived from the SPBM (Dimitriadis, Fuller and Rogers, 1991) and the CLPT model (Wang and Rogers, 1991b) are the same except for the replacement of the induced bending moment coefficient C''_0 by C_0 (SPBM) and C'_0 (CLPT) respectively. C_0 and C'_0 are defined as follow

$$C_0 = -E \frac{1 + \nu_a}{1 - \nu} \frac{P}{1 + \nu - (1 + \nu_a)P} \frac{2}{3} \left(\frac{h}{2}\right)^2 \quad (2.73)$$

where

$$P = -\frac{E_a}{E} \frac{1 - \nu^2}{1 - \nu_a^2} \frac{3t_a \left(\frac{h}{2}\right)(h + t_a)}{2\left[\left(\frac{h}{2}\right)^3 + t_a^3\right] + 3\left(\frac{h}{2}\right)t_a^2} \quad (2.74)$$

and

$$C'_0 = t_a(h + t_a) \frac{E_a}{1 - \nu_a} \quad (2.75)$$

To compare C_0 , C'_0 and C''_0 , the characteristic curves of C_0/C''_0 and C'_0/C''_0 varying the modulus and thickness ratios of plate and actuator are shown in Figures 13(a) and

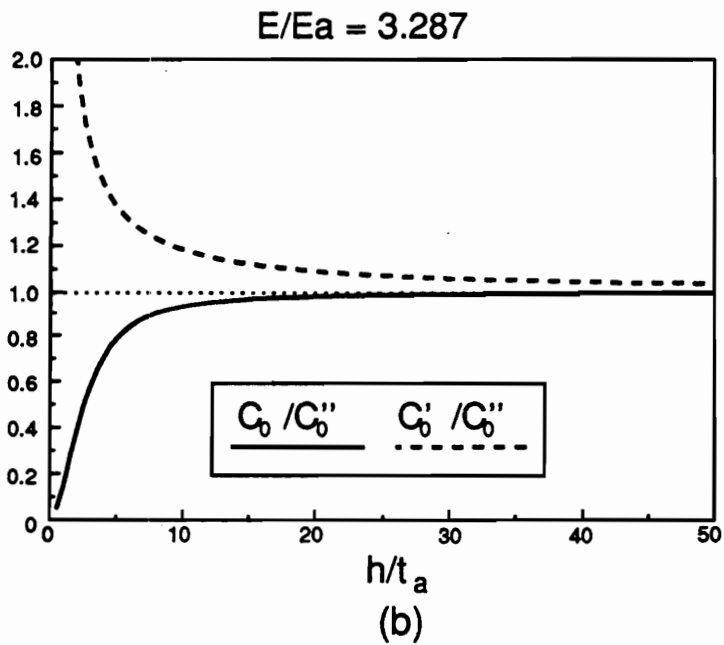
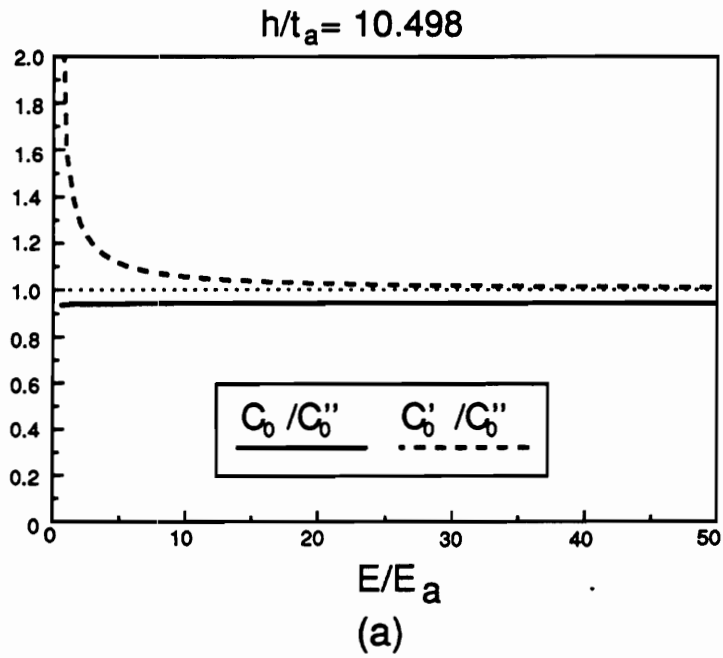


Figure 13. Illustration of C_0/C''_0 and C'_0/C''_0 by varying thickness and modulus ratios

13(b) respectively. As seen in Fig 13(a), if E/E_a is very large, C'_0/C''_0 approaches to unity, and C_0/C''_0 approaches to 0.94. This can be explained by determining C_0 , C'_0 and C''_0 with the assumption of $E \gg E_a$. Therefore, C_0 , C'_0 and C''_0 become

$$C_0 = t_a(h + t_a) \frac{E_a}{1 - \nu_a} \frac{1}{1 + 6\left(\frac{t_a}{h}\right)^2 + 8\left(\frac{t_a}{h}\right)^3} \quad (2.76)$$

$$C'_0 = C''_0 = t_a(h + t_a) \frac{E_a}{1 - \nu_a} \quad (2.77)$$

As observed, both C'_0 and C''_0 converge, and C'_0 is actually not changed. However, C_0 has a slightly different form. The main difference among the induced moment coefficients is the last term of Equation (3.76), which is 0.94 for this case study. This corresponds to the result shown in Figure 13(a). If we let $h \gg t_a$, then

$$C_0 = C'_0 = C''_0 = t_a h \frac{E_a}{1 - \nu_a} \quad (2.78)$$

The induced moment coefficients are equal. This agrees to what is observed in Figure 13(b). When h/t_a increases, both C_0/C''_0 and C'_0/C''_0 approach to unity. In summary, either the SEM, CLPT or SPBM converges and agree with each other, if plate thickness is much greater than actuator thickness while their modulus are fixed. In this situation, the interaction effect between the plate and actuators is relatively insignificant, and induced moment coefficients are simply proportional to the plate thickness. If the modulus ratio of plate and actuator increases while their thickness are fixed, the SPBM has a slight discrepancy from the SEM and CLPT, as shown in Equations (3.76) and (3.77). This can be explained that these models have different assumptions of strain

distribution in piezoceramic patches. The SEM assumes linear; the GLPT uniform; the SPBM trapezoid.

As shown in previous results for the one-dimensional beam, the SPBM underestimates the dynamic response for low thickness ratios. On the other hand, the CLPT model generally overestimates the resultant force and moment. The SEM is more favorable than both the SPBM and the CLPT model for a wide range of modulus and thickness ratios. Only the characteristic curves of C''_0 are shown as follows.

Figure 14(a) shows the induced line moment distribution obtained by varying the modulus ratio of the plate and the actuator for different thickness ratios of the plate and the actuator, while the physical properties of the piezoelectric actuators were assumed to be unchanged, i.e., t_a and E_a remain constant. As the modulus ratio increases, the line moment generally increases. That is to say, a stiffer plate with the same specified piezoelectric actuation will result in a higher line moment. However, the line moment will approach a constant when the modulus ratio is very large. For low modulus ratios, the line moment is more sensitive when the modulus ratio is increased, especially for those of low thickness ratios. The typical modulus ratios for steel and aluminum are 3.49 and 1.12 respectively, as shown in the plot.

Figure 14(b) shows the line moment distribution for SEM model obtained by varying the thickness ratio of the plate and actuator for various modulus ratios. It can be seen that the line moment increases as the thickness ratio increases; and it appears that there is a linear relationship between the line moment and the thickness ratio for high thickness and modulus ratios. The magnitude of the induced equivalent line moment is strongly relative to the plate thickness.

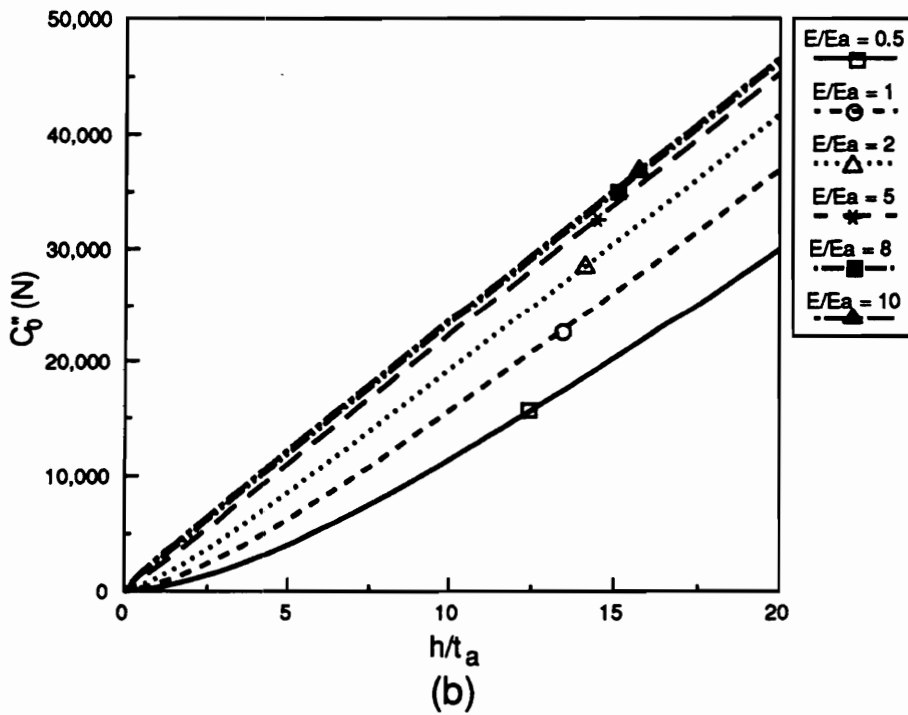
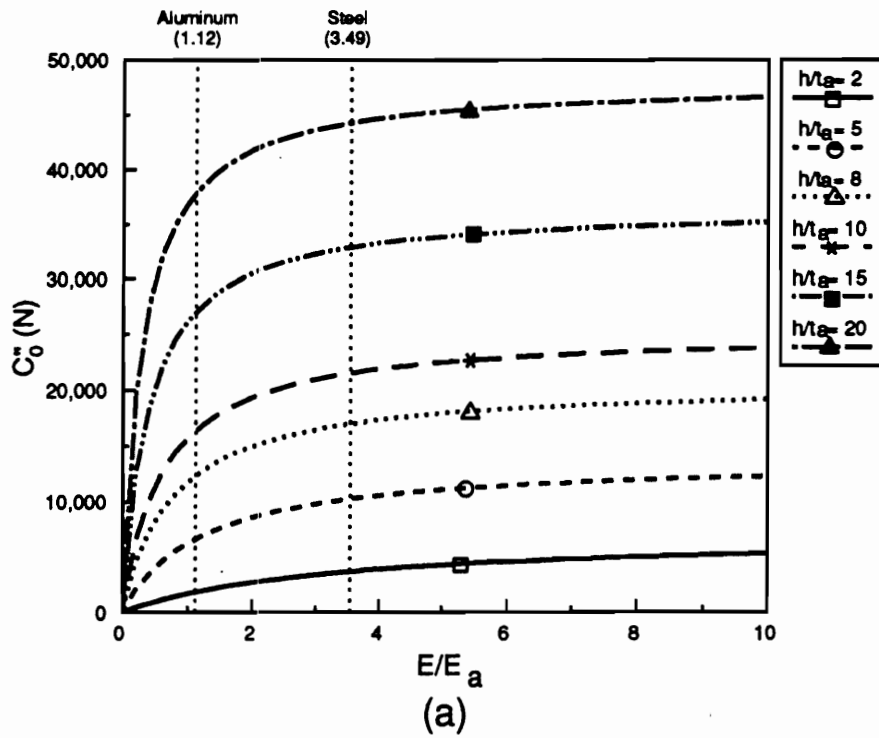


Figure 14. Illustration of C''_0 by varying thickness and modulus ratios

2.2.2.2 One Isotropic Layer with Two Piezoceramic Patches (Pure Extension)

In this case study, a similar plate was considered as that in the previous case study except that the applied voltages $V_1 = V_2 = V$. The $[A]$, $[B]$ and $[D]$ matrices are unchanged, and

$$E_{ij} = 2\bar{Q}_{ij}^a V(1 - K) \quad (2.79)$$

$$F_{ij} = 0 \quad (2.80)$$

The equations of motion can be reduced to

$$A_{11} \frac{\partial^2 u}{\partial x^2} + A_{66} \frac{\partial^2 u}{\partial y^2} + (A_{12} + A_{66}) \frac{\partial^2 v}{\partial x \partial y} = \rho h \frac{\partial^2 u}{\partial t^2} + (E_{11}d_{31} + E_{12}d_{32}) \frac{\partial R}{\partial x} \quad (2.81)$$

$$(A_{12} + A_{66}) \frac{\partial^2 u}{\partial x \partial y} + A_{66} \frac{\partial^2 v}{\partial x^2} + A_{22} \frac{\partial^2 v}{\partial y^2} = \rho h \frac{\partial^2 v}{\partial t^2} + (E_{21}d_{31} + E_{22}d_{32}) \frac{\partial R}{\partial y} \quad (2.82)$$

$$D_{11} \frac{\partial^4 w}{\partial x^4} + 2(D_{12} + D_{66}) \frac{\partial^4 w}{\partial x^2 \partial y^2} + D_{22} \frac{\partial^4 w}{\partial y^4} + \rho h \frac{\partial^2 w}{\partial t^2} = q(x, y, t) \quad (2.83)$$

One can observe that Equations (2.81) and (2.82) are coupled, and the piezoelectric effects are included; however, Equation (2.83) is independent without any actuation terms. Therefore, this example results in pure extension rather than the pure bending of the previous example. In Equations (2.81) and (2.82), the terms involved $\partial R/\partial x$ and $\partial R/\partial y$ which represent the in-plane forces along the edges are the equivalent external forces induced by the piezoceramic patches.

2.2.2.3 Two-Layered ($\theta^\circ / -\theta^\circ$) Laminate with One Piezoceramic Patch

Considered a two-layer, angle-ply laminate with one piezoceramic patch embedded within the laminate and between the two lamina. The laminated plate is illustrated in Figure 15. The following relations can be found

$$A_{ij} = \frac{h}{2} [(\bar{Q}_{ij})_1 + (\bar{Q}_{ij})_2] \quad (2.84)$$

$$B_{ij} = \frac{h^2}{8} [(\bar{Q}_{ij})_1 - (\bar{Q}_{ij})_2] \quad (2.85)$$

$$D_{ij} = \frac{h^3}{24} [(\bar{Q}_{ij})_1 + (\bar{Q}_{ij})_2] \quad (2.86)$$

$$E_{ij} = \bar{Q}_{ij}^a V(1 - K) \quad (2.87)$$

$$F_{ij} = 0 \quad (2.88)$$

It is noted that actuator bending-twisting stiffnesses, F_{ij} , are zero. That is to say, there is no bending and twisting induced by the piezoceramic patch; however, bending and extension are coupled due to the non-symmetric, angle-ply laminate. This coupling can be seen from the following equations of motion.

$$\begin{aligned} & [A_{11} \frac{\partial^2 u}{\partial x^2} + 2A_{16} \frac{\partial^2 u}{\partial x \partial y} + A_{66} \frac{\partial^2 u}{\partial y^2} + A_{16} \frac{\partial^2 v}{\partial x^2} + (A_{12} + A_{66}) \frac{\partial^2 v}{\partial x \partial y} + A_{26} \frac{\partial^2 v}{\partial y^2}] \\ & - [B_{11} \frac{\partial^3 w}{\partial x^3} + 3B_{16} \frac{\partial^3 w}{\partial x^2 \partial y} + (B_{12} + 2B_{66}) \frac{\partial^3 w}{\partial x \partial y^2} + B_{26} \frac{\partial^3 w}{\partial y^3}] \\ & = \rho h \frac{\partial^2 u}{\partial t^2} + (E_{11}d_{31} + E_{12}d_{32}) \frac{\partial R}{\partial x} \end{aligned} \quad (2.89)$$

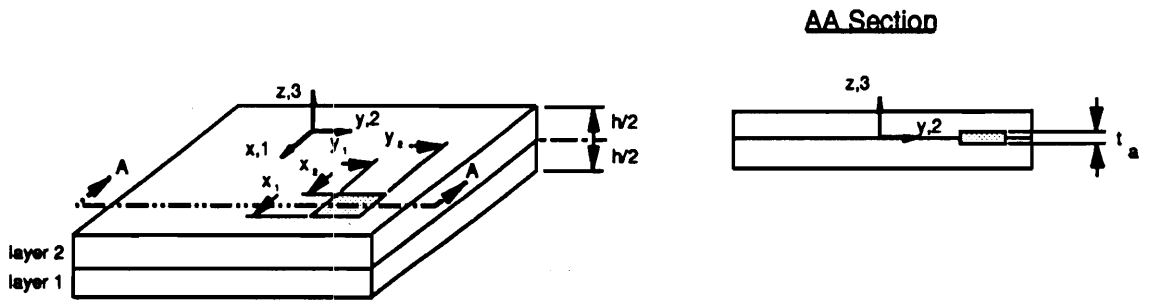


Figure 15. Two-layered ($\theta^\circ / -\theta^\circ$) laminate with one piezoceramic patch

$$\begin{aligned}
& [A_{16} \frac{\partial^2 u}{\partial x^2} + (A_{12} + A_{66}) \frac{\partial^2 u}{\partial x \partial y} + A_{26} \frac{\partial^2 u}{\partial y^2} + A_{66} \frac{\partial^2 v}{\partial x^2} + 2A_{26} \frac{\partial^2 v}{\partial x \partial y} + A_{22} \frac{\partial^2 v}{\partial y^2}] \\
& - [B_{16} \frac{\partial^3 w}{\partial x^3} + (B_{12} + 2B_{66}) \frac{\partial^3 w}{\partial x^2 \partial y} + 3B_{26} \frac{\partial^3 w}{\partial x \partial y^2} + B_{22} \frac{\partial^3 w}{\partial y^3}] \quad (2.90) \\
& = \rho h \frac{\partial^2 v}{\partial t^2} + (E_{21}d_{31} + E_{22}d_{32}) \frac{\partial R}{\partial y}
\end{aligned}$$

$$\begin{aligned}
& [B_{11} \frac{\partial^3 u}{\partial x^3} + 3B_{16} \frac{\partial^3 u}{\partial x^2 \partial y} + (B_{12} + 2B_{66}) \frac{\partial^3 u}{\partial x \partial y^2} + B_{26} \frac{\partial^3 u}{\partial y^3} \\
& + B_{16} \frac{\partial^3 v}{\partial x^3} + (B_{12} + 2B_{66}) \frac{\partial^3 v}{\partial x^2 \partial y} + 3B_{26} \frac{\partial^3 v}{\partial x \partial y^2} + B_{22} \frac{\partial^3 v}{\partial y^3}] \quad (2.91) \\
& - [D_{11} \frac{\partial^4 w}{\partial x^4} + 4D_{16} \frac{\partial^4 w}{\partial x^3 \partial y} + 2(D_{12} + 2D_{66}) \frac{\partial^4 w}{\partial x^2 \partial y^2} + 4D_{26} \frac{\partial^4 w}{\partial x \partial y^3} + D_{22} \frac{\partial^4 w}{\partial y^4}] \\
& = \rho h \frac{\partial^2 w}{\partial t^2} - q(x,y,t)
\end{aligned}$$

All three equations, Equations (2.89)-(2.91), are coupled. The actuator patch results in two equivalent external forces which are the last terms of Equation (2.89) and (2.90) respectively. To calculate the responses, Equations (2.89)-(2.91) must be solved simultaneously.

2.3 Summary

1. This chapter presents a strain-energy model for a laminate actuator-beam which is essentially based upon the conservation of strain energy. The induced strain con-

stant which relates the induced strain to the free strain of the piezoelectric actuator was derived. Therefore, the equivalent induced force and moment of the actuators can be determined.

2. The strain-energy model for a laminate actuator-beam was then extended to a two-dimensional problem, i.e., a laminate actuator-plate, with the utilization of classical laminate plate theory and Heaviside functions to represent the size and location of the spatially distributed actuator patches.
3. A case study example of pure bending for an actuator-beam including both static and dynamic analyses was presented, and a comparison among several models was made. This work agrees favorably with those of the pin-force model (Lazarus and Crawley, 1989), the spherical pure bending model (Clark, Fuller and Wicks, 1990a) and the finite element model developed by Robbins and Reddy (1990). In particular, the present model, SEM, is more suitable than SPBM over a wide range of thickness and modulus ratios of beam and actuator in comparison to the FEM results.
4. A case study example of pure bending for an actuator-plate was presented. The induced bending moment coefficients derived from the SEM, C''_0 , was compared to C_0 from the SPBM and C'_0 from the GLPT. The discrepancy is due to the different assumption of strain distribution in piezoceramic patches. According to the one-dimensional results, the SEM for two-dimensional plate should be more favorable than the CLPT and SPBM.
5. Case study examples of pure extension and a general problem with the coupling of bending and extension for a laminate actuator-plate were also presented.

6. The proposed model is capable of predicting the equivalent axial force and bending moment induced by multiple spatially distributed actuators attached or embedded in laminate beams or plates, and provides a general approach of considerable utility for the use of induced strain actuators in active noise and vibration control.

Chapter 3 : Active Control of Sound Radiation

In recent years, the problem of actively controlling sound and vibration has generated strong interest both in industry and in the engineering research community. Advances in control theory combined with recent developments in fast computing have made possible the treatment of problems on active structural sound and vibration control that were infeasible only a few years ago. However, it is becoming increasingly clear that the development of corresponding control transducers has generally been lagging behind. Thus, in response to this need, a strong interest has also arisen in new concepts for control actuators and sensors. This chapter concerns the use of the proposed piezoelectric actuator (discussed in Chapter 2) which consists of layers of piezoelectric material bonded to the surface of the elastic structure to provide control inputs.

It has been suggested that a structurally radiated sound can be best suppressed by directly applying active forces to the structure so as to affect the sound radiating vibrations (Fuller, 1988). It was seen in the analysis (Fuller, 1988) as well as in companion experiments (Fuller et al., 1989) that point force actuators (i.e. electromagnetic shakers), while providing excellent sound reduction, have some disadvantages, such as their

weight/volume and their need for a support structure. Such drawbacks, inherent to point actuators, can be remedied by distributed actuators which are more compact in nature. A type of compact actuator has been developed for the control of beam vibration by Crawley and de Luis (1987). Their actuator (as discussed in the previous Chapter) consisted of thin strips of piezoelectric material which were bonded to the beam surface and activated to vibrate parallel to the beam surface by an oscillating electric voltage, applied across the piezoelectric electrodes.

Chapter 2 has presented a strain-energy model for a laminate beam or plate with embedded or attached spatially distributed piezoelectric actuators. It was further proposed that the piezoelectric strain can be employed to affect the plate vibrations and to suppress the coupled sound radiation. The feasibility of using a single surface mounted piezoelectric element to actively control sound transmission through a clamped circular plate was demonstrated by Dimitriadis and Fuller (1989). It was shown that when the excitation frequency was low, such that the fundamental mode of vibration was dominant, the radiated field could be significantly attenuated by a single actuator. However, as the frequency of excitation is increased, the modal response and corresponding radiation becomes "richer", and the single actuator appears to be insufficient. Recent preliminary experiments of Fuller, Hansen and Snyder (1990c) have confirmed these observations and supported the analytical results of Dimitriadis and Fuller (1989) and Dimitriadis, Fuller and Rogers (1991). It is apparent that the appropriate tailoring of the actuators as far as their number, position and size concerned becomes increasingly important for higher modes.

It is suggested here that multiple independently controlled piezoelectric actuators should greatly enhance the control effectiveness by further reducing the control spillover.

This observation is based on the work similar to that of Meirovitch and Norris (1984) in which it is analytically demonstrated that as many point force actuators as the number of modes to be controlled are required to globally reduce beam vibration. However, in the present study of this thesis, we are only interested in controlling those panel modes which are significant radiators of sound, and this markedly reduces the required number of actuators. In other words, as demonstrated in (Fuller, 1988), the radiated field can be highly attenuated in some cases without significantly reducing overall plate vibrational amplitude with a reduced number of actuators.

This chapter will first examine the dynamic response of a simply-supported rectangular plate subjected to four types of external loads: (1) point force, (2) uniformly distributed pressure, (3) incident plane acoustic wave and (4) piezoceramic patch. These external loads will be used to model both primary (disturbance) and secondary (control) inputs where appropriate. The steady-state sound radiation of the baffle simply-supported rectangular plate is then studied. Both near-field and far-field sound pressure expressions are derived from the Rayleigh formula, which couples the structural dynamic response to sound radiation. When any type of external load is applied as a control source, linear quadratic optimal control theory (LQOCT), which is a minimization technique developed by Lester and Fuller (1990), is applied to calculate the optimal control voltages to be applied to the actuators, so as to minimize a cost function. The cost functions considered here are based on the use of: (1) distributed pressure sensor, (2) discrete pressure sensor (microphone), (3) distributed acceleration sensor, and (4) discrete acceleration sensor (accelerometer). Some special topics associated with structural acoustics, such as time-averaged intensity, plate wavenumber analysis, transmission loss (TL) and radiation efficiency(σ), are also addressed. Finally, several case studies are presented to show the active control of sound radiation as follows:

1. a harmonically excited structural disturbance input (uniformly distributed pressure) controlled by multiple piezoelectric actuators to show the feasibility of using compact distributed actuators in ASAC;
2. an incident plane acoustic wave controlled by point force or piezoelectric actuators to evaluate the performance of the actuators (a transmission problem);
3. near-field pressure and intensity distribution and plate wavenumber analysis for a point force disturbance controlled by piezoelectric actuators to further understand the characteristic and mechanism of LMS adaptive control approaches in ASAC;
4. a point force disturbance controlled by piezoelectric actuators to compare different forms of cost functions in conjunction with the use of LMS adaptive control approaches.

3.1 Plate Vibration

Figure 16 shows the arrangement and coordinates of an elastic, simply-supported, rectangular plate with infinite rigid baffle. If the plate is subjected to an external load, then, under the assumption of harmonic excitation, the displacement of the simply-supported plate can be written as

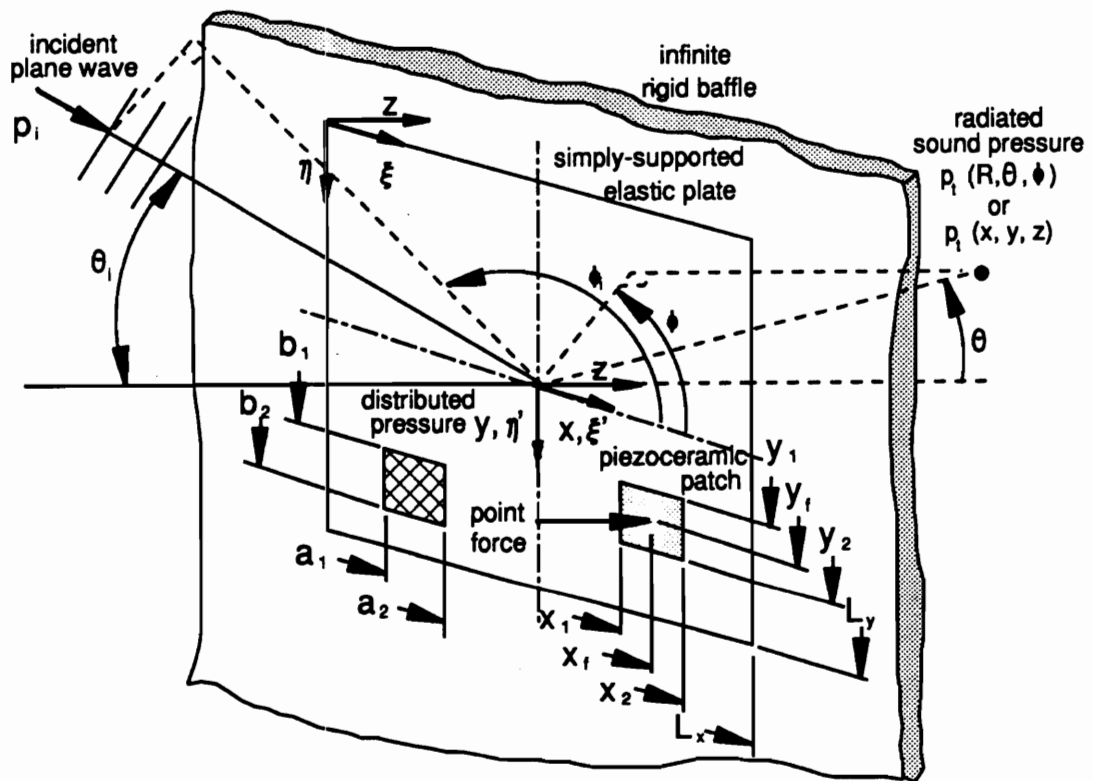


Figure 16. Arrangement and coordinates of the baffled simply-supported plate

$$w(\xi, \eta, t) = e^{j\omega t} \sum_{m=1}^{\infty} \sum_{n=1}^{\infty} W_{mn} \sin \kappa_m \xi \sin \kappa_n \eta \quad (3.1)$$

where the eigenvalues, i.e., the plate wavenumbers, are

$$\kappa_m = \frac{m\pi}{L_x} \quad m = 1, 2, \dots \quad (3.2)$$

$$\kappa_n = \frac{n\pi}{L_y} \quad n = 1, 2, \dots \quad (3.3)$$

and the plate modal amplitude is given by

$$W_{mn} = \frac{P_{mn}}{\rho_p h (\omega_{mn}^2 - \omega^2)} \quad m, n = 1, 2, \dots \quad (3.4)$$

Here, P_{mn} is the modal force which depends on the exact description of the applied external load. In other words, P_{mn} is the modal component of the generalized force describing disturbance or control inputs. For the present analysis, the plate response is calculated for light fluid loading, and thus radiation loading effects on plate dynamics are ignored. Structural damping is also assumed to be negligible.

3.1.1 Point Force

For a point force of amplitude, F , the modal force, P'_{mn} , is given as follow (Pilkey and Chang, 1975):

$$P_{mn}^f = \frac{4F}{L_x L_y} \sin \kappa_m x_f \sin \kappa_n y_f \quad (3.5)$$

where x_f and y_f are the coordinates of the point force, as shown in Figure 16, and the superscript f will signify the point force.

3.1.2 Uniformly Distributed Pressure

For a uniformly distributed pressure of amplitude, q , located between coordinates a_1, a_2, b_1 and b_2 , as shown in Figure 16, the modal force can be written as (Pilkey and Chang, 1975)

$$P_{mn}^q = \frac{4q}{mn\pi^2} (\cos \kappa_m a_1 - \cos \kappa_m a_2)(\cos \kappa_n b_1 - \cos \kappa_n b_2) \quad (3.6)$$

where the superscript q will hereafter signify the uniformly distributed pressure.

3.1.3 Incident Plane Wave

For an obliquely incident plane wave of amplitude, P_i , and incident polar and azimuthal angles, θ_i and ϕ_i , Roussos (1985) derived the modal force $P_{mn}^{p_i}$ as follows:

$$P_{mn}^{p_i} = 8P_i \bar{I}_m \bar{I}_n \quad (3.7)$$

where \bar{I}_m and \bar{I}_n are functions of θ_i and ϕ_i given in (Roussos, 1985). The superscript p_i denotes the incident plane wave.

3.1.4 Piezoelectric Excitation

For an actuator consisting of two identical piezoceramic patches bonded symmetrically on the two opposite plate surfaces and activated 180° out-of-phase, the corresponding expression of modal force for piezoelectric excitation P_{mn}^a can be derived (Dimitriadis, Fuller and Rogers, 1991) as follow:

$$P_{mn}^a = \frac{4C''_0\Lambda}{mn\pi^2} (\kappa_m^2 + \kappa_n^2) (\cos \kappa_m x_1 - \cos \kappa_m x_2) (\cos \kappa_n y_1 - \cos \kappa_n y_2) \quad (3.8)$$

where x_1, x_2, y_1 and y_2 are the coordinates of the piezoelectric actuator, and the superscript a will signify the piezoelectric actuator. The parameter $C''_0\Lambda$ was defined in Chapter 2; C''_0 , as shown in Equation (2.72), is a constant of the piezoelectric material properties and dimensions; $\Lambda = d_{31}V/t_a$ is the strain induced by an unconstrained piezoelectric layer of thickness, t_a , when a voltage V is applied along its polarization direction, while d_{31} is the piezoelectric dielectric strain constant.

By superposition, the total plate dynamic response by a number of external loads can be evaluated by the composite of individual response. For N_s primary sources or N_c control sources, the plate displacement can be derived as follows

for primary sources:

$$w_n(\xi, \eta, t) = e^{j\omega t} \sum_{j=1}^{N_s} \sum_{m=1}^{\infty} \sum_{n=1}^{\infty} W_{mnj}^n \sin \kappa_m \xi \sin \kappa_n \eta \quad (3.9)$$

for control sources:

$$w_c(\xi, \eta, t) = e^{j\omega t} \sum_{j=1}^{N_c} \sum_{m=1}^{\infty} \sum_{n=1}^{\infty} W_{mnj}^c \sin \kappa_m \xi \sin \kappa_n \eta \quad (3.10)$$

If the primary and control sources act simultaneously, the resultant plate displacement can be viewed as a superposition of the above given plate displacement for steady-state harmonic excitation. The total plate displacement can be written as

$$w_t = w_n + w_c = \sum_{j=1}^{N_s} G_j \hat{B}_j + \sum_{j=1}^{N_c} H_j \hat{A}_j \quad (3.11)$$

where \hat{B}_j and \hat{A}_j are the plate displacement distribution functions for the j -th primary source and the j -th control source respectively, given by

$$\hat{B}_j(\xi, \eta) = \sum_{m=1}^{\infty} \sum_{n=1}^{\infty} Q_{mnj}^n \sin \kappa_m \xi \sin \kappa_n \eta \quad (3.12)$$

$$\hat{A}_j(\xi, \eta) = \sum_{m=1}^{\infty} \sum_{n=1}^{\infty} Q_{mnj}^c \sin \kappa_m \xi \sin \kappa_n \eta \quad (3.13)$$

where

$$Q_{mnj}^n = \frac{W_{mnj}^n}{G_j} \quad (3.14)$$

$$Q_{mnj}^c = \frac{W_{mnj}^c}{H_j} \quad (3.15)$$

in which G_j and H_j are the amplitudes of the j -th primary and the j -th control sources respectively. G_j and H_j can be substituted by F_j for point force, q_j for uniformly distributed pressure, $(P_i)_j$ for incident plane wave, and $(C''_0\Lambda)_j$ for piezoelectric excitation.

3.2 Sound Radiation

3.2.1 Sound Pressure in the Near-Field

The radiated sound pressure is related to the plate vibration. The Rayleigh integral which relates the plate velocity to the transmitted pressure is shown as follow (Roussos, 1985):

$$p(R, \theta, \phi) = \int_{\xi'=-L_x/2}^{L_x/2} \int_{\eta'=-L_y/2}^{L_y/2} \frac{j\rho\omega}{2\pi r'} \frac{\partial w(\xi', \eta', t)}{\partial t} e^{-j\omega r'/c} d\xi' d\eta' \quad (3.16)$$

where (R, θ, ϕ) are the radiation coordinates, and (ξ, η) and (ξ', η') the plate coordinates are defined as follow:

$$\xi' = \xi - \frac{L_x}{2}$$

$$\eta' = \eta - \frac{L_y}{2}$$

and

$$r' = \sqrt{(x - \xi')^2 + (y - \eta')^2 + z^2}$$

Both the plate and radiation field coordinates are illustrated in Figure 16. By the substitution of Equation (3.1) into Equation (3.16), the radiated sound pressure can be expressed as follow:

$$p(x, y, z, t) = \frac{-\rho\omega^2}{2\pi} e^{j\omega t} \sum_{m=1}^{\infty} \sum_{n=1}^{\infty} W_{mn} \int_{\xi'=-L_x/2}^{L_x/2} \int_{\eta'=-L_y/2}^{L_y/2} \frac{e^{-j\left\{\frac{\omega}{c} \sqrt{(x-\xi')^2 + (y-\eta')^2 + z^2}\right\}}}{\sqrt{(x-\xi')^2 + (y-\eta')^2 + z^2}} \sin\left\{\kappa_m\left(\xi' + \frac{L_x}{2}\right)\right\} \sin\left\{\kappa_n\left(\eta' + \frac{L_y}{2}\right)\right\} d\xi' d\eta' \quad (3.17)$$

3.2.2 Sound Pressure in the Far-Field

The above integral must be evaluated numerically. However, a closed-form solution for this integral can be obtained in the far-field. Junger and Feit (1986) used the stationary phase method while Roussos (1985) has used a solution of the Rayleigh's integral at a large radial distance to derive a general expression for the far-field sound pressure radiated from a vibrating panel. By superposition, their analysis can be extended to describe the sound radiation from a panel excited by various primary and control sources. Thus, for N_p primary sources or N_c control sources, the sound pressure radiated to a point, $p(R, \theta, \phi)$, in the far-field can be derived as follow:

for primary sources:

$$p_n(R, \theta, \phi) = K \sum_{j=1}^{N_p} \sum_{m=1}^{\infty} \sum_{n=1}^{\infty} W_{mnj}^n I_m I_n \quad (3.18)$$

for control sources:

$$p_c(R, \theta, \phi) = K \sum_{j=1}^{N_c} \sum_{m=1}^{\infty} \sum_{n=1}^{\infty} W_{mnj}^c I_m I_n \quad (3.19)$$

where the constant K and the quantities I_m and I_n can be found in Roussos (1985) as functions of (R, θ, ϕ) .

When the primary and control sources act simultaneously, the resulting sound pressure field can be viewed as a superposition of the above given sound pressures for steady-state harmonic excitation. The total pressure can be conveniently written as

$$p_t = p_n + p_c = \sum_{j=1}^{N_p} G_j B_j + \sum_{j=1}^{N_c} H_j A_j \quad (3.20)$$

where B_j and A_j are the sound pressure distribution functions for the j -th primary source and the j -th control source respectively, given by

$$B_j(R, \theta, \phi) = K \sum_{m=1}^{\infty} \sum_{n=1}^{\infty} Q_{mnj}^n I_m I_n \quad (3.21)$$

$$A_j(R, \theta, \phi) = K \sum_{m=1}^{\infty} \sum_{n=1}^{\infty} Q_{mnj}^c I_m I_n \quad (3.22)$$

in which Q_{mnj}^n and Q_{mnj}^c are given in Equations (3.14) and (3.15) respectively.

3.3 Linear Quadratic Optimal Control

The most general cost function can be formed as the integral of the mean squared sound pressure over a hemisphere of radius R in the far-field. Such a cost function gives a global sense of sound attenuation (in particular, it is proportional to the total radiated acoustic power); however, in practical application, it is difficult to measure a distributed surface pressure. Instead, a finite number of microphones can be used to measure sound pressures in the radiating field. Similarly, the cost function can also be defined through a finite number of accelerometers or distributed accelerometers located over the plate. The objective here is to apply an minimization procedure for a quadratic function developed by Lester and Fuller (1990) using tensor calculus, and to calculate the input amplitude of the control source such that a selected cost function can be minimized. The derivation for each type of cost function is shown individually.

3.3.1 Distributed Pressure Sensor

If a pressure sensor is assumed to be distributed over an hemisphere of radius R in the radiating far-field, then the cost function can be defined as the integral of the mean squared sound pressure over the hemisphere as follow:

$$\Phi_p = \frac{1}{R^2} \int_s |p_t|^2 ds = \int_0^{2\pi} \int_0^{\frac{\pi}{2}} |p_t|^2 \sin \theta d\theta d\phi \quad (3.23)$$

and it is proportional to the radiated acoustic power. When the expression of p_t from Equation (3.20) is substituted into Equation (3.23), the cost function is obviously quad-

quadratic and positive definite and possesses a unique minimum. A minimization procedure (Lester and Fuller, 1990) for the quadratic function was employed to calculate the optimal control parameters.

The total pressure of Equation (3.20) can be expressed in vector form as:

$$p_t = \bar{B}^T \bar{G} + \bar{A}^T \bar{H} \quad (3.24)$$

where

$$\bar{B} = \begin{bmatrix} B_1 \\ B_2 \\ \cdot \\ \cdot \\ B_{N_s} \end{bmatrix}_{N_s \times 1} \quad (3.25)$$

$$\bar{A} = \begin{bmatrix} A_1 \\ A_2 \\ \cdot \\ \cdot \\ A_{N_e} \end{bmatrix}_{N_e \times 1} \quad (3.26)$$

$$\bar{G} = \begin{bmatrix} G_1 \\ G_2 \\ \cdot \\ \cdot \\ G_{N_s} \end{bmatrix}_{N_s \times 1} \quad (3.27)$$

$$\bar{H} = \begin{bmatrix} H_1 \\ H_2 \\ \cdot \\ \cdot \\ \cdot \\ H_{N_c} \end{bmatrix}_{N_c \times 1} \quad (3.28)$$

Then

$$|p_t|^2 = \bar{H}^T [\bar{A} \bar{A}^*{}^T] \bar{H}^* + 2 \text{Real}\{\bar{G}^T [\bar{B} \bar{A}^*{}^T] \bar{H}^*\} + \bar{G}^T [\bar{B} \bar{B}^*{}^T] \bar{G}^* \quad (3.29)$$

where * denotes complex conjugate, and T denotes transpose of matrix; hence, the cost function can be written in matrix form as

$$\Phi_p = \bar{H}^T [\tilde{A}] \bar{H}^* + 2 \text{Real}\{\bar{G}^T [\tilde{B} \tilde{A}] \bar{H}^*\} + \bar{G}^T [\tilde{B}] \bar{G}^* \quad (3.30)$$

where

$$[\tilde{A}]_{N_c \times N_c} = \int_0^{2\pi} \int_0^{\frac{\pi}{2}} [\bar{A} \bar{A}^*{}^T] \sin \theta d\theta d\phi \quad (3.31)$$

$$[\tilde{B} \tilde{A}]_{N_s \times N_c} = \int_0^{2\pi} \int_0^{\frac{\pi}{2}} [\bar{B} \bar{A}^*{}^T] \sin \theta d\theta d\phi \quad (3.32)$$

$$[\tilde{B}]_{N_s \times N_s} = \int_0^{2\pi} \int_0^{\frac{\pi}{2}} [\bar{B} \bar{B}^*{}^T] \sin \theta d\theta d\phi \quad (3.33)$$

Since

$$[\overline{AA}^*T]_{N_c \times N_c} = \begin{bmatrix} A_1 \\ A_2 \\ \vdots \\ A_{N_c} \end{bmatrix}_{N_c \times 1} [A_1^* A_2^* \dots A_{N_c}^*]_{1 \times N_c} = \begin{bmatrix} A_1 A_1^* & A_1 A_2^* & \dots & A_1 A_{N_c}^* \\ A_2 A_1^* & A_2 A_2^* & \dots & A_2 A_{N_c}^* \\ \vdots & \vdots & \dots & \vdots \\ A_{N_c} A_1^* & A_{N_c} A_2^* & \dots & A_{N_c} A_{N_c}^* \end{bmatrix}_{N_c \times N_c} \quad (3.34)$$

a typical element of $[\overline{AA}^*T]$ is

$$A_r A_s^* = K_r K_s^* \sum_{k=1}^{\infty} \sum_{l=1}^{\infty} \sum_{m=1}^{\infty} \sum_{n=1}^{\infty} Q_{klr}^c Q_{mns}^c I_{klr}^c I_{mns}^c \quad (3.35)$$

where $I_{mn} = I_m I_n$, and then for a typical element of $[\tilde{A}]_{N_c \times N_c}$

$$\tilde{A}_{rs} = \int_0^{2\pi} \int_0^{\frac{\pi}{2}} K_r K_s^* \sum_{k=1}^{\infty} \sum_{l=1}^{\infty} \sum_{m=1}^{\infty} \sum_{n=1}^{\infty} Q_{klr}^c Q_{mns}^c I_{klr}^c I_{mns}^c \sin \theta d\theta d\phi \quad (3.36)$$

Similarly, a typical element of $[\tilde{BA}]_{N_s \times N_c}$ is as follows:

$$\tilde{BA}_{rs} = \int_0^{2\pi} \int_0^{\frac{\pi}{2}} K_r K_s^* \sum_{k=1}^{\infty} \sum_{l=1}^{\infty} \sum_{m=1}^{\infty} \sum_{n=1}^{\infty} Q_{klr}^n Q_{mns}^c I_{klr}^n I_{mns}^c \sin \theta d\theta d\phi \quad (3.37)$$

and a typical element of $[\tilde{B}]_{N_s \times N_s}$

$$\tilde{B}_{rs} = \int_0^{2\pi} \int_0^{\frac{\pi}{2}} K_r K_s^* \sum_{k=1}^{\infty} \sum_{l=1}^{\infty} \sum_{m=1}^{\infty} \sum_{n=1}^{\infty} Q_{klr}^n Q_{mns}^{n*} I_{klr}^n I_{mns}^{n*} \sin \theta d\theta d\phi \quad (3.38)$$

Since $(\bar{G}^T[\tilde{B}]\bar{G}^*)$ is a constant, the cost function was then redefined as

$$\tilde{\Phi}_p = \Phi_p - \bar{G}^T[\tilde{B}]\bar{G}^* \quad (3.39)$$

If we let

$$\bar{F}^T = -\bar{G}^T[\tilde{B}A] \quad (3.40)$$

then the optimal solution for the cost function can be found as (Lester and Fuller, 1990)

$$\bar{H} = [\tilde{A}]^{-1} \bar{F} \quad (3.41)$$

It is noted that \bar{H} is the optimized vector which is defined in Equation (3.28).

3.3.2 Discrete Pressure Sensor (Microphone)

If a finite number of microphones located in the radiating field serve as error sensors, then the cost function can be defined as follow:

$$\Psi_p = \sum_{i=1}^{N_{mike}} |p_i(R_i, \theta_i, \phi_i)|^2 \quad (3.42)$$

If the total pressure is expressed in vector form as Equation (3.24), then the cost function can be written in matrix form as

$$\Psi_p = \bar{H}^T [\tilde{A}] \bar{H}^* + 2 \text{Real}\{\bar{G}^T [\tilde{B} \bar{A}] \bar{H}^*\} + \bar{G}^T [\tilde{B}] \bar{G}^* \quad (3.43)$$

where

$$[\tilde{A}]_{N_c \times N_c} = \sum_{i=1}^{N_{mike}} [\bar{A} \bar{A}^*{}^T] \quad (3.44)$$

$$[\tilde{B} \bar{A}]_{N_s \times N_c} = \sum_{i=1}^{N_{mike}} [\bar{B} \bar{A}^*{}^T] \quad (3.45)$$

$$[\tilde{B}]_{N_s \times N_s} = \sum_{i=1}^{N_{mike}} [\bar{B} \bar{B}^*{}^T] \quad (3.46)$$

Since

$$[\bar{A} \bar{A}^*{}^T]_{N_c \times N_c} = \begin{bmatrix} A_1 \\ A_2 \\ \vdots \\ A_{N_c} \end{bmatrix}_{N_c \times 1} [A_1^* \ A_2^* \ \dots \ A_{N_c}^*]_{1 \times N_c} = \begin{bmatrix} A_1 A_1^* & A_1 A_2^* & & A_1 A_{N_c}^* \\ A_2 A_1^* & A_2 A_2^* & & A_2 A_{N_c}^* \\ \vdots & \vdots & \dots & \vdots \\ \vdots & \vdots & & \vdots \\ A_{N_c} A_1^* & A_{N_c} A_2^* & & A_{N_c} A_{N_c}^* \end{bmatrix}_{N_c \times N_c} \quad (3.47)$$

a typical element of $[\bar{A} \bar{A}^*{}^T]$ is

$$A_r A_s^* = K_r K_s^* \sum_{k=1}^{\infty} \sum_{l=1}^{\infty} \sum_{m=1}^{\infty} \sum_{n=1}^{\infty} Q_{klr}^c Q_{mns}^c I_{klr}^c I_{mns}^c \quad (3.48)$$

and then for a typical element of $[\tilde{A}]_{N_c \times N_c}$

$$\tilde{A}_{rs} = \sum_{l=1}^{N_{mike}} K_r K_s^* \sum_{k=1}^{\infty} \sum_{l=1}^{\infty} \sum_{m=1}^{\infty} \sum_{n=1}^{\infty} Q_{klr}^c Q_{mns}^c I_{klr}^c I_{mns}^c \quad (3.49)$$

Similarly, a typical element of $[\tilde{BA}]_{N_s \times N_c}$ is as follows:

$$\tilde{BA}_{rs} = \sum_{i=1}^{N_{mike}} K_r K_s^* \sum_{k=1}^{\infty} \sum_{l=1}^{\infty} \sum_{m=1}^{\infty} \sum_{n=1}^{\infty} Q_{klr}^n Q_{mns}^c I_{klr}^n I_{mns}^c \quad (3.50)$$

and a typical element of $[\tilde{B}]_{N_s \times N_s}$

$$\tilde{B}_{rs} = \sum_{i=1}^{N_{mike}} K_r K_s^* \sum_{k=1}^{\infty} \sum_{l=1}^{\infty} \sum_{m=1}^{\infty} \sum_{n=1}^{\infty} Q_{klr}^n Q_{mns}^f I_{klr}^n I_{mns}^f \quad (3.51)$$

Since $(\bar{G}^T [\tilde{B}] \bar{G}^*)$ is a constant, the cost function was then redefined as

$$\tilde{\Psi}_p = \Psi_p - \bar{G}^T [\tilde{B}] \bar{G}^* \quad (3.52)$$

If we let

$$\bar{F}^T = -\bar{G}^T [\tilde{BA}] \quad (3.53)$$

then the optimal solution for the cost function can be found as (Lester and Fuller, 1990)

$$\bar{H} = [\tilde{A}]^{-1} \bar{F} \quad (3.54)$$

It is noted that \bar{H} is the optimized vector which is defined in Equation (3.28).

3.3.3 Distributed Acceleration Sensor

As illustration of distributed pressure sensors in Section 3.3.1, a similar distributed accelerometer can also be assumed to be located over the plate to measure the plate dynamic response. Although, in practice, it is very difficult to implement, this type of distributed sensor represents the out-of-plane vibration energy density over the plate. On the other hand, as discussed in Chapter 1, distributed *strain* sensors, such as PVDF film sensors attached to the plate surface (Clark and Fuller, 1990b), can also be constructed to be utilized in ASAC. These types of *strain* sensors, in contrast to the distributed acceleration sensor discussed here which is phase independent, will tend to average out information over the plate with associated phase changes. This subject, however, is out of the context of the present work. The cost function corresponding to the distributed acceleration sensor can be defined as follow:

$$\Phi_w = \int_A |\ddot{w}_t|^2 dA = \int_0^{L_y} \int_0^{L_x} |\ddot{w}_t|^2 dx dy \quad (3.55)$$

It is noted that Φ_w can be viewed as the out-of-plane vibration energy density. When the expression of w_t from Equation (3.11) is substituted into Equation (3.55), the cost function is obviously quadratic and positive definite and possesses a unique minimum.

A minimization procedure (Lester and Fuller, 1990) for the quadratic function was employed to calculate the optimal control parameters.

The total plate displacement of Equation (3.11) can be expressed in vector form

$$w_t = \overline{B} \overline{G} + \overline{A} \overline{H} \quad (3.56)$$

where

$$\overline{B} = \begin{bmatrix} \hat{B}_1 \\ \hat{B}_2 \\ \vdots \\ \hat{B}_{N_c} \end{bmatrix}_{N_c \times 1} \quad (3.57)$$

$$\overline{A} = \begin{bmatrix} \hat{A}_1 \\ \hat{A}_2 \\ \vdots \\ \hat{A}_{N_c} \end{bmatrix}_{N_c \times 1} \quad (3.58)$$

Then

$$|\dot{w}_t|^2 = \overline{H}^T [\overline{A} \overline{A}^{*T}] \overline{H}^* + 2 \text{Real}\{\overline{G}^T [\overline{B} \overline{A}^{*T}] \overline{H}^*\} + \overline{G}^T [\overline{B} \overline{B}^{*T}] \overline{G}^* \quad (3.59)$$

where * denotes complex conjugate, and T denotes transpose of matrix; hence, the cost function can be written in matrix form as

$$\Phi_w = \bar{H}^T [\tilde{A}] \bar{H}^* + 2\text{Real}\{\bar{G}^T [\tilde{BA}] \bar{H}^*\} + \bar{G}^T [\tilde{B}] \bar{G}^* \quad (3.60)$$

where

$$[\tilde{A}]_{N_c \times N_c} = \int_0^{L_y} \int_0^{L_x} [\bar{A} \quad \bar{A}^{*T}] d\xi d\eta \quad (3.61)$$

$$[\tilde{BA}]_{N_s \times N_c} = \int_0^{L_y} \int_0^{L_x} [\bar{B} \quad \bar{A}^{*T}] d\xi d\eta \quad (3.62)$$

$$[\tilde{B}]_{N_s \times N_s} = \int_0^{L_y} \int_0^{L_x} [\bar{B} \quad \bar{B}^{*T}] d\xi d\eta \quad (3.63)$$

Since

$$[\bar{A} \quad \bar{A}^{*T}]_{N_c \times N_c} = \begin{bmatrix} \hat{A}_1 \\ \hat{A}_2 \\ \vdots \\ \hat{A}_{N_c} \end{bmatrix}_{N_c \times 1} [\hat{A}_1^* \hat{A}_2^* \dots \hat{A}_{N_c}^*]_{1 \times N_c} \quad (3.64)$$

$$= \begin{bmatrix} \hat{A}_1 \hat{A}_1^* & \hat{A}_1 \hat{A}_2^* & \dots & \hat{A}_1 \hat{A}_{N_c}^* \\ \hat{A}_2 \hat{A}_1^* & \hat{A}_2 \hat{A}_2^* & \dots & \hat{A}_2 \hat{A}_{N_c}^* \\ \vdots & \vdots & \dots & \vdots \\ \hat{A}_{N_c} \hat{A}_1^* & \hat{A}_{N_c} \hat{A}_2^* & \dots & \hat{A}_{N_c} \hat{A}_{N_c}^* \end{bmatrix}_{N_c \times N_c}$$

a typical element of $[\bar{A} \quad \bar{A}^{*T}]$ is

$$\hat{A}_r \hat{A}_s^* = \sum_{k=1}^{\infty} \sum_{l=1}^{\infty} \sum_{m=1}^{\infty} \sum_{n=1}^{\infty} Q_{klr}^c Q_{mns}^c S_{klr}^c S_{mns}^c \sin \theta d\theta d\phi \quad (3.65)$$

where $S_{mn} = \sin \kappa_m \xi \sin \kappa_n \eta$, and then a typical element of $[\tilde{A}]_{N_c \times N_c}$

$$\tilde{A}_{rs} = \int_0^{L_y} \int_0^{L_x} \sum_{k=1}^{\infty} \sum_{l=1}^{\infty} \sum_{m=1}^{\infty} \sum_{n=1}^{\infty} Q_{klr}^c Q_{mns}^c S_{klr}^c S_{mns}^c d\xi d\eta \quad (3.66)$$

Similarly, a typical element of $[\tilde{B}\tilde{A}]_{N_r \times N_c}$ is as follows:

$$\tilde{B}A_{rs} = \int_0^{L_y} \int_0^{L_x} \sum_{k=1}^{\infty} \sum_{l=1}^{\infty} \sum_{m=1}^{\infty} \sum_{n=1}^{\infty} Q_{klr}^n Q_{mns}^c S_{klr}^n S_{mns}^c d\xi d\eta \quad (3.67)$$

and a typical element of $[\tilde{B}]_{N_s \times N_s}$

$$\tilde{B}_{rs} = \int_0^{L_y} \int_0^{L_x} \sum_{k=1}^{\infty} \sum_{l=1}^{\infty} \sum_{m=1}^{\infty} \sum_{n=1}^{\infty} Q_{klr}^n Q_{mns}^n S_{klr}^n S_{mns}^n d\xi d\eta \quad (3.68)$$

Since $(\bar{G}^T[\tilde{B}]\bar{G})$ is a constant, the cost function, in order to provide the optimal solution, can then be redefined as

$$\tilde{\Phi}_w = \Phi_w - \bar{G}^T[\tilde{B}]\bar{G} \quad (3.69)$$

If we let

$$\bar{F}^T = -\bar{G}^T[\tilde{B}A] \quad (3.70)$$

then the optimal solution to minimize the cost function can be found as (Lester and Fuller, 1990)

$$\bar{H} = [\tilde{A}]^{-1}\bar{F} \quad (3.71)$$

It is noted that \bar{H} is the optimized vector which is defined in Equation (3.28). The minimized value of cost function, therefore, represents the residual vibrational energy density over the plate after control.

3.3.4 Discrete Acceleration Sensor (Accelerometer)

If a finite number of accelerometers located on the plate serve as error sensors, then the cost function can be defined as the sum of the mean square acceleration:

$$\Psi_w = \sum_{i=1}^{N_{acc}} |\ddot{w}_{t_i}(x_{p_i}, y_{p_i})|^2 \quad (3.72)$$

Hence, the cost function can be written in matrix form as

$$\Psi_w = \bar{H}^T [\tilde{A}] \bar{H}^* + 2 \text{Real}\{\bar{G}^T [\tilde{B}A] \bar{H}^*\} + \bar{G}^T [\tilde{B}] \bar{G}^* \quad (3.73)$$

where

$$[\tilde{A}]_{N_c \times N_c} = \sum_{i=1}^{N_{acc}} \begin{bmatrix} \bar{A} & \bar{A}^{*T} \end{bmatrix} \quad (3.74)$$

$$[\tilde{B}A]_{N_s \times N_c} = \sum_{i=1}^{N_{acc}} \begin{bmatrix} \bar{B} & \bar{A}^{*T} \end{bmatrix} \quad (3.75)$$

$$[\tilde{B}]_{N_s \times N_s} = \sum_{i=1}^{N_{acc}} \begin{bmatrix} \bar{B} & \bar{B}^{*T} \end{bmatrix} \quad (3.76)$$

Since

$$[\bar{A} \quad \bar{A}^{*T}]_{N_c \times N_c} = \begin{bmatrix} \hat{A}_1 \\ \hat{A}_2 \\ \vdots \\ \vdots \\ \hat{A}_{N_c} \end{bmatrix}_{N_c \times 1} [\hat{A}_1^* \hat{A}_2^* \dots \hat{A}_{N_c}^*]_{1 \times N_c} \quad (3.77)$$

$$= \begin{bmatrix} \hat{A}_1 \hat{A}_1^* & \hat{A}_1 \hat{A}_2^* & \dots & \hat{A}_1 \hat{A}_{N_c}^* \\ \hat{A}_2 \hat{A}_1^* & \hat{A}_2 \hat{A}_2^* & \dots & \hat{A}_2 \hat{A}_{N_c}^* \\ \vdots & \vdots & \dots & \vdots \\ \vdots & \vdots & \dots & \vdots \\ \hat{A}_{N_c} \hat{A}_1^* & \hat{A}_{N_c} \hat{A}_2^* & \dots & \hat{A}_{N_c} \hat{A}_{N_c}^* \end{bmatrix}_{N_c \times N_c}$$

a typical element of $[\bar{A} \quad \bar{A}^{*T}]$ is

$$A_r A_s^* = \sum_{k=1}^{\infty} \sum_{l=1}^{\infty} \sum_{m=1}^{\infty} \sum_{n=1}^{\infty} Q_{klr}^c Q_{mns}^c S_{klr}^c S_{mns}^c \quad (3.78)$$

and then for a typical element of $[\tilde{A}]_{N_c \times N_c}$

$$\tilde{A}_{rs} = \sum_{i=1}^{N_{acc}} \sum_{k=1}^{\infty} \sum_{l=1}^{\infty} \sum_{m=1}^{\infty} \sum_{n=1}^{\infty} Q_{klr}^c Q_{mns}^c S_{klr}^c S_{mns}^c \quad (3.79)$$

Similarly, a typical element of $[\tilde{B}\tilde{A}]_{N_c \times N_c}$ is as follows:

$$\tilde{B}A_{rs} = \sum_{l=1}^{N_{acc}} \sum_{k=1}^{\infty} \sum_{l=1}^{\infty} \sum_{m=1}^{\infty} \sum_{n=1}^{\infty} Q_{klr}^n Q_{mns}^c S_{klr}^n S_{mns}^c \quad (3.80)$$

and a typical element of $[\tilde{B}]_{N_r \times N_s}$

$$\tilde{B}_{rs} = \sum_{i=1}^{N_{acc}} \sum_{k=1}^{\infty} \sum_{l=1}^{\infty} \sum_{m=1}^{\infty} \sum_{n=1}^{\infty} Q_{klr}^n Q_{mns}^f S_{klr}^n S_{mns}^f \quad (3.81)$$

Since $(\bar{G}^T[\tilde{B}]\bar{G}^*)$ is a constant, the cost function was then redefined as

$$\tilde{\Psi}_w = \Psi_w - \bar{G}^T[\tilde{B}]\bar{G}^* \quad (3.82)$$

If we let

$$\bar{F}^T = -\bar{G}^T[\tilde{B}A] \quad (3.83)$$

then the optimal solution for the cost function can be found as (Lester and Fuller, 1990)

$$\bar{H} = [\tilde{A}]^{-1}\bar{F} \quad (3.84)$$

It is noted that \bar{H} is the optimized vector which is defined in Equation (3.28).

In summary, Φ_p and Φ_w are measured by ideal sensors, which may not be practical in reality; however, Φ_p and Φ_w represent the power of sound radiation or energy density of out-of-plane structural vibration respectively. They can be used as an index of control effectiveness. For practical application, Ψ_p and Ψ_w are the alternative option. A reasonable number and location of sensors shall be selected to estimate the actual system

distributed response, such that an optimal solution can be found without losing the general nature of the response.

3.4 Special Topics in Structural Acoustics

3.4.1 Plate Transmission Loss

For an incident acoustic plane wave at angle θ_i , the incident acoustic power to the plate of dimension L_x and L_y is easily shown to be (Roussos, 1985)

$$\Pi_i = \frac{P_i^2 L_x L_y \cos \theta_i}{2\rho c} \quad (3.85)$$

where ρ and c are mass density of air and sound speed in air, and the total radiated acoustic power from the plate (on the other side) associated with Equation (3.23) can be shown as

$$\Pi_r = \int_0^{2\pi} \int_0^{\frac{\pi}{2}} \frac{|p_r|^2}{\rho c} R^2 \sin \theta d\theta d\phi = \frac{R^4}{\rho c} \Phi_p \quad (3.86)$$

Then, the plate transmission loss (TL) through the plate can be defined as follow

$$TL = 10 \log\left(\frac{\Pi_i}{\Pi_r}\right) \quad (3.87)$$

Transmission loss is an evaluation of the inverse of sound transmission efficiency; hence, the larger the value of TL, the less sound power is transmitted through the panel with a corresponding improvement in reduction of global sound radiation.

3.4.2 Time-Averaged Intensity

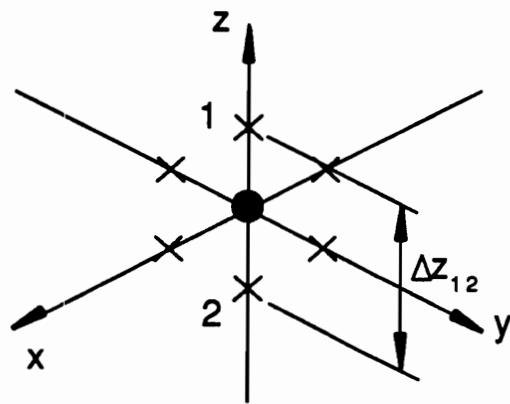
The distribution of vectors associated with the magnitude and direction of intensity in acoustic fields have been proved useful in studying the flow of energy. The two microphone technique (Pettersen, 1979), which is based on the finite difference method, has been widely adopted to measure or calculate the acoustic intensity for its simplicity (Krishnappa and McDougall, 1989; Kristiansen, 1981). The schematic used for the intensity calculation by the finite difference method is shown in Figure 17 for the z-direction. From the fundamental relationship between acoustic pressure and velocity and the finite difference approximation, the averaged acoustic pressure and particle velocity in the z-direction (for example) between points 1 and 2 can be formulated as follows (Pettersen, 1979):

$$p_{12} \simeq \frac{(p_1 + p_2)}{2} \quad (3.88)$$

$$u_{z12} \simeq \frac{-(p_2 - p_1)}{j\rho\omega\Delta z_{12}} \quad (3.89)$$

where

$$p_1 = |p_1| e^{j\phi_1}, \quad \phi_1 = \tan^{-1}\left(\frac{\text{Im}\{p_1\}}{\text{Re}\{p_1\}}\right) \quad (3.90)$$



$$I_{z_{12}} = \frac{|p_1| |p_2|}{2 \omega \rho \Delta z_{12}} \sin(\phi_1 - \phi_2)$$

$$p_1 = |p_1| e^{j\phi_1}$$

$$p_2 = |p_2| e^{j\phi_2}$$

Figure 17. Schematic of intensity calculation

$$p_2 = |p_2| e^{j\phi_2}, \quad \phi_2 = \tan^{-1} \left(\frac{\text{Im}\{p_2\}}{\text{Re}\{p_2\}} \right) \quad (3.91)$$

Hence, the time-averaged intensity in the z-direction between the two points can be shown to be (Pettersen, 1979)

$$I_{z_{12}} = \frac{|p_1| |p_2|}{2\rho c \Delta z_{12}} \sin(\phi_1 - \phi_2) \quad (3.92)$$

Similarly, the time-averaged intensity distribution for other directions can also be derived by the replacement of the separated distance Δz_{12} and the appropriate variables. The total intensity is then the vector sum of the intensities in the x,y and z directions.

3.4.3 Plate Wavenumber Analysis

The plate velocity distribution derived from Equation (3.1) can be transformed to the central origin plate coordinates (ξ', η') as

$$\dot{w}(\xi', \eta', t) = j\omega e^{j\omega t} \sum_{m=1}^{\infty} \sum_{n=1}^{\infty} W_{mn} \sin \kappa_m(\xi' + L_x/2) \sin \kappa_n(\eta' + L_y/2) \quad (3.93)$$

The wavenumber transform, which is the Fourier integral transform, of plate velocity is then given by (Fahy, 1985)

$$\begin{aligned} \tilde{V}(\kappa_x, \kappa_y) &= \int_0^{L_y} \int_0^{L_x} \dot{w}(\xi', \eta') e^{-j(\kappa_x \xi' + \kappa_y \eta')} d\xi' d\eta' \\ &= j\omega e^{j\omega t} \sum_{m=1}^{\infty} \sum_{n=1}^{\infty} W_{mn} V_{mn} \end{aligned} \quad (3.94)$$

where

$$\begin{aligned}
 V_{mn}(\kappa_x, \kappa_y) = & \frac{4\kappa_m\kappa_n}{(\kappa_m^2 - \kappa_x^2)(\kappa_n^2 - \kappa_y^2)} \{ [\sin^2(m\pi/2) \sin^2(n\pi/2) \cos(\kappa_x L_x/2) \cos(\kappa_y L_y/2) \\
 & - \cos^2(m\pi/2) \cos^2(n\pi/2) \sin(\kappa_x L_x/2) \sin(\kappa_y L_y/2)] \quad (3.95) \\
 & - j[\sin^2(m\pi/2) \cos^2(n\pi/2) \cos(\kappa_x L_x/2) \sin(\kappa_y L_y/2) \\
 & + \cos^2(m\pi/2) \sin^2(n\pi/2) \sin(\kappa_x L_x/2) \cos(\kappa_y L_y/2)] \}
 \end{aligned}$$

Hence, the plate spectral velocity distribution can be obtained from the inverse Fourier transform

$$\dot{w}(\xi', \eta') = \frac{1}{2\pi} \int_{-\infty}^{\infty} \int_{-\infty}^{\infty} \tilde{V}(\kappa_x, \kappa_y) e^{-j(\kappa_x \xi' + \kappa_y \eta')} d\kappa_x d\kappa_y \quad (3.96)$$

The radiated power has been shown in (Fahy, 1985) to be related to the integration of the modulus square of $\tilde{V}(\kappa_x, \kappa_y)$ over the wavenumber domain. Therefore, it is of interest to evaluate the wavenumber modulus spectrum of plate velocity, $|\tilde{V}(\kappa_x, \kappa_y)|^2$. It is noted that the wavenumber modulus spectrum of modal velocity is a function of κ_x, κ_y and is composed of a double infinite sum of modes. Only wavenumber components satisfying the condition $(\kappa_x^2 + \kappa_y^2) < \kappa^2$ (i.e., supersonic wavenumbers) contribute to sound power radiation; other components are associated with reactive near-field radiation loadings (Fahy, 1985). Thus the range of integration is limited to $-\kappa < \kappa_x < \kappa$ and $-\kappa < \kappa_y < \kappa$.

The sound pressure in the radiated acoustic far-field can also be evaluated from the wavenumber transform of plate acceleration using the method of stationary phase (Junger and Feit, 1986) as

$$\begin{aligned}
 p(r, \theta, \phi) &= \frac{\rho e^{j\kappa r}}{2\pi r} \tilde{w}(\kappa_x, \kappa_y) = j \frac{\omega \rho e^{j\kappa r}}{2\pi r} \tilde{V}(\kappa_x, \kappa_y) \\
 &= -\frac{\rho \omega^2 e^{j\kappa r}}{2\pi r} \sum_{m=1}^{\infty} \sum_{n=1}^{\infty} W_{mn} V_{mn}
 \end{aligned} \tag{3.97}$$

where the points of stationary phase are

$$\kappa_x = \kappa \sin \theta \cos \phi \tag{3.98}$$

$$\kappa_y = \kappa \sin \theta \sin \phi \tag{3.99}$$

One can demonstrate that Equation (3.97) is equivalent to Equation (3.20).

3.4.4 Radiation Efficiency

The mechanism of structural sound radiation has been a great deal of interest. For the appropriate design of sound radiation control, it is necessary to understand structural radiation characteristics. The radiation efficiency of a vibrating structure quantifies the degree of acoustic coupling between sound radiation and structural vibration. The following will show the definition and derivation of the individual mode radiation efficiency and the average radiation efficiency, which is associated with total radiated power from a series of modes existing simultaneously.

3.4.4.1 Mode Radiation Efficiency

The plate displacement distribution corresponding to the (m,n) mode can be shown to be as follow:

$$w_{mn}(\xi, \eta, t) = e^{j\omega t} W_{mn} \sin \kappa_m \xi \sin \kappa_n \eta \quad (3.100)$$

and the plate velocity corresponding to the (m,n) mode is:

$$u_{mn}(\xi, \eta, t) = j\omega e^{j\omega t} W_{mn} \sin \kappa_m \xi \sin \kappa_n \eta \quad (3.101)$$

The sound pressure in the far-field from Equation (3.20) can also be expressed as:

$$p_t = \sum_{m=1}^{\infty} \sum_{n=1}^{\infty} (p_t)_{mn} \quad (3.102)$$

where $(p_t)_{mn}$ is the sound pressure corresponding to the (m,n) plate flexural mode. The radiation efficiency of the (m,n) mode is defined as (Wallace, 1972):

$$\sigma_{mn} = \frac{\Pi_{mn}}{\rho c L_x L_y \langle |\bar{u}_{mn}| \rangle^2} \quad (3.103)$$

where

$$\Pi_{mn} = \int_0^{2\pi} \int_0^{\frac{\pi}{2}} \frac{|(p_t)_{mn}|^2}{\rho c} R^2 \sin \theta d\theta d\phi \quad (3.104)$$

$$\begin{aligned}
\langle |\bar{u}_{mn}| \rangle^2 &= \frac{1}{L_x L_y} \int_0^{L_y} \int_0^{L_x} \frac{|u_{mn}|^2}{2} dx dy \\
&= \frac{1}{8} \omega^2 W_{mn}^2
\end{aligned}
\tag{3.105}$$

In Equation (3.104), Π_{mn} is the radiated power due to the (m,n) mode response, and $\langle |\bar{u}_{mn}|^2 \rangle$, in Equation (3.105), is the temporal and spatial average of the square of the (m,n) mode plate velocity. By substituting Equations (3.104) and (3.105) into Equation (3.103), the radiation efficiency of the (m,n) mode can be expressed as:

$$\sigma_{mn} = \frac{8\Pi_{mn}}{\rho c L_x L_y \omega^2 W_{mn}^2}
\tag{3.106}$$

It is noted that σ_{mn} represents the radiation efficiency of the (m,n) mode and can be considered as a structural-acoustic property which indicates the acoustic coupling between mechanical vibration of particular mode and sound radiation. Radiation efficiency is defined as the ratio of the acoustic power radiated from the elastic plate to the power radiated from a rigid piston of same area vibrating with an amplitude equal to the time-spatial average of the plate velocity. For illustration, Figure 18 (Wallace, 1972) shows the modal radiation efficiency for a square plate plotted against the wavenumber ratio (note that the modal radiation efficiencies for the rectangular plate used in the numerical examples in Section 3.5.4.1 are shown in Figures 56 and 57). The wavenumber ratio is defined as:

$$\gamma = \frac{\kappa}{\kappa_p}
\tag{3.107}$$

where

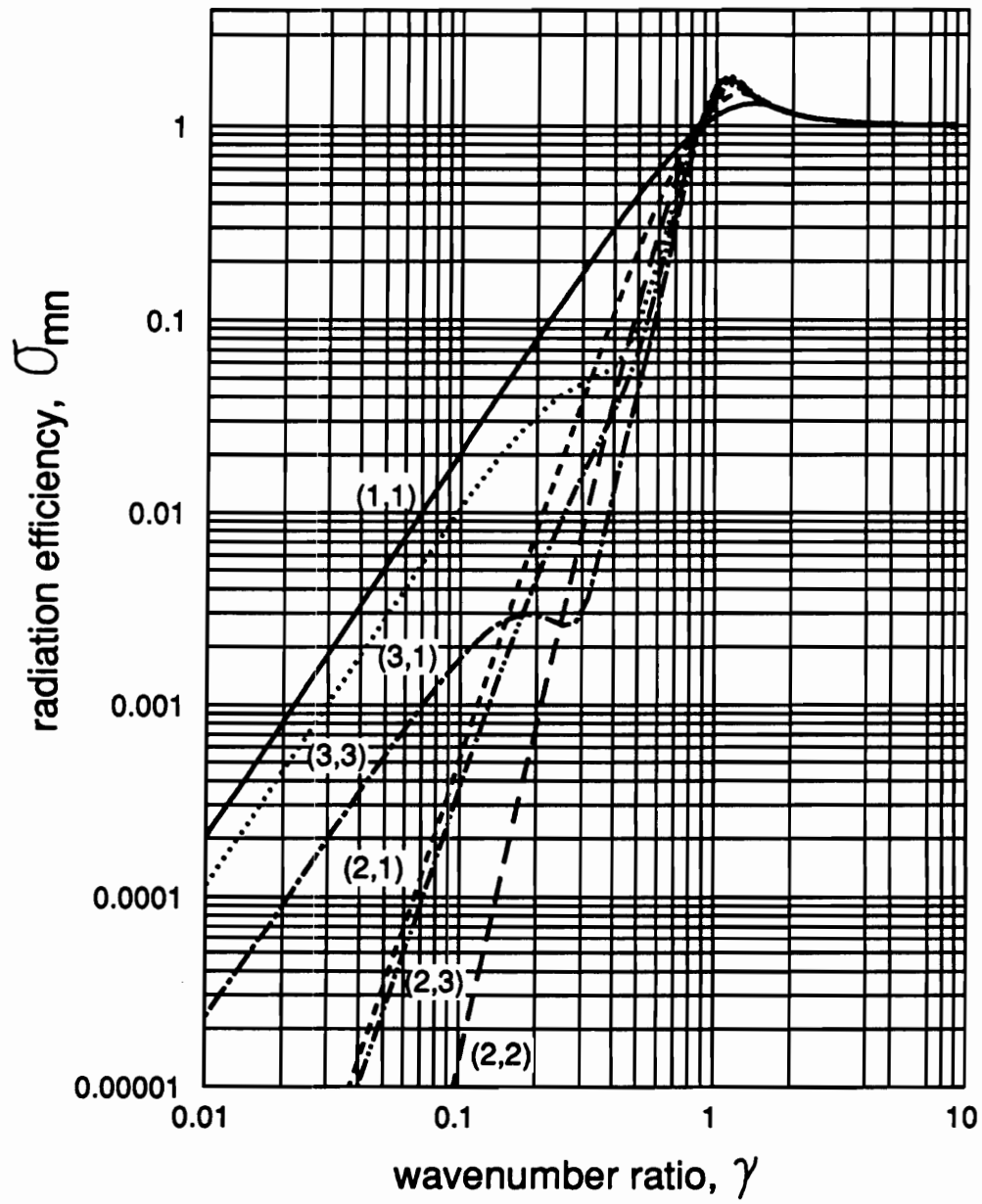


Figure 18. The radiation efficiency of the (m,n) mode for a square plate (Wallace, 1972)

$$\kappa_p = \left(\frac{\omega^2 \rho h}{D} \right)^{1/4} \quad (3.108)$$

When the wavenumber ratio equals to 1 (i.e., $\gamma = 1$), the "critical frequency" can be defined as follow:

$$\omega_c = c^2 \sqrt{\frac{\rho h}{D}} \quad (3.109)$$

For low wavenumber ratios, the odd-odd modes, such as the (1,1), (3,1) and (3,3) modes which strongly couple the sound radiation and mechanical vibration, have higher radiation efficiency than the odd-even or even-odd modes ((2,1) or (2,3) modes) and the even-even mode ((2,2) mode), which are subjected to the radiation cancellation. The physical reason that even modes generally do not radiate efficiently is due to volumetric cancellation. At low frequencies, fluid from one cell is "shunted" over to an adjacent cell of equal area but moving out-of-phase. Radiation comes from energy due to a change in momentum associated with a change in the direction of fluid motion. For γ greater than 1, i.e., excitation frequency above the critical frequency, the radiation efficiency approaches asymptotically to unity for all modes. This indicates that each mode has an equivalent contribution in terms of acoustic coupling. For $\gamma \gg 1$, the acoustic wavelength becomes shorter than distance between "cell" on the plate, so they do not interact but radiate independently.

Also, the primary structural wavenumber, κ_{mn} , can be defined as:

$$\kappa_{mn} = (\kappa_m^2 + \kappa_n^2)^{1/2} \quad (3.110)$$

If $\frac{\kappa}{\kappa_{mn}} = 1$, then the "modal critical frequency" for the (m,n) mode can be defined as:

$$\omega_{mn}^c = c^2 \frac{\rho h^{1/4}}{D} \sqrt{\omega_{mn}} \quad (3.111)$$

Table 5 shows the definition of the associated wavenumbers and frequencies. Figure 19 illustrates the distributions of wavenumbers and their physical interpretation regarding to radiation characteristic of an elastic plate. As shown on the top of Figure 19 (Mathur, Gardner and Burge, 1990), wavenumbers are plotted against frequency. The thick solid line denotes the acoustic wavenumber, which is linearly related to the excitation frequency. The thin solid line denotes the free structural wavenumber while the circle mark denotes the primary structural wavenumber. The critical frequency is defined in Equation (3.109), when the acoustic wavenumber equals to the free structural wavenumber. For excitation frequencies above the critical frequency denoted as Region (3), the corresponding wavenumber distribution in the wavevector domain is shown on the bottom-right of Figure 19 (Maidanik, 1974). In this region, the resonant modes near κ_p are included in what are termed "surface modes", which are the most effective radiators, since they are driven well above $\gamma = 1$. For excitation frequencies below the critical frequency, two regions can be characterized: Region (1): $\kappa < \kappa_p < 2^{1/2}\kappa$; and Region (2): $\kappa_p > 2^{1/2}\kappa$. κ_p is the free structural wavenumber while κ is the acoustic wavenumber corresponding to the excitation frequency. In Region (1), the sound radiation is contributed from the surface modes and the resonant modes, which include both the edge and corner modes as shown on the left-bottom of Figure 19. In Region (2), the resonant modes include only both the x- and y-edge modes while there is still some surface modes.

To physically understand the corner, edge and surface mode radiations, Figure 20 depicts the displacement pattern for each type of radiation. The relative phases are indicated by + and -, and the uncanceled areas are shaded. Figure 20(a) shows the cor-

Table 5. Summary of frequency and wavenumber

excitation frequency	ω
natural frequency of plate	$\omega_{mn} = \sqrt{\frac{D}{\rho_p h}} (\kappa_m^2 + \kappa_n^2)$
critical frequency	$\omega_c = c^2 \sqrt{\frac{\rho_p h}{D}}$
modal critical frequency	$\omega_{mn}^c = c \left(\frac{\rho_p h}{D} \right)^{1/4} \sqrt{\omega_{mn}}$
acoustic wavenumber	$\kappa = \frac{\omega}{c}$
free structural wavenumber	$\kappa_p = \left(\frac{\omega^2 \rho_p h}{D} \right)^{1/4}$
primary structural wavenumber	$\kappa_{mn} = \sqrt{\kappa_m^2 + \kappa_n^2}$
structural normal mode wavenumber	$\kappa_m = \frac{m\pi}{L_x}$ $\kappa_n = \frac{n\pi}{L_y}$
structural modal wavenumber	$\kappa_x = \kappa \sin \theta \cos \phi$ $\kappa_y = \kappa \sin \theta \sin \phi$

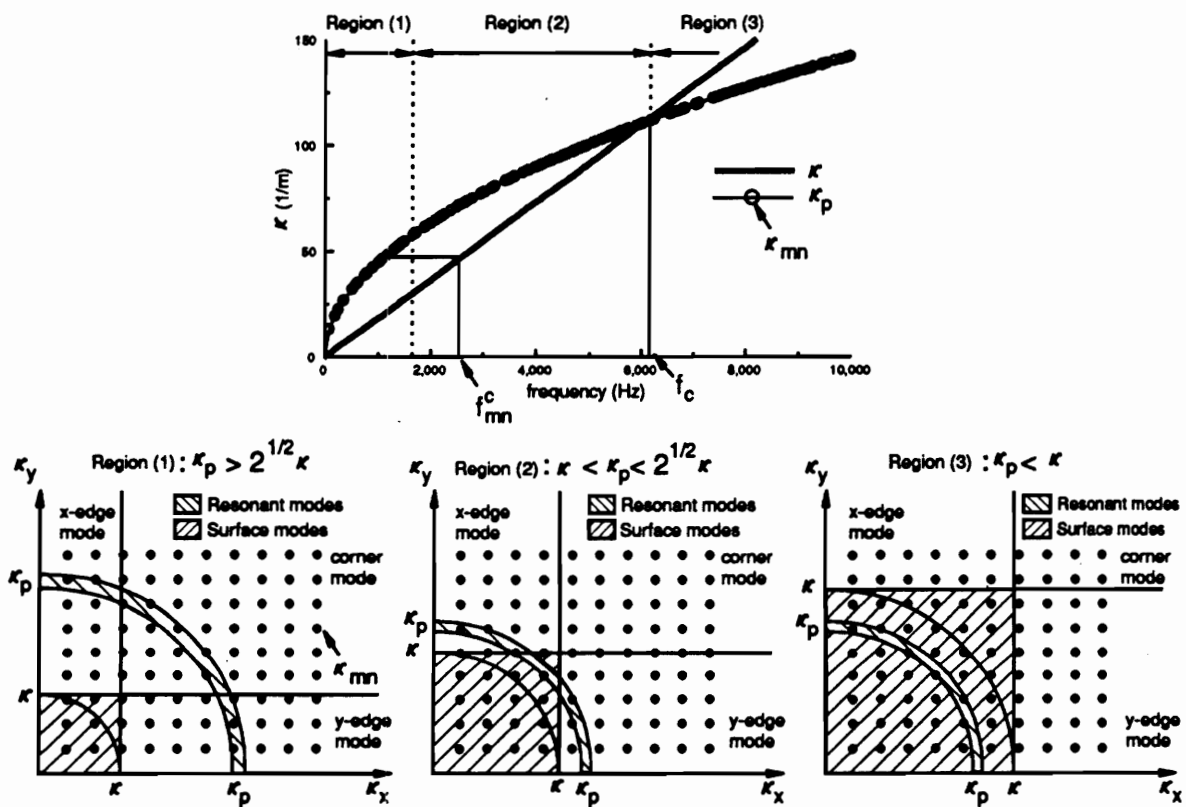
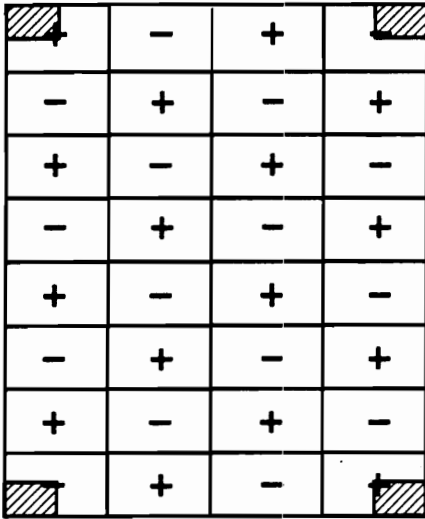
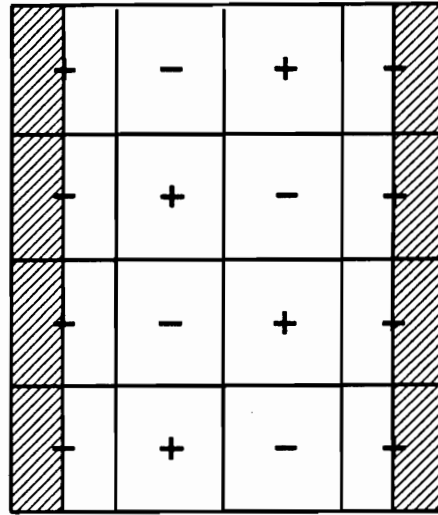


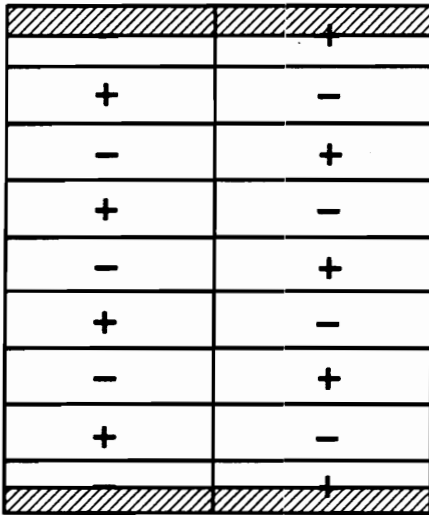
Figure 19. Illustration of wavenumber distribution (Mathur, Gardner, and Burge, 1990; Maidanik, 1974)



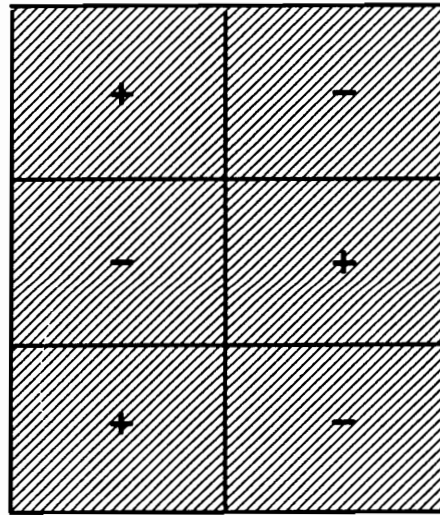
(a) corner mode radiation



(b) x-edge mode radiation



(c) y-edge mode radiation



(d) surface mode radiation

Figure 20. Illustration of corner, edge and surface mode radiations (Fahy, 1985)

ner mode radiator for those structural normal mode wavenumbers greater than acoustic wavenumber (i.e., $\kappa_m > \kappa, \kappa_n > \kappa$). The central region of the plate motion is subjected to quadrupole or dipole cancellation due to a structural wavelength shorter than the acoustic wavelength. Thus, only four corner cells acts as four monopole sources effectively radiating power. Figures 20(b) and (c) show the x-edge ($\kappa_m < \kappa, \kappa_n > \kappa$) and y-edge ($\kappa_m > \kappa, \kappa_n < \kappa$) mode radiators respectively. There is cancellation in the middle of the plate and leads to leaving uncanceled strips at both edges radiating power. Figure 20(d) shows the surface mode radiator ($\kappa_m < \kappa, \kappa_n < \kappa$). The cancellation phenomenon breaks down due to the structural wavelength being much greater than acoustic wavelength, and thus the entire plate contributes to far-field radiation.

3.4.4.2 Average Radiation Efficiency

Similar to definition of the (m,n) mode radiation efficiency, the average radiation efficiency can also be defined as (Berry, Guyada, and Nicolas, 1990)

$$\sigma = \frac{\Pi}{\rho c L_x L_y \langle |\bar{u}|^2 \rangle} \quad (3.112)$$

where the total power radiated from the plate, Π , is

$$\Pi = \int_0^{2\pi} \int_0^{\frac{\pi}{2}} \frac{|p|^2}{\rho c} R^2 \sin \theta d\theta d\phi = \frac{R^4}{\rho c} \Phi_p \quad (3.113)$$

and $\langle |\bar{u}|^2 \rangle$ is the temporal and spatial average of the square of the plate velocity.

$$\begin{aligned}
\langle |\bar{u}| \rangle^2 &= \frac{1}{L_x L_y} \int_0^{L_y} \int_0^{L_x} \frac{|u|^2}{2} dx dy \\
&= \frac{\omega^2}{8} \sum_{m=1}^{\infty} \sum_{n=1}^{\infty} W_{mn}^2
\end{aligned} \tag{3.114}$$

By substituting Equations (3.113) and (3.114) to Equation (3.112), the average radiation efficiency can be expressed as:

$$\sigma = \frac{8\Pi}{\rho c L_x L_y \omega^2 \sum_{m=1}^{\infty} \sum_{n=1}^{\infty} W_{mn}^2} \tag{3.115}$$

The average radiation efficiency indicates the overall acoustic coupling between the total mechanical vibration and sound radiation for the baffled simply-supported plate subjected to a specific disturbance input. In contrast to Equation (3.106), Equation (3.115) also includes the summation of the cross product of modal amplitudes (W_{mn}). This cross product has significant effect on the average radiation efficiency. On the other hand, the radiation efficiency of the (m,n) mode as shown in Equation (3.106), which only considers the (m,n) mode contribution, is independent of disturbance input and can be viewed as a structural-acoustic property of the free plate system.

3.5 Analytical Results

As mentioned in Chapter 1, different forms of disturbance inputs have significantly different radiation characteristics. Point force inputs generally drive situations in Regions (1) and (2), as illustrated in Figure 19, while incident plane wave inputs drive

modes for Region (3) due to the constant phase and pressure over the plate. Hence, different types of disturbance inputs will result in different radiation characteristics in term of the distribution of plate wavenumber components.

To study the plate vibration and sound radiation characteristics, several fundamental mode shapes of simply-supported rectangular plate and (m,1) mode radiation directivity are illustrated in Figure 21 for future reference. It is noted, in Figure 21 (b), that the "+" and "-" indicate the sign of the pressure phase angle. For $\gamma \gg 1$, the (m,1) mode radiation directivity shows m-1 dips across the xz-plane. For $\gamma \ll 1$, radiation patterns associated with higher order modes are similar to higher mode radiation directivities appears as lower mode radiation characteristics. In the following numerical examples, the latter condition of $\gamma \ll 1$ is presented.

3.5.1 Structural Disturbance Input Controlled by Piezoelectric Actuators

This section is concerned with an analysis of the optimization of the complex voltages needed to be applied to one or more independent piezoelectric actuators so as to minimize the total radiated sound power from a baffled, simply supported, rectangular plate. The optimization procedure is shown in Section 3.3.1. The disturbance for the primary plate excitation is assumed to be a set of one or more non-contacting electromagnetic exciters. The applied force by such a disturbance source is approximated by a constant amplitude, single frequency, uniformly distributed pressure over a small square area on the plate.

A few representative examples are given below to show the effects of number, size, and location of actuators under different disturbance conditions. All cases considered

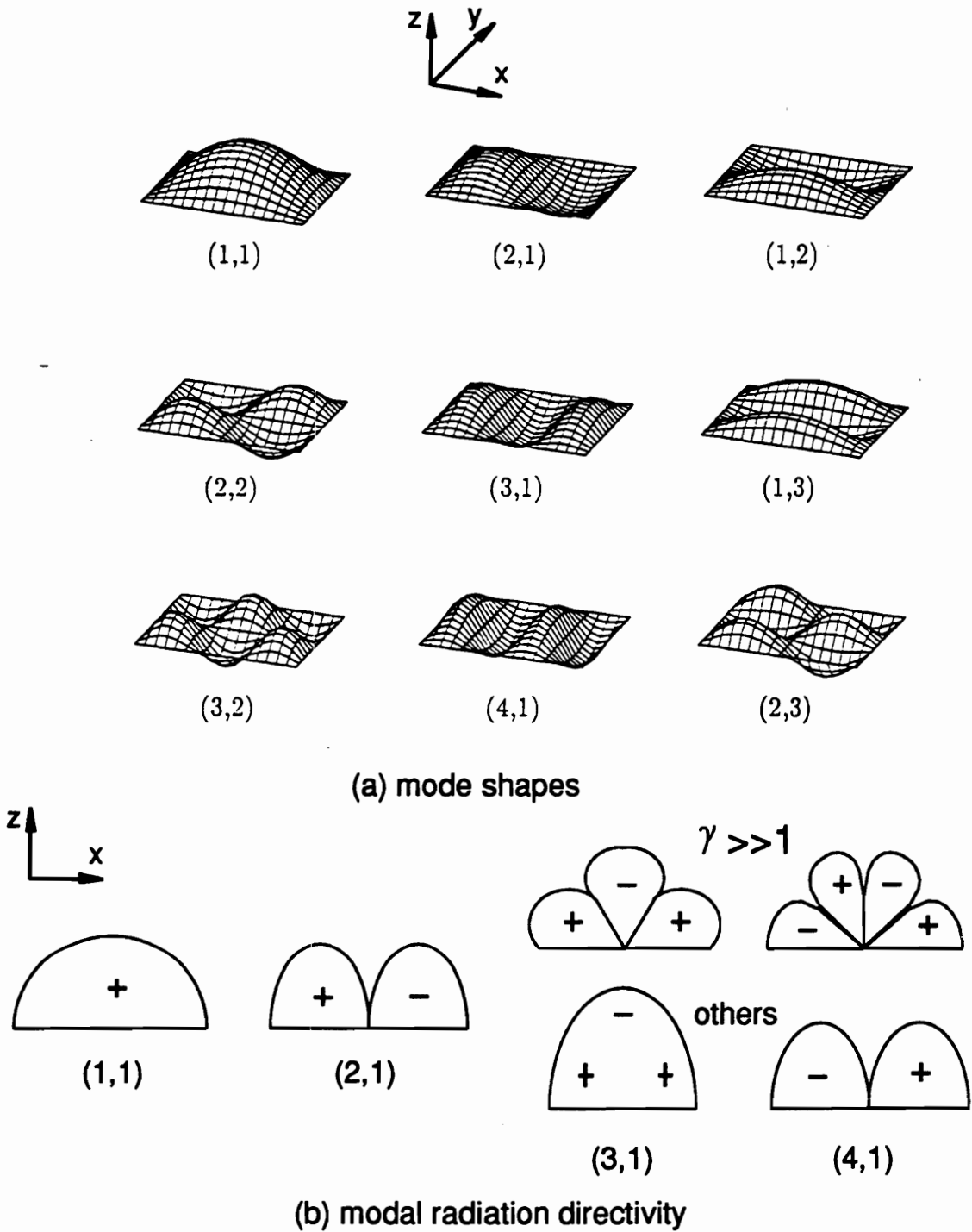


Figure 21. Illustration of mode shapes of simply-supported rectangular plate and modal radiation directivity (Clark and Fuller, 1990b)

are below coincidence corresponding to the cases in Region (1) as shown in Figure 19. Table 6 shows the specifications of the steel plate used in the simulations. Natural frequencies are tabulated in Table 7 (Pilkey and Chang, 1978). Note, for the following results, that no damping was included in the analysis. In order to calculate the plate response and radiated field, it was necessary to truncate the modal sums in the above equations. Upon consideration of computing time, k , l , m , and n were truncated at 5 (i.e., 25 modes were considered), and it was found to provide sufficient convergence of series in Equations (3.1) and (3.16). In particular, for the cases of low wavenumber excitation considered here, the plate displacement and the radiated sound pressure amplitude have no more than 0.01 % difference in comparison to those results which included 100 modes (i.e., $m = n = 10$).

The following results consist of the distribution of plate vibrational amplitude plotted along the $y = L_y/2$ horizontal plate midline. The results are normalized by the largest amplitude obtained in each case. Radiation directivity patterns are also presented along the $y = L_y/2$. For convenience, all θ angular positions to the left of the origin in the directivity pattern plots below correspond to $\phi = \pi$ far-field positions. Similarly, the right half of each plot corresponds to $\phi = 0$. In this case, the input disturbance amplitude is fixed at $q = 20\text{N/m}^2$, which gives an input force of 0.32 N located at $a_1 = 0.06\text{m}$, $a_2 = 0.1\text{m}$, $b_1 = 0.06\text{m}$ and $b_2 = 0.1\text{m}$. The plate is assumed to radiate into the air; the radiated pressure is plotted in dB *re* 20×10^{-6} Pa. In order to show the shape of the residual radiation directivity, some figures reveal negative dB, which corresponds to pressure less than the reference level. The total radiated pressure was calculated at a distance of 1.8 m from the plate central origin using the far-field pressure expression of Equation (3.20). These variables, as well as radiated acoustic power in dB *re* 10^{-12}W ,

Table 6. Plate specification

$E = 207 \times 10^9 \left(\frac{\text{N}}{\text{m}^2} \right)$	$\nu = 0.292$	$L_x = 0.38 \text{ (m)}$
$\rho_p = 7870 \left(\frac{\text{kg}}{\text{m}^3} \right)$	$h = 1.5875 \text{ (mm)}$	$L_y = 0.30 \text{ (m)}$

Table 7. Natural frequencies of plate $h = 1.5875$ mm (Hz)

$m \setminus n$	1	2	3	4	5
1	69.62	198.29	412.74	712.96	1098.97
2	149.82	278.48	492.93	793.16	1179.16
3	283.47	412.14	626.59	926.82	1312.82
4	470.60	599.26	813.71	1113.94	1499.94
5	711.18	839.85	1054.30	1354.52	1740.53

are presented for a range of frequencies and different primary source arrangements in order to demonstrate the effectiveness of the multiple piezoelectric induced control.

3.5.1.1 Effect of Number of Actuators

Figure 22 presents the vibration amplitude distribution of the plate for differing number and arrangement of piezoelectric control actuators, when the disturbance excitation frequency was 68.4 Hz, near the resonant frequency of the (1,1) mode given in Table 7. At the side of Figure 22 and all the following figures, the plate with prescribed disturbance input and actuator locations and size are drawn to scale looking into the plate from the radiated field. The black block represents the primary source, while the blank block depicts the size and location of the piezoelectric actuators.

In Figure 22, the solid line depicts the displacement distribution for the primary field, and it can be seen to be very close to that of the (1,1) mode as expected, since it is near its resonant frequency. When the various configuration of control actuators were applied, the vibration amplitudes were significantly reduced, and the (1,1) mode was well controlled for all cases.

Figure 23 shows the corresponding radiation directivities to the cases of Figure 22. As expected, the radiation directivity is uniform corresponding to a monopole source case, the (1,1) mode dominates the radiated primary field due to its high structural response and radiation efficiency. When one actuator was used, the (1,1) mode is controlled, and the (2,1) mode becomes significant. By applying two actuators as shown in Figure 23, the (1,1) modes and the (2,1) modes can be controlled simultaneously still

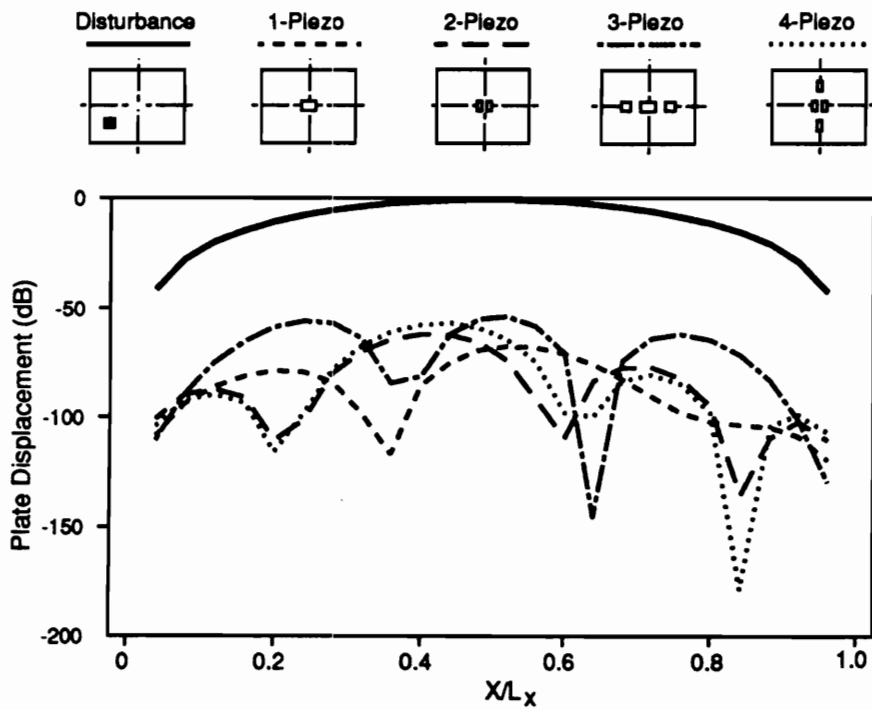


Figure 22. Plate displacement distribution for different number of piezoelectric actuators, $f = 68.4$ Hz

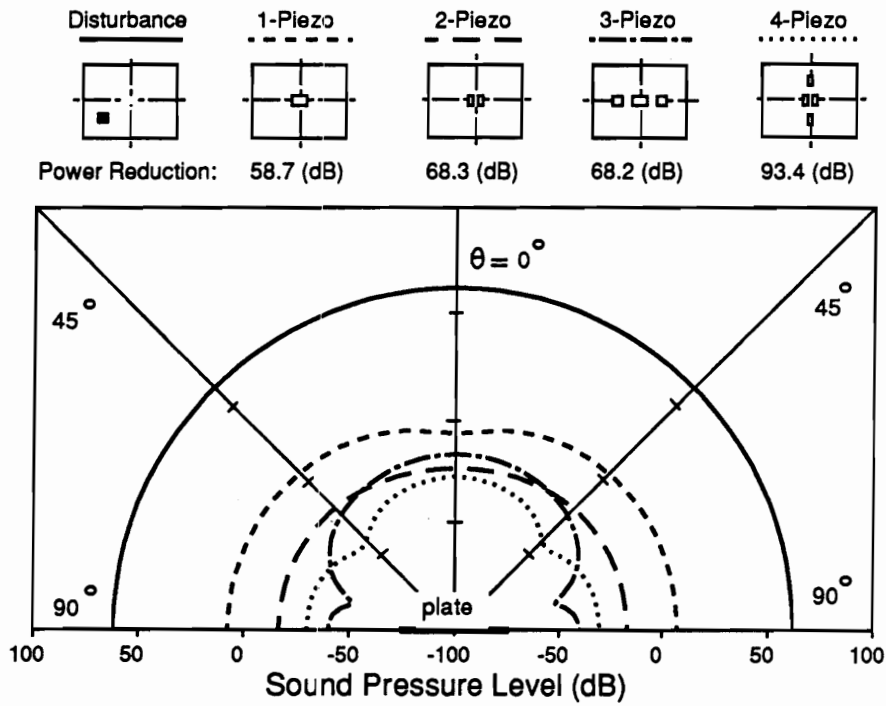


Figure 23. Radiation directivity pattern for different number of piezoelectric actuators, $f = 68.4$ Hz

leaving the (1,1) mode to contribute significantly to the residual radiation field. Further reduction is observed with the use of three and four actuators, and the residual sound field appears to be composed of a combination of the (3,1) and (1,1) modes. Additionally, the total reduction in radiated acoustic power is shown at the bottom of Figure 23 in dB. It is apparent that, for this frequency, as the number of (appropriately positioned) actuators is increased, the corresponding radiated acoustic power decreases. However, on resonance one actuator is seen to provide maximum attenuation level that would be achievable in practice (due to background noise, controller accuracy limitation, etc.)

Next, Figure 24 and Figure 25 show the vibration amplitude distribution and sound radiation directivity for different actuator configurations and a disturbance excitation frequency of 148.8 Hz, near the (2,1) resonant frequency of Table 7. The results of Figure 24 indicate that the displacement distribution of the disturbance is close to the (2,1) mode with some (1,1) contribution (as the driving frequency is not right on resonance). When one actuator located in the center of the plate is used, very little control is achieved, as the actuator in this position cannot couple into the (2,1) mode. In fact, the displacement distribution becomes more symmetric and lobe indicating that the (1,1) mode has been controlled. When two actuators are used as shown in the scale diagrams, the (2,1) mode is significantly reduced, and the (3,1) mode becomes the dominant residual mode. Increasing the number of actuators to three and then four leads to further small reductions in the amplitude. However, the main effect is that the displacement distribution becomes far more complex. This complex distribution in conjunction with phase reversals across the plate leads to a low radiation efficiency and a reduction in radiated power without significantly controlling the plate vibration as shown in Figures 24 and 25. Similar results have been seen in (Fuller, 1988; Dimitriadis and Fuller, 1989).

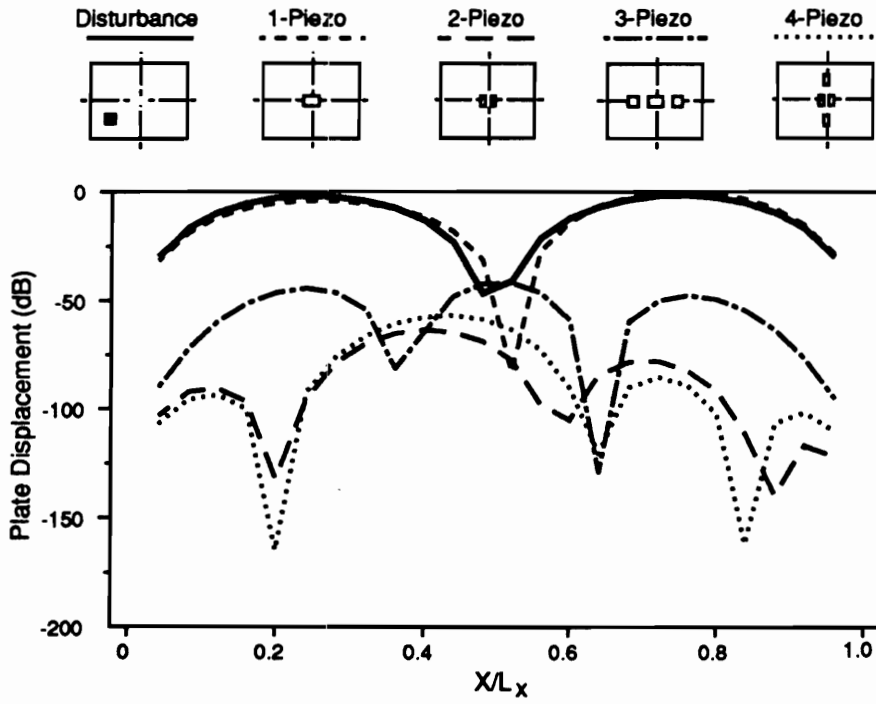


Figure 24. Plate displacement distribution for different number of piezoelectric actuators, $f = 148.8$ Hz

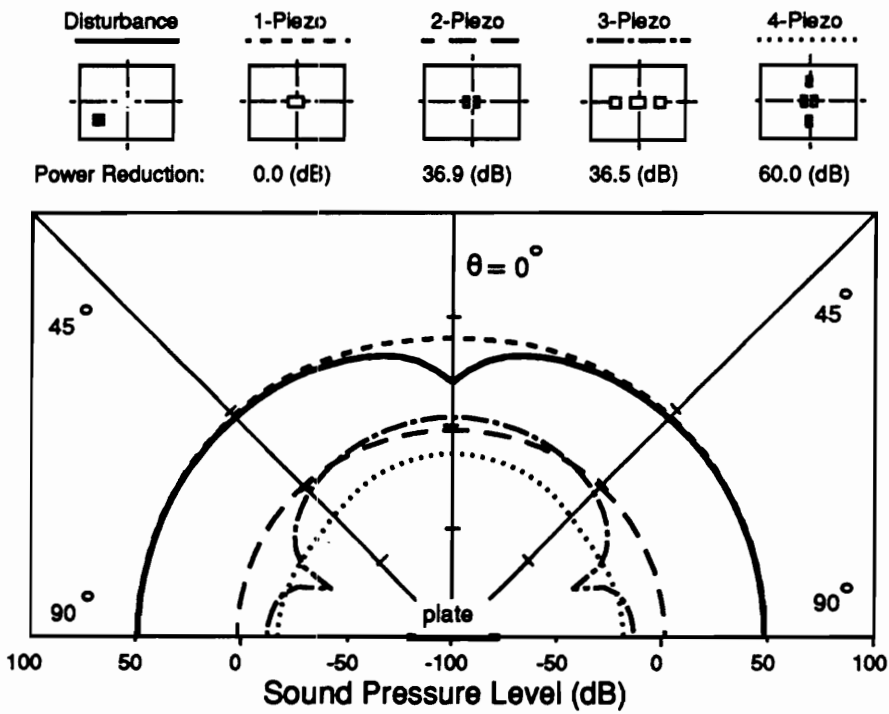


Figure 25. Radiation directivity pattern for different number of piezoelectric actuators, $f = 148.8$ Hz

This behavior is apparently due to the actuators controlling the lower order panel modes and leaving the more complex higher order modes, which also have lower radiation efficiency, as residuals.

Figure 25 indicates that for a disturbance input frequency of 148.8 Hz the (2,1) mode dominates the radiation field. When one actuator is employed, it can be seen from Figure 22 that virtually no reduction is achieved. It can also be seen that for the $L_y/2$ plane the sound levels near $\theta = 0$ have increased with one control applied. However, out of this plane, the levels should be slightly reduced. When two actuators are employed, significant reductions are now achieved. Increasing the number of actuators to three has little effect, as the centrally located actuators do not effectively couple into important n modes. However, when four actuators, arranged as shown in Figure 25, are used to control the m - and n -modal response simultaneously, and a further reduction in radiated levels and corresponding radiated power is achieved. In this case, to achieve maximum attenuation, the results indicate that multiple actuators will be required.

Figure 26 shows the radiation directivity for the same actuator and disturbance configurations, except for a excitation frequency of 108 Hz, i.e. an off-resonance excitation case located between the (1,1) and (2,1) modes. For this disturbance input, the (1,1) mode dominates the radiated primary field, as the (1,1) mode has a high structural response and radiation efficiency. When one actuator was used as shown in Figure 26, the radiated field is somewhat reduced but not nearly to the degree of the resonance case of Figure 23. This is also illustrated by the corresponding total power reductions which are 16.9 dB and 58.7 dB respectively.

This behavior can be understood with the help of the radiation patterns in Figure 26. For the case of one actuator, it is apparent that two modes, the (1,1) and (2,1), are

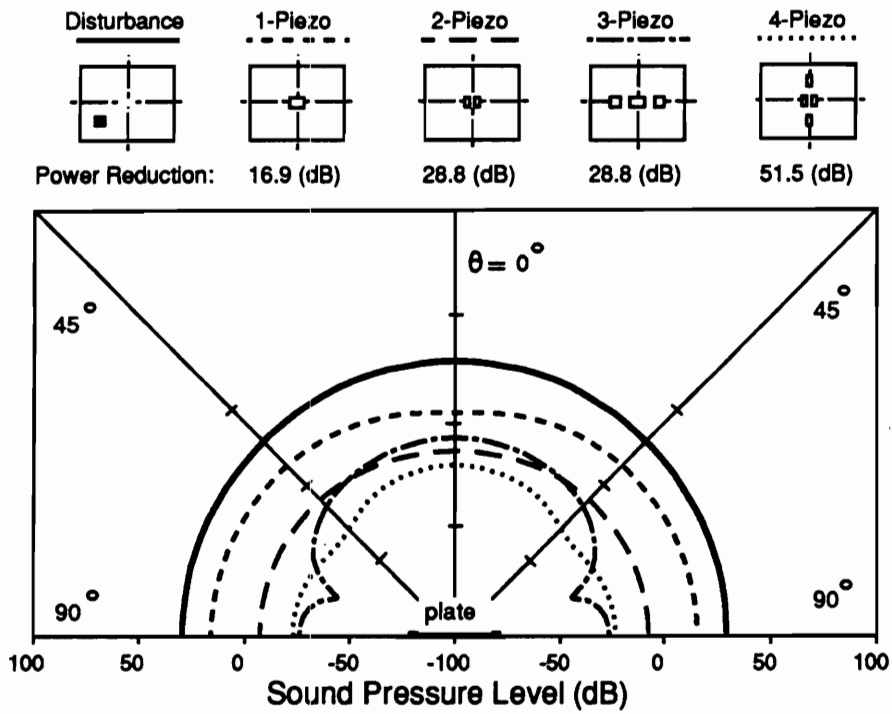


Figure 26. Radiation directivity pattern for different number of piezoelectric actuators, $f = 108.0$ Hz

contributing to the radiated field, as evidenced by the slight dip at $\theta = 0^\circ$. Thus the single actuator minimizes the field by acting on the (1,1) mode while the (2,1) mode becomes important. The optimal voltage is then a compromise between the contribution of each mode, i.e. further minimizing the (1,1) mode will lead to an increase in the (2,1) due to spillover and vice-versa.

By applying two actuators, Figure 26 shows that further reduction is possible by controlling the (2,1) and (1,1) simultaneously. Increasing the number of actuators from three and then four leads to increased attenuation, as more modes are simultaneously controlled. The final residual radiation field appears to have contributions from both the (3,1) and (1,1) modes.

The off-resonance case thus requires more actuators for high control due to the higher number of modes responding relatively strongly (in terms of radiated pressure) being higher. The importance of the (1,1) mode, due to its high radiation efficiency, is evident through the residual plots of Figure 26, even though the excitation frequency is well off its natural resonance frequency.

Finally, Figure 27 presents the radiated acoustic power over a range of frequencies up to $kL_x = 6.96$. The solid line denotes the radiated acoustic power for the disturbance source alone. Several peaks are observed to occur where natural frequencies are located, and the plate response is high. Note however (for examples) that large peaks are not observed at the (2,1), (1,2), and (2,2) frequencies, as these modes have a low radiation efficiency.

It is clear from Figure 27 that when the piezoelectric actuators are located along the $L_y/2$ axis, effective sound radiation control at low frequencies including the (1,1), (2,1)

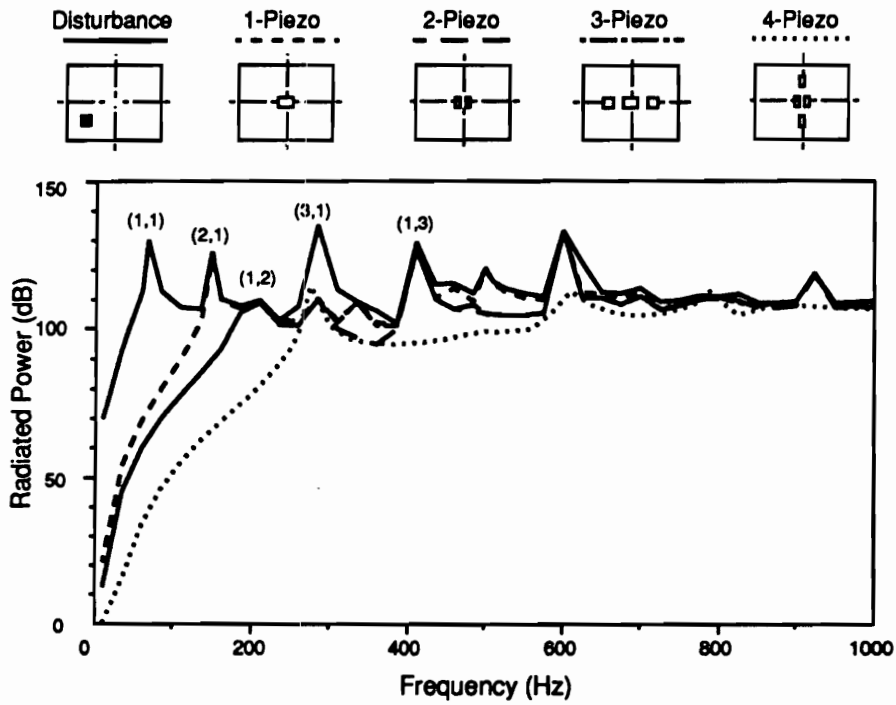


Figure 27. Radiated power for different number of piezoelectric actuators

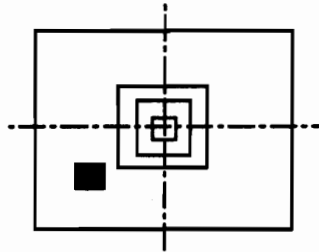
and (3,1) modes is obtained. However, for this symmetric configuration the (1,2), (2,2) and (1,3) are uncontrollable, as can be observed in Figure 27. Increasing the piezoelectric actuators to four (case (4) with some positioned off the $L_x/2$ axis) leads, nevertheless, to improved broad band power reduction. At very high frequencies, $f \approx 1000$ Hz, very little attenuation is obtained. For example, for $f = 1000$ Hz, the wavenumber ratio $\gamma = 0.41$ indicates that the radiation efficiencies of higher modes increase. Hence, a higher modal density of the plate response is contributing to sound radiation. In other words, a large number of plate modes is significantly involved in the sound radiation to the far-field. More actuators or other control strategies, such as edge or corner radiation control which is under investigation, are needed to control sound radiation from plates subjected to high frequency excitation.

The results of Figure 27 are very encouraging, because they predict that the radiated power from the plate can be controlled over the frequency range from $0 < f \leq 750$ Hz with just four actuators (whose positions are not optimized). Table 7 shows that the number of plate modes encompassed in this frequency range is 13. This result illustrates the efficiency of the control approach.

3.5.1.2 Effect of Size of Actuators

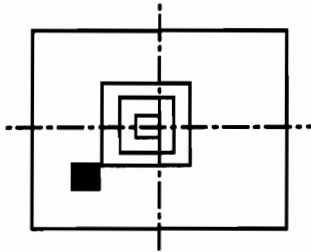
In order to study the size effects of the actuators, a single primary source and single actuator with a fixed central (of the actuator) location was studied at two different frequencies. For Table 8, the center of the patch is at $x = 190$ mm, $y = 150$ mm. For Table 9, the center of the patch is located at $x = 170$ mm, $y = 150$ mm, in other words, asymmetrically positioned so that it can couple into the (2,1) mode. Table 8 and 9 give

Table 8. Effect of size of piezoelectric actuators, $f = 68.4$ Hz



case	size of piezoceramic patch x×y (cm ×cm)	Voltage of piezoceramic patch (volt)	radiated power reduction (dB)
1	1×1	221.55	
2	2×2	55.51	
3	3×3	24.76	
4	4×4	14.00	
5	6×6	6.32	
6	10×10	2.38	
7	12×12	1.71	
8	15×15	1.16	
9	20×20	0.75	
10	38×30	0.47	

Table 9. Effect of size of piezoelectric actuators, $f = 148.8$ Hz



case	size of piezoceramic patch xxy (cm×cm)	Voltage of piezoceramic patch (volt)	radiated power reduction (dB)
1	2×2	119.00	15.1
2	4×4	30.31	15.1
3	6×6	13.90	15.0
4	8×8	8.17	14.9
5	10×10	5.54	14.8
6	14×14	3.31	14.5

the required optimal control voltage amplitude (with a different magnitude of $q = 1 \text{ N/m}^2$ from that in the previous case studies) for a driving frequency of 68.4 and 148.8 Hz respectively. The location of the disturbance input and actuator is again symbolically shown on the top of the tables.

Table 8 demonstrates that when the size of the actuator was increased, while the power reduction was generally the same, the optimal voltage was decreased. Similar results can be observed in Table 9. It may be concluded that (at least for the two cases considered here) the size of the piezoceramic patch does not appear to significantly affect sound attenuation. However, the input voltages of the actuators are strongly dependent upon size. Thus it is essential to choose the proper size of actuators such that the applied voltages are in the specified operating range for the piezoelectric material. Of course, for other driving frequencies when the expanding patch may cross nodal lines of important modes, then different results may be obtained. The above examples are meant only to illustrate an important operating characteristic of the piezoelectric element. To determine the optimal voltages and size of piezoceramics for more general configurations is out of the scope of this thesis.

3.5.1.3 Effect of Location of Actuators

In order to study the effect of actuator location, the number of disturbance inputs has been increased to two each with magnitude of $q = 20 \text{ N/m}^2$ and located symmetrically at both side of the plate and driven 180° out-of-phase such that the (2,1) mode can be efficiently excited. The coordinates of the two uniformly distributed pressure disturbance inputs are: (1) $a_1 = 0.12\text{m}$, $a_2 = 0.16\text{m}$, $b_1 = 0.13\text{m}$, $b_2 = 0.17\text{m}$; (2) $a_1 = 0.22\text{m}$, $a_2 = 0.26\text{m}$, $b_1 = 0.13\text{m}$, $b_2 = 0.17\text{m}$.

Figure 28 and Figure 29 show the vibration amplitude distribution and radiation directivity for primary sources arranged to excite the (2,1) mode at 148.8 Hz, near the (2,1) mode resonant frequency. When one actuator located in the center of the plate is used, no control is achieved, because the actuator cannot couple into the (2,1) mode. Next, the actuator was moved slightly to the left as shown (1b) in Figure 28 so that its edge is located next to the nodal line. In this case, the vibration amplitude is significantly reduced, but the radiation field of Figure 29 shows only a relatively small reduction in level (although total power is reduced by over 18 dB) due to spillover into the (1,1) mode as can be observed from the uniform radiation pattern. To effectively eliminate the (2,1) mode with little spillover into the (1,1) mode, two independent actuators are needed, as shown for case (2) in Figure 28. In this case, the vibration amplitude is reduced to be a higher order residual, and the radiation field of Figure 28 shows very high reductions in levels and power.

Finally, Figure 30 shows the radiated acoustic power versus frequency for the configurations of Figures 28 and 29. The solid line for the primary sources does not demonstrate any high peaks at odd-odd, odd-even and even-odd mode natural frequencies due to the arrangement of the primary input. In Figure 30, the results for one centrally located actuator (case 1a) are coincident with that for the disturbance; no control is achievable for this actuator position. The actuator next to the (2,1) nodal line (case 1b) can only reduce the radiated power by 18 dB at 148.8 Hz. However, two actuators can be seen to provide high attenuations in radiated acoustic power over a wide range of frequencies. Note that there is no attenuation at 490 Hz near the (4,1) mode resonant frequency due to such a symmetrical arrangement of actuators.

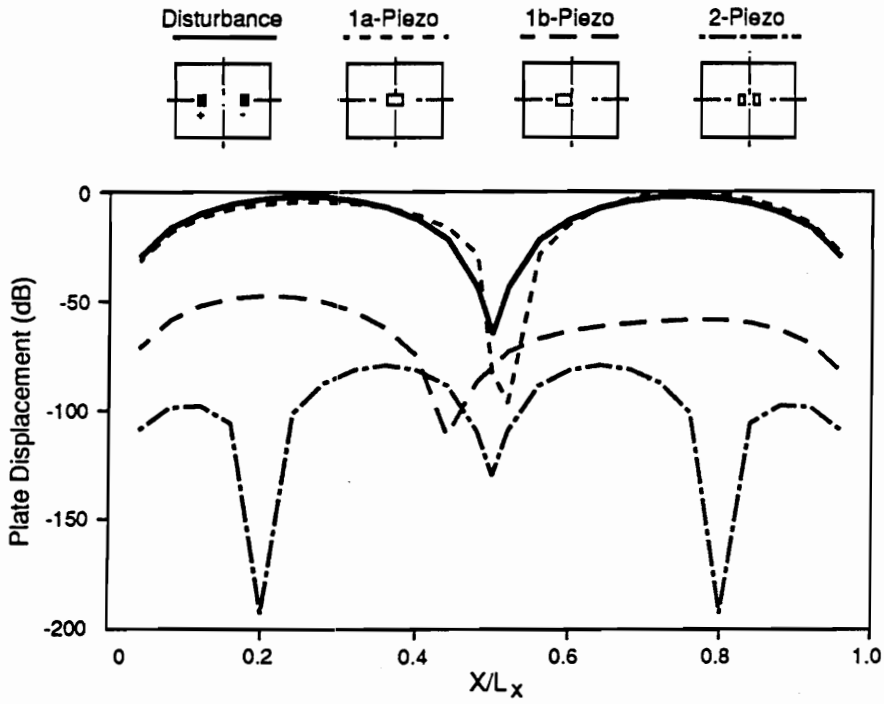


Figure 28. Plate displacement distribution for different location of piezoelectric actuators, $f = 148.8$ Hz

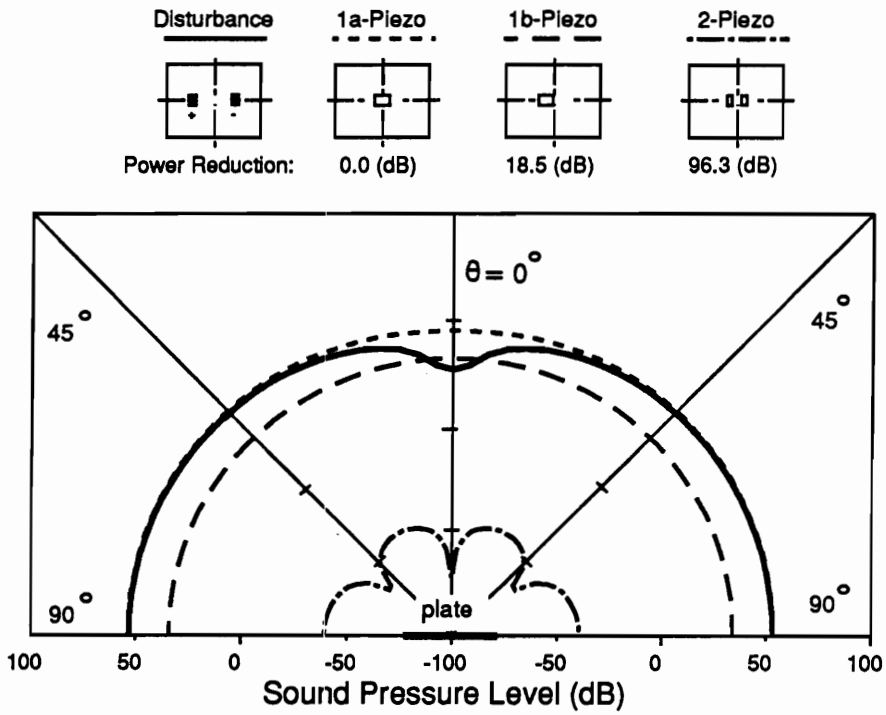


Figure 29. Radiation directivity pattern for different location of piezoelectric actuators, $f = 148.8$ Hz

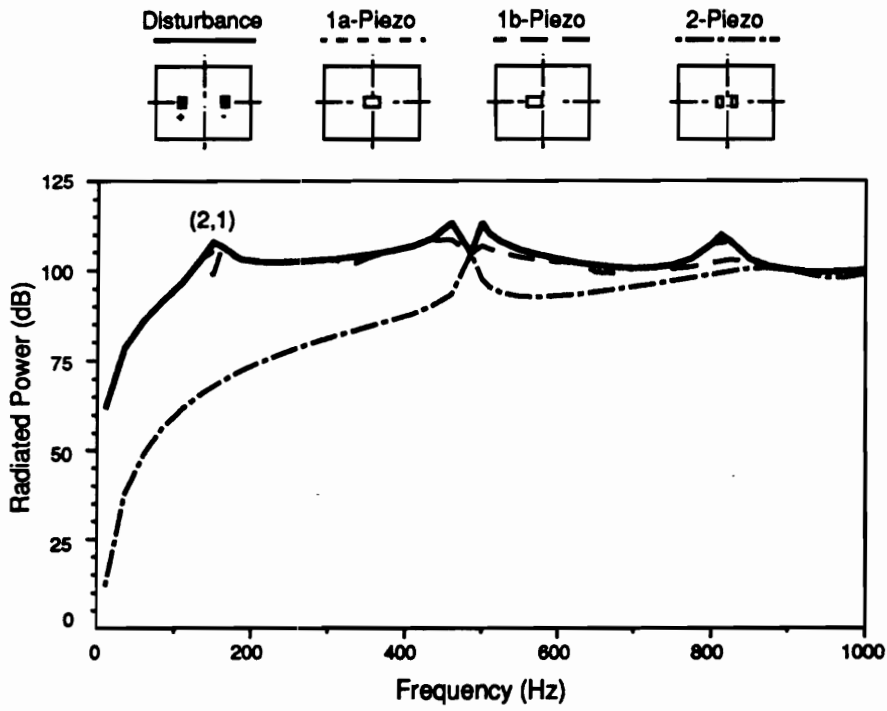


Figure 30. Radiated power for different location of piezoelectric actuators

3.5.1.4 Summary

Active control of structurally radiated sound from a modally responding panel has been analytically studied. The control inputs were multiple independently controllable piezoelectric patches bonded to the panel surface. The work demonstrates that multiple piezoelectric actuators have much potential for control of vibration and its associated radiated primary field. Several significant observations may be summarized as follows:

- Multiple piezoelectric actuators generally have better sound radiation control characteristics than single actuators due to reduced spillover.
- The location and number of actuators significantly affect the amount of sound reduction achievable. For on-resonance, high attenuation can be generally achieved with only one properly located actuator. However, for off-resonance, multiple actuators are needed.
- With proper choice of number and location of actuators, high sound attenuation over a broad frequency range up to approximately $kL_x = 5$ for the configurations considered here can be achieved.
- Within limits, the size of the piezoelectric patch does not appear to significantly affect sound attenuation. However, the input optimal voltages are strongly dependent on the size of the piezoceramic patch.

3.5.2 Incident Plane Wave Disturbance Controlled by Point Force or Piezoelectric Actuators

In this section, plane acoustic waves incident on a simply-supported thin rectangular plate are considered as a primary input. Such a plane wave disturbance input will result in high modal contribution at low plate wavenumbers as previously discussed. The phase motion is thus dominantly by lower order modes acting as surface modes in Region (3) of Figure 19. Either piezoelectric or point force actuators are employed as structural control inputs to reduce the sound transmission through the plate. An optimal control theory (Lester and Fuller, 1990), as discussed in Section 3.3, is adopted to optimize the input complex voltages to the piezoelectric or point force actuators so as to minimize the total radiated acoustic power, Φ_p , as shown in Equation (3.23). The optimal solution (i.e., the optimal voltages to be applied to actuators), is shown in Equation (3.41). This has the effect of increasing the transmission loss of the plate. The performance of the piezoelectric and point force actuators is evaluated for various input frequencies and number and location of control inputs. Finally, a comparison between the effectiveness of piezoelectric actuators versus point force actuators in terms of reduction of transmitted sound and power is made. The investigation is thought to lay out the fundamental aspects of piezoelectric devices in terms of practical applications to active control of sound transmission, in such applications as aircraft interior noise, machine hull noise and high transmission loss lightweight barriers.

The physical properties of the rectangular plate which was used for illustrating results here are the same as those shown in Table 6 except for the plate thickness $h = 2$ mm. Table 10 shows the natural frequencies of the simply supported plate for modes

(m,n). The optimal process is suitable for controlling multiple primary sources; however, only a harmonic incident plane wave with input parameters, $\theta_i = 45^\circ$, $\phi_i = 0^\circ$ and $P_i = 10 \text{ N/m}^2$, was considered for the following results. Both the radiation directivity and plate displacement distribution were presented to demonstrate the control effectiveness of sound transmission by using piezoelectric or point force actuators.

3.5.2.1 Effect of Number of Control Sources

3.5.2.1.1 Piezoelectric Actuators

Figure 31 shows the radiation directivity for the disturbance input consisting of an incident plane wave on the plate at $\theta_i = 45^\circ$, $\phi_i = 0^\circ$ with circular frequency 85 Hz near the (1,1) mode controlled by one, two and three piezoelectric actuators respectively. The locations and size of the piezoelectric actuators are sketched to scale on the top of Figure 31. The primary source radiation directivity denoted by the solid line has the characteristic shape of the dominant mode (1,1), as shown in Figure 21. For one piezoelectric actuator located in the middle of the plate, the (1,1) mode is well controlled. The remaining significant residual mode in terms of radiation is the (2,1) as shown in Figure 31.

For two independently controlled piezoelectric actuators as illustrated on the top of Figure 31, the actuators can control not only the (1,1) mode but also the (2,1) mode, so that the (3,1) mode becomes the dominant mode. When three independently controlled piezoelectric actuators are applied as shown in Figure 31, the actuators can simultaneously control several modes such as modes (1,1), (2,1) and (3,1); thereafter, the remaining dominant radiating mode is a combination of modes (1,1) and (3,1). The total

Table 10. Natural frequencies of plate $h = 2$ mm (Hz)

m \ n	1	2	3	4	5
1	87.71	249.81	519.98	898.22	1384.53
2	188.74	350.85	621.02	999.25	1485.56
3	357.13	519.23	789.40	1167.64	1653.95
4	592.88	754.98	1025.15	1403.39	1889.69
5	895.98	1058.08	1328.25	1706.48	2192.79

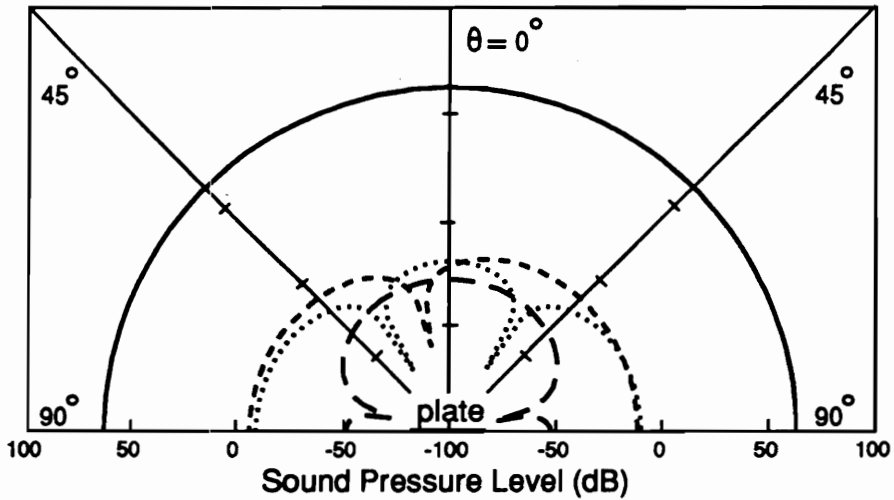
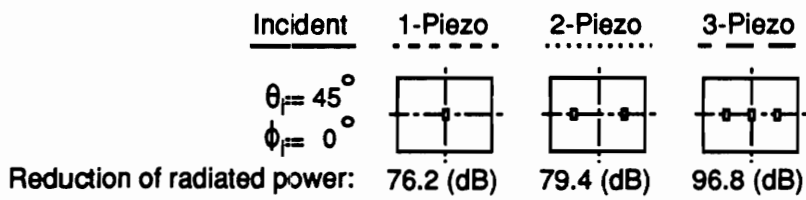


Figure 31. Radiation directivity pattern for different location of piezoelectric actuators, $f=85$ Hz

reduction of radiated acoustic power shown in Table 11 is 76.16 dB for one piezoelectric actuator, 79.42 dB for two and 96.81 dB for three. It may be concluded that increasing the numbers of actuators leads to an increase in reduction of radiated acoustic power. For all cases, however, significant reduction in the radiated sound pressure levels is demonstrated. For this case, the practical limit of attenuation is seen to be achieved with just one actuator.

Figure 32 presents the plate displacement distribution corresponding to the cases of Figure 31. These distributions, partially decomposed into modal amplitudes of varying m with $n=1$, are also given in Table 12. The modal amplitude of the (m,n) mode expressed in dB is normalized by that of the $(1,1)$ mode due to the incident plane wave alone. As expected, the $(1,1)$ mode dominates the plate vibration due to the disturbance input harmonically excited near the $(1,1)$ mode resonant frequency. When one piezoelectric is employed, the $(1,1)$ mode is well controlled; however, the significant energy is spilled into the $(3,1)$ mode, and the amplitude of the $(3,1)$ mode is raised. The residual plate displacement distribution thus takes on the shape of the $(3,1)$ mode. Note, however, that the $(2,1)$ amplitude is unchanged due to the central location of the single actuator. This result accounts for the sound radiation pattern observed in Figure 31. When two actuators are employed, the $(2,1)$ amplitude is now reduced, but further control spillover occurs into the $(3,1)$. However, the total sound power radiated falls due to cancellation of other plate modes leading to plate displacement distribution appearing as higher mode response with a lower radiation efficiency as discussed in Section 3.4.4. The results correspond to what is termed "modal restructuring" (Fuller, Hansen and Snyder, 1990c). Finally, when three actuators are used, the $(1,1)$ and $(2,1)$ amplitudes remain attenuated, and control spillover to the $(3,1)$ is now observed in Table 12. This is also reflected in the displacement plot of Figure 32 which appears to have a shape,

Table 11. Total reduction of radiated acoustic power (dB)

number of actuators	$f = 85$ (Hz)		$f = 140$ (Hz)		$f = 190$ (Hz)	
	piezoceramic patch	point force	piezoceramic patch	point force	piezoceramic patch	point force
1	76.16	76.34	34.49	34.55	0	0
2	79.42	92.83	39.52	54.54	28.75	48.65
3	96.81	108.03	60.09	70.79	56.74	66.73

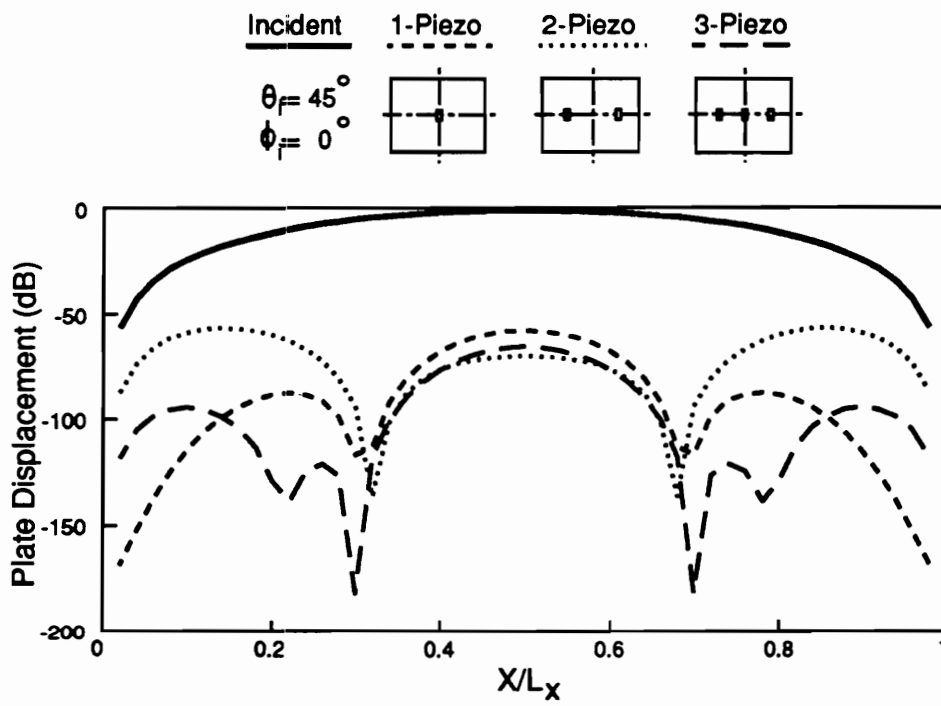


Figure 32. Plate displacement distribution for different location of piezoelectric actuators, $f = 85$ Hz

Table 12. Modal amplitude of plate vibration (dB), $f=85$ Hz

m	Incident n = 1	1-Piezo n = 1	2-Piezo n = 1	3-Piezo n = 1
1	0.00	-43.07	-43.23	-48.18
2	-55.25	-55.25	-89.71	-89.72
3	-57.87	-35.35	-30.51	-43.66
4	-82.97	-82.91	-68.89	-68.89
5	-78.73	-44.79	-45.04	-44.85

due to the response, of many higher order modes. This higher mode plate response results in volumetric cancellation, and thus explain the high power reduction as observed in Figure 31.

For the next results, the circular frequency of the incident plane wave was increased to 190 Hz near the resonance of the (2,1) mode. Figure 33 shows the resultant radiation directivity for one, two and three piezoelectric actuators with the same size and locations as those in Figure 31. As can be seen, the primary field appears to have the shape of a distorted (2,1) mode; that is logical, since the mode is near the excitation frequency and will dominate the response. This is supported by the results of Table 13 which are maximum contributions of plate modes to the total radiated sound pressure at $R = 10$ m. This table reveals that the (2,1) mode is indeed dominant, and the next most important mode is the (1,1); both modes account for the distorted radiation directivity pattern due to the oblique incident plane wave $\theta_i = 45^\circ$, $\phi_i = 0^\circ$.

When one piezoelectric actuator is used, Table 13 shows that the (1,1) contribution is reduced, and this is supported by Figure 33 which now shows a symmetric radiation pattern similar to the (2,1) thus confirming the removal of the (1,1) contribution; however, there again has been significant spillover into the (3,1) mode which accounts for the mode at $\theta = 0^\circ$ not being identically zero. The (2,1) is uncontrollable due to the central location of the actuator.

The number of actuators were again increased to two, and now significant control of the (2,1) contribution is observed both in Figure 33 and Table 13. This is, of course, due to the location of the two piezoelectric element which can now couple into the (2,1) mode. Note that the residual field in this case has the characteristic shape of the (3,1)

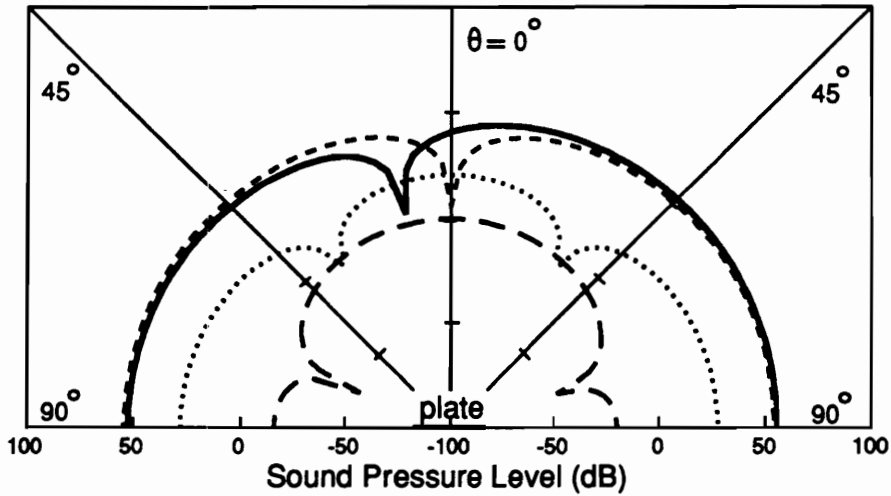
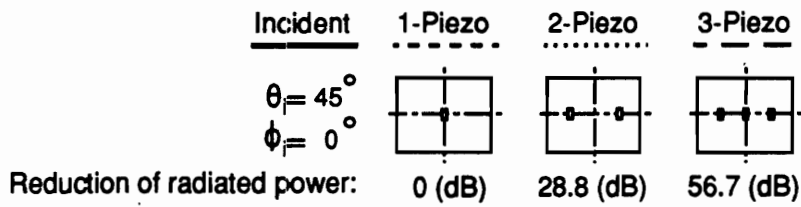


Figure 33. Radiation directivity pattern for different location of piezoelectric actuators, $f = 190$ Hz

Table 13. Modal amplitude of sound pressure (dB), $f=190$ Hz

m	Incident n = 1	1-Piezo n = 1	2-Piezo n = 1	3-Piezo n = 1
1	-13.10	-22.04	-9.92	-26.48
2	0.00	0.00	-68.55	-68.55
3	-43.06	-23.55	-7.26	-31.76
4	-68.92	-68.92	-54.49	-54.49
5	-70.46	-39.87	-28.40	-38.11

mode. On increasing the number of actuators to three, control is now achievable over the (1,1), (2,1) and (3,1) contributions simultaneously, and large reductions are achieved.

Figure 34 gives the displacement distribution corresponding to the cases of Figure 34. It is interesting to note that little change occurs in the displacement distribution when one control element is used, although significant change in the radiation field are observed. This result is due to the fact that the (1,1) mode has a much higher radiation efficiency than the (2,1), thus its displacement response may be far lower than the (2,1), but it can still contribute significantly to the radiated field; hence, small changes in plate response can lead to large changes in the radiated field. It is also apparent that the total plate response increases at $x/L_x = 0.5$, and this is due to spillover into the (3,1) mode. However, this is again not manifest in an increase in radiated levels due to the phenomenon of "modal restructuring" (Fuller, Hansen, and Snyder, 1990c). The characteristic of modal restructuring implies that when control is applied, the plate response is not globally reduced but possibly even increased and changed to a higher order response. This higher order plate response generally has a smaller radiation efficiency; therefore, sound radiation from the plate is eventually attenuated, even though plate response has increased. Similar results can be observed for other actuator configurations in Figure 34 and correspond well to what is seen in Figure 33 and Table 13.

3.5.2.2 Comparison Between Piezoelectric and Point Force Actuators

It will be of great interest to compare the control performance between piezoelectric and point force actuators. Piezoelectric actuators have been recently introduced to active structural acoustic control, while point force actuators are customarily used. The radiation directivity patterns and displacement distributions for using point force

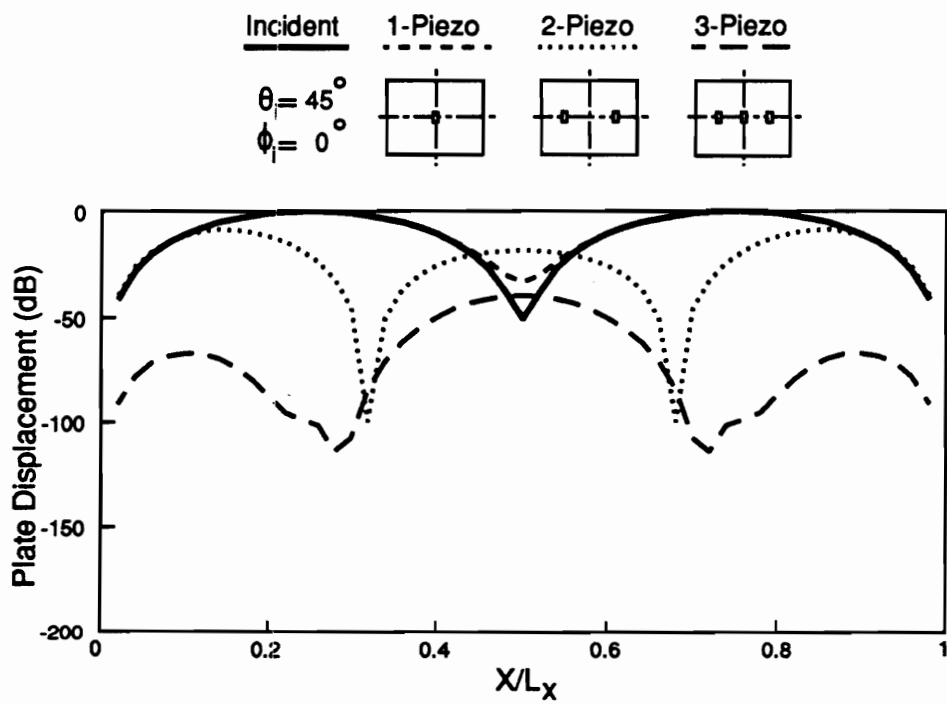


Figure 34. Plate displacement distribution for different location of piezoelectric actuators, $f = 190$ Hz

actuators were found to be similar to those for using piezoelectric actuators in Figures 31, 32, 33 and 34. Thus, these results were not shown, instead, a comparison between piezoelectric and point force actuators in terms of control performance was made. In order to compare the control effectiveness of piezoelectric actuators with that of point force actuators, the point force was chosen to be located at the center of a piezoceramic patch. The effects of size and location of the piezoceramic patch, however, were not addressed in this paper. Previous section discussed these effects and demonstrated that the locations of actuators were best chosen where the plate has the largest response. Here the radiation directivity, plate displacement distributions and total reduction of radiated acoustic power were shown to evaluate the relative performance of piezoelectric and point force actuators.

3.5.2.2.1 One Actuator

Figure 35 shows the radiation directivity for a frequency of $f = 85$ Hz near the (1,1) mode resonant point. In this case, the control achieved by a single centrally located piezoelectric element and point force actuator is compared. Both the piezoelectric and point force actuators have nearly the same control effectiveness of sound radiation; however, the results of Figure 36, which are plate displacement distribution, indicates that the point force actuator gives better performance in terms of plate displacement, and its residual amplitude is less than that of the piezoelectric element. This can be interpreted as the point force actuator leading to less control spillover than the piezoelectric element contrary to what was previously understood about distributed actuators. The reason for this behavior is not presently understood; however, it is under investigation. Some potential ideas will be discussed in Section 3.5.2.2.3.

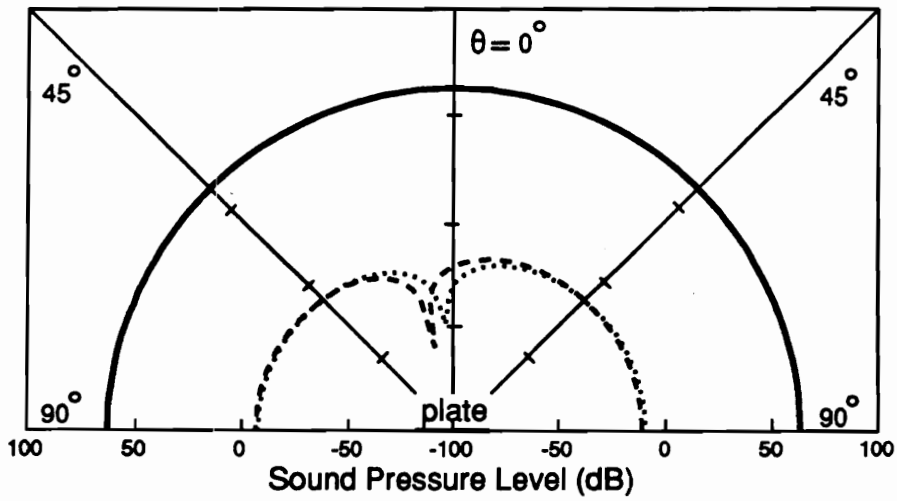
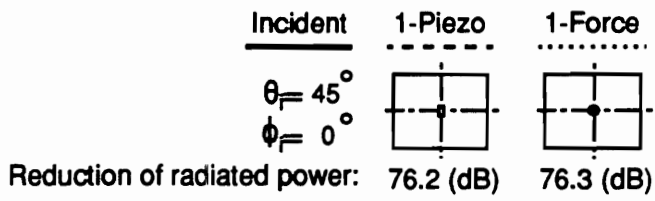


Figure 35. Radiation directivity pattern for one disturbance and one actuator, $f = 85$ Hz

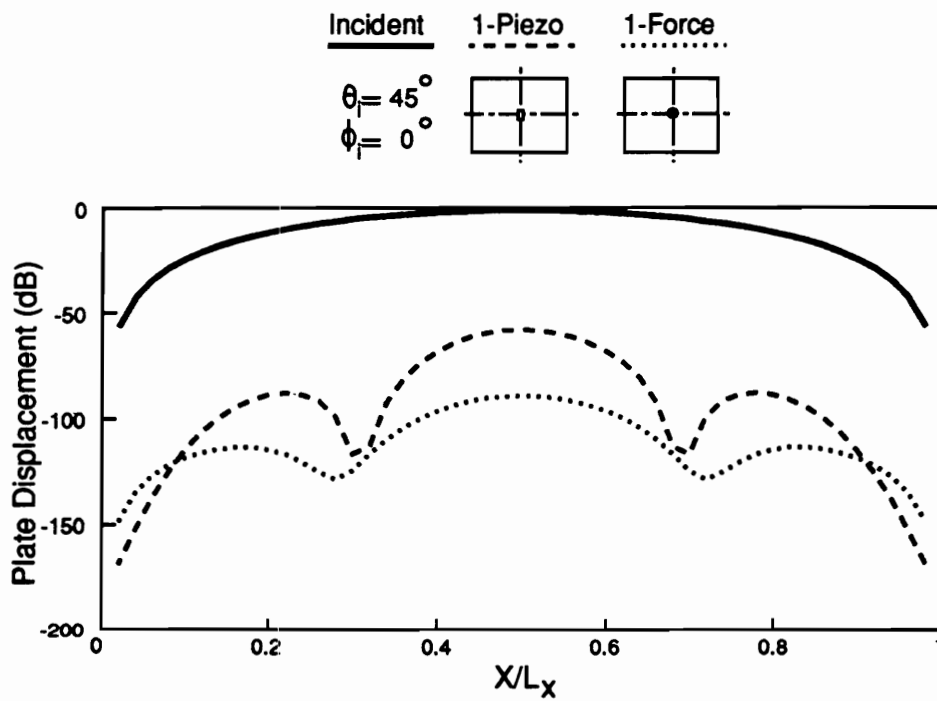


Figure 36. Plate displacement distribution for one disturbance and one actuator, $f = 85$ Hz

3.5.2.2.2 Two Actuators

In the next comparison, the excitation frequency was increased to 190 Hz near the (2,1) mode resonant frequency. In this case, the (2,1) mode dominates the radiation field with significant contribution from the (1,1) mode, and the point force actuators clearly out perform the piezoelectric actuators in terms of reduction of radiated levels as shown in Figure 37. This is also observed in Figure 38 which are plots of the corresponding displacement distributions. It is apparent that the use of point force actuators has again lead to significantly less spillover into the residual (3,1) mode than the use of piezoelectric actuators.

3.5.2.2.3 Three Actuators

For a stringent comparison test, the excitation frequency was now reduced to 140 Hz which is off-resonance between the (1,1) and (2,1) mode resonant frequencies. Being off-resonance, it is expected that more modes can contribute to the plate response, and the radiated field thus exacerbating control spillover effects. Figures 39 and 40 give the radiation directivities and displacement distribution of this frequency. Again, it is apparent that the point control forces lead to less spillover and improved control performance in terms of reduction of radiated sound level than piezoelectric excitations.

Finally, Table 11 summarizes the total reduction of radiated acoustic power for three different excitation frequencies with either one, two or three piezoelectric patches or point forces as control sources. These results confirm that point forces indeed give better performance on a global basis than the piezoelectric elements. As stated previously, this result is somewhat contrary to what was expected. The distributed control (i.e. in this case piezoelectric elements) is expected to give improved performance due to

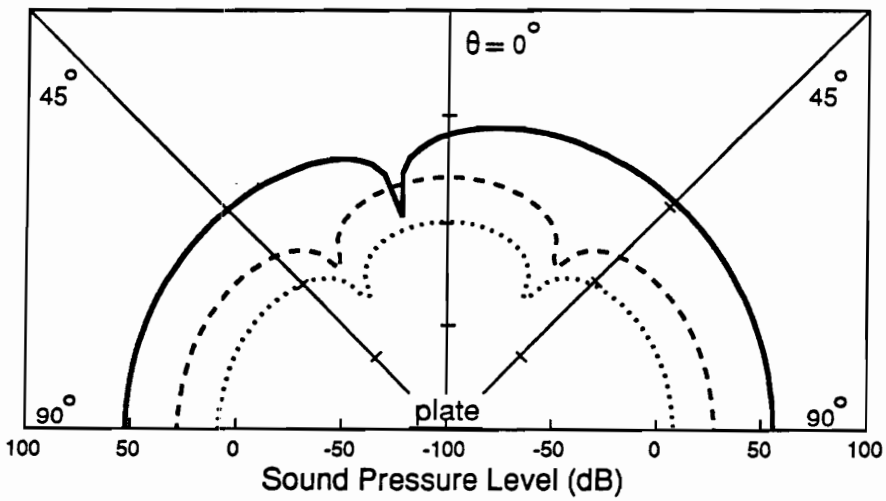
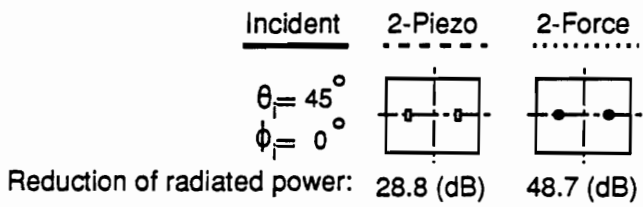


Figure 37. Radiation directivity pattern for one disturbance and two actuators, $f = 190$ Hz

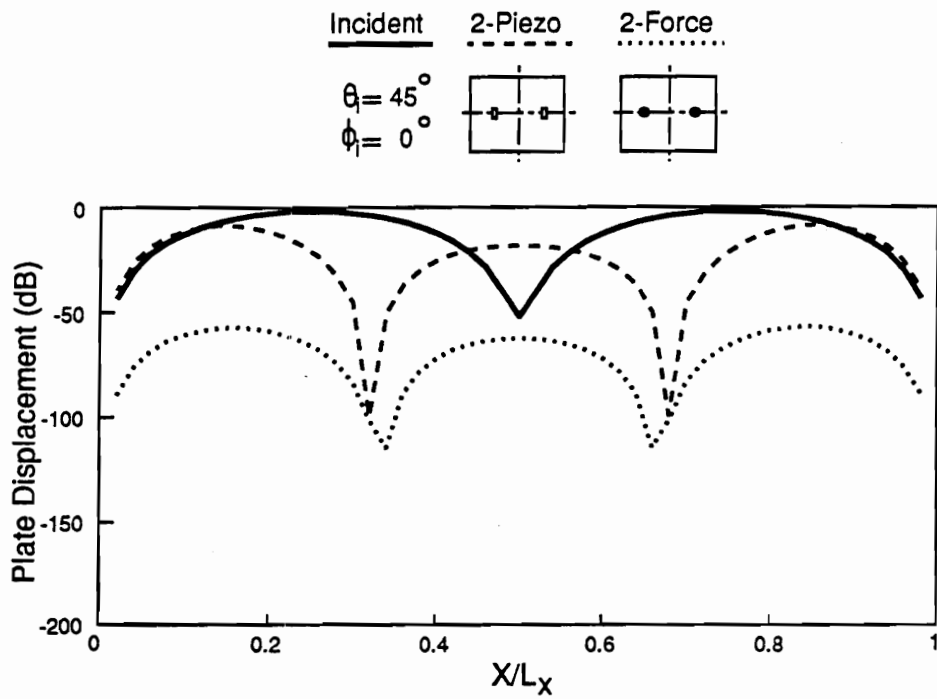


Figure 38. Plate displacement distribution for one disturbance and two actuators, $f = 190$ Hz

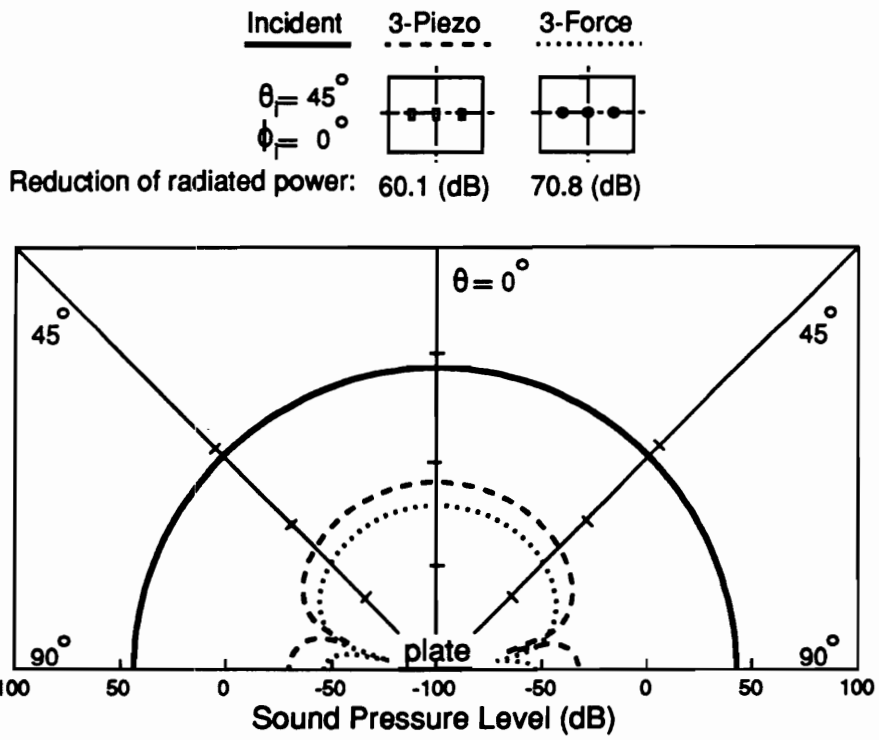


Figure 39. Radiation directivity pattern for one disturbance and three actuators, $f = 140$ Hz

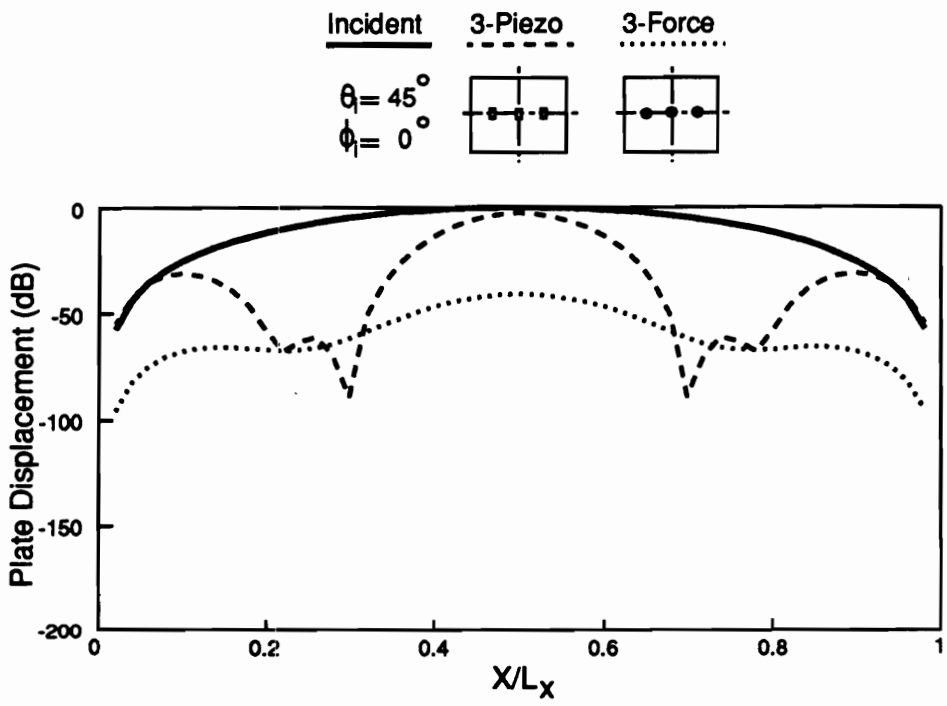


Figure 40. Plate displacement distribution for one disturbance and three actuators, $f = 140$ Hz

the fact that the distributed element can couple into less modes leading to less spillover. However, on-going work stimulated by this result tends to point toward this distributed nature to be a disadvantage rather than an advantage, because the piezoelectric actuator generates line moments along the edges of the actuator, but not in the form of distributed inputs over the area of the piezoceramic patch. This work has revealed that sound reduction occurs by the plate system assuming new eigenvalues and eigenfunctions (mode shapes) under feedforward control (Burdisso and Fuller, 1990). Highest reduction in sound levels is achieved by creating new modes with the lowest total response and/or radiation efficiency. In this case, a point force is an ideal actuator, as it is equally coupled to all uncontrolled modes in the wavenumber domain, while the piezoelectric element has reduced coupling and thus resulted in a reduced range of achievable modal modification, (i.e., the degree of modal restructuring is limited). However, this topic is out of the context of this thesis and will be the subject of another work. It is also interesting to note that the original concepts concerning the improved performance with distributed control were made from studies which considered an infinite number of point forces distributed over a beam (Meirovitch and Norris, 1984). Although piezoceramics are in a sense distributed, they exert a constant control input over finite regions of the structure, which is significantly different from the configuration of Meirovitch and Norris (1984), and this characteristic is believed to lead to the different conclusion observed in this work.

Transmission loss defined in Equation (3.87), is an index of how much acoustic power is transmitted through the panel. Figure 41 shows the transmission loss over the frequency range 10 to 1000 Hz for the disturbance input of an incident plane wave and involving four separated cases of comparative control. For the controlled cases, the

heavy lines correspond to piezoelectric actuators while the light lines correspond to point force control.

For the incident plane wave disturbance, the transmission loss can be seen to dip at the resonant frequencies of the plate; however, the magnitude of the dip depends on the resonance modal number. For example, near 190 Hz the dip is fairly small. This behavior is due to the (2,1) mode being a very inefficient radiator, and thus its plate response needs to be extremely high (i.e., right on resonance) for it to dominate the sound radiation field.

It can be seen that the use of both types of actuators leads to increased transmission loss over the frequency range except at a number of frequencies corresponding to asymmetric modes in modal number n . These modes have nodal lines at the actuator locations and are thus uncontrollable.

Figure 41 also exhibits an interesting behavior. As the number of actuators is increased, not only the transmission loss is seen to increase but also the dips which indicate the resonant frequencies of the controlled plate system have been shifted to higher frequencies. These shifted dips can be possibly visualized as the new eigenproperties of the controlled plate system as studied by Burdisso and Fuller (1990) for feed-forward control of a one dimensional beam. One would expect that the transmission loss would dip at the new eigenvalues or resonant frequencies of the closed loop system. It is thought that the phenomenon investigated by Burdisso and Fuller (1990) is occurring here.

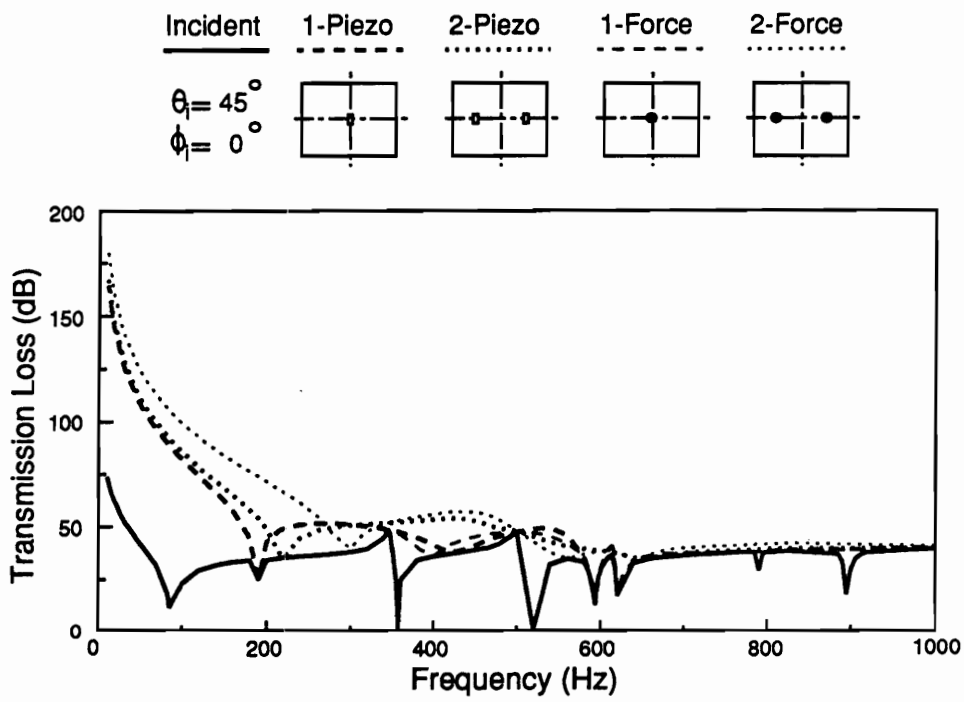


Figure 41. Plate transmission loss versus excitation frequency

For the single actuator, the piezoelectric and point force actuators give about the same performance especially at lower frequencies. However, some differences are observed about the (3,1) resonance for the reasons discussed above.

3.5.2.3 Summary

The active control of a plane sound wave transmitting through a rectangular plate at an angle has been analytically studied. Both piezoelectric and point force actuators are considered while the control cost function is derived from the far-field radiated acoustic power. The performance of the control system for an increasing number of control inputs is studied, and the attenuations obtained for point force and piezoelectric actuators are compared. The results show that both piezoelectric and point force actuators provide high reductions of sound transmitted through the plate if the proper size, number and location of actuators are chosen. In general, as the number of actuators is increased, higher reductions are observed.

A very interesting result observed was that point force actuators were seen to perform slightly better than piezoelectric actuators. This result is contrary to present beliefs about distributed actuators and is presently under detailed investigation. However, piezoelectric actuators possess a number of advantages, such as lightweight, low cost and compactness, over point force transducers. The study thus indicates that piezoelectric patch type actuators show much potential for active control of sound and vibration.

3.5.3 Near-Field Pressure and Intensity Distributions

Previous sections have demonstrated the potential of multiple piezoelectric actuators as control sources in conjunction with distributed pressure sensors in the far-field to actively control sound radiation from structures, and showed the importance of properly selecting the number and location of actuators as key to efficient control of sound radiation. The far-field radiation directivity patterns as well as plate displacement distributions were presented to evaluate the control performance and mechanisms. However, little work has been done on studying the near-field pressure distributions and the radiated intensity distributions under the same conditions. These parameters are important for a number of reasons amongst which are they provide further insight into the control physical processes. It is also hoped to overcome the use of error microphones located in the far-field by the use of sensors near or on the structure. In this context, near-field pressure should provide insight into the configurations of near-field sensors required in order to provide reduction in far-field pressures.

The objective of this section is to extend the analysis presented in previous sections to evaluate near-field pressure and time-averaged intensity distributions. In order to obtain the intensity distributions, the finite difference method of Pettersen (1979) will be used. A brief discussion is given in Section 3.4.2. This method has been used successfully by a number of authors to efficiently evaluate intensity distributions in complex radiating acoustic fields (Krishnappa and McDougall, 1989; Kristiansen, 1981). As discussed by Thompson and Tree (1981), the finite difference approximation errors in acoustic intensity measurements are less than 2 dB from 0 to 10 kHz for a spatial sampling separation of 8 mm.

In this study, a simply-supported finite plate embedded in an infinite rigid baffle was considered as the structure. The plate was excited by a steady state harmonic disturbance in the form of an oscillating point force. Control inputs were applied by piezoelectric actuators bonded to plate surfaces, while error information was taken from a number of microphones located in the radiated acoustic far-field. In contrast to Sections 3.5.1 and 3.5.2 in which the total radiated power (distributed pressure sensors) is chosen as a cost function, the sum of mean square pressures measured by a number of discrete microphone sensors is now considered as the cost function. The optimal solution derived from Linear quadratic optimal control theory is shown in Section 3.5.3. Under this control condition, the near-field pressure (Equation (3.17)) and time-averaged intensity distributions (Equation (3.92)) were evaluated, while the plate uncontrolled and controlled motion was studied in this Section in the wavenumber domain.

For brevity, this section only considers response of the plate of thickness 2 mm near the (3,1) response frequency. Table 6 gives the physical properties of the rectangular simply supported plate (except $h = 2$ mm), while Table 10 provides the associated natural frequencies of the plate. For simplicity, a single harmonic point force of amplitude $F = 1$ N located at $x_f = 0.3163$ m, $y_f = 0.15$ m (i.e., at one sixth of the plate length and middle of the plate width), in order to effectively excite the (3,1) mode, was used as the primary disturbance. Likewise, a single control piezoelectric actuator of thickness $t_a = 0.1905$ mm and dielectric constant of $d_{31} = 166 \times 10^{-12}$ m/V was employed, centrally located at $x_1 = 0.15825$ m, $x_2 = 0.22175$ m, $y_1 = 0.1309$ m, $y_2 = 0.16905$ m. The piezoelectric actuator is arranged not to activate even-even, even-odd and odd-even modes so as to simplify the control situation. Therefore, the mechanism and characteristics of this control technique can be conveniently studied. A single error sensor was assumed lo-

cated at either $(R, \theta, \phi) = (1.8\text{m}, 0^\circ, 0^\circ)$; termed mike # 1 or $(1.8\text{m}, 50^\circ, 0^\circ)$; termed mike # 2.

Both pressure and the normal time-averaged intensity (i.e., the z component) to the x-y plane were calculated at a distance of 20 mm above the plate and expressed in dB *re* $20\mu\text{ Pa}$ for pressure and dB *re* 10^{-12}W/m^2 for intensity. In addition, the vector intensity components in x-z plane (i.e., vector sum of the z and x component) located at the central line of the plate in the y direction (i.e., $y = L_y/2$) as well as the far-field radiation directivity in the same plane at a distance of $R = 1.8\text{ m}$ were calculated. A κ -plane (plate wavenumber) analysis of the plate response, which is discussed in Section 3.4.3, was performed. The wavenumber spectra of modal velocity was plotted along the κ_x and κ_y axis. The κ_x and κ_y are structural modal wavenumber, as tabulated in Table 5.

The near-field pressure was obtained directly by integrating Equation (3.17) using the Simpson's one-third rule approach. These complex pressures were then used in the finite difference calculations of the intensity equations of Section 3.4.2 with a spacing of 1 mm. The modal sums in the above equations were truncated at $m=n=5$, i.e., 25 modes were included in the analysis. This number of modes was found to provide sufficient convergence of series in Equations (3.1) and (3.16). In particular, for the study of the behavior of the (3,1) mode, the plate displacement and the radiated sound pressure have no more than 0.01 % difference in comparison to those results for including 100 modes (i.e., $m=n=10$).

3.5.3.1 Pressure and Intensity Distributions

Figure 42 presents the far-field radiation directivity patterns for a frequency of 357 Hz, which can be seen from Table 10 to be close to the (3,1) resonance point. The solid line denotes the primary field and can be seen to be fairly constant with radiation angle. This behavior is due to the relatively long wavelength of the acoustic radiation relative to plate size, leading to the higher order plate mode giving a radiation field which is volumetric or monopole-like, i.e., the situation corresponds to an edge mode of case (b) of Figure 20 discussed previously.

The controlled field is shown as a dashed line when the error sensor is located at $\theta = 0^\circ$; the primary field is strongly attenuated globally, and the residual field exhibits a dipole like radiation pattern due to the position of the error microphone. When the error microphone is moved to $\theta = 50^\circ$, similar values of attenuation are achieved; however, the null in the residual radiation field has moved to this angle.

Although the different location of error microphone results in different residual radiation pattern, the optimal voltages peak-to-peak applied to the piezoelectric actuator are 24.96 V and 24.93 V for the error microphone at $\theta = 0^\circ$ and 50° respectively. The total acoustic power reduction achieved in the two cases are 57.18 dB for $\theta = 0^\circ$ and 51.68 dB for $\theta = 50^\circ$ respectively. The slight difference of voltage inputs and total power reduction for these two cases is due to the (3,1) mode response which results in non-uniform radiation directivity (i.e., different sound pressure level at the locations of the two error microphone positions). As seen in Figure 42, the sound pressure level at $\theta = 0^\circ$ is higher than that at $\theta = 50^\circ$. While the error microphone signal is to be driven

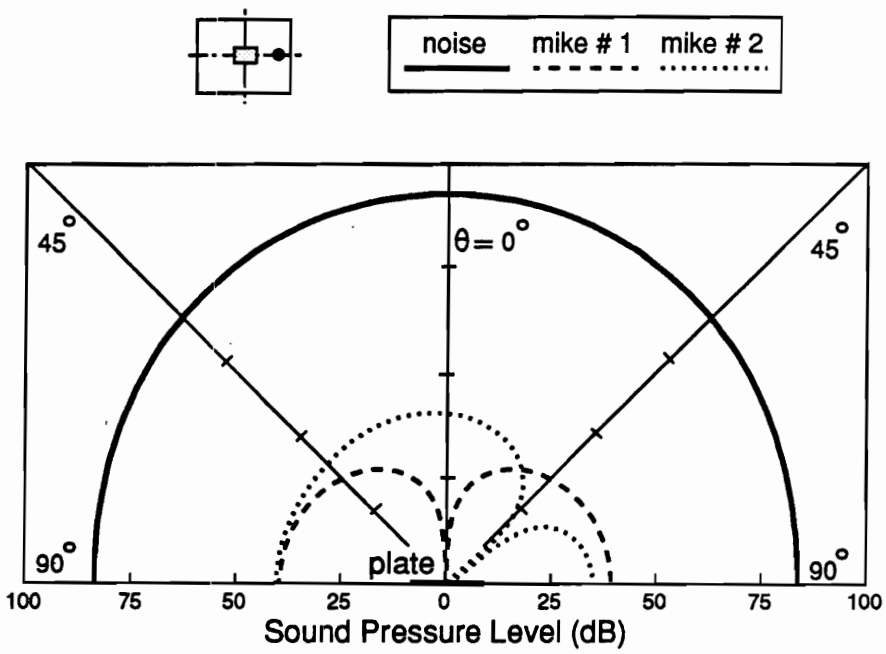


Figure 42. Radiation directivity for 2 mm plate, $f = 357$ Hz

to zero, the use of the error microphone at $\theta = 0^\circ$ will result in more pressure reduction than that at $\theta = 50^\circ$. Therefore, the case of error microphone at $\theta = 0^\circ$ requires additional 0.03 V of control voltage and perform slightly better than the case of error microphone at $\theta = 50^\circ$.

The corresponding near-field pressure distributions in the x-y plane for the primary and controlled (error microphone at $\theta = 0^\circ$) fields are shown in Figures 43 and 44 respectively. The primary field can be seen to exhibit the cell-like behavior associated with the (3,1) mode shape of the plate, however, it is slightly distorted due to contribution from the (1,1) mode. When control is applied, two changes in the near-field pressure distribution of Figure 44 are observed. Firstly, the overall pressure amplitudes is reduced by around 10 dB. Secondly, the complexity of the pressure field is markedly increased, and there appears to be a semblance of a pressure node located around $x = 100$ mm. It is this kind of behavior that is interesting for the design of near-field sensors. The overall fall in near-field pressure indicates that if a distributed pressure sensor is located above and completely covers the plate, then minimizing the near-field sensor output might have the same control influence as a far-field point sensor, at least for plate modes on resonances. In effect, the use of a large distributed pressure sensor located near the plate may lead to an "unloading" of the plate radiation field and a drop in power; the plate will "see" a radiation impedance approaching zero.

Figures 45 and 46 give the corresponding normal intensity distributions to Figures 43 and 44. Regions of outgoing and ingoing intensity to the plate are marked (+) and (-) respectively. The primary field of Figure 45 strongly indicates the (3,1) plate behavior. As can be seen, the two outer cells give positive or outgoing intensity, while the inner cell has negative or in-going intensity. However, as discussed in works, such as

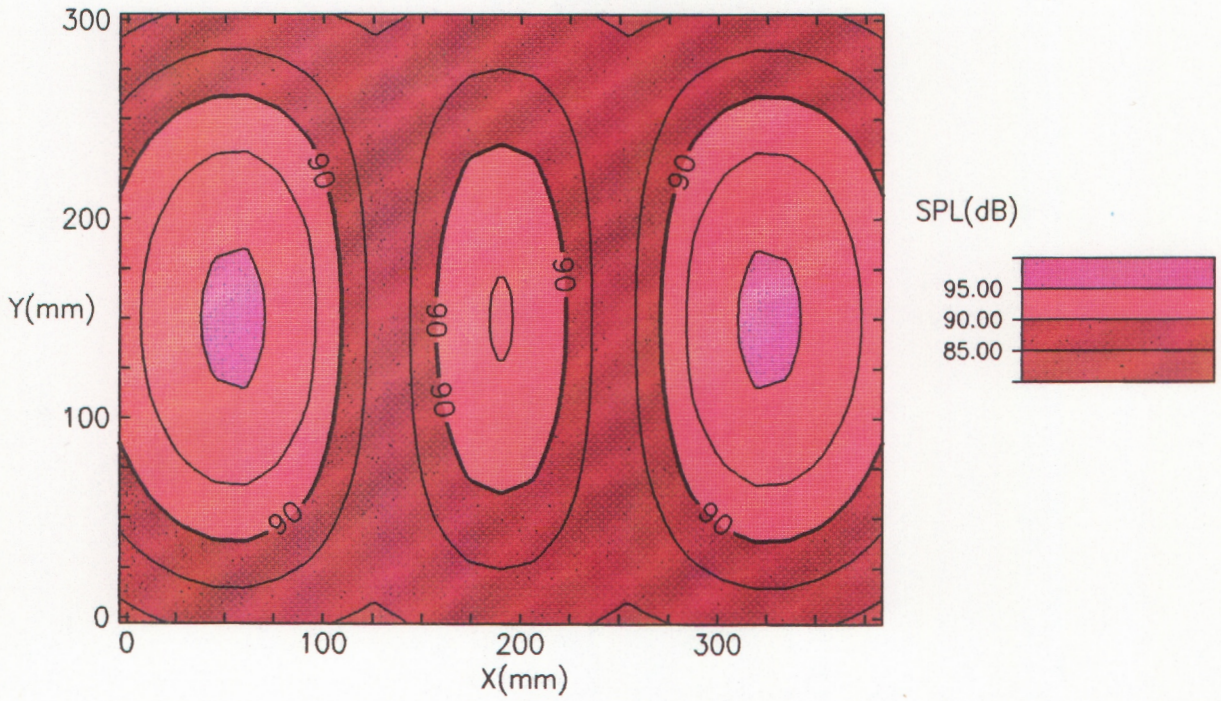


Figure 43. Pressure distribution (xy-plane) for the primary source only, 2 mm plate, $f=357$ Hz

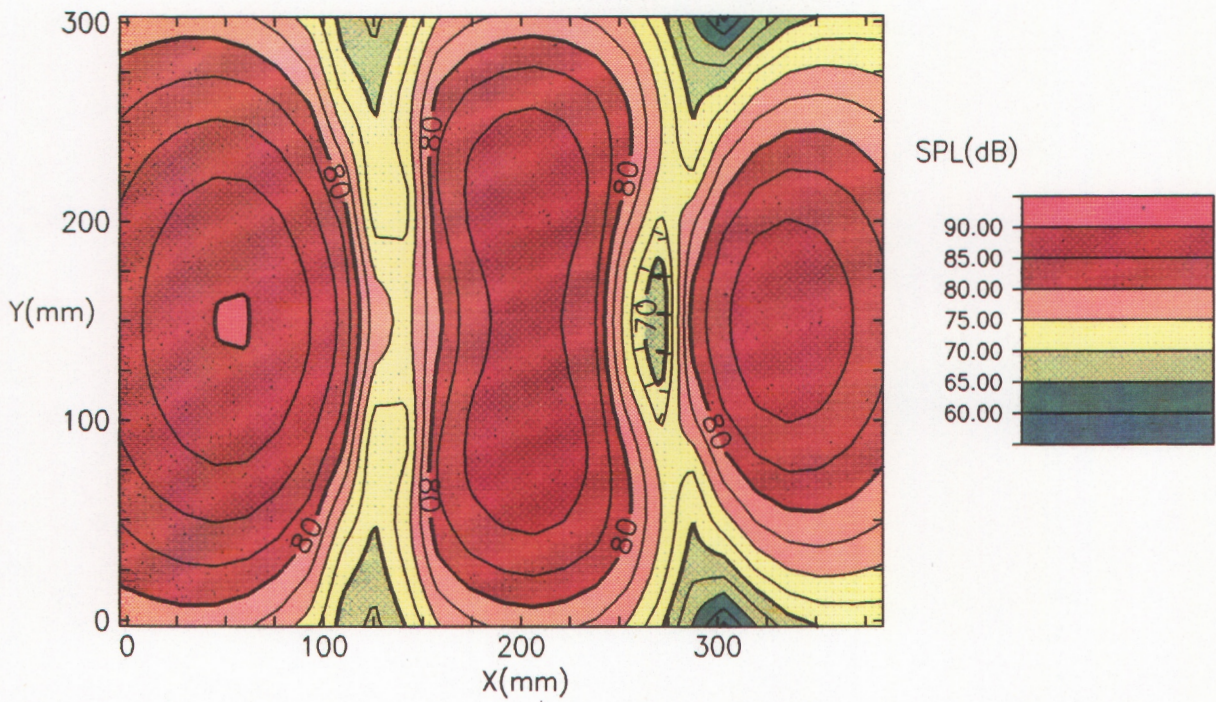


Figure 44. Pressure distribution (xy-plane) for the controlled, 2 mm plate, $f = 357$ Hz, error mike at (1.8 m, 0° , 0°)

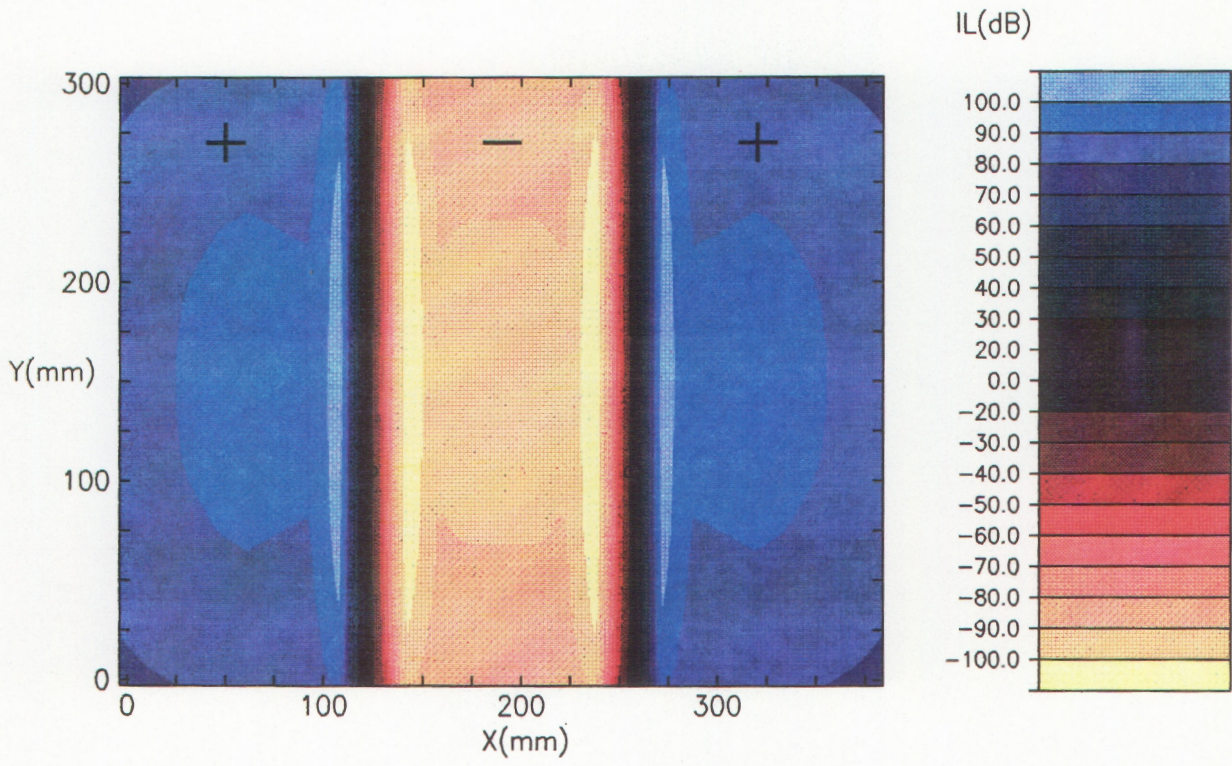


Figure 45. Time-averaged intensity distribution (xy-plane) for the primary source only, 2 mm plate, $f=357$ Hz

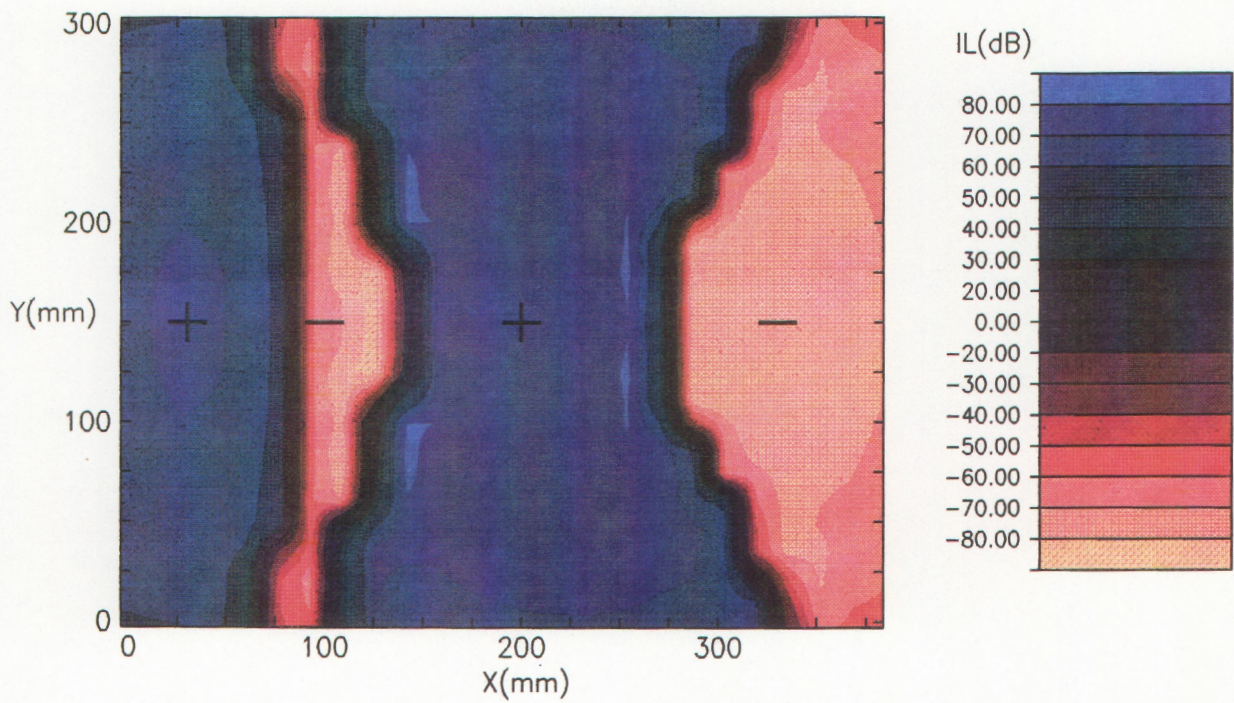


Figure 46. Time-averaged intensity distribution (xy-plane) for the controlled, 2 mm plate, $f = 357$ Hz, error mike at $(1.8 \text{ m}, 0^\circ, 0^\circ)$

Maidanik (1974), the net effect for long acoustic wavelength relative to plate size is in-plane edge radiation, which appears like a monopole type source in the far-field. As the acoustic wavelengths are relatively long, radiation of each cell interacts with its neighbor leading to cancellation for the inner portions of the plate. The situation here corresponds to Region (1) in Figure 19 and Case (b) in Figure 20. When control is applied the intensity distribution is markedly changed. Figure 46 shows that the apparent plate source is far more complex and higher order. An integration of the intensity vector over the plate surface shows that the net power has been strongly attenuated. Since the single actuator can suppress strongly responding modes (in this case the (3,1) mode), the residual plate modes are usually higher order. It is observed that both the controlled pressure and intensity fields of Figures 44 and 46 have a shape very similar to the (4,1) mode. This higher mode pattern has lower radiation efficiency, and this, in addition to the reduction in amplitude, leads to a drop in radiated pressure. The first effect has been called "modal suppression" and the second "modal restructuring" (Fuller, Hansen, and Snyder, 1990c).

Figures 47 and 48 show the controlled pressure field and normal intensity distribution when the error microphone is located at $\theta = 50^\circ$. The near-field pressure field appears to be fairly similar to the distribution when the error microphone was located at $\theta = 0^\circ$, as shown in Figure 44; however, the intensity distribution is markedly different. In this case, the central cell, in which intensity flows into the plate, has greatly expanded, while the edge radiation components appear to have been reduced. In particular, the net power flow from the edge of the plate on the same side as the error microphone has been markedly attenuated.

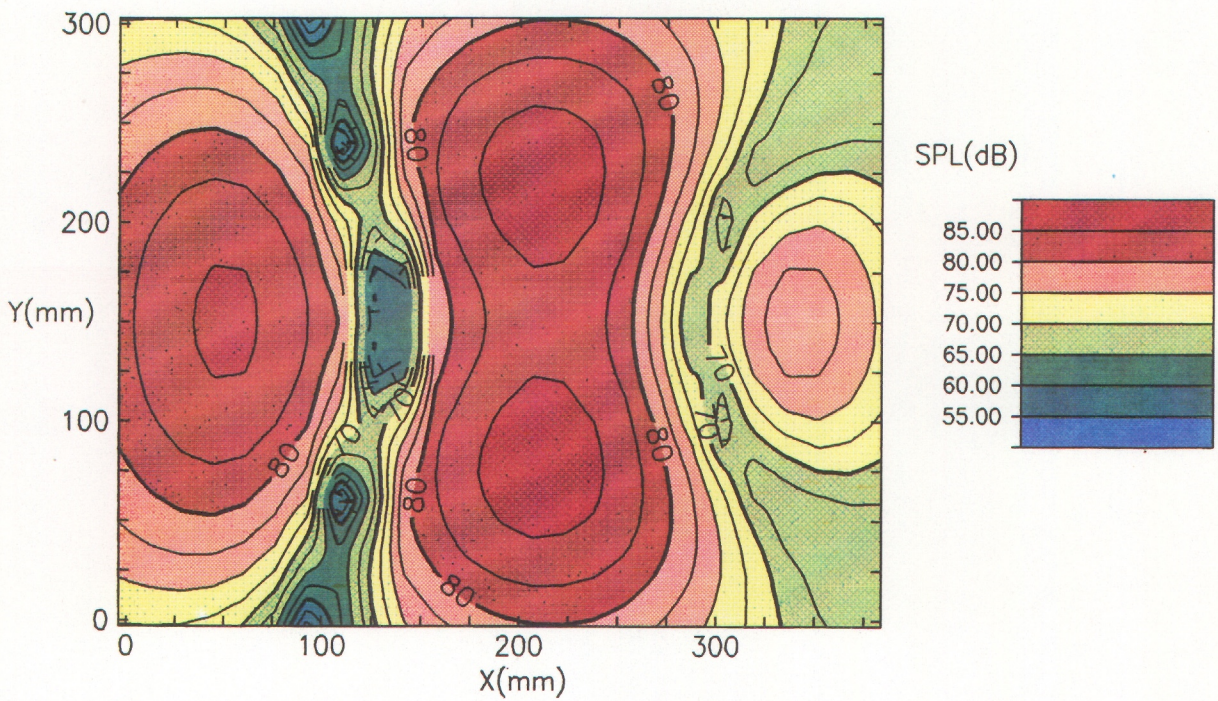


Figure 47. Pressure distribution (xy-plane) for the controlled, 2 mm plate, $f=357$ Hz, error mike at (1.8 m, 50° , 0°)

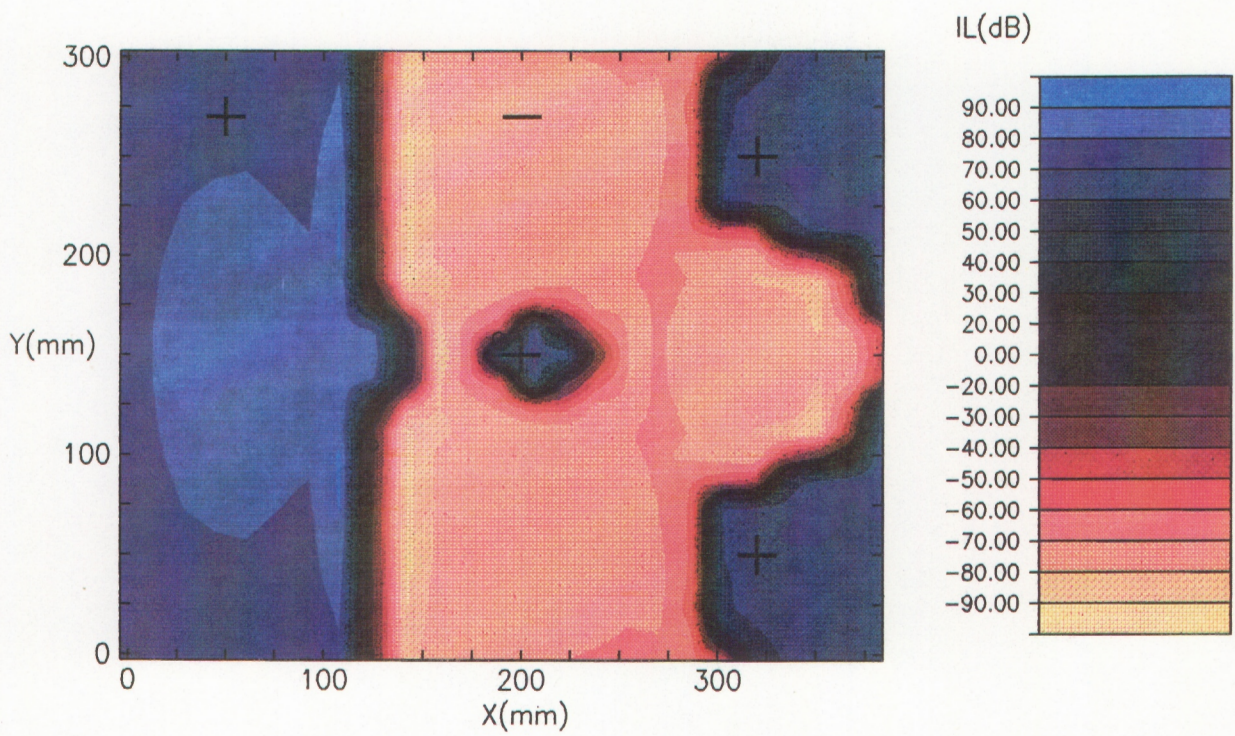


Figure 48. Time-averaged intensity distribution (xy-plane) for the controlled, 2 mm plate, $f = 357$ Hz, error mike at (1.8 m, 50° , 0°)

Figures 49 and 50 present the near-field pressure distribution and intensity vector distribution in the central x - z plane for the primary source. Note that the intensity vector plots were calculated at a distance 20 mm above the plate and normalized in log-scale to the maximum recorded value. The maximum intensity level and the corresponding vector is depicted at the bottom of the figure for scaling purpose. Note that decibels are scaled linearly in vector length. The pressure distributions clearly illustrate the volumetric radiation nature of the (3,1) mode at this low value of $\kappa L_x = 2.48$. Near the plate, the pressure distribution exhibits the three cell nature associated with the (3,1) mode; however, as the observation point moves to the far-field, the radiation field becomes progressively more uniform and monopole like in behavior. Similarly, the intensity distributions of Figure 50 shows that the inner cell of the plate acts as an acoustic sink, and the radiated energy from the plate comes from near the edges.

When control is applied, the pressure and intensity distributions for the error microphone at $\theta = 0^\circ$ demonstrate a marked change as shown in Figures 51 and 52. Two characteristics are again evident. Firstly, the overall pressure levels have fallen (due to response of the plate decreasing). Close to the plate, the pressure field exhibits behavior like the (3,1) mode; however, it is apparent that strong nodal type region of low pressure has been generated starting near $x/L_x = 0.4$. Likewise, the intensity vector distribution for this case given in Figure 52 show that the net radiation from the edges has been effectively cancelled. It is interesting to note from Figure 52 that the primary source appears to be acting as an energy sink in this case.

Moving the error microphone to $\theta = 50^\circ$ gives additional interesting results, as can be seen in the pressure plots of Figure 53 and intensity vector plots of Figure 54. Again, the controlled pressure field exhibits behavior very similar to the (3,1) mode near the

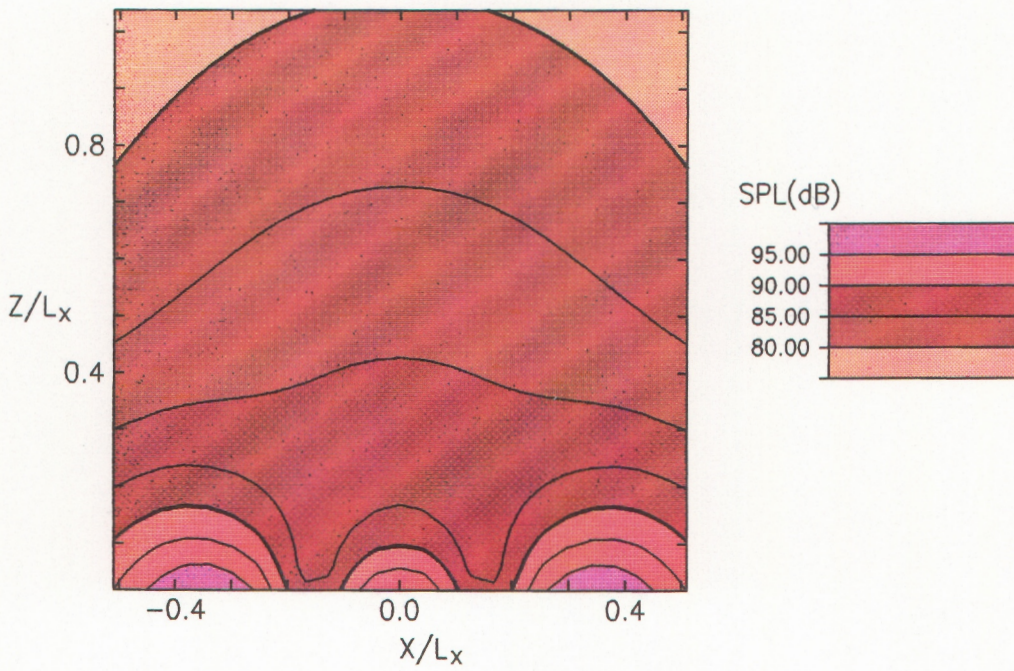


Figure 49. Pressure distribution (xz-plane) for the primary source only, 2 mm plate, $f = 357$ Hz

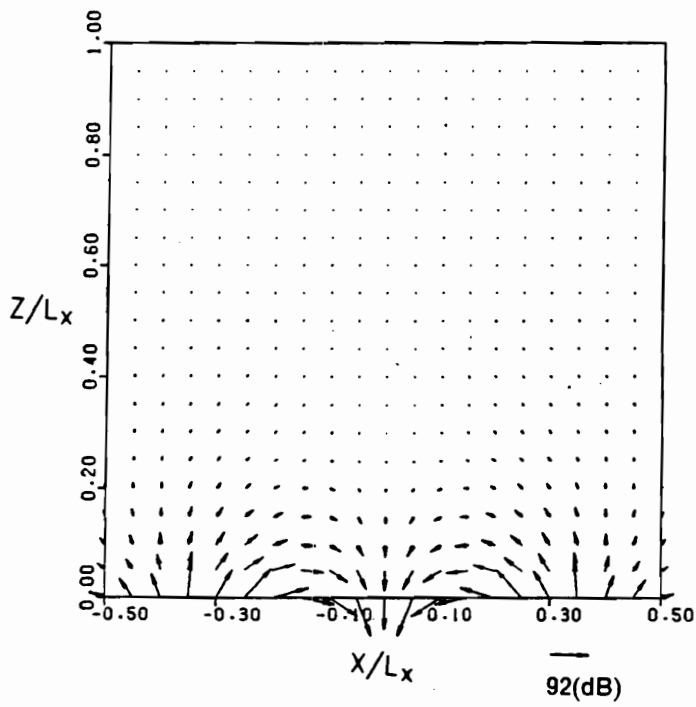


Figure 50. Intensity vector (xz-plane) for the primary source only, 2 mm plate, $f = 357$ Hz

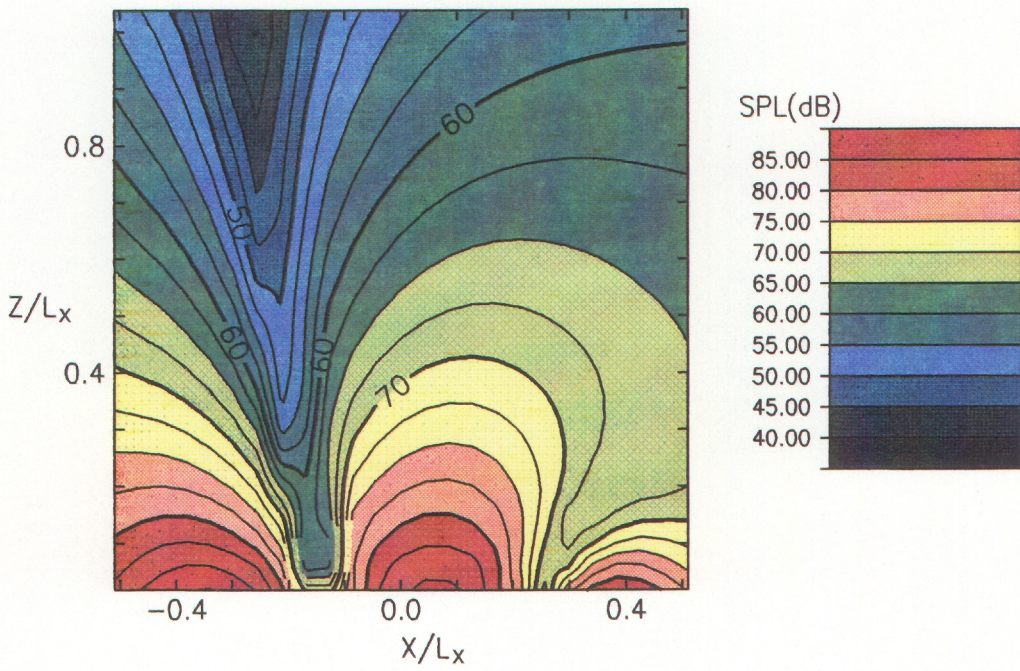


Figure 51. Pressure distribution (xz-plane) for the controlled, 2 mm plate, $f = 357$ Hz, error mike at (1.8 m, 0° , 0°)

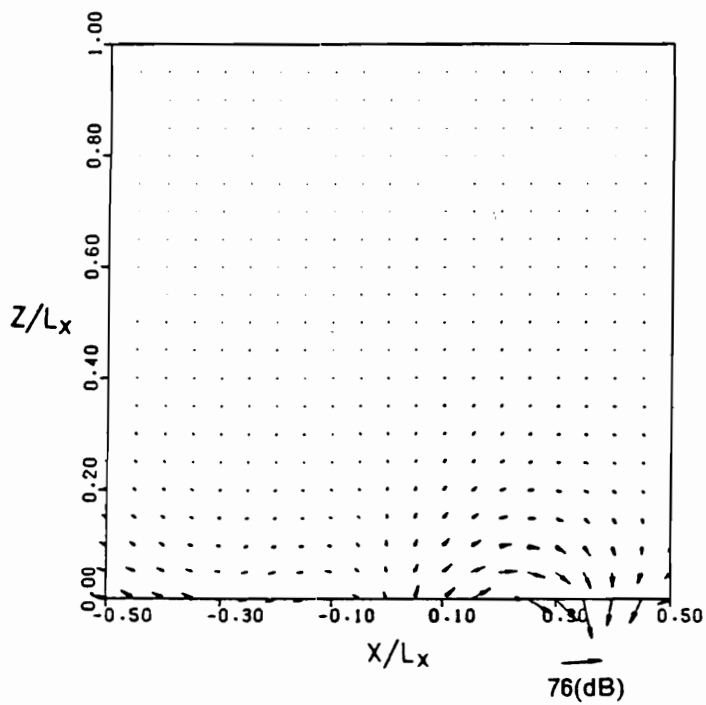


Figure 52. Intensity vector (xz-plane) for the controlled, 2 mm plate, $f=357$ Hz, error mike at (1.8 m, $0^\circ, 0^\circ$)

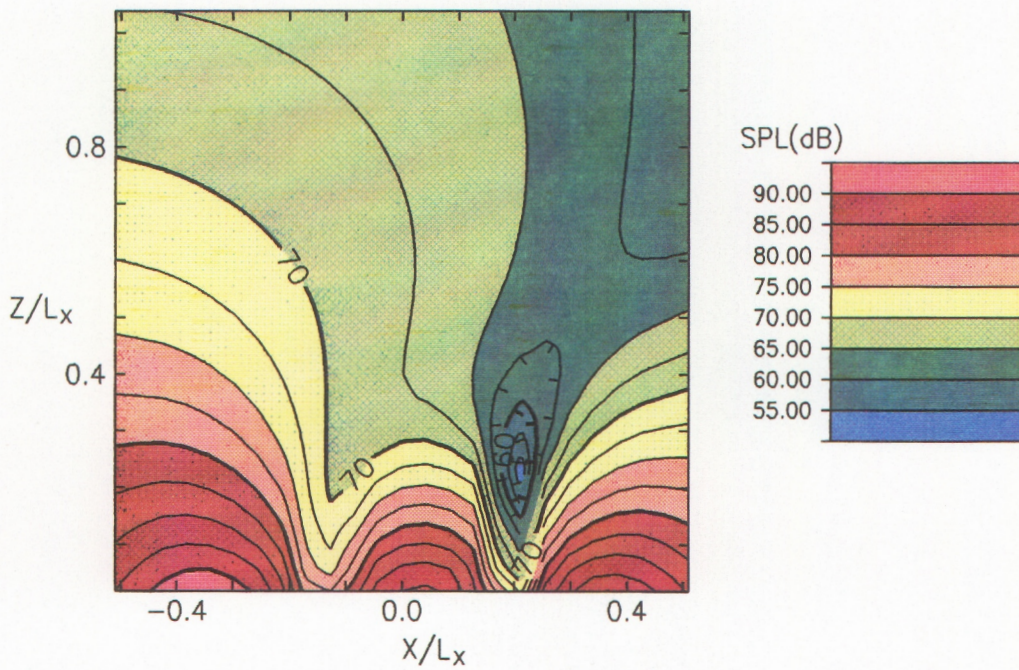


Figure 53. Pressure distribution (xz-plane) for the controlled, 2 mm plate, $f = 357$ Hz, error mike at (1.8 m, $50^\circ, 0^\circ$)

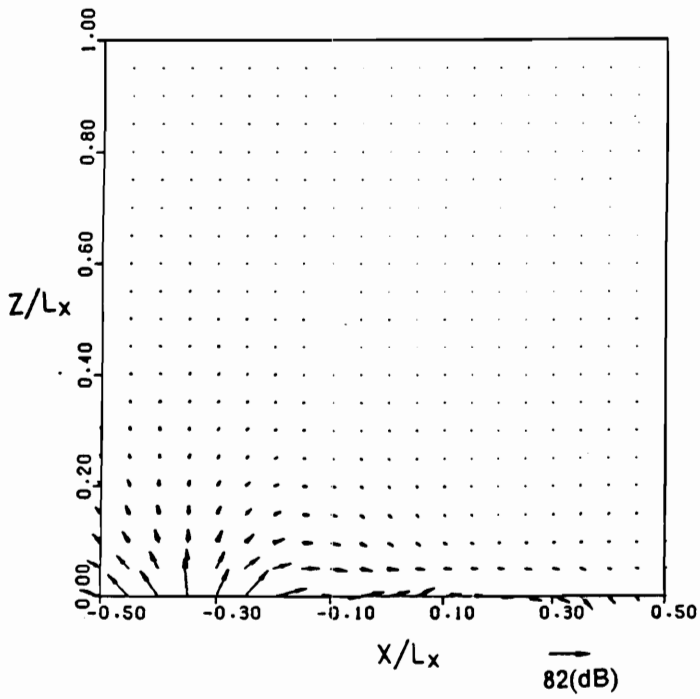


Figure 54. Intensity vector (xz-plane) for the controlled, 2 mm plate, $f=357$ Hz, error mike at (1.8 m, $50^\circ, 0^\circ$)

plate without large changes in level; however, at increasing distances from the plate, the pressure field becomes increasingly more complex exhibiting a nodal type low pressure region towards the location of the error microphone. The intensity plots of Figure 54 again demonstrate that the edge radiation is effectively reduced, this time on the side of the plate closest to the error microphone. In this control case, it appears that the energy leaving one side of the plate flows across the plate surface and is absorbed at the other side.

Thus two important effects have been illustrated apart from the fact that control leads to a general lowering of radiation acoustic pressure. The results demonstrate that application of control leads to a change in the volumetric, monopole nature of the (3,1) mode in the far-field and also a reduction in the edge radiation component.

3.5.3.2 Wavenumber Distributions

In connection with the last observation, it is interesting to examine the wavenumber spectrum of the plate-baffle system uncontrolled and controlled response. Figures 55(a) and 55(b) give the modulus squared (the autospectrum) of the plate wavenumber components along κ_x and κ_y axis respectively. It is noted that only the positive components of κ_x and κ_y are shown in Figures 55(a) and 55(b) for brevity; however, the complete plate wavenumber spectrum should also include negative components. As the modes on the plate are separable, we can completely represent the plate wavenumber distribution by the κ_x and κ_y plots.

In Figures 55(a) and 55(b), the solid line denotes the spectrum of the primary field, while the short-dash line represents the controlled field for the error microphone at

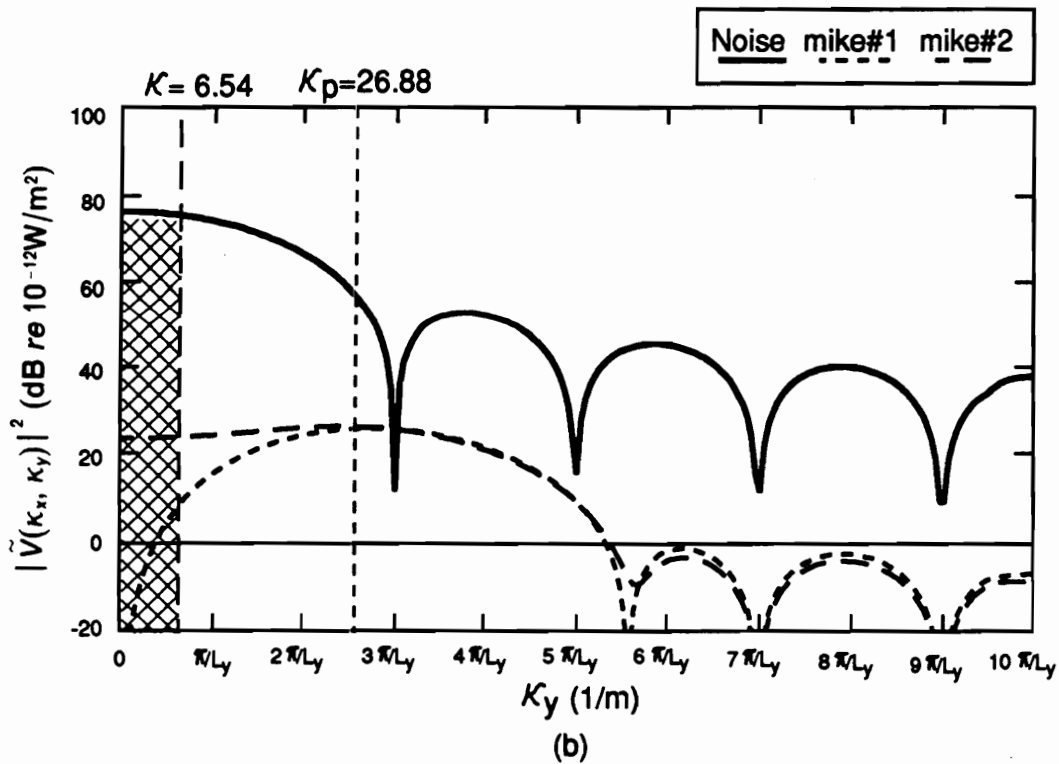
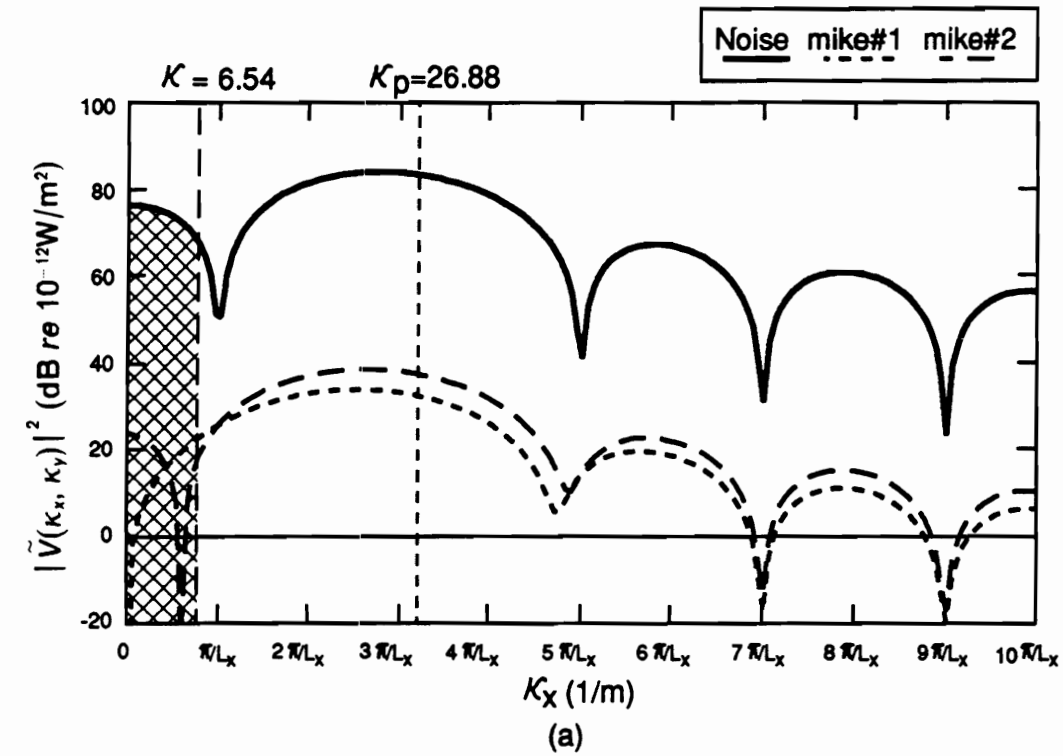


Figure 55. Wavenumber spectra of modal velocity along κ_x and κ_y axis

$\theta = 0^\circ$, $\phi = 0^\circ$ and the long-dash line for the case of the error microphone at $\theta = 50^\circ$, $\phi = 0^\circ$. The spectrum of the primary field can be seen from Figures 55(a) to peak near values of $\kappa_x = 3\pi/L_x$ and $\kappa_y = 0$ indicating that the plate response, as expected, is dominated by the (3,1) mode whose eigenvalues are $\kappa_x = 3\pi/L_x$, $\kappa_y = \pi/L_y$ respectively. Figure 55(a) also indicates that there is substantial spectral component at $\kappa_x = 0$ indicating that there is significant (1,1) mode content in the plate response. This observation explains why the pressure and intensity fields of Figures 43 and 45 are slightly distorted from the pure (3,1) distribution.

The spectral content of the controlled response can be seen to be strongly reduced at all wavenumbers for both microphone positions. This indicates that the plate response has globally fallen explaining the overall drop in near-field pressure observed previously. Also shown on the plots of Figures 55(a) and 55(b) is the position of the wavenumber component $\kappa_x = \kappa_y = \kappa$; for this frequency $\kappa = \omega/c = 6.54 \text{ m}^{-1}$. It is noted that the case considered here corresponds to Region (1) in Figure 19. The resonant mode includes the (3,1) mode which is the dominant radiator recognized as x-edge radiation. As discussed by Maidanik (1974), wavenumber components above this line are subsonic and do not contribute to far-field pressure. However, the supersonic components below κ do contribute to the far-field pressure. Thus it is interesting to note a number of further observations from Figure 55(a). Firstly, the wavenumber spectrum can be seen to be zero at $\kappa_x = 0$ and $\kappa_x = 5 \text{ m}^{-1}$ for the controlled cases with the error microphone at $\theta = 0^\circ$ and 50° respectively. This result supports the stationary phase result of Equations (3.97), (3.98) and (3.99) which states that radiation at a particular angle corresponds to discrete wavenumber components at $\kappa_x = \kappa \sin \theta \cos \phi$ and $\kappa_y = \kappa \sin \theta \sin \phi$. Thus, when the pressure is minimized in the far-field at a particular angle, the corresponding wavenumber component is suppressed in the structure. This

result suggests that a controller could be formulated in the wavenumber domain to remove particular wavenumber components from the structure. The radiated pressure would then be minimized at the corresponding angle without the use of a microphone in the far-field. Control formulations of this nature have recently been completed by Fuller and Burdisso (1990b).

The second interesting point of Figure 55(a) is that the supersonic components have also been more strongly reduced than the subsonic components. As discussed by Fahy (1985), the supersonic components (corresponding to the shaded rectangular area, i.e., surface modes, in Figure 19) arise because of the finiteness of the plate embedded in the baffle (the reader is reminded that the wavenumber transform considers the complete plate-baffle system). As discussed previously, the resonance (3,1) mode, within the subsonic components, are the dominant radiator related to the edge motion of the plate. The phenomena is termed "edge radiation" (Maidanik, 1974). Reduction in the subsonic components thus implies a reduction or change in the edge radiation mechanism, and this is precisely the behavior that was observed in the intensity vector plots of Figures 52 and 54 discussed previously.

Finally, the controlled wavenumber distributions of Figures 55(a) and 55(b) show that the oscillations in the spectral distributions at low wavenumbers has been smoothed. This indicates that the residual response of the plate-baffle system is dominated by high wavenumber components or short wavelength high modal number motion, as observed in the residual or controlled pressure and normal intensity plots.

Thus wavenumber analysis appears to be a powerful alternative tool to investigate the system behavior. For example, what was previously term "modal suppression" (Fuller, Hansen and Snyder, 1990c), when the plate response falls globally corresponds

to a fall in wavenumber components across the spectrum. What was previously termed "modal restructuring" (Fuller, Hansen and Snyder, 1990c), which corresponds to a change or increase in plate vibration amplitude and complexity while radiated pressure falls, corresponds to a reduction in supersonic components while the subsonic components may even increase. This has also been referred to previously in this thesis as the controlled residual response having an overall lower radiation efficiency. Both of these types of behavior have been observed in the wavenumber domain in companion experiments (Clark and Fuller, 1990b). It is also apparent that the control behavior can be viewed in a number of ways; each of which provides valuable insight into system behavior.

3.5.3.3 Summary

This section presented an analytical study of the near-field pressure and intensity distributions of actively controlled plate radiated sound. The results presented, although limited to the (3,1) mode resonance case, reveal a number of interesting characteristics. In general, when control was applied, a number of important characteristics were observed. Firstly, for this case of resonance, applying control leads to an overall fall in the magnitudes of near-field pressure and intensity vectors, because the mode on resonance has been significantly suppressed. Secondly, the controlled field appeared to exhibit radiation behavior similar to a higher order anti-symmetric mode. The monopole like nature of the far-field radiation pattern of the (3,1) mode was modified to a pattern with a nodal region near the location of the error microphone. Thirdly, the application of control appeared to reduce the acoustic intensity leaving the edges of the plate (edge radiation) resulting in an overall drop in radiated acoustic power. In connection with this, while the location of the error mike had little effect on the overall power reduction

and optimal control voltages, it had a significant effect on the near field pressures and intensity distributions (in particular, edge radiation characteristics).

The results provide further insight into the mechanisms associated with the active structural control approach studied here. In particular, the results indicate possible strategies for the design of near-field sensors to minimize the far-field radiated power. For "on resonance" case, one strategy may be to use a distributed sensor which provides an error signal proportional to the average of the acoustic pressure over the plate surface. Another strategy could be to use a strip distributed error sensor which could be located at the very low pressure regions of the controlled distribution. This would have the effect of forcing an asymmetry into the radiation field which has been shown in this section to be associated with a lower total radiated acoustic power. Finally, wavenumber analysis of the plate vibration has been shown to be a powerful alternative tool for studying the mechanisms of control.

3.5.4 Comparison of Different Forms of Cost Functions

This section evaluates the use of different forms of cost functions defined in Section 3.3. To compare the control effectiveness of different forms of cost functions, an on-resonance and off-resonance excitation will be considered. Both the radiation directivity and plate displacement distribution are presented as well as the average radiation efficiency and radiated power, which are plotted against the excitation frequency. Additionally, wavenumber domain analysis is also discussed.

Numerical examples presented are based on the plate specification as shown in Table 6 (except the plate thickness which is now $h = 2$ mm), and the plate natural fre-

quencies are tabulated in Table 10. For simplicity, a single harmonic point force of amplitude $F = 1$ N located at $x_f = 0.3163$ m, $y_f = 0.15$ m was used as the primary disturbance. Likewise, a single control piezoelectric actuator of thickness $t_a = 0.1905$ mm with a dielectric constant of $d_{31} = 166 \times 10^{-12}$ m/V was employed, located at $x_1 = 0.15825$ m, $x_2 = 0.22175$ m, $y_1 = 0.1309$ m, $y_2 = 0.16905$ m. When a single error sensor was used, the microphone at $(R, \theta, \phi) = (1.8\text{m}, 0^\circ, 0^\circ)$ in the far-field or an accelerometer located at $(x_p, y_p) = (0.19\text{m}, 0.15\text{m})$ on the plate is considered.

3.5.4.1 Modal Radiation Efficiency

As discussed previously, the radiation efficiency of the (m,n) mode can be considered as a fixed structural acoustic property of the plate geometry. Figure 56 and 57 show the modal radiation efficiency for the simply-supported rectangular plate ($h = 2$ mm) plotted against wavenumber ratio and the excitation frequency respectively. The $(1,1)$, $(3,1)$ and $(3,3)$ modes, (the odd-odd modes), have higher radiation efficiency than the $(2,1)$, $(2,3)$, (the odd-even and even-odd modes), and the $(2,2)$ modes, (the even-even mode). This indicates that the odd-odd modes are the effective radiating modes for $\gamma < 1$ with strongly acoustic coupling between sound radiation and mechanical vibration, and the even-even modes, subjected to radiation cancellation, have smaller radiation efficiencies. When the excitation frequency is greater than the modal critical frequency, which is tabulated in Table 14, the radiation efficiencies approach asymptotically to unity. The surprising observation from Figure 57 is that the $(2,1)$ modal radiation efficiency is greater than the $(3,1)$ modal radiation efficiency between 300 Hz and 1000 Hz which is within our study range (357 Hz for the $(3,1)$ resonant mode). The $(2,1)$ mode, previously thought to be a less effective radiator, actually has significant contribution.

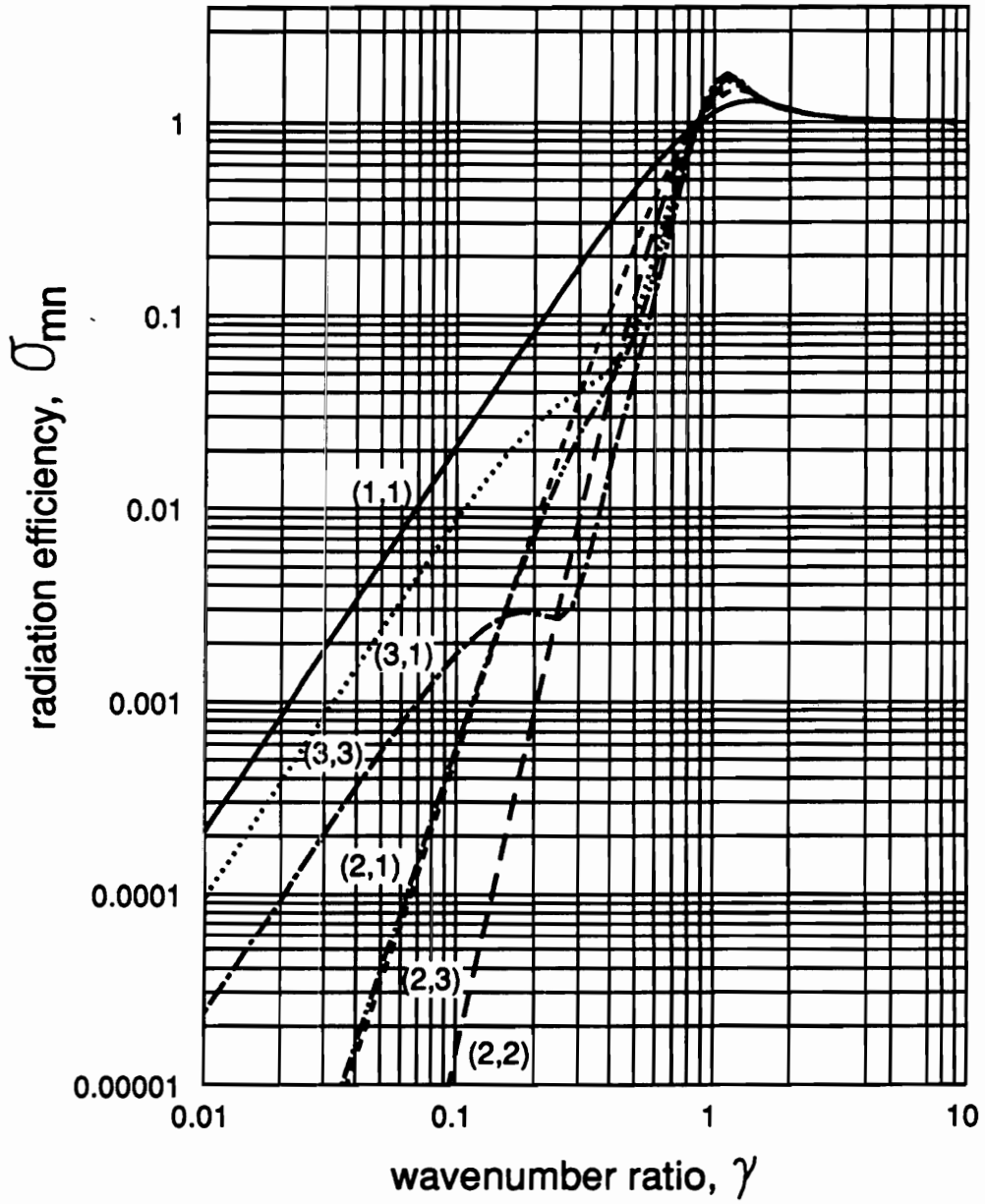


Figure 56. The (m,n) mode radiation efficiency versus wavenumber ratio

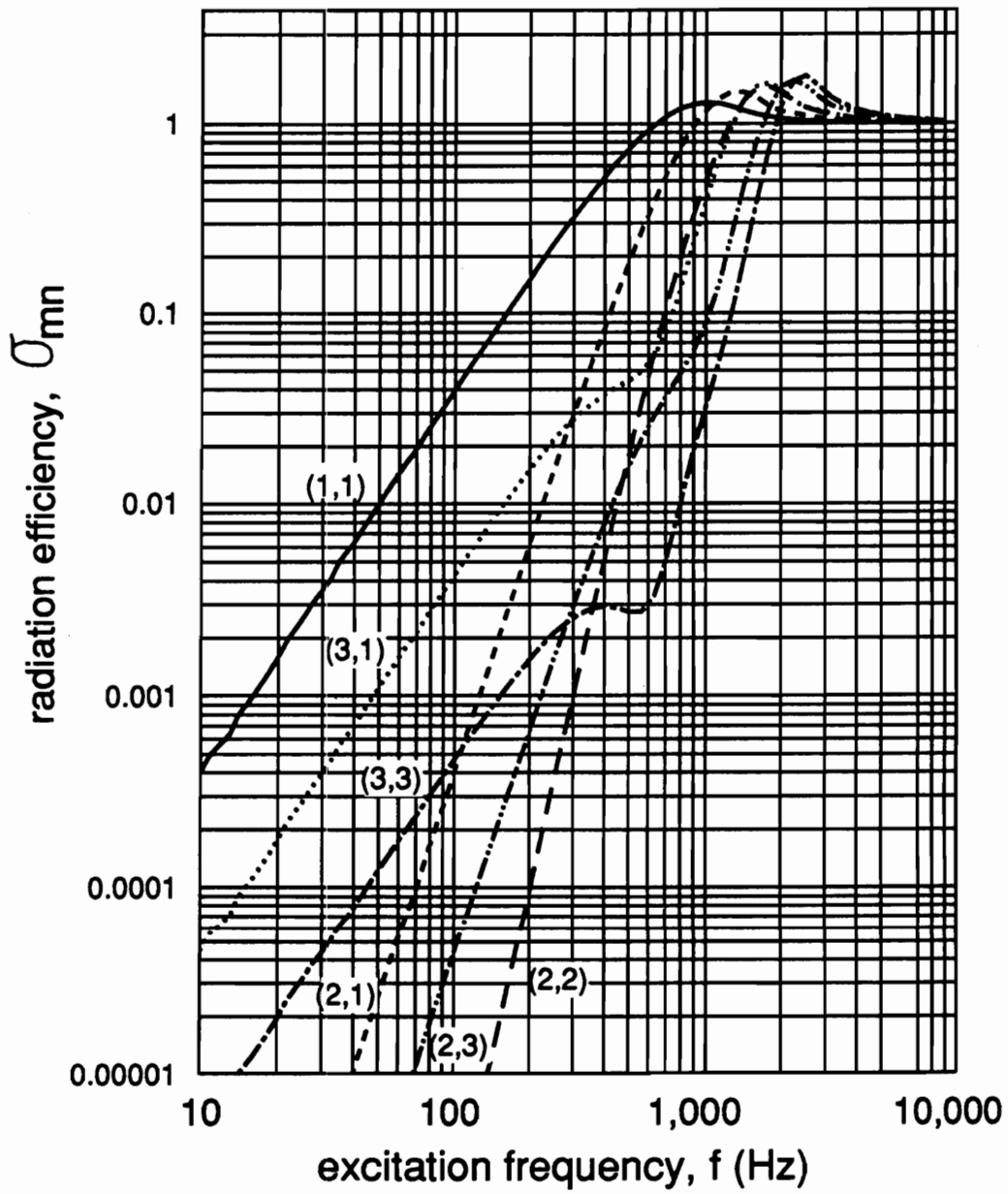


Figure 57. The (m,n) mode radiation efficiency versus excitation frequency

Table 14. Modal critical frequencies of plate (Hz)

m \ n	1	2	3	4	5
1	728.3	1229.2	1773.4	2330.8	2893.7
2	1068.4	1456.7	1938.0	2458.4	2997.5
3	1469.7	1772.1	2185.0	2657.4	3162.8
4	1893.6	2136.9	2490.0	2913.4	3380.7
5	2327.8	2529.7	2834.3	3212.6	3641.7

For infinite plates, with the excitation frequency below the critical frequency, the plates do not radiate. Above the critical frequency, infinite plates do contribute sound radiation to the far-field. However, for finite plates, the radiation characteristics become more complex because of the finiteness of the plate. With excitation frequency below the critical frequency in region (1), as shown in Figure 19, in addition to the surface modes, the resonant modes include the x- and y-edge modes and the corner modes. In region (2), the resonant modes thus include the x- and y-edge modes only. With excitation frequency above the critical frequency, i.e., region (3), only surface modes radiate to the far-field. The following illustrated examples are located in region (1).

3.5.4.2 On-Resonance Excitation

Figure 58 shows the radiation directivity of the point force disturbance with a excitation frequency of 357 Hz near the (3,1) mode controlled by one piezoelectric actuator, which is sketched on the top of Figure 58. The primary sound radiation directivity, denoted by a solid line, can be seen to be fairly constant with radiation angle. This behavior is due to the relatively long wavelength of the acoustic radiation relative to plate size, leading to the higher order plate (3,1) mode giving a radiating field which is volumetric or monopole like.

If the distributed pressure sensors over a hemisphere of radiating far-field are used, the corresponding cost function (Φ_p) can be constructed as defined in Equation (3,23). The sound pressure level can be thus reduced globally over the radiating field as it is observed at all angles. The residual radiation directivity exhibits a combination of the (1,1) and (2,1) mode responses whose radiation characteristics are illustrated in Figure 21. If a discrete pressure sensor (the corresponding cost function, Ψ_p , defined in

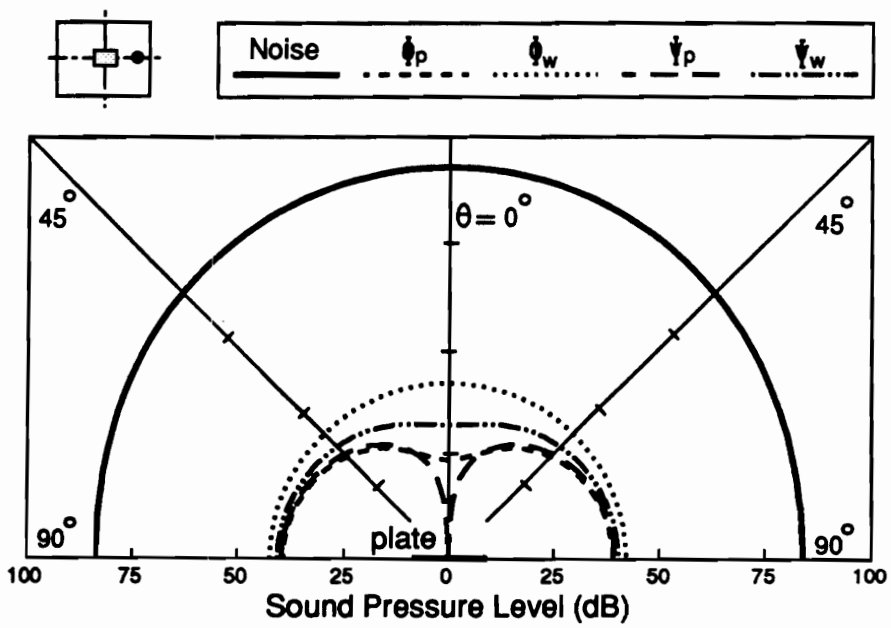


Figure 58. Radiation directivity for on-resonance excitation, $f = 357$ Hz

Equation (3.42)) is used and located at $(R, \theta, \phi) = (1.8\text{m}, 0^\circ, 0^\circ)$, the residual radiation directivity reveals a dipole response, because the sound pressure at the location of the error microphone is reduced to zero. Similarly, a distributed or discrete acceleration sensor located at $(x, y) = (0.19\text{m}, 0.15\text{m})$ on the plate can be used, and the cost functions are then defined in Equations (3.55) (Φ_w) and (3.72) (Ψ_w) respectively. The residual radiation directivity for these two selected cost functions, Φ_w and Ψ_w , exhibits a monopole or a distorted monopole response. Generally, for on resonance, any one of the cost functions results in a global reduction of the far-field sound radiation; however, there are slight differences between the residual radiation pattern for different types of the cost function. These subtle differences reveal important insights into the different control mechanisms associated with each form of the cost function; and these effects are enhanced for off-resonance control. The results again show that the pressure sensor is superior to the acceleration sensor in sound radiation control as discussed by Fuller and Jones (1987a), because the pressure sensor supplies the coupling information between sound radiation and mechanical vibration while the acceleration sensor supplies only the information of mechanical vibration. In other words, the pressure sensor directly measures the correct variable(s) to be minimized.

Figure 59 shows the plate displacement distribution corresponding to the case of Figure 58. As expected, the (3,1) mode dominates the plate vibration due to the primary input frequency being near the (3,1) resonant point. For control with the use of one piezoelectric actuator, the plate response is attenuated globally for all cost functions and shows a slightly complex pattern. As observed, the residual plate response for Φ_w is generally the lowest, and there is a zero response at $x/L_x = 0.5$ for Ψ_w because of the central location of the accelerometer. Note that using accelerometer sensors will result in more attenuation of plate displacement than using pressure sensors; however, the

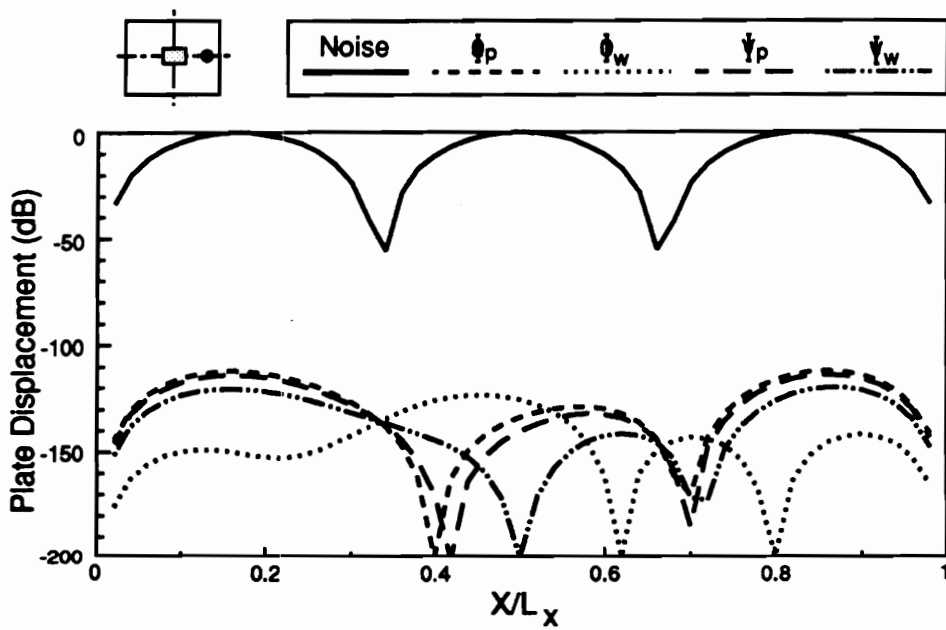


Figure 59. Plate displacement distribution for on-resonance excitation, $f=357$ Hz

corresponding sound pressure levels are not generally attenuated to the degree that the plate displacement is attenuated.

Table 15 shows the applied voltage to the piezoelectric actuator and the reduction of cost function and radiated power as well as the average radiation efficiency, when different forms of cost functions were used. The distributed pressure sensor is seen to be the most effective giving the most reduction of radiated power and the lowest average radiation efficiency. All four cost functions have nearly the same control voltages. Both the distributed and discrete pressure sensors have about the same reduction of radiated power, and generally perform better than the acceleration sensors, either distributed or discrete.

Figures 60(a) and 60(b) show the plate wavenumber spectrum along axis κ_x and κ_y , respectively. Only the positive components of κ_x and κ_y are shown for brevity. The spectrum of the primary field is denoted by a solid line shown in Figures 60(a). A peak near values of $\kappa_x = 3\pi/L_x$ and $\kappa_y = 0$ indicates that the plate response is dominated by the (3,1) mode whose eigenvalues are $\kappa_x = 3\pi/L_x$, $\kappa_y = \pi/L_y$, respectively. Figure 60(a) also indicates that there is a substantial spectral component at $\kappa_x = 0$, i. e., the (1,1) mode is significant in the plate response. The spectral content of the controlled response can be seen to be strongly reduced at all wavenumbers for all of the cost functions. This indicates that the plate response has globally fallen explaining the overall drop in the plate response in Figure 59. Also shown on the plots of Figures 60(a) and 60(b) are the acoustic wavenumber, $\kappa = \omega/c = 6.54 \text{ m}^{-1}$, and free structural wavenumber, $\kappa_p = (\omega^2 \rho h / D)^{1/4} = 26.92 \text{ m}^{-1}$. This case study here corresponds to Regions (2) in Figure 19. As is well known, only supersonic wavenumbers components (i.e., $(\kappa_x^2 + \kappa_y^2)^{-1/2} < \kappa$) radiate sound to the far-field. When control is applied, all supersonic wavenumber

Table 15. Summary of on- and off-resonance excitation cases

on-resonance excitation, $f = 357$ Hz				
	control voltage V (volts)	average radiation efficiency, σ	reduction of cost function (dB)	reduction of radiated power (dB)
Disturbance		0.03366		
Φ_p	24.958	0.00449	57.46	57.46
Φ_w	25.037	0.11336	54.56	49.28
Ψ_p	24.967	0.00566	144.03	57.18
Ψ_w	24.990	0.01584	153.81	54.74
off-resonance excitation, $f = 272$ Hz				
	control voltage V (volts)	average radiation efficiency, σ	reduction of cost function (dB)	reduction of radiated power (dB)
Disturbance		0.01275		
Φ_p	6.3449	0.00885	0.82	0.82
Φ_w	16.573	0.04977	1.03	-4.88
Ψ_p	4.7574	0.00938	152.85	0.77
Ψ_w	17.572	0.05296	153.63	-5.16

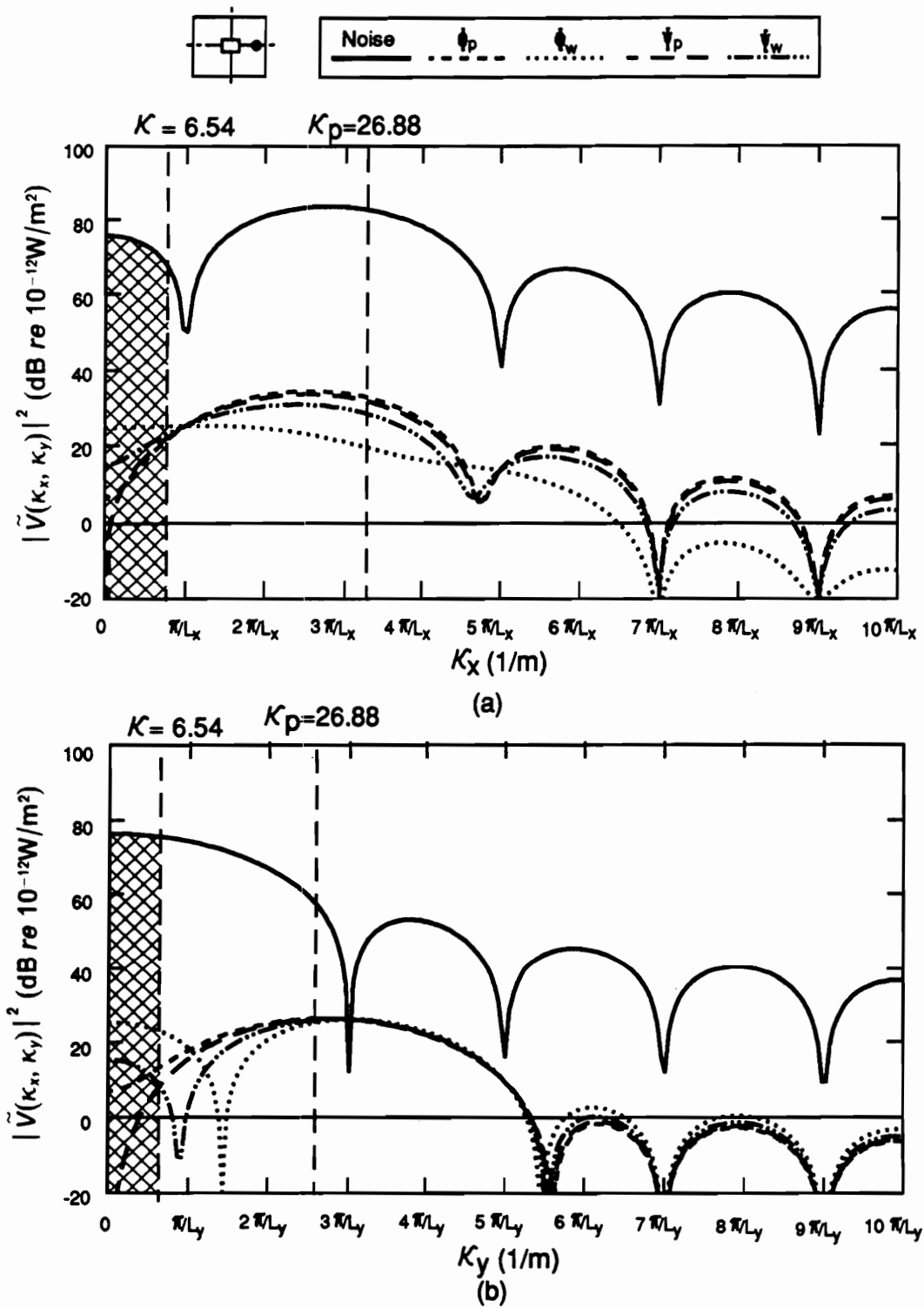


Figure 60. Wavenumber spectra of plate modal velocity along κ_x and κ_y axis, for on-resonance excitation, $f = 357$ Hz

components are seen to be reduced, corresponding to global control of sound radiation. When a discrete pressure sensor is used, the wavenumber components around $\kappa_x, \kappa_y = 0$ are observed to be strongly attenuated, corresponding to a high local reduction in sound at the error microphone.

Another interesting observation from Figure 60 is that the oscillations in the spectral distributions at low wavenumbers has been smoothed. This indicates that the residual plate-baffle response is dominated by high wavenumber components or short wavelength, higher modal order motion. Thus two control mechanisms are observed. The first, termed "modal suppression" (Fuller, Hansen and Snyder, 1990c), implies that the plate response falls globally and corresponds to a fall in wavenumber components across the complete spectrum. The second, termed "modal restructuring" (Fuller, Hansen and Snyder, 1990c), implies that the plate residual response becomes more complex (higher modal order) with a lower radiation efficiency. Conversely "modal restructuring" corresponds to a decrease in the supersonic wavenumber components while the subsonic components remain unchanged or even increase. Such behavior has also been observed in companion experiments (Clark and Fuller, 1990c) and is shown to be enhanced for off-resonance conditions studied in the next section.

3.5.4.3 Off-Resonance Excitation

Figure 61 shows the radiation directivity of the disturbance with an excitation frequency of 272 Hz between the (2,1) and (3,1) modes, controlled by one piezoelectric actuator as sketched on the top of Figure 61. The primary sound radiation directivity is denoted by a solid line, and can be seen to have a small dip at $\theta = 0^\circ$. This indicates

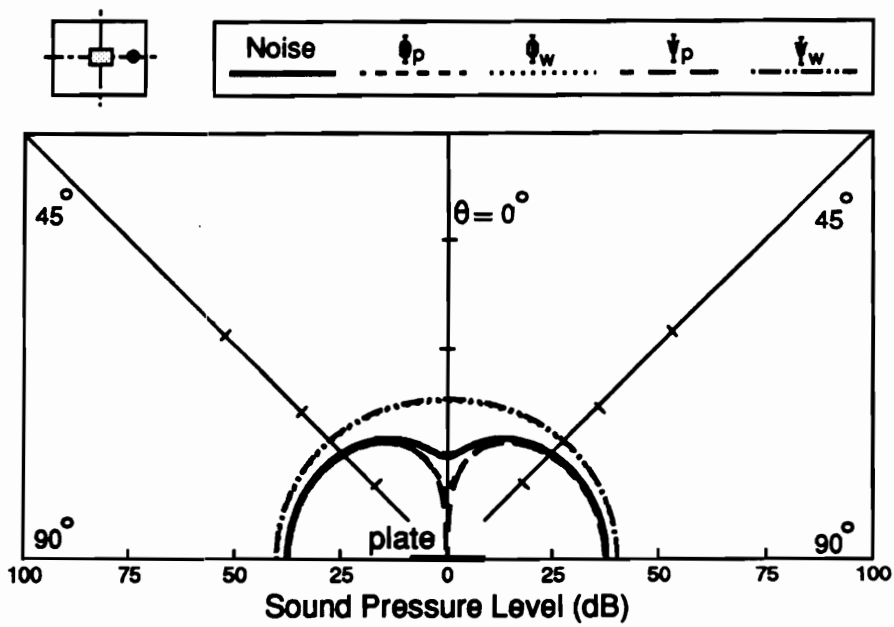


Figure 61. Radiation directivity for off-resonance excitation, $f = 272$ Hz

that the primary sound radiation directivity is contributed significantly by the (1,1) and (2,1) modes. The reduction of radiated power is only 0.82 (dB) and 0.77 (dB) for distributed and discrete pressure sensors respectively. In the case of using pressure sensors, the discrete sensor has about the same residual response as the distributed except at $\theta = 0^\circ$, where the sound pressure is reduced to zero, because of the location of the discrete pressure sensor. Only a small amount of reduction of sound pressure level can be achieved. In the case of using acceleration sensors, the residual radiation directivity reveals spillover to the sound pressure in the far-field. Although the plate vibration energy density or vibrational levels have been reduced (i.e., the reduction of cost function Φ_w or Ψ_w , which is referenced to 10^{-12} W/m²), as observed in Table 15, the total reduction of radiated power is negative for acceleration sensors, i.e., the radiation field shows spillover. The control voltages required by acceleration sensors is higher than those by pressure sensors.

Figure 62 shows the displacement distribution corresponding to the cases of Figure 61. In contrast to the radiation directivity shown in Figure 61, in which the (1,1) and (2,1) modes dominates the sound radiation to the far-field, the plate response is dominated by the (3,1) mode. As shown in Figure 57, the (1,1) and (2,1) modes have higher radiation efficiency than the (3,1) at $f=272$ Hz; therefore, the (1,1) and (2,1) modes become the dominant radiating modes rather than the (3,1) mode. When pressure sensors are used, the plate residual displacement distribution is close to the (3,1) mode, but slightly distorted, and only attenuated a little. Thus control has achieved only 0.82 dB of power reduction as shown in Table 15. This is because the central location of piezoelectric actuator cannot excite the (2,1) mode which is one of the dominant radiating modes. In the case of using acceleration sensors, the plate response was attenuated, and the (3,1) modal contribution has been cut down while the (1,1) and (2,1)

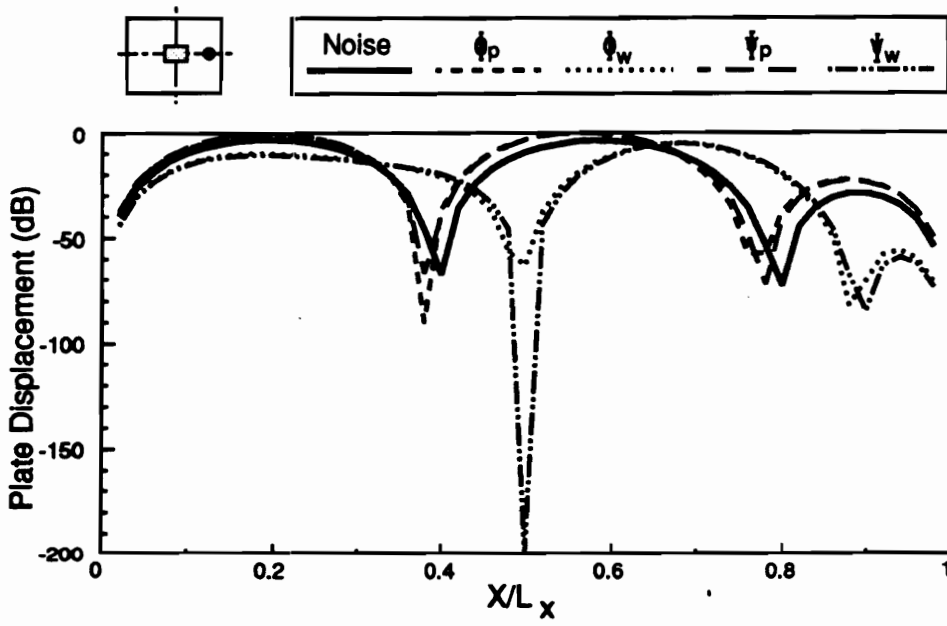


Figure 62. Plate displacement distribution for off-resonance excitation, $f = 272$ Hz

modes become dominant. This leads to the spillover in the radiating field and a monopole like response, because the (1,1) and (2,1) modes have higher radiation efficiencies. These results demonstrate a very important effect. Attenuating plate motion does not necessarily lead to reduction in radiated sound. In fact, for off-resonance cases, the inverse is often true with radiated sound levels increasing, while overall plate response decrease.

Figure 63(a) and 63(b) show the plate wavenumber spectrum along axis κ_x and κ_y respectively corresponding to the cases of Figures 61 and 62. From Figure 63(a), the primary field reveals a maximum between $2\pi/L_x$ and $3\pi/L_x$ near the $\kappa_p = 23.29 \text{ m}^{-1}$, for this off-resonance excitation of $f=272 \text{ Hz}$, and the spectra become smooth for supersonic waves. The acoustic wavenumber ($\kappa = 4.98\text{m}^{-1}$) is also marked as a dash line in Figures 63(a) and 63(b). As discussed previously, above this line the wavenumber components recognized as subsonic waves do not contribute to the sound radiation; however, supersonic waves, i.e., wavenumber components below the acoustic wavenumber, do radiate to the far-field. In the case of using pressure sensors, the supersonic components have been reduced while the subsonic components were increased. This results in a small amount of radiated power reduction as shown in Table 15, and the phenomenon is termed "modal restructuring", i.e., the plate vibration pattern become close to the (3,1) mode, as seen in Figure 62. In other words, the significant radiation modes have been changed to less efficient mode radiators due to the change of plate vibration pattern, and this change, thus, leads to a reduction or radiated power. In particular, the wavenumber spectrum equals to zero at $\kappa_x = \kappa_y = 0$, with the discrete pressure sensor located at (1.8m, 0° , 0°). This can be explained from Equations (3.97), (3.98) and (3.99), as discussed previously. When the pressure is minimized in the far-field at a particular angle, the corresponding wavenumber component to that angle is suppressed. In the case of using

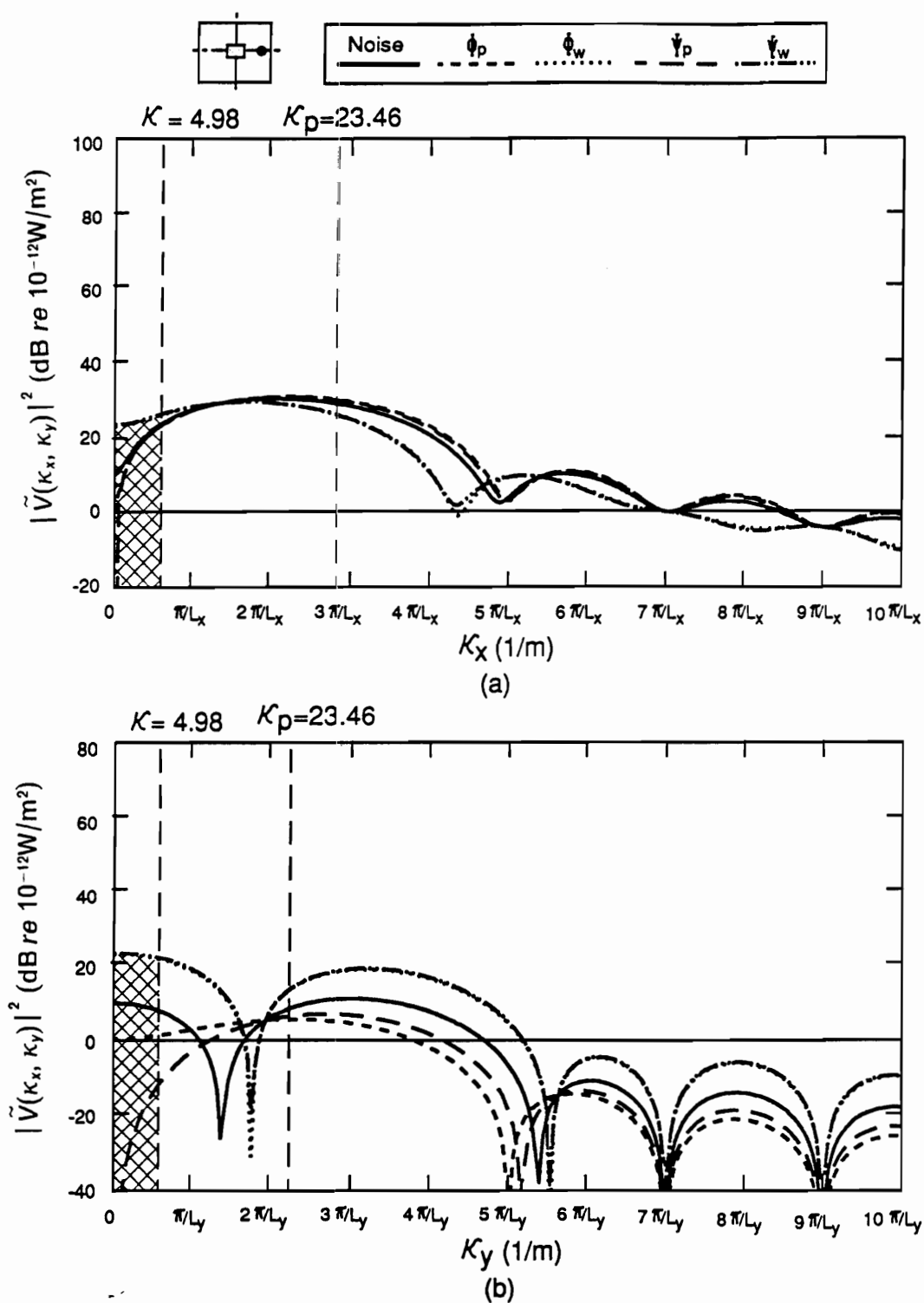


Figure 63. Wavenumber spectra of plate modal velocity along κ_x and κ_y axis, for off-resonance excitation, $f = 272$ Hz

acceleration sensors, the subsonic components have been reduced while the supersonic components were increased. The increase at $\kappa_x = \kappa_y = 0$ especially indicates spillover of control energy into the (1,1) mode. This explains why the residual radiation directivity reveals a monopole response in the case of using acceleration sensors as shown in Figure 61. Figure 63(b) shows the similar plot along the κ_y axis. The disturbance denoted by a solid line reveals a $n=1$ dominant mode pattern, i.e., the (3,1) mode. Again, the analysis of wavenumber spectra also demonstrates that pressure sensors perform better than acceleration sensors. In effect, the distributed far-field pressure sensor acts as distributed structural-wavenumber sensor. They observe every radiating point on the plate and also every supersonic wavenumber component while not observing the subsonic components.

3.5.4.4 Radiated Power and Average Radiation Efficiency

Figure 64 shows the radiated power for the disturbance with and without control plotted against the excitation frequency for different forms of cost functions corresponding to the previous case. The solid line denotes the disturbance and reveals several peaks, such as at 87, 190, 357, 520 and 620 Hz, which are near the natural frequencies of the simply-supported plate. In the case of using pressure sensors, both discrete and distributed sensors have about the same residual radiated power, and a large amount of power reduction is achieved below 180 Hz near the (2,1) mode. For higher frequency excitation, since more high modal responses contribute to the sound radiation, only a slight reduction can be achieved for using just one actuator. Additionally, there is no improvement at excitation of the even modes, such as the (2,1), (2,2), (4,1) and (4,2) modes, because of the central location of the piezoelectric actuator. Of course, atten-

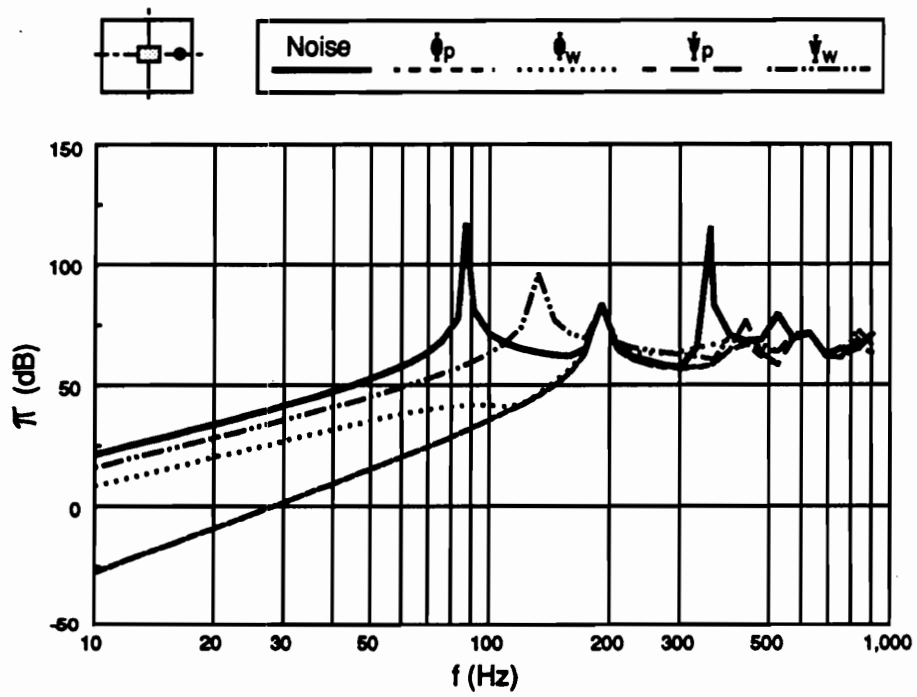


Figure 64. Radiated power versus excitation frequency

uation could be achieved with multiple, appropriately located actuators as shown Section 3.5.1.

In the case of using acceleration sensors, the radiated power has been attenuated at low frequency range, but the reduction is not as much as that using pressure sensors. The distributed acceleration sensor, located over the plate, generally performs better than the discrete acceleration sensor, located at the center of the plate. For the discrete acceleration sensor, the radiated power increases between 105 and 190 Hz, i.e., between the (1,1) and (2,1) modes, while the radiated power decreases for other selection of sensors. This is because the accelerometer cannot effectively observe the plate response at the central location in this range of excitation frequency, where the (2,1) mode dominates the plate response. The residual radiated power in the case of using distributed acceleration sensors is close to that of using pressure sensors between 110 and 190 Hz, but is higher at frequencies below 110 Hz. This can be explained by the observation that controlling the (1,1) plate modal response is not effective in the reduction of sound radiation within this range. However, controlling the (2,1) plate modal response is effective since the (2,1) mode is the dominant radiator to radiated field in this frequency band.

Figure 65 shows the average radiation efficiency plotted against the excitation frequency corresponding to the cases of Figure 64 with and without control. The average radiation efficiency generally agrees with the radiated power because of the coupling relations as shown in Equation (3.112). The disturbance denoted by a solid line reveals no peaks, unlike what was observed in Figure 64 for radiated power. In the case of using pressure sensors, average radiation efficiency generally decreases, except where the control is not achievable, such as 190 and 280 Hz. In the case of using acceleration sensors, the average radiation efficiency increases over some frequency range where the overall

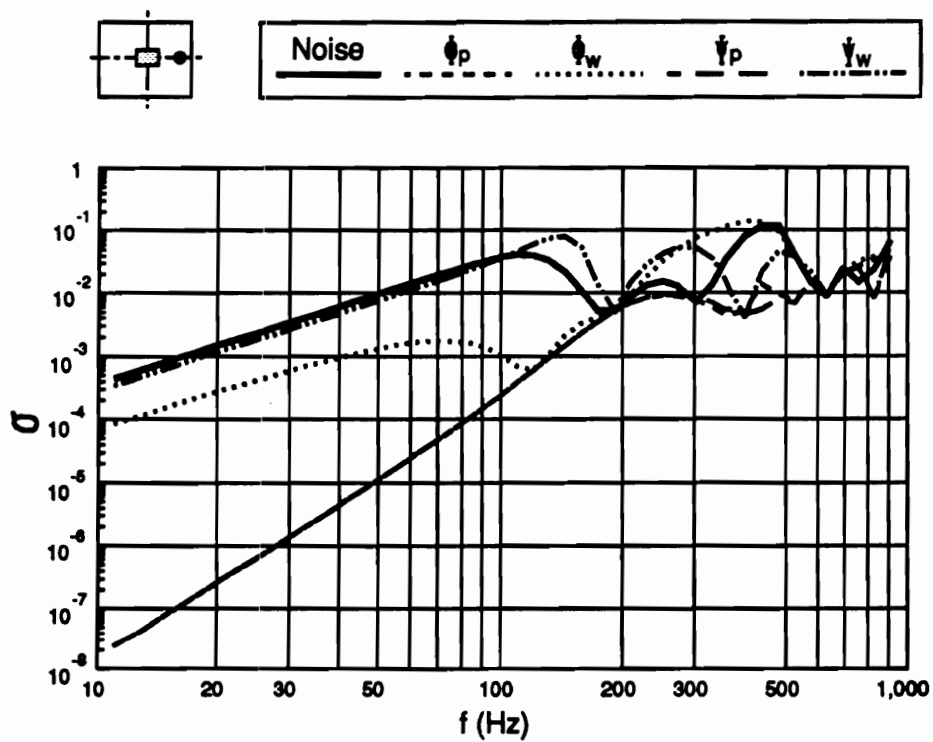


Figure 65. Average radiation efficiency versus excitation frequency

acoustic coupling was intensified. For example, the average radiation efficiency for disturbance with control using acceleration sensors is increased at $f = 272$ Hz; In other words, control spillover occurs in the radiated pressure field.

3.5.4.5 Summary

This section evaluates the control effectiveness and control mechanism for different forms of cost functions used in the feedforward quadratic optimal control approach applied to ASAC. The cost functions are constructed based on the use of either distributed or discrete pressure and acceleration sensors, with one piezoelectric actuator as the control input. Numerical examples illustrate the role of modal radiation efficiency which is associated with the structural acoustic coupling properties of the plate and is independent of the nature of disturbance. For low wavenumber, the odd-odd modes generally have higher radiation efficiency than even-odd, odd-even or even-even modes. The average radiation efficiency, which is associated with the sum of all of modal contributions and is thus dependent on the nature of disturbance, represents acoustic coupling between sound radiation and the residual mechanical vibration. Wavenumber domain analysis is also discussed and shown to be a very powerful tool which provides an alternative view of ASAC.

Results also showed that distributed sensors which can reveal global system response generally perform better than discrete sensors which can only provide a few point responses; however, in practice, a finite number of discrete sensors can only be used. In term of the reduction of radiated power, pressure sensors are superior to acceleration sensors, because pressure sensors inherently supply the structural acoustic coupling information while acceleration sensors can only provide the mechanical vibration infor-

mation. The proposed control strategy can be applied to obtain the optimal location of actuators and sensors and to design near-field pressure sensors with the effect of minimizing the far-field pressure.

3.6 Summary

This chapter presents the theoretical analysis of active control of sound radiation from a vibrating plate with the use of multiple distributed actuators (i.e., piezoceramic patches) and pressure or acceleration sensors. The cost function was constructed based upon the adoption of a feedforward control approach. Linear quadratic optimal control theory is then employed to obtain the optimal control voltages applied to actuators so as to minimize the cost function which is linear quadratic in nature. Some important results are summarized as follow:

1. Multiple piezoelectric actuators generally have better sound radiation control characteristics than single actuator due to reduced spillover. However, on resonance, high levels of attenuation, close to the practical limit of present control systems, can be generally obtained with a single actuator.
2. With proper choice of number and location of actuators, a large amount of sound attenuation can be achieved over a broad frequency range for low wavenumber excitation up to approximately $\kappa L_x = 5$.

3. The size of piezoelectric actuator does not significantly affect sound attenuation; however, the input optimal voltages are strongly dependent on the size of the piezoelectric patch.
4. Point force actuators perform slightly better than piezoelectric actuators; however, piezoelectric actuators possess a number of practical advantages, such as lightweight, low cost and compactness, over point force transducers.
5. Applying control can lead to an overall fall in the magnitudes of near-field pressure and intensity vectors and lead to a residual higher order radiation behavior similar to anti-symmetric modes. The observation indicates that a sheet or a strip of distributed pressure sensor over the plate surface could be used as an effective error sensor in order to reduce far-field pressure.
6. Plate wavenumber domain analysis demonstrates the influence of radiation characteristics. An overall drop in wavenumber components corresponds to "modal suppression", while a drop in supersonic wavenumber components and an increase in subsonic correspond to "modal restructuring". Modal suppression means that the plate vibration levels have been overall attenuated. And, modal restructuring indicates that the plate vibration pattern has been changed to a less efficient mode radiator, even though the plate displacement has not been reduced but may have been increased.
7. Distributed sensors perform generally better than discrete sensors, and pressure sensors have considerable advantages over acceleration sensors in sound radiation control. Therefore, under the consideration of performance and practical use, a near-field distributed pressure sensor is desired.

Chapter 4 : Optimal Placement of Piezoelectric Actuators for Controlling Sound Radiation from Plates

Piezoelectric actuators have been widely used in structural sound and vibration control. Chapter 3 has presented the theoretical analysis of the mechanics of piezoelectric actuators, and demonstrated their potential as transducers in structural sound control. However, the proper selection of number and location of piezoelectric actuators is critical to efficiently control structural sound radiation. Therefore, the determination of the optimal placement and number of piezoelectric actuators in sound radiation control is an important and interesting issue.

Previous works, however, on optimal placement of actuators are mostly concerned with vibration control and particularly for feedback control system with the use of traditional force transducers, such as point force shakers, (Norris and Skelton, 1989; Chang and Soong, 1980; Hamidi and Juang, 1981; Juang and Rodriguez, 1979). For state feedback control, a state space equation is first constructed to represent the system

model, and a performance index, which is a quadratic form in the state and control effort, can then be defined. Finally, the optimal location is to be determined by minimizing the performance index. Only a few literatures deal with the optimal location of distributed actuators, which are widely used in conjunction with so called "smart" structures. Jia (1990) studied the optimal position of piezoelectric actuators for beam vibration control by adopting independent modal space control approach (IMSC). Jia showed that the optimal location and size of piezoelectric actuators can be found by minimizing the objective function which can be either the structural response, control effort, residual response, spillover effect or combinations of all/any of these variables. However, Jia's work is limited to consider only one-dimensional vibration control.

Adaptive feedforward control, on the other hand, has been adopted for structural sound radiation control in recent years (Gibbs and Fuller, 1990; Burdisso and Fuller, 1990; Simpson et al., 1989). The control algorithm is flexible, because it is not as crucial as feedback approaches to accurately model the system response. The adaptive feedforward controller can learn the system parameters by itself and converge to the optimal solution using various "training" approaches. However, little work has been discussed on the optimal placement of actuators, particularly distributed in nature, for feedforward control. This chapter is thus concerned with the formulation of the optimization problem for the placement of piezoelectric actuators in feedforward control systems, in particular for the ASAC.

In this chapter, a general formulation for the optimal placement of piezoelectric actuators in a feedforward control approach is first presented and then applied to a typical sound radiation control system using piezoelectric actuators and microphone sensors. A baffled, simply-supported, rectangular plate is considered as an idealized

system. The plate is harmonically excited by a primary source (point force), and piezoelectric actuators are applied to control the plate vibration in order to reduce the associated sound radiation. The objective here is to determine the optimal location of piezoelectric actuators such that the sound pressure measured from the error microphones can be most efficiently reduced (i.e., with lowest actuator power and/or number of actuators). A solution strategy is proposed to calculate the applied voltages to piezoelectric actuators with the use of linear quadratic optimal control theory, as discussed in Section 3.3.3. The location of the piezoelectric actuator(s) is then determined by minimizing the objective function, which is defined as the sum of the mean square sound pressure measured by a number of error microphones. The optimal locations for multiple piezoelectric actuators, up to three, were considered. The results show that the optimally placed actuators achieve a far better reduction of sound radiation than actuators whose positions are arbitrarily chosen.

4.1 Mathematical Formulation for Optimization Problem

4.1.1 Design Variable

As shown in Figure 66, the optimal placement of the i -th piezoelectric actuator located inside the boundaries of the plate can contain five variables, $\bar{x}_i, \bar{y}_i, C_{x_i}, C_{y_i}$ and V_i . The variables C_{x_i} and C_{y_i} denote the size of the i -th piezoelectric actuator, while \bar{x}_i and \bar{y}_i denote the central location of the actuator, and V_i is the applied voltage to the

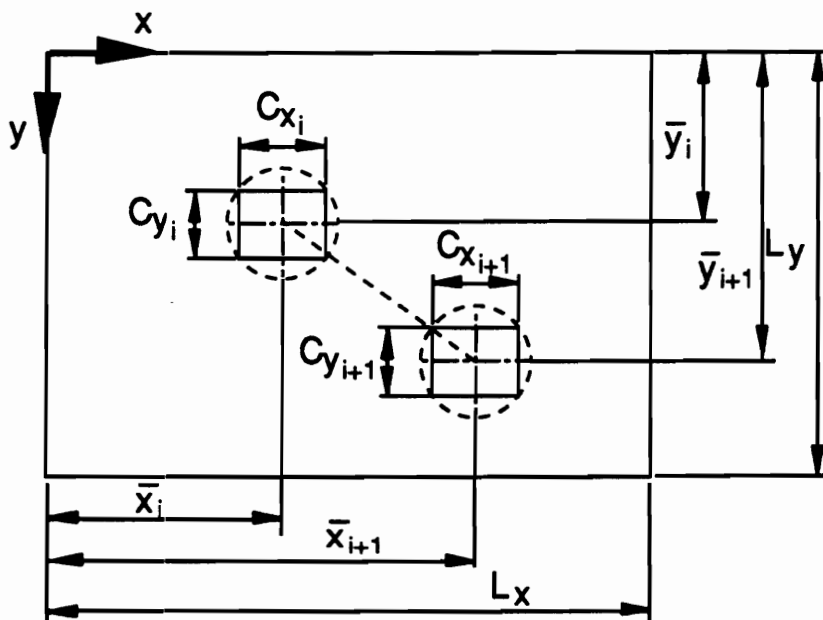


Figure 66. Illustration of design variables

piezoelectric actuator. If the primary source is known, and piezoelectric actuators are used as control sources, then the total radiated sound pressure can be shown as follow:

$$p_t = p_t(\bar{x}_i, \bar{y}_i, C_{x_i}, C_{y_i}, V_i) \quad i = 1, \dots, N_c \quad (4.1)$$

As discussed in Chapter 3, V_i can be calculated from the linear quadratic optimal control theory (LQOCT). The total radiated sound pressure can then be written as follow:

$$p_t = p_t(\bar{x}_i, \bar{y}_i, C_{x_i}, C_{y_i}, V_i(\bar{x}_i, \bar{y}_i, C_{x_i}, C_{y_i})) \quad i = 1, \dots, N_c \quad (4.2)$$

However, if the size of piezoelectric actuators was first fixed, then the total radiated sound pressure become

$$p_t = p_t(\bar{x}_i, \bar{y}_i, V_i(\bar{x}_i, \bar{y}_i)) \quad i = 1, \dots, N_c \quad (4.3)$$

The design variables, $\bar{x}_i, \bar{y}_i, C_{x_i}, C_{y_i}$ and V_i , can be properly selected based upon the concern of the size, location or both of the piezoelectric actuator and the control effort (i.e., the voltages or power required for piezoelectric actuators).

4.1.2 Objective Function

There are various choices for the objective function. Wang, Dimitriadis and Fuller (1990) chose the integral of the square of radiated sound pressure over a hemisphere of the radiating field, (i.e., Φ_p , as shown in Equation (3.23), is proportional to the radiated power) as the cost function. However, such a cost function, in practice, is not useful. Wang and Fuller (1991c) constructed a cost function which is the sum of the mean square radiated sound pressures measured by a limited number of microphones, i.e., Ψ_p ,

as shown in Equation (3.42). The consideration of the above two types of objective functions is particular of interest in sound radiation control. Since the sound radiation is strongly coupled with the structural vibration, the objective function may also be chosen as the sum of the mean square plate acceleration measured by a limited number of accelerometers or the integral of the square of plate acceleration over the vibrating surface. The possible candidates of the objective function used in sound radiation control have been discussed in Section 3.3 and recalled as follows:

(1) Distributed pressure sensors

$$\Phi_p = \frac{1}{R^2} \int_s |p_t|^2 ds = \int_0^{2\pi} \int_0^{\frac{\pi}{2}} |p_t|^2 \sin \theta d\theta d\phi \quad (4.4)$$

(2) Discrete pressure sensors

$$\Psi_p = \sum_{i=1}^{N_{mike}} |p_{t_i}(R_i, \theta_i, \phi_i)|^2 \quad (4.5)$$

(3) Distributed accelerometer sensors

$$\Phi_w = \int_A |\ddot{w}_t|^2 dA = \int_0^{L_y} \int_0^{L_x} |\ddot{w}_t|^2 dx dy \quad (4.6)$$

(4) Discrete accelerometer sensors

$$\Psi_w = \sum_{i=1}^{N_{acc}} |\ddot{w}_t(x_i, y_i)|^2 \quad (4.7)$$

It is noted that Φ_p and Φ_w are measured by ideal distributed sensors, which may not be practical in reality; however, Φ_p and Φ_w represent the power of sound radiation or energy density of out-of-plane structural vibration. They can be used as an index of control effectiveness. For practical applications, Ψ_p and Ψ_w are the alternative options. A reasonable number and location of sensors shall be selected to reflect the actual system response, such that an optimal solution can be found without losing the global nature of the problem. In effect, the discrete sensors should approach a form of numerical integration of the objective function associated with the distributed sensors to be truly global.

4.1.3 Design Constraint

The design constraints have to be specified to confine the design variables within a reasonable range. The design constraints are necessary for providing a reasonable result by maintaining the rectangular shape of piezoelectric actuators, locating actuators inside the plate boundaries, avoiding overlapping between actuators, and operating actuators within the working voltage range. It is noted that the constraint set (iii) for avoiding overlapping is conceptually sketched in Figure 66. For the rectangular-shaped piezoelectric actuators as shown in Figure 66, the constraint sets are listed as follows:

(i) To maintain the piezoelectric actuator a rectangular shape:

$$\begin{aligned} 0 < C_{x_i} &\leq L_x/2 \\ 0 < C_{y_i} &\leq L_y/2 \end{aligned} \tag{4.8}$$

(ii) To maintain the piezoelectric actuator inside of the plate:

$$\begin{aligned}
\bar{x}_i - C_{x_i}/2 &\geq 0 \\
\bar{x}_i + C_{x_i}/2 &\leq L_x \\
\bar{y}_i - C_{y_i}/2 &\geq 0 \\
\bar{y}_i + C_{y_i}/2 &\leq L_y
\end{aligned}
\tag{4.9}$$

(iii) To avoid overlapping between piezoelectric actuators:

$$\begin{aligned}
\bar{x}_{i+1} - \bar{x}_i &> 0 \\
\bar{y}_{i+1} - \bar{y}_i &> 0 \\
\left[(\bar{x}_{i+1} - \bar{x}_i)^2 + (\bar{y}_{i+1} - \bar{y}_i)^2 \right]^{1/2} - \frac{1}{2} \left[(C_{x_i}^2 + C_{y_i}^2)^{1/2} + (C_{x_{i+1}}^2 + C_{y_{i+1}}^2)^{1/2} \right] &> 0
\end{aligned}
\tag{4.10}$$

(iv) To specify the working range of piezoelectric actuators:

$$|V_i| \leq 150(\text{volt p-p}) \tag{4.11}$$

Note that the control power to the actuators is not an optimization variable. However, constraint (iv) ensures that the piezoelectric actuator is within a working range.

4.2 Application to Optimal Placement of Piezoelectric

Actuators

For a simple application of the previous theoretical formulation to sound radiation control, the size of piezoelectric actuators is assumed fixed, i.e., $C_{x_i} = C_{y_i} = \text{constant}$. The applied voltage to the i -th piezoelectric actuator, V_i , can be calculated from

LQOCT, as discussed in Chapter 3. Only the optimal location of piezoelectric actuators, \bar{x}_i and \bar{y}_i , will be determined. The objective function is chosen as the sum of the mean square sound pressure measured by a number of microphones in the far-field. Therefore, the optimization problem can be written as:

$$\text{Objective function : } \Psi_p = \Psi_p(\bar{x}_i, \bar{y}_i, V_i(\bar{x}_i, \bar{y}_i)) = \sum_{j=1}^{N_{mike}} |p_{t_j}(R_i, \theta_i, \phi_i)|^2 \quad i = 1, \dots, N_c \quad (4.12)$$

$$\text{design variables : } (\bar{x}_i, \bar{y}_i) \quad i = 1, \dots, N_c \quad (4.13)$$

$$\text{design constraints : constraint set (ii), (iii) and (iv)} \quad (4.14)$$

The design variables are to be determined by minimizing the objective function subjected to a set of design constraints. Now, a suitable optimization algorithm must be adopted to solve the optimal solution.

4.3 Optimization Algorithm

An IMSL subroutine named N0ONF (IMSL, 1989), for solving a general nonlinear programming problem using the successive quadratic programming algorithm and a finite difference gradient, was adopted to calculate the optimal solution. The optimization problem is stated as follows:

$$\min_{\mathbf{x} \in \mathcal{R}^n} f(\mathbf{x})$$

subject to $g_j(\mathbf{x}) = 0$, for $j = 1, \dots, m_e$

(4.15)

$$g_j(\mathbf{x}) > 0, \text{ for } j = m_e + 1, \dots, m$$

$$\mathbf{x}_l \leq \mathbf{x} \leq \mathbf{x}_u$$

where the objective function, f , and the constraint functions, $g_j(\mathbf{x})$, are assumed to be continuously differentiable. The suggested method is to obtain a sub-problem by using a quadratic approximation of the Lagrangian and by linearizing the constraints. The sub-problem is stated as:

$$\min_{\mathbf{x} \in \mathcal{R}^n} \frac{1}{2} \mathbf{d}^T \mathbf{B}_k \mathbf{d} + \nabla f(\mathbf{x}_k)^T \mathbf{d}$$

subject to $\nabla g_j(\mathbf{x}_k)^T \mathbf{d} + g_j(\mathbf{x}_k) = 0$, for $j = 1, \dots, m_e$

(4.16)

$$\nabla g_j(\mathbf{x}_k)^T \mathbf{d} + g_j(\mathbf{x}_k) \geq 0, \text{ for } j = m_e + 1, \dots, m$$

$$\mathbf{x}_l - \mathbf{x}_k \leq \mathbf{d} \leq \mathbf{x}_u - \mathbf{x}_k$$

where \mathbf{B}_k is a positive definite approximation of the Hessian, and \mathbf{x}_k is the current iterate.

Let \mathbf{d}_k be the solution of the sub-problem. A line search is used to find a new point

\mathbf{x}_{k+1}

$$\mathbf{x}_{k+1} = \mathbf{x}_k + \lambda \mathbf{d}_k, \quad 0 < \lambda < 1 \quad (4.17)$$

such that a merit function will have a lower value at the new point. Here the merit function is the augmented Lagrange function.

The algorithm requires a high accuracy arithmetic in estimating the gradient. The central finite difference method was applied to approximate the gradient by adopting the IMSL CDGRD subroutine (IMSL, 1989).

4.4 Solution Strategy

To solve the above optimization problem, a solution strategy was developed. The flow chart of solution strategy is shown in Figure 67. The procedure to solve the problem is first to set up the initial guess of the optimal central location of the i -th actuator, $(\bar{x}_i)_k, (\bar{y}_i)_k$, where k denote the number of iteration. The following steps are then proceeded:

1. utilize the linear quadratic optimal control theory to obtain the applied voltages, $(V_i)_k$, to actuators at the current location, $(\bar{x}_i)_k, (\bar{y}_i)_k$.
2. evaluate the objective function and constraints at the current location, $(\bar{x}_i)_k, (\bar{y}_i)_k$.
3. evaluate the gradients of the objective function and constraints at the current location, $(\bar{x}_i)_k, (\bar{y}_i)_k$.

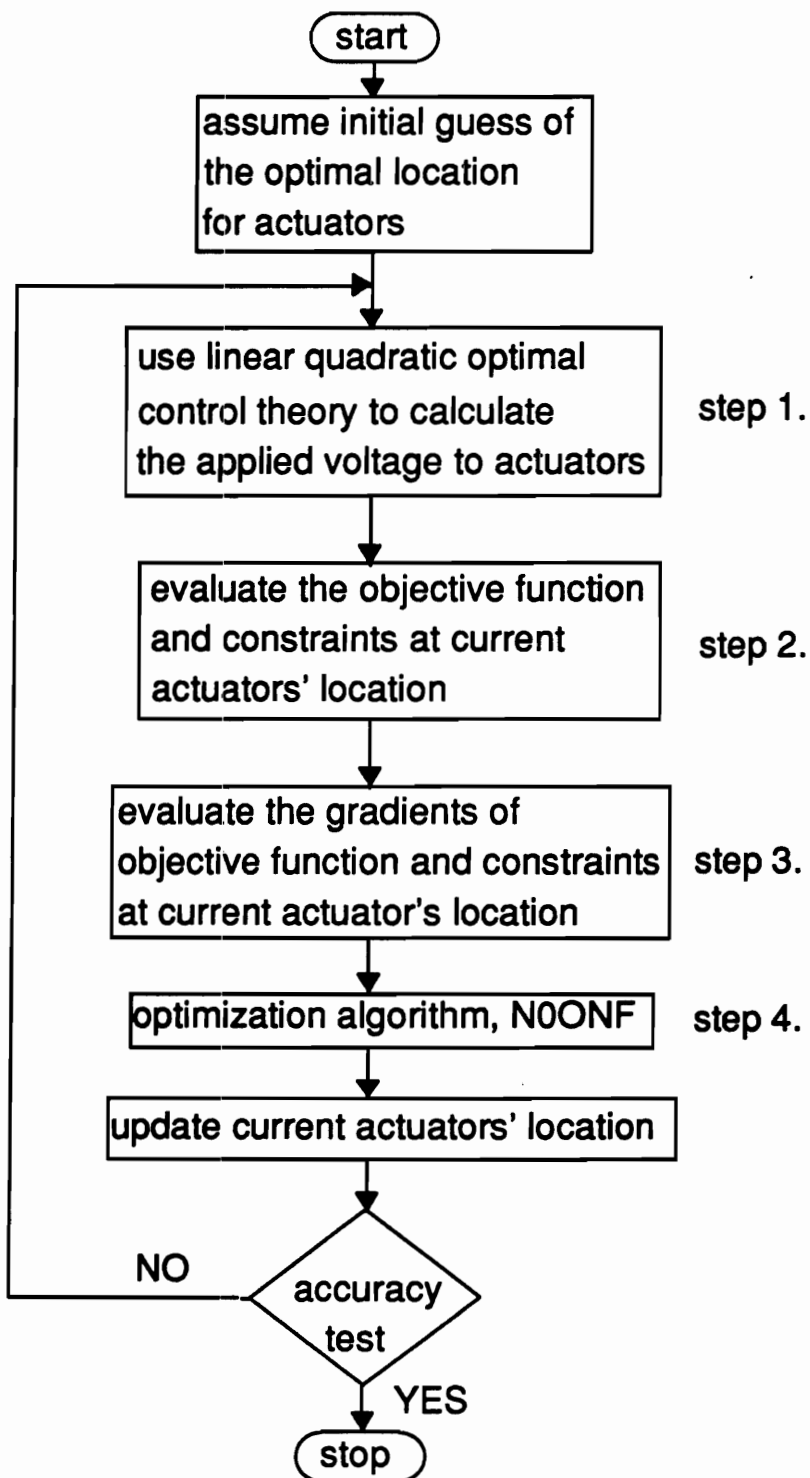


Figure 67. Flow chart of solution strategy

4. employ an optimization algorithm, N0ONF, to update the optimal location, $(\bar{x}_i)_{k+1}, (\bar{y}_i)_{k+1}$.
5. stop the procedure if the results pass the accuracy test; otherwise, update the current optimal location of actuators and repeat the above steps.

It is noted that the design variables, the central location of piezoelectric actuators (\bar{x}_i, \bar{y}_i) , was normalized by the plate length and width (L_x, L_y) respectively such that the design variables will be relocated between zero and one. This normalization process will benefit the solution process of the optimization problem.

4.4.1 LQOCT for Solving Applied Voltages to Actuators

Lester and Fuller (1990) presented an optimization algorithm to obtain the minimum for a linear quadratic function. Chapter 3 has shown the use of linear quadratic optimal control theory (LQOCT) to determine the applied voltages to minimize the selected objective function which is quadratic. Here, the LQOCT is adopted to solve the voltages independently. One of the advantages is that the optimal voltages can be always determined whenever the location of actuators is known. The other reason to evaluate the optimal voltage separately because the order of voltage and the central location of piezoelectric actuator is not consistent arithmetically, even after the normalization process. Hence, upon the consideration of numerical difficulty and the number of design variables, it is beneficial to obtain the optimal voltage using LQOCT separately from solving the optimization problem.

4.5 Analytical Results

Table 6 shows the physical properties of the simply-supported plate (except $h=2$ mm) used for the following simulations. The structural disturbance was assumed to be a point force with magnitude of $F_1 = 1$ N and located at $x_{f_1} = 0.08$ m, $y_{f_1} = 0.08$ m. Nine error microphone sensors, whose locations are tabulated and listed in Table 16 and shown in Figure 68, were used; therefore, the objective function defined in Equation (4.5), which is the sum of mean square measured pressure, can be constructed. The reason to choose this number of microphones is based on the consideration of computing time and a reasonable approximation to the continuous integral of pressure over the complete radiation hemisphere. Too few microphones will not reveal the actual system global radiation response. On the other hand, too many microphones will require too much computing effort to solve the optimization problem. The microphones located in the far-field are arranged five in a row across the central line of the plate in both the x- and y- directions, as shown in Table 16. The size of piezoelectric actuators is fixed, $C_{x_i} = 0.06$ m and $C_{y_i} = 0.04$ m. The location and applied voltages of piezoelectric actuators are to be determined.

4.5.1 Sub-Region Search Method

The determination of the optimal location of piezoelectric actuators is dependent on the excitation frequency. A different excitation frequency will lead to a different optimal location. For a particular frequency of excitation, all of the plate modes can be excited;

Table 16. Location of error microphones

the i-th microphone	(R, θ, ϕ)
1	$(1.8, 75^\circ, 180^\circ)$
2	$(1.8, 45^\circ, 180^\circ)$
3	$(1.8, 0^\circ, 0^\circ)$
4	$(1.8, 45^\circ, 0^\circ)$
5	$(1.8, 75^\circ, 0^\circ)$
6	$(1.8, 75^\circ, 90^\circ)$
7	$(1.8, 45^\circ, 90^\circ)$
8	$(1.8, 45^\circ, 270^\circ)$
9	$(1.8, 75^\circ, 270^\circ)$

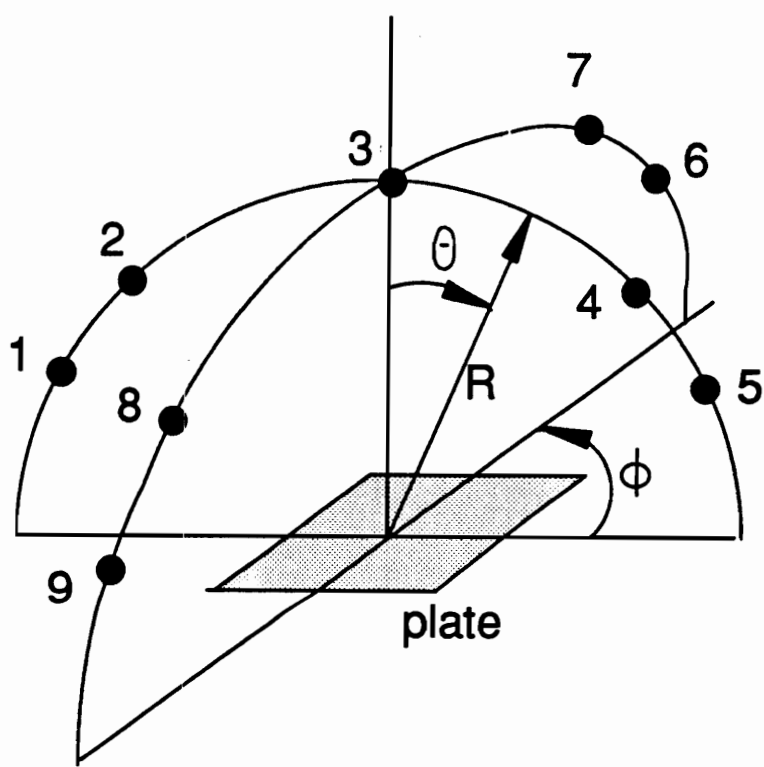


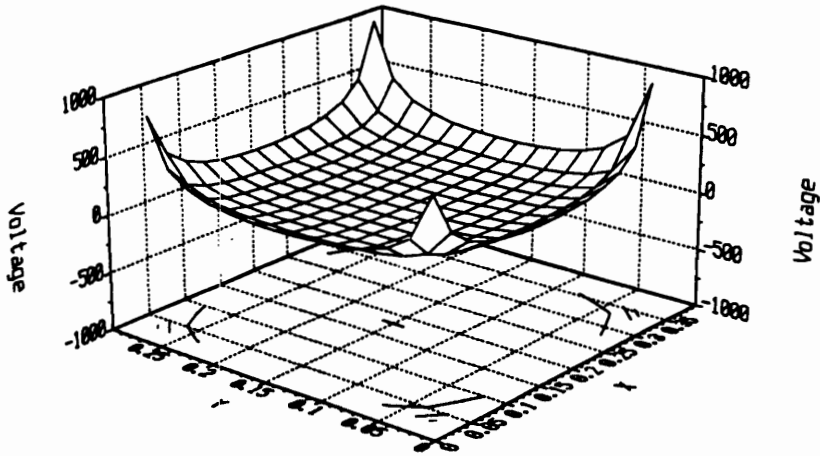
Figure 68. Location of error microphones

however, only the plate modes near the excitation frequency will contribute significantly to the plate response as well as the sound radiation. It is clear that if the plate was excited near the (1,1) mode, the plate response will be shown as a convex surface. Similar characteristic can be found for the objective function. If the plate was excited at 87 Hz near the (1,1) mode, and the central location of piezoelectric actuator was varied and moved around the plate, then the objective function and the applied voltage can be calculated from LQOCT (presented in Section 3.3.2) and plotted as shown in Figure 69. Because the objective function is shown as a convex surface, an optimal location of the piezoelectric actuator can be always found to guarantee the minimum of the objective function. It is also noted, from Figure 69, that high control voltages are required for the actuator located near the corner of the plate to achieve sound radiation control. The actuator having the minimum control effort is located at about the same position as the actuator having the minimum objective function.

Also shown in Figure 70, for an excitation frequency $f = 357$ Hz near the (3,1) mode, the objective function and the applied voltage reveal as a (3,1) mode shape. There are more than one minimum for the objective function; in fact, there is one local minimum at each division separated by nodal lines. This characteristic, related to the plate mode shapes, is similar to what has been seen in Figure 69. If the actuator is located near the nodal line of the plate mode, then sound radiation control is not effective, at least for on-resonance excitation, because of high control voltage and small control authority.

Figure 71 shows the similar plots as Figures 69 and 70 except that the excitation frequency, $f = 272$ Hz, is between the (2,1) and (3,1) modes. One can see that those distributions become complex and results from combination of several plate modal re-

Voltage Distribution
 $f = 87$ (Hz)



Objective Function Distribution
 $f = 87$ (Hz)

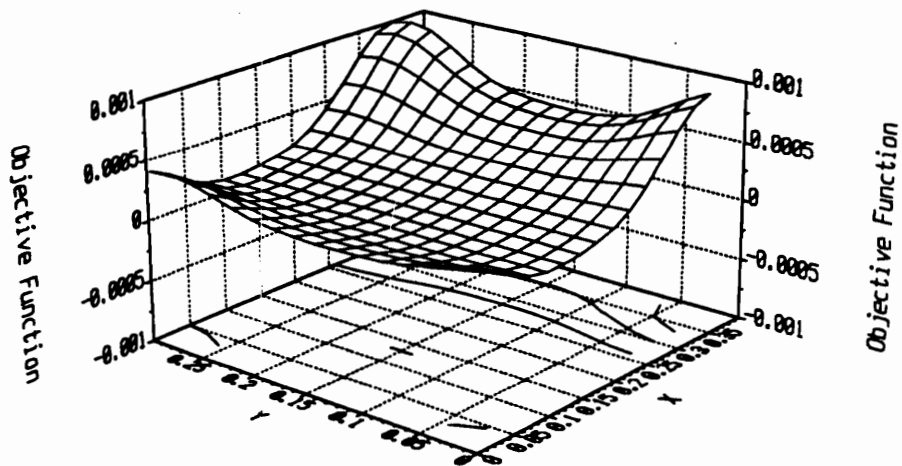


Figure 69. Distribution of objective function and control voltage for $f=87$ Hz

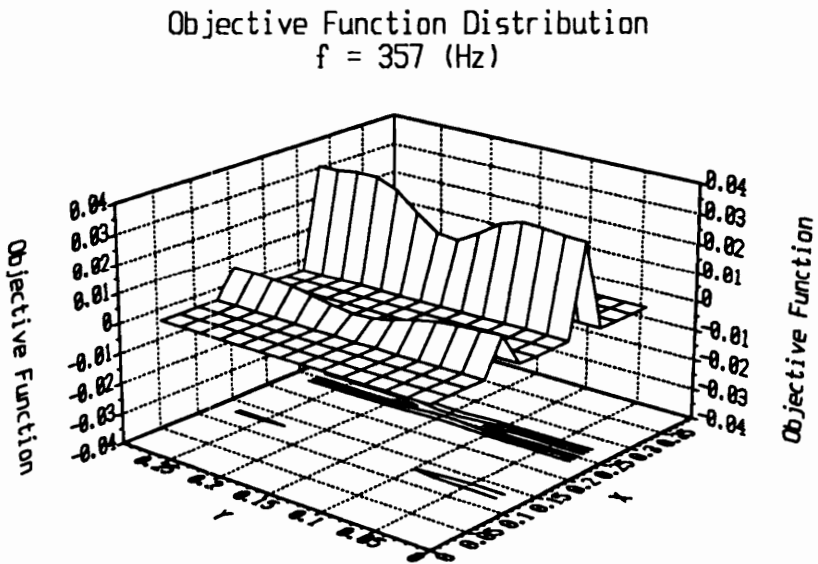
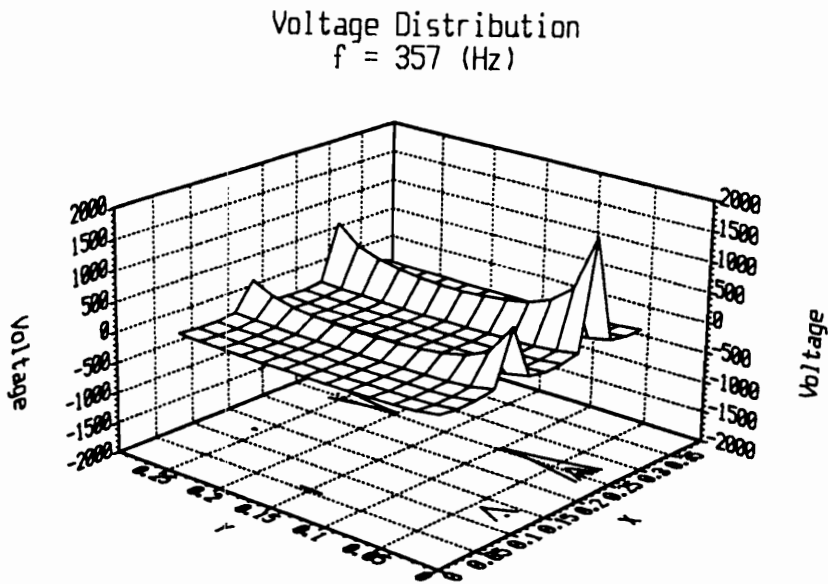
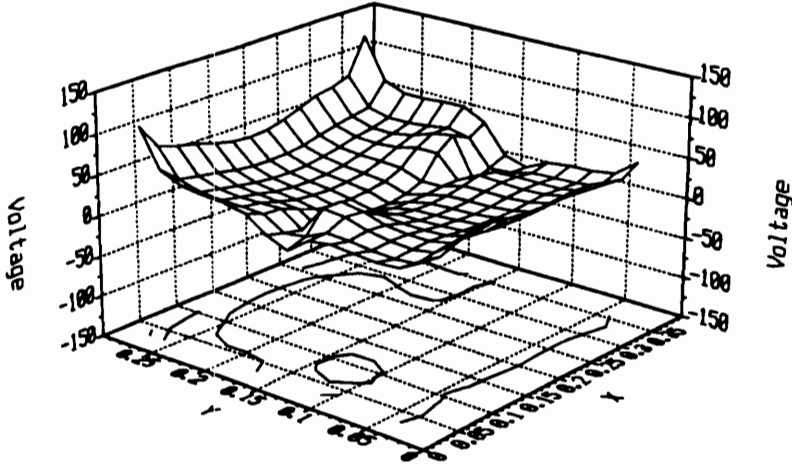


Figure 70. Distribution of objective function and control voltage for $f = 357 \text{ Hz}$

Voltage Distribution
 $f = 272$ (Hz)



Objective Function Distribution
 $f = 272$ (Hz)

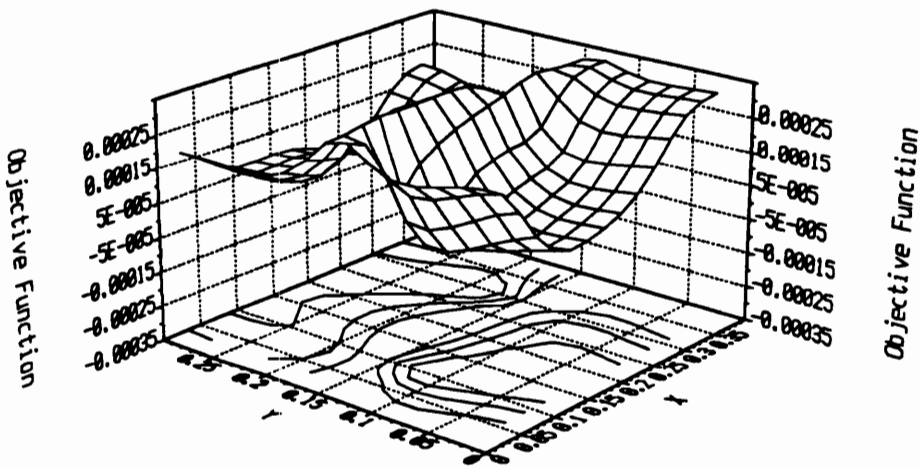


Figure 71. Distribution of objective function and control voltage for $f = 272$ Hz

sponses. Again, there are multiple minima; this makes the optimization procedure to find a global minimum difficult. However, according to the characteristics shown in Figures 69 and 70, a sub-region search method, which comes from the nature of the objective function distribution similar to that of the plate mode shapes, can be proposed. This search technique is to subdivide the plate into several cells based on the nodal lines of the plate mode shapes, which are set up to be the bound of the locations for the actuators. In other words, in addition to the design constraints illustrated previously, the upper and lower bounds of the locations for actuators can also be specified according to the nodal lines associated with the plate mode shapes.

4.5.2 Optimal Location of One Actuator for Different Excitation Frequencies

As discussed previously, the optimal location of piezoelectric actuators is dependent on the excitation frequency due to the variation of modal transfer function in frequencies. The optimal location of actuator has been of interest for many concerns. As discussed by Juang and Rodriguez (1979), to control a single mode of beam vibration, there are multiple optimal locations for one actuator in high-mode control. If several modes contribute to the response simultaneously, and only a few actuators are applied, then the optimal location will be much different from that for single mode control. The feedforward control approach adopted here is to minimize the objective function, which is the mean square of sound pressure measured by error microphones, and thus to control all of the modal contributions at the same time. Therefore, the optimal location and applied voltage of the actuator is solved under a compromise to eliminate the significant modal responses; however, this compromise will probably incur spillover to other higher

modes, which do not radiate efficiently to the error microphones, causing an increase in plate response.

When one piezoelectric actuator was considered, the normalized optimal central location of the piezoelectric actuator and the applied voltage to the actuator are tabulated in Table 17 as well as the reduction of the objective function, radiated power and pressure modal amplitude. Table 17 is shown for different excitation frequencies varying from 87 Hz to 357 Hz, i.e., between the (1,1) and (3,1) modes. The underlined values are for on-resonance excitation, such as 87 Hz near the (1,1) mode, 190 Hz near the (2,1) mode and 357 Hz near the (3,1) mode. One can see that the optimal central location of the actuator is located at about one third of the plate length and width, in the left-bottom quadrant of the plate, i.e., the same quadrant where the point force disturbance is located. As the excitation frequency increases, the optimal central location of the actuator moves in the direction toward the corner of the plate. This can be understood by the realization that when the excitation frequency increases, the contribution of higher modes becomes significant, and thus the optimal location of the actuator is placed where it can couple into all higher mode responses. In applying one actuator, for example $f = 87$ Hz near the resonance of the (1,1) mode, the actuator attempt to control all of the significant radiating mode responses, including the (1,1) and (2,1) modes, instead of just the (1,1) mode. Therefore, the optimal location is determined under a compromise to eliminate the significant modes; however, as one can see in Table 17, there is spillover to higher modes, such as (3,1), (4,1) and (5,1) modes. This result indicates that the optimal location of single actuator is to eliminate the significant modal response near the excitation frequency; however, this will result in spillover to higher modes, which ultimately limit the amount of attenuation.

Table 17. Results for one actuator with different excitation frequencies

On the other hand, when the excitation frequency increases, for example $f = 357$ Hz near the (3,1) mode excitation, the radiation from (3,1) mode is controlled as well as the (1,1) and (2,1) modes, but with less reduction. There is still spillover to the higher modes but less than at the lower frequency excitations. This can be explained that the (1,1) and (2,1) modes, having high radiation efficiency (see Figure 57), can contribute a larger amount of sound radiation to the far-field, even though the (3,1) mode is dominant on the plate due to the excitation frequency. Therefore, the optimal location is determined from a result of compromise to efficiently eliminate the most significant radiating modes, i.e., the (1,1), (2,1) and (3,1) modes in this case. However, this effort causes the spillover to higher modes, such as (4,1) and (5,1) modes, which have lower radiation efficiency (Wallace, 1972). It is also noted, from Table 17, that for on-resonance excitation, the reduction of radiated power is generally larger, and the control effort (voltage) is higher than those cases for off-resonance excitation. It is due to the fact that modes on resonance always contributes considerably more to the modal response and thus require more control effort.

4.5.3 Optimal Location of Multiple Actuators for Different Excitation Frequencies

4.5.3.1 On-Resonance Excitation, $f = 357$ Hz, Near (3,1) Resonant Mode

Table 18 shows the optimal central location and applied voltages of piezoelectric actuators as well as the reduction of objective function and radiated power for an excitation frequency of $f = 357$ Hz. As one can see, although the reduction of objective

Table 18. On-resonance excitation, $f = 357$ (Hz), near (3,1) mode

case	the i-th actuator	\bar{x}_i/L_x	optimal location \bar{y}_i/L_y	optimal voltage V_i (volt)	reduction of objective function, Ψ_p (dB)	reduction of radiated power, Φ_p (dB)
one actuator	(1)	0.25487305	0.34166509	53.346	148.75	78.26
two actuators	(1)	0.25117468	0.28520923	100.54	189.06	66.70
	(2)	0.55045424	0.61431935	27.977		
three actuators	(1)	0.24998040	0.28460496	56.654	192.78	66.56
	(2)	0.54191292	0.60523995	50.616		
	(3)	0.82236029	0.21986429	61.098		
three actuators (Lab)	(1)	0.167	0.5	24.111	61.60	60.28
	(2)	0.5	0.833	25.730		
	(3)	0.833	0.167	10.782		

function increases when more actuators are applied, the amount of attenuation of radiated power is not always increased. This means the optimization algorithm does work to find a better solution. However, the minimization of the objective function, which is the sum of mean square pressures measured by error microphones, will not guarantee the reduction of radiated power due to the spillover of sound pressure to other locations than the position of error microphones. In term of the attenuation of radiated power, to properly locate one actuator in controlling sound radiation is more effective than to use two or three actuators when a set of microphones are used as error sensors, as it reduces unnecessary spillover.

Figure 72 shows the radiation directivity pattern for the excitation frequency $f = 357$ Hz. The point force disturbance input and piezoelectric actuator patches are sketched to scale on the top of Figure 72. The disturbance response denoted by a solid line indicates a monopole like response, but is nonuniform, and evidently shows the existence of the (3,1) mode and a significant (1,1) modal contribution. The optimal location of one actuator is at the left-bottom quadrant of the plate similar to the primary source. The residual pressure field is shown to be a combination of the (3,1) and (1,1) modes, whose characteristic radiation shapes are shown in Figure 21, and have a global reduction.

For two-actuator control as shown on the top of Figure 72, the first optimally located actuator is somewhat near the optimal location for one-actuator control, and the second one is located at the up-right quadrant of the plate near the central line. As shown in Table 18, the reduction of objective function is increased, but the reduction of radiated power is decreased. A result such as this implies that more error microphones need to be used, due to spillover effects to unobserved radiation points. Never-

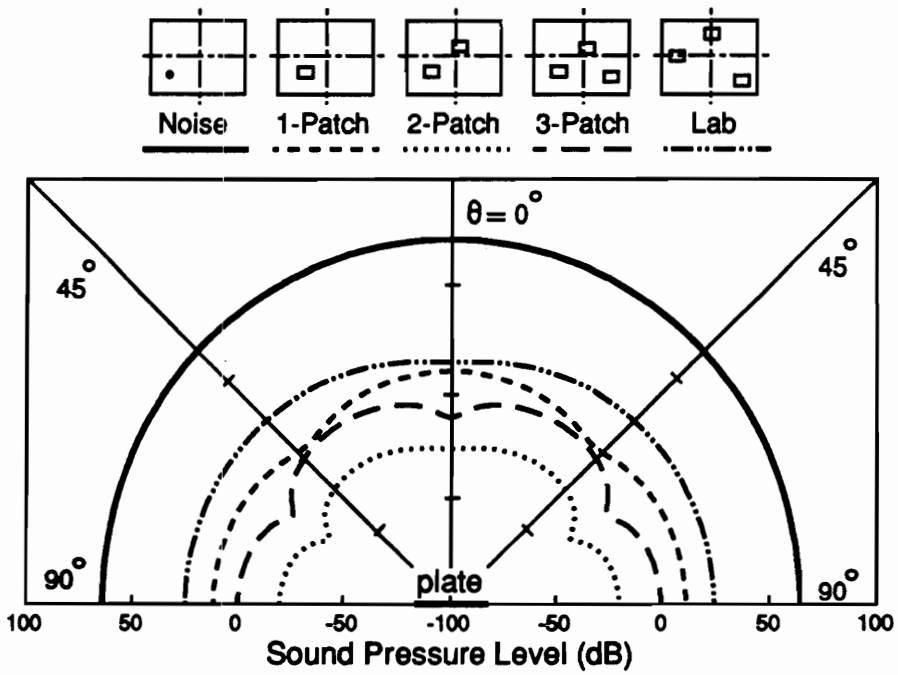


Figure 72. Radiation directivity pattern for $f = 357$ Hz

theless, the sound pressure level along the central line of the plate in both x- and y-direction is less than that using one actuator and exhibits a combination of the (4,1) and (1,1) modes. It can be seen that there are dips at $\theta = 0^\circ, 75^\circ$ for $\phi = 0^\circ$, and 75° for $\phi = 180^\circ$ where the error microphones are located. For three-actuator control, the optimal location of the first two actuators are close to those of two-actuator control, and the third one is located at the bottom-right quadrant of the plate. Again, the objective function has been further minimized. As shown in Figure 72 the dips at $\theta = 0^\circ, 75^\circ$ for $\phi = 0^\circ$ and 75° for $\phi = 180^\circ$ are enhanced, but the reduction of radiated power has not increased.

An interesting feature can be observed from the above results indicating that a one-by-one search method may be used to solve for the location of the successive actuator. The idea is first to find an optimal location for one-actuator control, and then to find a second optimal location for two-actuator control having the same location for the first actuator, and so on. With this searching technique, the computing time can be largely reduced, since it would cost less to optimize a reduced-parameter problem than a full-parameter problem. This method was tried; however, the results were not encouraging, since the selected objective function cannot be attenuated further due to numerical difficulty (even though double precision number was used in program), while an additional actuator was considered. The author believes that if the objective function is reconstructed as the radiated power rather than the mean square pressure, the one-by-one search method would be appropriate and can reduce significant computing effort for multiple actuator control. Also, it appears that each actuator is optimally configured for separate modes, since their locations stay the same. Hence, an independent optimization procedure for each mode and its associated radiation might be tried.

Also shown in Figure 72 is an arbitrary selection of multiple actuators located at one sixth of the plate length or width (denoted lab arrangement). This arrangement is assigned to control the low modal number excitation based upon the nature of the plate mode shapes and was used in companion experiments (Clark and Fuller, 1990b). The results show that optimally configured one-, two- or three-actuator control is superior to the arbitrarily chosen actuators for the on-resonance excitation in terms of both objective function and radiated power.

Figure 73 shows the plate displacement distribution corresponding to the cases of Figure 72. The solid line depicts the disturbance response and reveals that the (3,1) mode is dominant. With control, the plate displacement has been reduced globally and exhibits a more complex pattern, and the (3,1) mode has been attenuated considerably. Further comments on the behavior are as in previous section.

4.5.3.2 Off-Resonance Excitation, $f = 272$ Hz, Between (2,1) and (3,1) Resonant Modes

Table 19 shows the optimal central location and applied voltages of piezoelectric actuators as well as the reduction of objective function and radiated power for an excitation frequency $f = 272$ Hz between the (2,1) and (3,1) modes. The control effort (i.e., the control voltages) is not necessary smaller than that for on-resonance excitation, unlike the previous observation for one-actuator control. In fact, either one of the actuators may require extremely high control voltages; however, others may simultaneously need only a small voltage. The optimal location and required control voltages for multiple actuators are determined in a way not only to suppress the disturbance response but also to reduce the interactive spillover effects due to actuators themselves.

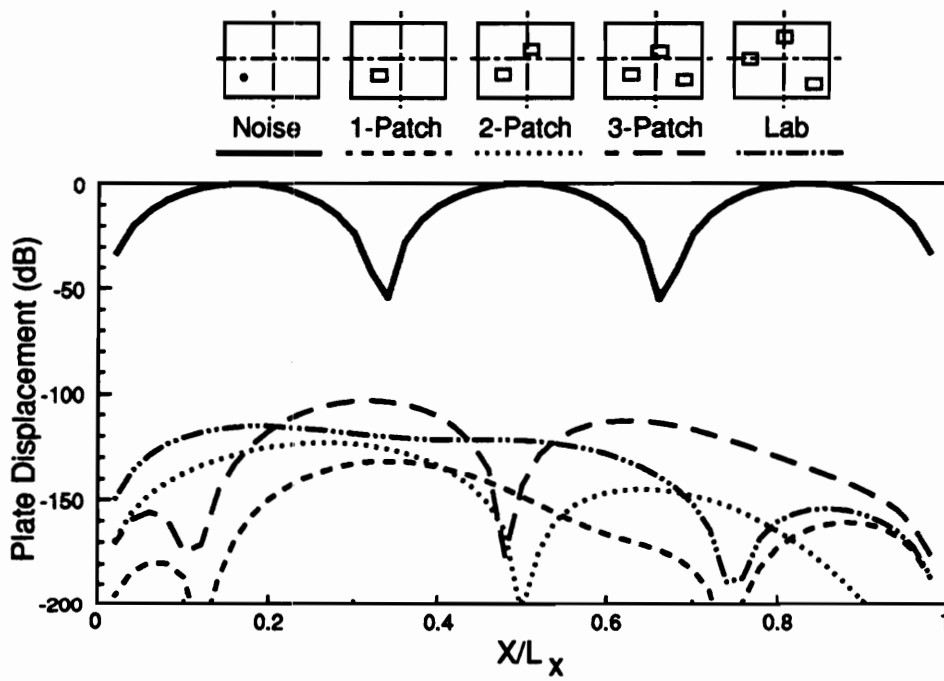


Figure 73. Plate displacement distribution for $f = 357$ Hz

Table 19. Off-resonance excitation, $f = 272$ (Hz), between (2,1) and (3,1) modes

case	the i-th actuator	\bar{x}_i/L_x	optimal location \bar{y}_i/L_y	optimal voltage V_i (volt)	reduction of objective function, Ψ_p (dB)	reduction of radiated power, Φ_p (dB)
one actuator	(1)	0.29457708	0.35335895	59.687	104.73	34.66
two actuators	(1)	0.25544169	0.29783527	100.56	144.38	21.77
	(2)	0.60311850	0.68038840	33.174		
three actuators	(1)	0.23874597	0.27626540	94.250	165.90	24.55
	(2)	0.50366424	0.63539936	32.148		
	(3)	0.77011748	0.40446361	6.7039		
three actuators (Lab)	(1)	0.167	0.5	39.814	25.43	19.95
	(2)	0.5	0.833	98.242		
	(3)	0.833	0.167	122.64		

Figures 74 and 75 show the radiation directivity pattern and the plate displacement distribution respectively corresponding to the case in Table 19 for the off-resonance excitation. The optimal location of piezoelectric actuators, sketched on the top of Figure 74, are very similar to that of the on-resonance excitation. From Figure 74, the primary radiated sound denoted by a solid line shows a small dip at $\theta = 0^\circ$ indicating the strong response of the (2,1) mode. In applying one actuator, the residual response shows a combination of the (3,1) and (1,1) modes, and there are no dips at any location of the error microphones. In applying two and three actuators, the residual response reveals a more complex pattern similar to the (4,1) and (5,1) modes respectively. Dips can now be seen located at the error microphone locations. It is again shown that increased actuators can further attenuate the pressures at error microphone position; however, the overall radiated power is not necessarily reduced, because of spillovers in sound pressure into other locations than the position of the error microphones.

The plate displacement distribution for the case of disturbance, as shown in Figure 75, exhibits the (2,1) mode characteristic shape. With control, the residual plate response reveals a more complex pattern and is not attenuated globally as what was seen in Figure 75 for resonance excitation. This phenomenon is referred to as "modal restructuring" for the off-resonance excitation and "modal suppression" for the on-resonance excitation (Fuller, Hansen and Snyder, 1990c).

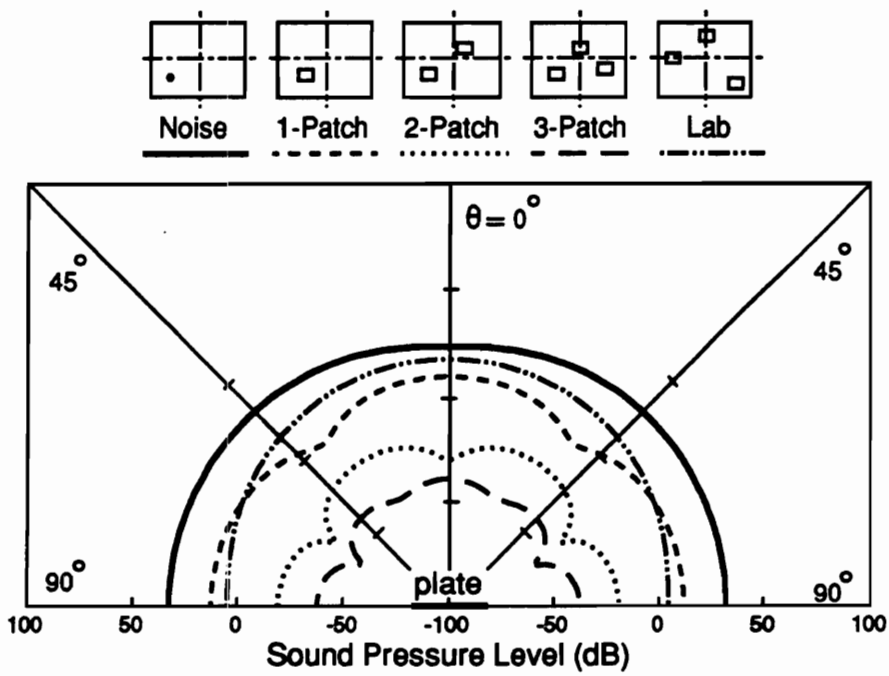


Figure 74. Radiation directivity pattern for $f = 272$ Hz

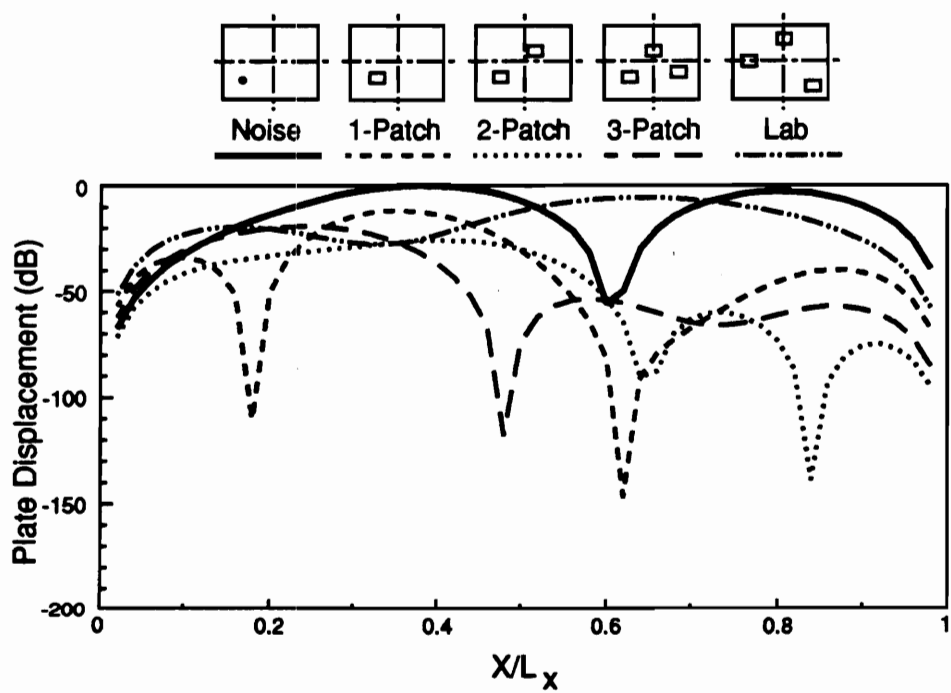


Figure 75. Plate displacement distribution for $f = 272$ Hz

4.6 Computing Time Analysis

In an optimization procedure, to find the gradient of objective function is generally the most difficult and the most CPU time consuming task. Table 20 shows the percentage of CPU time consumed for each step in the optimization procedure. It takes about 20% of CPU time for steps 1 and 2, i.e., the evaluation of objective function and the applied voltages to actuators, and over 70% (up to 90% for three actuators) of CPU time for step 3, i.e., the evaluation of the gradients of the objective function and constraints in the optimization procedure. However, it takes only a small percentage of time for step 4 in calculating the update actuator's location in the optimization subroutine. In order to efficiently solve the optimization problem, it is necessary to do a sensitivity analysis. For future work, it could be beneficial to apply an analytical or semi-analytical method rather than finite difference method to evaluate the gradients so that CPU time can be reduced for solving the optimization problem. Furthermore, the acoustic radiated power could also be considered as objective function to solve the optimal location of piezoelectric actuators.

4.7 Summary

This chapter has presented the mathematical formulation for the optimization problem of the placement of piezoelectric actuators in a feedforward control implementation of ASAC. The analysis is applied to an example problem to obtain preliminary

Table 20. Typical example of CPU time for optimization

case	number of iteration	CPU time (sec)	percentage of main program (%)				percentage of optimization program (%)			
			step 1,2	step 3	step 4	step 1,2	step 3	step 4		
one actuator	7	181	10.215	28.457	0.00401	26.411	73.575	0.01035		
two actuators	27	2787	17.519	65.252	0.00273	21.165	78.830	0.00329		
three actuators	7	2285	4.789	57.242	0.00131	7.721	92.276	0.00218		

information on how the optimization procedure performs. Four different forms of objective functions, which are differentiated by discrete or distributed and by vibrational or pressure sensor, are discussed for sound radiation control. An objective function, which is constructed based on the use of a number of discrete pressure sensors, is applied to the example of sound radiation control. Some significant observations may be summarized as follows:

- Different excitation frequencies will result in different optimal locations of piezoelectric actuators.
- The optimally located piezoelectric actuators can provide a large amount of reduction of sound radiated power and are seen to perform better than arbitrarily chosen locations.
- To properly locate one piezoelectric actuator generally gives higher reduction of radiated acoustic power than to use two or three actuators for the selected objective function which is the sum of mean square sound pressure measured by a limited number of microphones. This is due to control spillover resulting from driving down the error signals at all error microphones. An alternative would be to limit the attainable attenuation achieved at each error microphone or use the total radiated power as the objective function.
- A computing time analysis shows that the evaluation of the gradients of the objective function and constraints consumes most of the CPU time. Sensitivity analysis, which can be used to analytically or semi-analytically evaluate the gradients, is required for future research.

- This work, which lays out the theory for optimal location of piezoelectric actuators, will be the basis for design of "smart" structures for ASAC with distributed actuators and sensors.

Chapter 5 : Overall Conclusions and Recommendations

5.1 Overall Conclusions

This thesis consists of three main categories: (1) the development of a mechanics model for spatially distributed actuators embedded or attached to laminate beams or plates (Chapter 2), (2) the use of multiple piezoelectric actuators in conjunction with pressure or acceleration sensors in structural sound radiation control with the use of a feedforward control approach (Chapter 3), (3) the optimization of the locations of piezoelectric actuators in structural sound radiation control (Chapter 4).

5.1.1 Category (1)

A strain energy model (SEM) for laminate beams with embedded or attached, finite-length, distributed actuators was first developed and then extended to a two-dimensional case, i.e., a laminate plate, based upon the classical laminate plate theory (CLPT) with the use of Heaviside functions to represent the size and location of distributed actuators. The SEM was verified and compared to a finite element formulation (FEM) (Robbin and Reddy, 1990) and an analytical approach (Clark, Fuller, and Wicks, 1990a) based upon the assumption of spherical pure bending (SPBM) for both static and dynamic analyses in the case of one-dimensional pure bending. Results show a favorable agreement between the SEM and the FEM. Also, the SEM is a more accurate model than the SPBM over a wide range of thickness ratio, especially for low plate-actuator thickness ratios. Additionally, the SEM was also compared favorably to the CLPT (Wang and Rogers, 1991b) and the SPBM (Dimitriadis, Fuller and Rogers, 1991) for the case of two-dimensional pure bending. The proposed model, SEM (Wang and Rogers, 1991a), provides a general formulation to determine the equivalent external forces or moments induced by actuators attached or embedded in any layer or location of laminate beams or plates. The SEM can be applied to determine the equivalent external forces or moments induced by the distributed actuators used in structural vibration and sound radiation control.

5.1.2 Category (2)

Chapter 3 presents the analysis of active control of sound radiation from a baffled, simply-supported, rectangular plate subjected to a harmonically excited disturbance with

the use of multiple piezoelectric actuators in conjunction with distributed or discrete pressure and acceleration error sensors. The SEM is applied to determine the control force induced by piezoelectric actuators. Plate vibration is first examined and then used in conjunction with Rayleigh Integral and a stationary phase approach to determine radiated sound pressure in the near- and far-fields. The linear quadratic optimal control theory (LQOCT) is then applied to obtain the optimal control voltages to the piezoelectric actuators, while four forms of cost functions are considered. The cost functions are constructed based on the use of: (1) distributed pressure sensors, (2) discrete pressure sensors, (3) distributed acceleration sensors and (4) discrete acceleration sensors. Several special topics associated with structural acoustic characteristics, including (1) Plate Transmission Loss, (2) Time-average intensity, (3) Plate wavenumber analysis and (4) Plate radiation efficiency, are discussed to further study the control mechanism and effectiveness. Study cases are then presented and discussed. Some important results are summarized as follows:

1. The potential of using multiple piezoelectric actuators in structural sound radiation control is demonstrated.
2. Multiple piezoelectric actuators generally have better sound radiation control characteristics than single actuator, and the proper choice of the number and location of actuators are critical to effective structural sound radiation control.
3. Point force actuators perform slightly better than piezoelectric actuators; however, piezoelectric actuators possess a number of practical advantages, such as light weight, low cost and compactness, over point force transducers.

4. The near-field pressure and intensity distributions provide further insight into the mechanisms associated with the active structural control. This will lead to a design strategy of near-field pressure sensors having the same effect as far-field microphone sensors.
5. Distributed sensors which can reveal global system response are generally better than discrete sensors which can only provide discrete point responses; also, in practice, only a limited number of discrete sensors can be used. Pressure sensors, which can provide information of acoustic coupling between mechanical vibration and sound radiation, are superior to acceleration sensors, which can only provide the structural response. Therefore, to design a distributed near-field pressure sensor will be favorable for active noise control upon consideration of performance and practical use.

5.1.3 Category (3)

Chapter 4 develops a general formulation of optimization problem for the placement of distributed actuators in adaptive feedforward control for ASAC. The selection of objective function and identification of design variables and physical constraints are discussed separately. A case study for the optimal placement of multiple fixed-size piezoelectric actuators in sound radiation control is presented. A solution strategy is proposed to calculate the applied voltages to piezoelectric actuators with the use of linear quadratic optimal control theory. The optimal location of piezoelectric actuators is then determined by minimizing the objective function which is defined as the sum of the mean square sound pressures measured by a number of error microphones. The optimal

location of piezoelectric actuators for sound radiation control is determined for different excitation frequencies. Particularly, the optimal placement of multiple piezoelectric actuators for both on- and off-resonance excitation is presented. Results show that the optimally located piezoelectric actuators provide better sound radiation control than those whose position is arbitrarily selected. This work leads to a design methodology for adaptive or intelligent material structures and systems with highly integrated actuators and sensors.

5.2 Recommendations

Intelligent (“adaptive” or “smart”) materials structures and systems which are highly integrated with embedded or attached actuators and sensors have generated great interest for use in sound and vibration control. Distributed actuators and sensors have been increasingly developed and applied to the structural vibration and sound radiation control. Fast processible microprocessors are also available for implementation of adaptive versions of the feedforward algorithm with fast response time. Therefore, the “adaptive, smart, or intelligent material structures”, which are structures integrated with actuators/sensors under the direction of smart algorithms, have become a new era in active noise control. The work presented in this thesis has analytically demonstrated the fundamental use of such “smart” structures in structural sound radiation control by considering each element and then integrating them into a cohesive system designed to achieves a task: in this case, control of structurally radiated sound. As this new technology is in its early development, there are many topics of interest for future researches. A few further interesting such topics are recommended as follows:

1. Investigation of mechanical and acoustic coupling between distributed actuators/sensors and structures:

Plates, as plants, have been considered through out this thesis; however, other structures, used in practice such as cylinders and shells, are also of interest. In addition to including the shear and rotary inertia effects into the SEM for beams and plates, it is also of interest to expand the SEM into a three-dimensional shell problem. As discussed, near-field distributed pressure sensors are desirable for efficient active noise control. While the SEM is developed particularly for the case of distributed strain actuators, the formulation of sensor equations is also of concern. Undoubtedly, it is necessary and extremely important to fully understand the mechanical and acoustic coupling between actuators/sensors and structures so as to efficiently perform active noise control with compact transducers.

2. Hybrid active and passive control of structural sound radiation

This thesis recommends the use of compact distributed actuators (piezoceramic materials) to actively control sound radiation of elastic structures. Besides developing and applying other forms of distributed actuators in sound radiation control, it is also considerably advantageous to combine the technologies of active and passive control, for example, stiffened structures with the use of active mean forces, composite structures with piezoelectric configured as damping materials integrated with embedded induced strain actuators and sensors, and so on.

3. Optimal placement of distributed actuators/sensors in active control systems

As discussed, the location of actuators and sensors plays an important role in the performance of active control systems. Although much literature deals with the optimal placement of actuators and sensors in feedback control system for vibrations, little, if any, deals with the optimal placement of the distributed actuators and sensors in feedforward control. While the technology of adaptive smart material structures is growing, the placement of actuators and sensors embedded in structures is becoming an increasingly important issue. For future work, not only the optimal placement of actuators, as shown in Chapter 4, but also the optimal placement of sensors should be considered in the active noise control approach.

4. Single frequency control extended to broadband frequency control

Harmonically driven single frequency disturbance is assumed for all of the analytical work of this thesis; however, in practice, the disturbance can be random or broadband in nature. It would be of a great interest to extend the current work to broadband frequency excitation. This could be achieved by using the principal of superposition of response. As shown, the optimal location of actuators is dependent on the excitation frequency. Therefore, to find the optimal location for actuators and sensors associated with random disturbances will be desirable and of great practical interest.

Appendix A. Nomenclature

$[A]$	=	extensional stiffnesses
A	=	sound pressure distribution function for control source
\hat{A}	=	plate displacement distribution function for control source
a_1, a_2, b_1, b_2	=	location of uniformly distributed pressure
$[B]$	=	bending-twist coupling stiffnesses
B	=	sound pressure distribution function for primary source
\hat{B}	=	plate displacement distribution function for primary source
\mathbf{B}	=	positive definite approximation of the Hessian
b	=	beam width
b_a	=	actuator width
C_0	=	induced bending moment coefficient (SPBM) (Dimitriadis, Fuller and Rogers, 1989b)
C'_0	=	induced bending moment coefficient (CLPT) (Wang and Rogers, 1990b)
C''_0	=	induced bending moment coefficient (SEM) (Chapter 2)
C_{x_i}, C_{y_i}	=	size of the i -th piezoelectric actuator

c	=	sound speed in air
$[D]$	=	bending stiffnesses
D	=	flexural rigidity
$\{d\}$	=	piezoelectric strain coefficient vectors
$(d_{ij})_k$	=	piezoelectric strain coefficient for the k-th layer actuator patch
\mathbf{d}	=	design variables for sub-problem
$[E]$	=	actuator extensional stiffnesses
E	=	Young's modulus of an isotropic plate
E_{a_k}	=	Young's modulus of the k-th actuator
E_i	=	Young's modulus of the i-th layer lamina for beam
$[F]$	=	actuator bending-twisting stiffnesses
F	=	amplitude of point force
f	=	objective function
G	=	amplitude of primary source
\bar{G}	=	amplitude vector of primary source
g	=	constraint function
H	=	amplitude of control source
\bar{H}	=	amplitude vector of control source
$H(x - x_0)$	=	Heaviside function
h	=	thickness of laminate plate
h_k	=	thickness of the k-th layer lamina
I	=	moment of inertial of the beam
I_m, I_n	=	functions derived from Rayleigh's Integral solution (Roussos, 1985)
I_{mn}	=	$I_m I_n$
\bar{I}_m, \bar{I}_n	=	functions of modal force for incident plane wave (Roussos, 1985)
I_{z12}	=	time-averaged intensity in the z-direction

K	=	induced strain constant for pure bending of piezoelectric actuation (Chapter 2)
K	=	function derived from Rayleigh's Integral solution (Roussos, 1985) (Chapter 3)
K_k	=	induced strain constant of the k-th actuator for beams
$K_{k_x}, K_{k_y}, K_{k_{xy}}$	=	induced strain constant of the k-th actuator for plates
L	=	length of beam
L_a	=	length of actuator
L_x, L_y	=	length and width of laminate plate
$\{M\}$	=	resultant moment vector
M_{a_k}	=	bending moment induce by the k-th actuator
M_{eq}	=	equivalent bending moment induce by actuators
M_{eq}^k	=	equivalent bending moment induce by the k-th actuator
M_x, M_y, M_{xy}	=	resultant moments
m	=	number of actuator patches
$\{N\}$	=	resultant force vector
N_{acc}	=	number of accelerometers
N_{mike}	=	number of microphones
N_s	=	number of primary sources
N_c	=	number of control sources
N_x, N_y, N_{xy}	=	resultant forces
n	=	number of laminae
P_{a_k}	=	axial force induce by the k-th actuator
P_{eq}	=	equivalent axial force induce by actuators
P_{eq}^k	=	equivalent axial force induce by the k-th actuator
P_i	=	amplitude of incident plane wave

P_m	=	modal force for beam lateral vibration by piezoelectric actuation
P_{mn}	=	modal force for plate lateral vibration
P_{mn}^a	=	modal force induced by piezoelectric actuators
P_{mn}^f	=	modal force induced by point forces
P_{mn}^{Pi}	=	modal force induced by incident plane wave
P_{mn}^q	=	modal force induced by uniformly distributed pressure
p_c	=	sound pressure due to control sources (piezoelectric actuators)
p_n	=	sound pressure due to primary sources
p_t	=	total sound pressure
$[\bar{Q}]$	=	material properties matrix in (x,y,z) coordinates
$[Q]$	=	material properties matrix in (1,2,3) coordinates
\bar{Q}_{ij}	=	material properties in (x,y,z) coordinates
$(\bar{Q}_{ij})_k$	=	material properties of the k-th actuator in (x,y,z) coordinates
Q_{ij}	=	material properties in (1,2,3) coordinates
Q_{mn}^n	=	modal function for primary source
Q_{mn}^c	=	modal function for control source
Q_n	=	transverse shear in the normal direction
$q(x,y,t)$	=	transverse load (Chapter 2)
q	=	amplitude of uniformly distributed pressure (Chapter 3)
$R_k(x,y)$	=	generalized location function of the k-th actuator patch
(R, θ, ϕ)	=	polar coordinates of radiating field
(R_i, θ_i, ϕ_i)	=	the i-th microphone coordinates
TL	=	plate transmission loss
t	=	time constant
t_a	=	thickness of actuator patch
t_{a_k}	=	thickness of the k-th actuator patch

t_b	=	thickness of beam
u_{mn}	=	plate velocity corresponding to the (m,n) mode
(u_0, v_0, w_0)	=	plate midplane displacement, also expressed as (u, v, w)
V	=	applied voltage to piezoceramic patch
V_k	=	voltage applied to the k -th actuator patch
$\tilde{V}(\kappa_x, \kappa_y)$	=	wavenumber transform of plate velocity
W_m	=	modal amplitude for beam lateral vibration
W_{mn}	=	modal amplitude for plate lateral vibration
W_{mn}^c	=	modal amplitude for control sources
W_{mn}^n	=	modal amplitude for primary sources
w_c	=	plate lateral displacement due to control source
w_n	=	plate lateral displacement due to primary source
w_t	=	total plate lateral displacement
w_{mn}	=	plate lateral displacement due to the (m,n) mode
(x, y, z)	=	the laminated plate coordinates (Chapter 2)
(x, y, z)	=	Cartesian coordinates of radiating field (Chapter 3)
x_f, y_f	=	location of point force
$(x_i)_k, (y_i)_k$	=	position coordinates of actuator patches, $(i = 1, 2), (k = 1, 2, \dots, M)$
\bar{x}_i, \bar{y}_i	=	central location of the i -th piezoelectric actuator
x_p, y_p	=	location of accelerometer
x_1, x_2, y_1, y_2	=	location of piezoceramic patch
\mathbf{x}	=	design variables
\mathbf{x}_l	=	lower bound of design variables
\mathbf{x}_u	=	upper bound of design variables
z_k	=	thickness coordinate of the k -th layer
z_k^{+}, z_k^{-}	=	coordinate of actuator patch in z -direction

z_{ak}	=	coordinate of the k-th actuator
(1, 2, 3)	=	the principal material coordinates for a lamina
γ	=	κ/κ_p , wavenumber ratio
∇	=	divergence operator
Δz_{12}	=	distance between point 1 and 2
$\delta(x - x_0)$	=	Delta function
$\delta'(x - x_0)$	=	first derivative of Delta function
$\{\varepsilon\}$	=	total strain vector in (x,y,z) coordinates
$\{\bar{\varepsilon}\}$	=	total strain vector in (1,2,3) coordinates
$\{\varepsilon^m\}$	=	mechanical strain vector
$\{\varepsilon^0\}$	=	midplane mechanical strain vector
$\varepsilon_x, \varepsilon_y, \gamma_{xy}$	=	normal and shear strains
$\varepsilon_x^m, \varepsilon_y^m, \gamma_{xy}^m$	=	mechanical normal and shear strains
$\varepsilon_x^0, \varepsilon_y^0, \gamma_{xy}^0$	=	midplane normal and shear strains
$\varepsilon_1, \varepsilon_2, \gamma_{12}$	=	normal and shear strains in (1,2,3) coordinates
ε_d	=	assumed linear strain distributions below the actuator's location
ε_u	=	assumed linear strain distributions above the actuator's location
ε_k^+	=	magnitude of the assumed linear strain at the actuator's location
$\{\kappa\}$	=	midplane mechanical curvature vector
κ	=	ω/c , acoustic wavenumber
κ_{mn}	=	primary structural wavenumber
κ_m, κ_n	=	structural normal mode wavenumber
κ_p	=	free structural wavenumber
κ_x, κ_y	=	structural modal wavenumber (Chapter 3)
$\kappa_x, \kappa_y, \kappa_{xy}$	=	midplane mechanical curvature vector (Chapter 2)
$\{\Lambda\}$	=	actuator strain vector

Λ	=	$d_{31}V/t_a$, free strain of piezoceramic patch
Λ_k	=	free normal strain of the k -th actuator
$\Lambda_x, \Lambda_y, \Lambda_{xy}$	=	actuator normal and shear strain
λ	=	acoustic wavelength in air
λ_k	=	a force function for the k -th actuator
Π_i	=	radiated power due to incident plane wave
Π_{mn}	=	radiated power due to the (m,n) mode
Π_t	=	total radiated power
ρ	=	equivalent density of laminate (Chapter 2)
ρ	=	mass density of air (Chapter 3)
ρ_k	=	density of the k -th layer lamina
ρ_p	=	mass density of plate
ν	=	Poisson ratio of plate
ν_a	=	Poisson ratio of actuator
ξ, η	=	plate coordinates from edges of the plate
ξ', η'	=	transferred plate coordinates from the center of the plate
$\{\sigma\}$	=	stress vector in (x,y,z) coordinate
$\{\bar{\sigma}\}$	=	stress vector in (1,2,3) coordinate
σ	=	assumed stress distribution (Chapter 2)
σ	=	average radiation efficiency (Chapter 3)
σ_{a_k}	=	normal stress in the k -th actuator
σ_{mn}	=	the (m,n) mode radiation efficiency (Chapter 3)
$\sigma_x, \sigma_y, \sigma_{xy}$	=	normal and shear stress
Φ_p	=	cost function for continuous pressure sensor
Φ_w	=	cost function for continuous acceleration sensor
Ψ	=	nondimensional ratio of physical properties of beam and actuator

Ψ_p	=	cost function for discrete pressure sensor
Ψ_w	=	cost function for discrete acceleration sensor
ω	=	excitation frequency
ω_c	=	critical frequency
ω_m	=	natural frequency of beam
ω_{mn}	=	natural frequency of plate
ω_{mn}^c	=	modal critical frequency

Superscript

a	=	piezoelectric actuator
c	=	control
f	=	point force
m	=	mechanical
n	=	primary
P_i	=	incident plane wave
q	=	uniformly distributed force
0	=	midplane

Subscript

a	=	actuator
b	=	beam
k	=	k-th layer
n	=	normal direction
s	=	tangential direction

References

1. Bailey, T. and J. E. Hubbard, Jr., 1985, "Distributed Piezoelectric Polymer Active vibration Control of a Cantilever Beam," *AIAA Journal of Guidance and Control*, 8 (5), pp. 606-610.
2. Berry, A., J.-L. Guyada, and J. Nicolas, 1990, "A General Formulation for the Sound Radiation from Rectangular, Baffled Plates with Arbitrary Boundary Conditions," *Journal of the Acoustical Society of American*, Vol. 88(6), pp. 2792-2802.
3. Bullmore, A J., P. A. Nelson, A. R. D. Curtis, and S. J. Elliott, 1987, "The Active Minimization of Harmonic Enclosed Sound Fields, Part II: A Computer Simulation," *Journal of Sound and Vibration*, 117(1), pp.15-33.
4. Burdisso, R. A., and C. R. Fuller, 1990, "Theory of Feed-Forward Controlled System Eigenproperties," submitted to *Journal of Sound and Vibration*.

5. Chang, M. I. J., and T. T. Soong, 1980, "Optimal Controller Placement in Modal Control of Complex Systems," *Journal of Mathematical Analysis and Applications*, **75**, pp. 340-358.
6. Clark, R. L., C. R. Fuller, and A. L. Wicks, 1990a "Characterization of Multiple Piezoelectric Actuators for Structural Excitation," submitted to *Journal of the Acoustical Society of American*.
7. Clark, R. L., and C. R. Fuller, 1990b, "An Experimental Study of the Use of PVDF Piezoelectric Sensors in Active Structural Acoustic Approaches," *Journal of the Acoustical Society of American*, Vol. 88(s1), p. s148.
8. Claus, R. O, B. D. Zimmermann, K. A. Murphy, and A. M. Goette, 1989, "Distributed Strain Sensing in Structures Using Optical Fiber Time Domain Methods," *Proceeding of ASME Failure Prevention and Reliability Conference* , Montreal, pp. 251-254.
9. Collins, S. A., R. J. Notestine, C. E. Padilla, M. Ramey, E. Schmitz, and A. H. von Flotow, 1990, "Design, Manufacture, and Application to Space Robotics of Distributed film sensors," *Proceedings of the AIAA/ASME/ASCE/AHS 31st Structures, Structural Dynamics and Materials Conference*, Long Beach, CA, April 2-4, Paper No. AIAA-90-0949.
10. Cox, D. E., 1990, "Active Control of Flexible Structures Using Fiber Optic Modal Domain Sensors," Master Thesis, Electrical Engineering, VPI&SU, Blacksburg, Virginia.

11. Crawley, E. F., and J. de Luis, 1987, "Use of Piezoelectric Actuators as Elements of Intelligent Structures," *AIAA Journal*, **25** (10), pp. 1373-1385.
12. Deffayet, C., and P. A. Nelson, 1988, "Active Control of Low Frequency Harmonic Sound Radiated by a Finite Panel," *Journal of the Acoustical Society of America*, **84** (6), pp. 2192-2199.
13. Dimitriadis, E. K., and C. R. Fuller, 1989, "Investigation on Active Control of Sound Transmission Through Elastic Plates Using Piezoelectric Actuators," AIAA paper 89-1062.
14. Dimitriadis, E. K., C. R. Fuller, and C. A. Rogers, 1991, "Piezoelectric Actuators for Distributed Noise and Vibration Excitation of Thin Plates," *Journal of Vibration and Acoustics*, **113**, pp. 100-107.
15. Elliott, S. J., I. M. Stothers, and P. A. Nelson, 1987, "A Multiple Error LMS Algorithm and Its Application to the Active Control of Sound and Vibration," *IEEE Transactions on Acoustics, Speech, and Signal Processing*, Vol. ASSP-35, No. 10, October.
16. Fahy, F., 1985, *Sound and Structural Vibration: Radiation, Transmission and Response*, Academic Press, Inc., Orlando, Florida.

17. Fanson, J. L., and J. C. Chen, 1986, "Structural Control by the Use of Piezoelectric Active Members," *Proceedings of NASA/DOD Control-Structures Interaction Conference*, NASA CP-2447, Part II.
18. Fuller, C. R., and J. D. Jones, 1987, "Influence of Sensor and Actuator Location on the performance of Active Control Systems," 87-WA/NCA-9, presented at the ASME Annual Meeting, Boston, Massachusetts, December.
19. Fuller, C. R., 1988, "Analysis of Active Control of Sound Radiation from Elastic Plates by Force Inputs," *Proceedings of Inter-Noise 88*, 1061-1064.
20. Fuller, C. R., R. J. Silcox, V. L. Metcalf, and D. E. Brown, 1989, "Experiments on Structural Control of Sound Transmitted Through an Elastic Plate," *Proceeding of the American Control Conference*, pp. 2079-2084.
21. Fuller, C. R., 1990a, "Active Control of Sound Transmission/Radiation from Elastic Plates by Vibration Inputs. I Analysis." *Journal of Sound and Vibration*, **136** (1), pp.1-15.
22. Fuller, C. R., and R. A. Burdisso, 1990b, "A Wave Number Domain Approach to the Active Control of Sound and Vibration," to appear in *Journal of Sound and Vibration*.
23. Fuller, C. R., C. H. Hansen, and S. D. Snyder, 1990c, "Active Control of Sound Radiation From a Vibrating Rectangular Panel by sound sources and vibration inputs: An Experimental Comparison," to appear in *Journal of Sound and Vibration*.

24. Gibbs, G. P., and C. R. Fuller, 1990, "Experiments on Active Control of Vibrational Power Flow Using Piezoceramic Actuators and Sensors," *Proceedings of the AIAA/ASME/ASCE/AHS 31st Structures, Structural, Dynamics and Materials Conference*, Paper No. AIAA-90-1132, Long Beach, CA, April 2-4.
25. Gibbs, G. P., and C. R. Fuller, 1990, "Excitation of Thin Beam Using Asymmetric Piezoelectric Actuators," *Journal of the Acoustical Society of America*, Vol. 89(4), p. 1890 (abstract only).
26. Ha, S. K., and F.-K. Chang, 1990, "Finite Element Modeling of the Response of Laminated Composites with Distributed Piezoelectric Actuators," *Proceedings of the AIAA/ASME/ASCE/AHS 31st Structures, Structural Dynamics and Materials Conference*, Long Beach, CA, April 2-4, Paper No. AIAA-90-1131.
27. Hamidi, M., and J.-N. Juang, 1981, "Optimal Control and Controller Location for Distributed Parameter Elastic Systems," *Proceedings of the 20th IEEE conference on Decision and Control*, pp. 502-506.
28. Hubbard, Jr., J. E., 1987, "Distributed Sensors and Actuators for Vibration Control in Elastic Components," *Noise-Con 87*, pp.407-412.
29. Im, S., and S. N. Alturi, 1989, "Effects of a Piezo-Actuator on a Finitely Deformed Beam Subjected to General Loading," *AIAA Journal* Vol. 27, No. 12, December, pp. 1801-1807.

30. IMSL, 1989, *IMSL Math/Library*, IMSL Problem-Solving System Software System.
31. Jia, J., 1990, "Optimization of Piezoelectric Actuator Designs in Vibration Control Systems," PhD Thesis, Department of Mechanical Engineering, VPI&SU, Blacksburg, Virginia.
32. Jones, J. D., and C. R. Fuller, 1989, "Active Control of Sound Fields in Elastic Cylinders by Multiple Forces," Vol. 27, No. 7, pp. 845-852.
33. Jones, R. M., 1975, *Mechanics of Composite Materials*, McGraw-Hill Book Co., New York.
34. Juang, J.-N., and G. Rodriguez, 1979, "Formulations and Applications of Large Structure Actuator and Sensor Placements," *Proceedings of the Second VPI&SU/AIAA Symposium on Dynamics and Control of Large Flexible Spacecraft*, Blacksburg, Virginia, June.
35. Junger, M. C., and D. Feit, 1986, *Sound, Structures and their Interaction*, Second edition, The MIT Press, Cambridge, Massachusetts.
36. Krishnappa, G., and J. M. McDougall, 1989. "Sound Intensity Distribution and Energy Flow in the Nearfield of a Clamped Circular Plate," *Journal of Vibration, Acoustics, Stress, and Reliability in Design* , Vol. 111, pp. 465-471, October.

37. Kristiansen, U. R., 1981, "A Numerical Study of the Acoustic Intensity Distribution Close to a Vibrating Membrane," *Journal of Acoustical Society of America*, Vol. 76, No. 2, pp. 305-309.
38. Lazarus, K. B., and E. F. Crawley, 1989, *Induced Strain Actuation of Composite Plates*, GTL Report No. 197, Massachusetts Institute of Technology, Cambridge, Massachusetts.
39. Lee, C.-K., 1987, "Piezoelectric Laminates for Torsional and Bending Modal Control: Theory and Experiment," Doctoral Dissertation, Cornell University.
40. Lee, C.-K., 1990a, "Theory of Laminated Piezoelectric Plates for the Design of Distributed Sensors/Actuators. Part I: Governing Equations and Reciprocal Relationships," *Journal of the Acoustical Society of America*, **87** (3), pp. 1144-1158.
41. Lee, C.-K., and F. C. Moon, 1990b, "Modal Sensors/Actuators," *Journal of Applied Mechanics*, Vol. 57, June, pp. 434-441.
42. Lester, H. C., and C. R. Fuller, 1987, "Mechanisms of Active Control for Noise Inside a Vibrating Cylinder," *Noise-Con 87*, pp. 371-376.
43. Lester, H. C., and C. R. Fuller, 1990, "Active Control of Propeller Induced Noise Fields Inside a Flexible Cylinder," *AIAA Journal*, Vol. 28, No. 8, pp. 1374-1380.
44. Liang, C., J. Jia, and C. A. Rogers, 1989, "Behavior of Shape Memory Alloy Reinforced Composite Plates Part II: Results," AIAA paper 89-1331.

45. Lueg, 1936, "Process of Silencing Sound Oscillator," U. S. Patent No. 2,043,416.
46. Maidanik, G., 1974, "Vibrational and Radiative Classifications of Modes of a Baffled Finite Panel," *Journal of Sound and Vibration*, Vol. 34, No. 4, pp.447-455.
47. Mathur, G. P., B. K. Gardner, and P. L. Burge, 1990, "Wavenumber-Frequency Characteristics of Air and Structure Borne Sound Radiation by Finite Plates," *Proceeding of International Congress on Recent Developments in Air- and Structure-Borne Sound and Vibration*, March 6-8, Auburn University, Alabama.
48. Meirovitch, L., and M. A. Norris, 1984, "Vibration Control," *Proceeding of Inter-Noise 84*, pp. 477-482.
49. Meirovitch, L., and S. Thangjitham, 1990a, "Control of Sound Radiation From Submerged Plates," *Journal of Acoustical Society of America*, **88** (1), July, pp. 402-407.
50. Meirovitch, L., and S. Thangjitham, 1990b, "Active Control of Sound Radiation Pressure," *Journal of Vibration and Acoustics*, Vol. 112, April, pp. 237-244.
51. Norris, G. A., and R. E. Skelton, 1989, "Selection of Dynamic Sensors and Actuators in the Control of Linear Systems," *Journal of Dynamic Systems, Measurement, and Control*, Vol. 111, September, pp. 389-397.

52. Pettersen, O. K. O., 1979, "A Procedure for Determining the Sound Intensity Distribution Close to a Vibrating Surface," *Journal of Sound and Vibration*, 66(4), pp. 626-629.
53. Piezo Systems, 1987, *Piezoelectric Motor/Actuator Kit Manual*, Piezo Electric Products, Inc., Advanced Technology Group, Cambridge, Maryland.
54. Pilkey, W. D., and P. Y. Chang, 1978, *Modern Formulas for Statics and Dynamics*, McGraw-Hill, Inc., New York, pp. 330-338.
55. Robbins, D. H., and J. N. Reddy, 1990, *Finite Element Analysis of Piezoelectrically Actuated Beams*, personal correspondence.
56. Roussos, L. A., 1985, "Noise Transmission Loss of a Rectangular Plate in an Infinite Baffle," *NASA Technical Paper 2398*.
57. Saunders, W. R., H. H. Robertshaw, and C. A. Rogers, 1990, "Experimental Studies of Structural Acoustical Control for a Shape Memory Alloy Composite Beam," AIAA Paper No. 90-1090.
58. Simpson, M. A., T. M. Luong, C. R. Fuller, and J. D. Jonse, 1989, "Full Scale Demonstration Tests of Cabin Noise Reduction Using Active Vibration Control," AIAA paper 89-1074.

59. Thompson, J. K., and D. R. Tree, 1981, "Finite Difference Approximation Errors In Acoustic Intensity Measurements," *Journal of Sound and Vibration*, 75 (2), pp. 229-238.
60. Tzou, H. S. and C. I. Tseng, 1990, "Distributed Dynamic Identification and Controls of Flexible Shells," *Proceedings of the AIAA/ASME/ASCE/AHS 31st Structures, Structural Dynamics and Materials Conference*, Long Beach, CA, April 2-4, Paper No. AIAA-90-1089.
61. Wallace, C. E., 1972, "Radiation Resistance of a Rectangular Panel," *Journal of Acoustical Society of America*, Vol. 51, pp. 946-952.
62. Wang, B.-T., E. K. Dimitriadis, and C. R. Fuller, 1989, "Active Control of Panel-Radiated Noise Using Multiple Piezoelectric Actuators," *Journal of the Acoustical Society of America*, Vol. 86(s1), p. s84.
63. Wang, B.-T., E. K. Dimitriadis, and C. R. Fuller, 1990, "Active Control of Structurally Radiated Noise Using Multiple Piezoelectric Actuators," *Proceedings of the AIAA/ASME/ASCE/AHS 31st Structures, Structural Dynamics and Materials Conference*, Long Beach, CA, April 2-4, Paper No. AIAA-90-1172.
64. Wang, B.-T. and C. A. Rogers, 1991a, "Modeling of Finite-Length Spatially Distributed Induced strain Actuators for Laminate Beams and Plates," *Journal of Intelligent Material Systems and Structures*, Vol. 2, No. 1, pp. 38-58.

65. Wang, B.-T. and C. A. Rogers, 1991b, "Laminate Plate Theory for Spatially Distributed Induced strain Actuators," *Journal of Composite Materials*, Vol. 25, No. 4, pp. 433-452.
66. Wang, B.-T. and C. R. Fuller, 1991b, "Near-Field Pressure, Intensity and Wavenumber Distributions for Active Structure Control of Plate Radiation: Theoretical Analysis," submitted to *Journal of Sound and Vibration*.
67. Whitney, J. M., 1989, *Structural Analysis of Laminated Anisotropic Plates*, Technomic Publishing Co., Inc., Lancaster, Pennsylvania.

Vita

Bor-Tsuen Wang, also known as Peter, was born on October 24, 1961, in Taipei, Taiwan. He graduated from Hsinpu Junior College of Technology, Taipei, Taiwan, in June, 1981. After performing two-year obligatory military service, he joined Tamkang University, Taipei, Taiwan, and received a Bachelor of Science degree in Mechanical Engineering in June, 1985. He began graduate studies in Mechanical Engineering of Virginia Polytechnic Institute and State University in 1986. As soon as he received his Master of Science degree in May, 1988, he continued to pursue his Doctoral degree. This dissertation is the partial requirement for the Doctoral degree and completed in June, 1991. Upon his graduation, the author has accepted a faculty position in the Department of Mechanical Engineering of National Pingtung Polytechnic Institute, Taiwan, Republic of China.

A handwritten signature in black ink that reads "Bor-Tsuen Wang". The signature is written in a cursive, flowing style.